KINETIC MODELING AND MECHANISMS FOR CATALYTIC UPGRADE OF BIOMASS DERIVATIVES

by

Matthew A. Christiansen

A dissertation submitted to the Faculty of the University of Delaware in partial fulfillment of the requirements for the degree of Doctor of Philosophy in Chemical Engineering

Summer 2014

© 2014 Matthew A. Christiansen
All Rights Reserved

UMI Number: 3642300

All rights reserved

INFORMATION TO ALL USERS
The quality of this reproduction is dependent upon the quality of the copy submitted.

In the unlikely event that the author did not send a complete manuscript
and there are missing pages, these will be noted. Also, if material had to be removed,
a note will indicate the deletion.

UMI 3642300

Published by ProQuest LLC (2014). Copyright in the Dissertation held by the Author.

Microform Edition © ProQuest LLC.
All rights reserved. This work is protected against
unauthorized copying under Title 17, United States Code

ProQuest LLC.
789 East Eisenhower Parkway
P.O. Box 1346
Ann Arbor, MI 48106 - 1346

KINETIC MODELING AND MECHANISMS FOR

CATALYTIC UPGRADE OF BIOMASS DERIVATIVES

by

Matthew A. Christiansen

Approved: _____

Abraham M. Lenhoff, Ph.D.
Chair of the Department of Chemical and Biomolecular Engineering

Approved: _____

Babatunde A. Ogunnaike, Ph.D.
Dean of the College of Engineering

Approved: _____

James G. Richards, Ph.D.
Vice Provost for Graduate and Professional Education

I certify that I have read this dissertation and that in my opinion it meets the academic and professional standard required by the University as a dissertation for the degree of Doctor of Philosophy.

Signed: _____

Dionisios G. Vlachos, Ph.D.
Professor in charge of dissertation

I certify that I have read this dissertation and that in my opinion it meets the academic and professional standard required by the University as a dissertation for the degree of Doctor of Philosophy.

Signed: _____

Michael T. Klein, Sc.D.
Member of dissertation committee

I certify that I have read this dissertation and that in my opinion it meets the academic and professional standard required by the University as a dissertation for the degree of Doctor of Philosophy.

Signed: _____

Bingjun Xu, Ph.D.
Member of dissertation committee

I certify that I have read this dissertation and that in my opinion it meets the academic and professional standard required by the University as a dissertation for the degree of Doctor of Philosophy.

Signed: _____

Raymond J. Gorte, Ph.D.
Member of dissertation committee

I certify that I have read this dissertation and that in my opinion it meets the academic and professional standard required by the University as a dissertation for the degree of Doctor of Philosophy.

Signed: _____

Douglas J. Doren, Ph.D.
Member of dissertation committee

ACKNOWLEDGMENTS

First of all, I thank my advisor Professor Dion Vlachos for all of the mentoring, instruction, and time he provided while I pursued my degree at UD. His efforts to provide a well-rounded education for the members of his group are seldom duplicated in academia, and it has been a privilege to work with him. I am also grateful to Professors Jingguang Chen, Michael Klein, Bingjun Xu, Raymond Gorte, and Douglas Doren who, having each served as members of my committee at various times, provided valuable guidance and feedback. I thank the National Science Foundation and the U.S. Department of Energy for funding my research, the latter in connection with the Catalysis Center for Energy Innovation (CCEI). I am also grateful to have had access to computational resources through the Teragrid project, the Extreme Science and Engineering Discovery Environment (XSEDE), and the National Energy Research Scientific Computing Center (NERSC).

A number of other individuals have been especially helpful while I have carried out my graduate work. Sheila Boulden, Gina Frushon, Marguerite Mahoney, and Kathie Young have collectively helped me with the ins and outs of logistical and departmental matters more times than I can count, for which I am very grateful. I thank Dr. Jeffrey Frey and many others in UD IT for their efforts to administer the computer clusters and answer my questions. I sincerely thank Professor Giannis Mpourmpakis, Professor Michail Stamatakis, Professor Rafael Catapan, Dr. Stavros Caratzoulas, and Dr. Glen Jenness for the wonderful collaborations and discussions we have had. I am very grateful to Dr. Michael Salciccioli for technical guidance as I

learned microkinetic modeling and for regular mentoring discussions. Dr. Nasser Abukhdeir, Dr. Ying Chen, Dr. Danielle Hansgen, Dr. Bill Lonergan, Dr. Jake McGill, Dr. Matthew Mettler, Nima Nikbin, Dr. Jonathan Sutton, Dr. Sarah Tupy, and Vassili Vorotnikov graciously offered their time for discussions and provided valuable guidance and advice on everything from coursework and calculations to paper writing and presentations. I also thank Hannah Phillips for the work she did during a summer research project.

On a personal note, I am very grateful to my family for their support as I have pursued my degree. My wife Carrie and my daughter Grace always encouraged and motivated me to do my best. Likewise, my parents David and Cindy taught me from early on to go after challenges and to persevere. I am also grateful to God, my Heavenly Father, for guidance and support in all aspects of my life.

TABLE OF CONTENTS

LIST OF TABLES

LIST OF FIGURES

ABSTRACT

The utilization of biomass as a renewable feedstock for commodity chemicals may be greatly benefitted by the successful development and application of heterogeneous catalysts for selective deoxygenation. This dissertation combines density functional theory (DFT) and microkinetic modeling to describe the kinetics and mechanisms of converting oxygenated hydrocarbons to commodity chemicals. The results of these studies provide fundamental descriptions of hydrogenation and dehydration, essential component chemistries of the overall hydrodeoxygenation (HDO) processes that lead to valuable chemical products.

HDO catalysts typically possess multiple catalytic active sites, including a metallic site and an acidic functionality. A clear understanding of the individual capabilities of each site is achieved by first studying them in isolation. H_2 generation and management are essential aspects of HDO processes, with generation kinetics thought to be primarily controlled by the metal sites. Those kinetics were explored via microkinetic modeling, using ethylene glycol as a bio-derived hydrogen donor molecule with a Pt catalyst. The H_2 formation rates from steam reforming of ethylene glycol are found to be well-described by a Pt-based mechanism, confirming the role of the metal sites in promoting this chemistry. Initial/early dehydrogenation of ethylene glycol controls the overall reaction rate, while water facilitates the downstream conversion of carbon monoxide into carbon dioxide without affecting the upstream (de)hydrogenation rates.

γ-Al_2O_3 is a well-known acidic heterogeneous catalyst support that has been used in HDO processes. Using DFT, the adsorption of several oxygenate probe molecules were explored on various crystallographic facets to understand how the binding strength is influenced by (1) the identity of the acid site, and (2) surface hydration. Further, ethanol in particular was selected to examine the mechanisms of dehydration and etherification on this material, in order to understand how the surface acidity promotes these reactions. Exposed Al sites exhibit Lewis acidity, while partial hydration of the surface creates possible Brønsted acid sites. The stability of ethanol adsorbed directly on Al sites was found to be superior to adsorption on a Brønsted-like site. The energetically preferred pathways for dehydration and etherification are concerted Lewis-catalyzed mechanisms, namely E2 mechanisms for dehydration and S_N2 mechanisms for etherification. The strength of adsorption and the magnitude of the reaction barriers may be strongly affected by the character of the Al site and the presence of co-adsorbed water. These effects are qualitatively and (in certain cases) quantitatively captured by a descriptor derived from the calculated electronic states of the γ-Al_2O_3 surface. In addition, kinetic dependencies identified through these calculations rationalize experimental selectivity trends to ethylene and diethyl ether.

The DFT results were subsequently used to parameterize a multi-site (Al and O) mean-field microkinetic model for ethanol dehydration and etherification. Trends in experimental reaction orders were captured successfully by both the full model and analytical reduced rate expressions, and the E2 and S_N2 mechanisms are the rate-controlling steps in the network. This demonstrates the applicability of the DFT mechanisms to powdered γ-Al_2O_3 catalysts and makes a promising case for using multi-site mean-field models to understand acid-catalyzed metal oxide chemistries.

Chapter 1

INTRODUCTION

1.1 Biomass Utilization for Chemicals Production

There are currently a number of different drivers motivating the development of renewable feedstocks for chemical processes. These drivers are highly intertwined with the factors that influence the greater energy industry, and include risks and general uncertainty in economics, geopolitics, and environmental changes [1]. A time-honored strategy for mitigating risk is portfolio diversification, and this is the approach that is spurring increased interest and pursuit of renewable resources [1].

As a major source of renewable carbon [2], biomass is currently the leading resource being explored as an alternative to conventional fossil fuel feedstocks. Considering biomass derived from forestry and agricultural sources (including potential yields from energy crops) in the United States, the demonstrated potential to serve as a chemical feedstock is vast and underutilized [3]. Among the various proposed uses for biomass is the production of commodity chemicals. One reason for this is that the expected supply of non-food biomass should be sufficient to make a significant contribution to renewable chemicals production (in contrast to fuels where the picture is less optimistic) [4]. Another reason is that biomass, especially lignocellulosic material, intrinsically contains many functional groups that are required for commodity chemicals. In reality this material possesses excess oxygen and chemical functionality when compared to the target compound. Thus, the key

challenge for utilizing it as a feedstock is to selectively remove undesired functionality while preserving the structure needed for the final product.

The specific chemical transformations that take place during feedstock upgrade naturally depend on the structure of the feedstock. Depending on the level of saturation, either dehydration or hydrogenolysis reactions (or both) will take place, the latter necessitating a supply of hydrogen to accompany the reactant. The term hydrodeoxygenation (HDO) is commonly applied to processes that utilize a hydrogen source to upgrade bio-derived feedstocks [5]. A number of successful catalytic processes capable of upgrading low-molecular-weight oxygenates have been demonstrated in literature [6-9]. Frequently these processes utilize supported metal catalysts that contain two types of catalytic sites, usually a metallic site paired with an acidic functionality (frequently a metal oxide). The reports of these findings generally emphasize the importance of acid sites for removing oxygen from the reacting substrate. Yet, besides this observation, there is little understanding of how these catalysts work and there is no rational or systematic method for selecting a good catalyst for a given feed. This suggests important opportunities for research into new or improved materials for selective upgrade of oxygenates.

1.2 Fundamental Kinetic Modeling: Capabilities and Challenges

Among the most important measures of the performance of a catalytic process are overall activity and selectivity. The identification of the set of relationships between these macroscopic reactor-level metrics and the molecular-level properties and events leads to fundamental insights for designing and controlling catalytic reactions. Establishing such connections across scales falls within the scope of an approach known as multiscale modeling. This approach encompasses a suite of

modeling and simulation methods, each of which provides information at a distinct set of length and time scales. The power of multiscale modeling is rooted in the systematic exchange of information between and among each of the individual simulations through a series of equations, approximations, and correlations. As a result, the computational challenge of describing phenomena spanning several orders of magnitude in length and/or time is overcome. An in-depth review of multiscale modeling of chemical reactions is available elsewhere [10].

Microkinetic modeling falls under the umbrella of multiscale modeling, and refers to the simulation of a chemical reaction utilizing "a detailed reaction mechanism of elementary-like processes occurring on a catalyst" [10]. This approach requires the specification of parameters (the number of which is proportional to the size of the mechanism) that can be obtained from multiple sources. State-of-the-art models rely on data obtained from quantum mechanical calculations using methods such as density functional theory (DFT). This data is used in conjunction with principles from transition state theory [11] and mean-field theory to compute rates and pass them into design equations of transport, flow, and chemistry, thereby ultimately simulating the behavior and performance of a chemical reactor. By basing its predictions on elementary-level processes, microkinetic modeling promises insights into reaction mechanisms that in turn may ultimately lead to principles and tools that guide catalyst selection or reactor design.

Mean-field models rely on mass action kinetics (see Chapter 2) and, therefore, possess no information about spatial configuration, assuming a uniform distribution of reactants and catalyst sites. A related assumption commonly applied in the microkinetic modeling literature is that all of the catalyst sites are identical (a single

type of site). Upon tuning key parameters in the mechanism, such models have demonstrated (occasionally remarkable) success in capturing experimental kinetic trends [12]. This single-site approach has been most frequently used to study supported monometallic catalysts, which consist of nanoparticles that almost certainly contain more than one type of metal site. Therefore, a two-part hypothesis to explain the success of these models is that (1) the metal is primarily responsible for the catalytic activity in the systems studied and (2) the reaction mechanism is qualitatively the same on the various metal sites.

Considering the evidence that multiple catalytic functions are at work on HDO catalysts (i.e., both metal and acid sites), it is improbable that a single-site model could explain the performance of such materials. Figure 1.1 demonstrates that supported metal catalysts may in fact exhibit considerable complexity in the number and type of sites present. Besides the metal sites, there may be acid sites of multiple strengths on the support, metal-support interfacial sites, and surface species exchange between sites enabled via surface diffusion. This depiction emphasizes the challenges involved in utilizing mean-field kinetics for modeling chemical reactions on HDO materials. In addition, it underscores that at a minimum, the development of kinetic models with multiple catalytic sites is required to represent these processes.

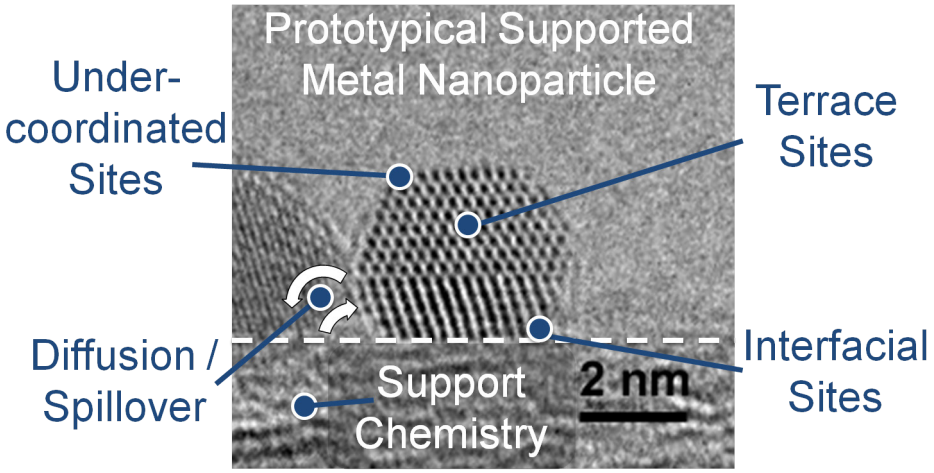

Figure 1.1: Illustration of the diversity of reaction sites present in supported metal nanoparticle catalysts. Nanoparticle image (Au on carbon support) used with permission from [13].

1.3 Dissertation Scope and Structure

At the current stage of research into catalytic HDO processes, the identity and roles of the individual catalytic site types are still unclear. Understanding of the mechanistic contributions of the acidic supports is particularly limited. A full understanding of a complete HDO catalyst is beyond the scope of this work. Instead, research will be focused on individual components of such a catalyst to understand their behavior in isolation, utilizing multi-site models where necessary. The methods employed to formulate, parameterize, and analyze microkinetic models are described in Chapter 2.

The hypothesized role of the metal sites on HDO catalysts is the promotion of (de)hydrogenation. Notably, some studies have examined catalytic transfer hydrogenation (CTH) in the context of HDO, in which an oxygenate is upgraded by a co-fed sacrificial donor molecule that supplies hydrogen to the system [14-15]. Another functionality of a metal is C–C bond scission, which can be exploited in order

to form syngas (a mixture of CO and H_2) and eventually H_2. Biomass-derived H_2 can be used to upgrade biomass via hydrogenation or HDO in remote locations where natural or shale gas is not available. The Pt-catalyzed steam reforming kinetics of ethylene glycol (a possible bio-derived hydrogen donor molecule) have been studied using microkinetic modeling. These findings shed light on the mechanism of hydrogen generation and the effect of water for this chemistry, and are presented in Chapter 3.

Chapters 4 through 6 of the dissertation are devoted to the study of reactions on γ-Al_2O_3, an acidic support commonly used in HDO catalysts. The hypothesized role of the acidic metal oxide is deoxygenation, and therefore the dehydration of ethanol was selected as a probe reaction to understand how the acid sites accelerate C–O bond-breaking mechanisms.

Chapter 4 presents a detailed examination of ethanol dehydration mechanisms and competing etherification mechanisms on the γ-Al_2O_3(100) facet using DFT methods. Lewis acid sites were found to catalyze the dominant mechanisms for both dehydration and etherification. These were the first calculations performed for such reactions on the γ-Al_2O_3(100) facet and the first report of a mechanism for γ-Al_2O_3-catalyzed diethyl ether formation from ethanol.

Chapter 5 examines the effect of acid site heterogeneity and surface hydration on adsorption and reaction of alcohols. The (110) and (100) facets of γ-Al_2O_3 collectively expose Lewis acidic Al sites with 3-, 4-, and 5-fold coordination. This site heterogeneity leads to substantial variation in adsorption strength and reaction barriers. The development of a descriptor and its success in capturing these variations are presented.

Chapter 6 discusses the development and performance of a multi-site, mean-field model of ethanol dehydration and etherification on γ-Al_2O_3. The γ-Al_2O_3(111) facet is used in DFT calculations to generate the model parameters. This represents the first DFT-based microkinetic model for these reactions on γ-Al_2O_3 and successfully demonstrates the applicability of the DFT mechanisms to powdered catalysts.

Chapter 7 summarizes the achievements of the dissertation. An outlook on future directions and extensions of the work is also set forth.

Chapter 2

KINETIC MODELING METHODOLOGY

Microkinetic modeling, a major component of this dissertation, aims at understanding how the properties of surfaces and adsorbed molecules affect thermodynamic and kinetic phenomena at the meso- and macro-scales. Quantum mechanics calculations (including methods, such as density functional theory), provide valuable information about molecular-level properties and transformations. However, drawing connections between quantum mechanical calculations and macroscopic measurements is difficult due to the vast differences in characteristic length and time scales [16]. Quantum chemistry calculations target systems of 10-100 atoms to obtain parameters for estimating rate constants, whereas systems of industrial interest span much larger scales. Developing a microkinetic model of a surface-catalyzed reaction and incorporating its results in a reactor model provides a consistent, systematic way of bridging the gap between scales. The techniques presented here focus on mean-field microkinetic models, in which the adsorbates are homogeneously distributed over the catalytic surface at each location of a chemical reactor, i.e., the distribution of adsorbates at each reactor location is assumed to be uniform but possibly varying with location. This makes averaging over microscopic configurations to compute the (mesoscale) reaction rate rather trivial. As a result, the well-known mass action kinetics for estimation of the reaction rate from the rate constants and local concentrations of adsorbates can be employed (see Section 2.7.1). There are several approaches for determining the values of the rate constants, and a number of tools for

assembling and analyzing the microkinetic model. The approaches and tools utilized in this dissertation are summarized in this chapter.

2.1 Transition State Theory, Collision Theory, and Rate Constants

Transition State Theory (TST) connects thermodynamic properties of adsorbates and of the transition state (TS) with the rate constant. Two main assumptions are made in TST. The first is that the time scale to either break or form a bond is longer than the time needed for energy redistribution among internal energy levels of a state along the reaction coordinate. This means that states, either initial or final, can be described using thermodynamics. The second assumption is that the molecules at the transition state are in quasi-equilibrium with the reactants. Under these assumptions, the reaction rate constant is described by the Eyring-Polanyi equation [11]:

$$k_i = \frac{k_B T}{h} e^{\left(\frac{-\Delta G_i^{\ddagger}}{k_B T}\right)} \qquad \text{Equation 2.1}$$

where k_B is Boltzmann's constant, T is the temperature, h is Planck's constant, and $\Delta G^{\ddagger} = G^{\ddagger} - \Sigma_i G_i$, where $G^{\ddagger}$ is the Gibbs energy at the transition state and G_i is the Gibbs energy of the i^{th} reactant ($\ddagger$ denotes the transition state).

The rate constant of a surface reaction is often expressed using the modified Arrhenius' law:

$$k_i = A_i \left(\frac{T}{T_0}\right)^{\beta_i} e^{\left(\frac{-E_{a,i}}{k_B T}\right)} \qquad \text{Equation 2.2}$$

where T_o is a reference temperature (generally 298 K), β_i is a temperature exponent, and $E_{a,i}$ is the reaction barrier. β is often used as a fitting constant to account for weak temperature dependence of the pre-exponential factor, while specifying a value of 0

assumes no pre-exponential temperature dependence. Depending on the units of the reaction rate, a normalizing factor of Γ^{n-1} is sometimes included in the denominator of the right-hand side of Equation 2.2, where Γ is the total concentration of binding sites and n is the number of reactants that are surface species (including surface vacancies). Comparing Equation 2.1 and Equation 2.2, one can easily map the Arrhenius parameters to those of TST:

$$A_i \left(\frac{T}{T_0} \right)^{\beta_i} = \frac{k_B T}{h} e^{\left(\frac{\Delta S_i^{\ddagger}}{k_B} \right)} \qquad \text{Equation 2.3}$$

$$E_{a,i} = \Delta H^{\ddagger} \qquad \text{Equation 2.4}$$

Adsorption reactions link the gas phase with the catalyst surface, and the physics of adsorption are described via collision theory. A general approach describing the adsorption process can be found elsewhere [17]. The rate of adsorption is calculated from the flux of molecules (Z_w) that impinge on a surface multiplied by a probability of a molecule to bind to the surface. This probability, the so called sticking coefficient (S), is a property of the adsorbate/surface pair. The sticking coefficient at zero coverage is denoted as S_0. The net flux of molecules (in molecules/m^2/s) impinging on a surface is calculated using the Hertz-Knudsen equation [18]:

$$Z_w = \frac{N_A P_k}{\sqrt{2\pi M_w RT}} \qquad \text{Equation 2.5}$$

In this expression, N_A is Avogadro's number, P_k is the partial pressure and M_w is the molecular weight of the k^{th} species. Assuming an ideal gas, the rate constant of (activated) adsorption at zero coverage is expressed by:

$$k_i = \frac{s_0}{\Gamma^n}\sqrt{\frac{k_B T}{2\pi M_w}} e^{\left(\frac{-E_{a,i}}{k_B T}\right)} \qquad \text{Equation 2.6}$$

Finally, in order to describe the rate of the backward reactions, the principle of microscopic reversibility is employed. This is implemented by relating the rate constants of the forward and reverse reaction rates to the equilibrium constant of the surface reaction:

$$K_{eq,i} = e^{\left(\frac{-\Delta G_{rxn,i}}{k_B T}\right)} = \frac{k_{i,f}}{k_{i,r}} \qquad \text{Equation 2.7}$$

The reverse rate constant is obtained using Equation 2.7 and computed values of the forward rate constant and equilibrium constant. This is essential for ensuring thermodynamic consistency of the mechanism, the details of which are discussed in Section 2.3.

2.2 Density Functional Theory Calculations

Quantum mechanics calculations, using methods such as density functional theory, are a powerful approach to parameterization of thermochemistry and rate constants in a microkinetic model. The development of DFT is based on Kohn and Hohenberg's mathematical theorem, which states that the ground state of the electronic energy can be calculated as a functional of the electron density [19]. The task of finding the electron density was solved by Kohn and Sham [20]. They derived a set of equations in which each equation is related to a single electron wave function. From the single electron wave functions one can easily calculate the electron density. In DFT computer codes, the electron density of the core electrons, i.e., those electrons that are not important for chemical bonds, are often represented by a pseudopotential

that reproduces important physical features so that the Kohn-Sham equations span only a select number of (valence) electrons. For each type of pseudopotential, a cutoff energy or basis set must be specified.

2.2.1 Exchange-Correlation Functionals

The challenge of DFT modeling is to design an exchange-correlation energy functional that correlates energy with the electron density. Failure to accurately account for Columbic interactions between electrons and quantum mechanical effects can result in poor prediction of the total energy. Several forms of the exchange-correlation functional have been proposed that achieve good results in a number of physical problems. A good review can be found elsewhere [11]. The simplest type of exchange-correlation functional is the so-called local density approximation (LDA). LDA assumes that the electron density behaves like a uniform electron gas, which is constant, and therefore no higher orders terms are included. The exchange-correlation functionals used for most calculations of adsorption employ the generalized gradient approximation (GGA), which includes the first derivative of the electron density. In this family, PW91 [21] (Perdew-Wang 1991), PBE [22] (Perdew-Burke-Ernzerhof) and RPBE [23] (Hammer-Hansen-Nørskov modified PBE) functionals are the most popular. Hammer et al. [23] compared the ability of various functionals to predict adsorption properties of simple adsorbates on well-defined surfaces using periodic slabs. In general, GGA functionals are better than LDA functionals at predicting adsorption properties due to the presence of a higher order scheme. In this dissertation, either PW91 or PBE functionals are utilized.

2.2.2 Systems with Periodic Symmetry

A periodic slab calculation takes advantage of the symmetry of a surface. A supercell of the system is created with atoms in a certain number of layers and vacuum space in the third dimension. Many DFT codes employ periodic boundary conditions in three dimensions. Consequently, materials that are susceptible to the formation of surface dipoles require careful consideration in order to avoid self-interaction errors [24-25]. After accounting for such interactions, one of the two surfaces exposed to the vacuum represents the active surface while the other is not utilized. To calculate the energy of a surface, the atoms in a certain number of layers adjacent to the surface where adsorption takes place are allowed to relax during optimization. The atoms in the remaining layers of the slab are fixed (frozen) in their initial positions to mimic the bulk phase. The number of layers to hold fixed and the total number of layers must be determined through computational convergence-like tests. The initial positions of the atoms are derived from the bulk crystal structure using the corresponding computationally-determined lattice constant. DFT packages that apply periodic boundary conditions use either the plane wave method (e.g., VASP [26-29]) or a linear combination of atomic orbitals (e.g., SIESTA [30]).

2.2.3 Transition State Searches

Stable states optimizations seek to minimize the energy of the system with respect to all degrees of freedom. In contrast, identifying transition states requires that the energy be a maximum for the degree of freedom associated with the reaction coordinate while the energy is minimized with respect to all other degrees of freedom. There are multiple methods for transition state searches [31], a full discussion of which is beyond the scope of this chapter. In this work, calculations utilizing the

SIESTA code employ the constrained optimization scheme for transition state searches [32-33]. Calculations in the VASP code utilize a combination of the climbing-image nudged elastic band (CI-NEB) [34] and dimer [35-37] methods for locating transition states.

2.2.4 Calculation of Vibrational Frequencies

Vibrational frequencies of the stable adsorbates are required to calculate thermodynamic properties using statistical thermodynamics as well as zero point energy corrections (discussed in Section 2.3). This is also true for transition state structures, with the additional purpose of confirming that a first-order saddle point has been located by checking for the existence of a single imaginary vibrational mode (corresponding to motion along the reaction coordinate). Within SIESTA and VASP, the vibrational frequencies are computed using the harmonic oscillator approximation based on numerical calculation of the Hessian matrix (for systems with supercells defined by orthogonal axes, VASP provides the option of an analytical Hessian by utilizing density functional perturbation theory). The optimization of the structure including the adsorbate must first be well-converged, using strict convergence criteria for the forces on atoms to minimize numerical errors. Then, the atoms of the slab are fixed in their optimized position while each atom of the adsorbate is slightly displaced independently in the three Cartesian directions and the energy recomputed after each displacement. Diagonalization of the resulting Hessian matrix produces eigenvalues that represent the vibrational frequencies of the normal vibrational modes of the adsorbates.

2.2.5 Density of States Analysis

The output of a DFT calculation utilizing a plane wave basis set includes the set of one-electron orbitals (eigenvectors) and the associated energies (eigenvalues). Grouping the energies and organizing them into a histogram leads to a plot known as the density of states (DOS). Typical plots present alternation between regions of one or more available states and regions where no states exist. Available states may be either occupied (valence states) or unoccupied (conduction states).

Further analysis is possible by projecting the orbitals onto another set of orbitals (e.g., molecular, atom-centered, etc.). This produces what is known as a projected density of states (PDOS). A detailed discussion of how the projection is accomplished is available elsewhere [38]. In this dissertation, the DOS is projected onto atom-centered orbitals and resolved by angular momentum for additional analysis.

2.2.6 Calculation of Energetics and Coverage Effects

Binding energies are calculated as:

$$E_{\mathrm{BE,i}} = E_{\mathrm{ads_i+surface}} - E_{\mathrm{ads_i}} - E_{\mathrm{surface}} \qquad \text{Equation 2.8}$$

where E_{ads} and E_{surface} are the total energies of the isolated adsorbate in vacuum and the clean surface, respectively, and $E_{\mathrm{ads+surface}}$ is the total energy of the adsorbate on the surface. The binding energy of an adsorbate depends in general on the coverage of adsorbates on the surface. For example, the heat of adsorption of CO on Ni (111) decreases by ~30 kcal/mol due to lateral interactions as the CO coverage increases from zero to 0.5 monolayer (ML) [39]. Hydrogen bonding can also occur for certain species, such as water [40-41], increasing the binding energy of such species. Lateral interactions also affect the activation barrier of a reaction by stabilizing or

destabilizing the transition state with respect to the initial or final state [42-43]. As an example, Hammer [42] showed using DFT calculations that the barrier for dissociation of N_2 on Ru (0001) strongly increases with increasing coverage of N*, O* and H*. This behavior was attributed to the repulsive interactions between the reaction complex and the adsorbates.

The binding energy is (implicitly) calculated at a certain coverage of adsorbates, which is determined by the unit cell size. This coverage is one-quarter ML when a monodentate adsorbate is placed on a 2×2 unit cell, one-ninth ML on a 3×3 cell, and so on. In order to obtain the heat of adsorption in the zero-coverage limit, the unit cell must be sufficiently large so that the effect of lateral (self) interactions is small. To account for the effect of coverage, the binding energy is computed as follows:

$$E_{BE,i}(\theta) = E_{BE,i}(\theta = 0) + \sum_{k=1}^{n} \alpha_{ik}\theta_k \qquad \text{Equation 2.9}$$

where α_{ik} is the lateral interaction parameter of species k on species i. θ_k is the coverage of species k and n is the number of species. The term "$\theta = 0$" stands for the adsorption property in the zero coverage limit. The above model assumes a linear dependence on coverage [44].

In order to calculate the lateral interaction parameter α_{ik}, DFT calculations are performed on species i in the presence of different coverages of species k, θ_k. Equation 2.10 is used repeatedly, at each value of θ_k, to compute the effective adsorption energy of species i in the presence of a coverage θ_k:

$$E_{BE,eff,i}(\theta_k) = E^{\theta_k}_{ads_i+surface} - E_{ads_i} - E^{\theta_k}_{surface} \qquad \text{Equation 2.10}$$

Here $E_{\mathrm{ads_i+surface}}^{\theta_k}$ is the energy of species i on the surface and also species k on the same surface with a coverage θ_k, $E_{\mathrm{ads_i}}$ is the energy of species i isolated in vacuum, and $E_{\mathrm{surface}}^{\theta_k}$ is the energy of the surface with species k adsorbed onto it with a coverage θ_k arranged in an identical configuration as in $E_{\mathrm{ads_i+surface}}^{\theta_k}$. Note that Equation 2.8 and Equation 2.10 are similar formulae for computing the adsorption energy of a surface species. The main difference is that in Equation 2.8 the adsorbate is alone on the slab, while in Equation 2.10 the adsorbate is surrounded by species k with a coverage θ_k. The various $E_{\mathrm{BE,eff,i}}(\theta_k)$ are then plotted as a function of θ_k. Then, assuming that the effective adsorption energies vary linearly with the coverage [44], a linear regression is performed. The value of α_{ik} is one-half the value of the slope parameter of the regression. The factor of one-half is used because of an assumed pairwise interaction. Since α_{ik} is a slope parameter, it represents the change in the adsorption energy of species i with changes in θ_k. The pairwise interaction assumption implies that half of the change in energy is associated with destabilization or stabilization of species i and half with species k.

A priori computation of the entire interaction matrix, even when neglecting many body effects, requires a total number of DFT calculations of the order of the square of the number of species. This brute-force solution is prohibitive for large mechanisms. Various hierarchical approaches have been suggested to avoid this large number of DFT calculations [10], and these are adopted for computing lateral interaction parameters in this dissertation.

2.3 Computing Thermodynamic State Properties

The coverage-dependent enthalpy of formation of an adsorbate, including the zero point energy correction, is defined as:

$$H_i(T,\theta) = H_i^{gas}(T_0) + E_{BE,i}(\theta = 0) + \Delta ZPE_i + \int_{T_0}^{T} C_{p,i}\,dT + \sum_{k=1}^{n} \alpha_{ik}\theta_k \qquad \text{Equation 2.11}$$

In Equation 2.11, $H_i^{gas}(T_0)$ is the enthalpy of formation in gas-phase at reference temperature T_0 that is obtained from standard thermodynamic databases. The value of $E_{BE,i}(\theta=0)$ depends on the method used for thermodynamic consistency at the enthalpic level (see Section 2.4). $C_{p,i}$ is the heat capacity at constant pressure of species i on the surface. The zero point energy (ZPE) correction is given by:

$$\Delta ZPE_i = \sum_k \frac{h\nu_k^{surf}}{2} - \sum_k \frac{h\nu_k^{gas}}{2} \qquad \text{Equation 2.12}$$

where ν_k is the k^{th} vibrational frequency on either the surface or in the gas phase as indicated. The entropy of an adsorbate at a specified temperature is computed as laid out in standard thermodynamics texts:

$$S_i(T) = \int_0^T \frac{C_{p,i}}{T}\,dT \qquad \text{Equation 2.13}$$

To compute state properties from statistical thermodynamics, the strength of adsorption must be considered as this determines the assumptions to be applied. In general, adsorbates that bind weakly to surfaces have a low barrier for surface diffusion, which makes them highly mobile on the surface. On the other hand, strongly bound adsorbates have a high barrier for surface diffusion and are assumed to be immobile on the surface. Except where noted, all systems studied in this dissertation feature strongly-bound adsorbates. A discussion of methods for treating weakly-bound adsorbates is available elsewhere [45].

For a strongly-bound adsorbate, all translational and rotational degrees of freedom present in the gas phase are assumed to be frustrated and converted into

vibrational modes between the adsorbate and the surface. Assuming that the PV contribution to the enthalpy is small (see [10] and references therein), the state properties can be calculated from the vibrational contributions alone. The expression for the heat capacity of a strongly-bound adsorbate is [46-47]:

$$C_{p,i}^{vib} = k_B \sum_{k}^{N} \left(\left(\frac{\Theta_{v,k}}{T} \right)^2 \frac{e^{-\frac{\Theta_{v,k}}{T}}}{\left(1 - e^{-\frac{\Theta_{v,k}}{T}} \right)^2} \right) \qquad \text{Equation 2.14}$$

where $\Theta_{v,k}$ stands for the characteristic vibrational temperature for each mode and is calculated as $\Theta_{v,k} = h\nu_k/k_B$. The summation runs over all N vibrational frequencies corresponding to a particular adsorbate.

2.4 Thermodynamic Consistency

In the context of model parameterization, ensuring thermodynamic consistency refers to the specification of parameter values in harmony with the fact that certain thermodynamic properties (e.g., entropy, enthalpy, free energy) are state functions. As illustrated in Figure 2.1, there are multiple pathways that connect any given pair of species in the reaction network. By definition, the appropriate sums of the corresponding state properties describing each of these pathways must be identical. This implies that only a subset of the state properties may be independently specified. The set of constraints are laid out elsewhere [48-49].

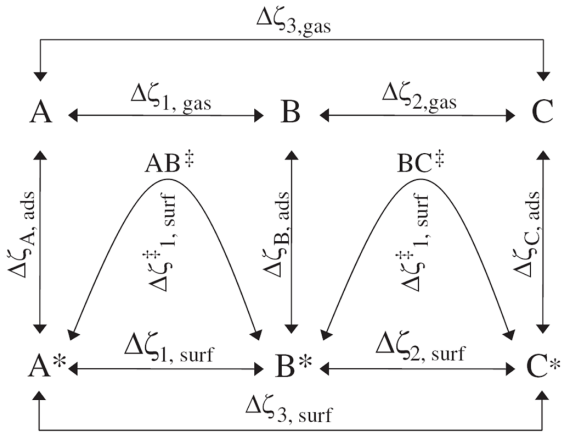

Figure 2.1: Illustration of state properties interrelating gas-phase and surface species in a simplified network. ζ is any thermochemical property, and * denotes a surface species. Reproduced with permission from [10].

Multiple methods for ensuring thermodynamic consistency have been developed [45, 48, 50-51]. The parameterization of models in this dissertation follow largely the approach of Ref. [51] (which in turn is based on Ref. [45, 48]). Specifically, the state properties of the gas-phase species were obtained from established databases of gas-phase thermochemistry [52-53] to ensure matching of known thermodynamic quantities and high thermodynamic accuracy of catalytic cycles involving reactants and products. The state properties of surface reactions (including between stable and transition states) are preserved as predicted from DFT calculations, in order to take advantage of cancelation of errors arising when computing differences in energies of similar structures. Finally, select species are selected as reference compounds for which the adsorption energies are specified by DFT, and the values of the remaining adsorption energies are constrained by

thermodynamic cycles. The specific reference species chosen, as well as any departures from this approach, are noted in subsequent chapters.

2.5 Semi-empirical Correlations: Brønsted-Evans-Polanyi Relationships

DFT-based microkinetic modeling is a powerful tool to provide a molecular-level understanding of chemical reactions on a single material, in particular for small molecular weight molecules. However, the need for screening different materials and modeling reactions for larger molecules calls for developing semi-empirical methods that are much less computationally demanding for predicting thermodynamic properties and kinetic parameters [10]. Such methods can be applied to produce a first-pass microkinetic model that in turn can be refined using more detailed theory, aided by analytical tools that identify key features of the model.

Brønsted-Evans-Polanyi relationships (BEPs) derived from DFT data make up one such class of methods [54-58]. A single BEP is a linear relationship between the activation energy and the reaction enthalpy of an elementary reaction. In general, a BEP can be written as:

$$E_a = \alpha \Delta H_{rxn} + \beta \qquad \text{Equation 2.15}$$

where α and β are the slope and intercept, respectively. Single-step bond-breaking reactions on transition metals follow BEP correlations. Example chemistries include CO oxidation reactions on flat and stepped pure metal surfaces [55] and thermal dehydrogenation of ethanol on Pt [56]. Analogous correlations have been developed for bond dissociation of small molecules (e.g., diatomics and methane) on metal oxide surfaces [57-58].

2.6 Multi-site Kinetics

The majority of microkinetic models assume a single type of active site in the formulation of the rate expressions. This is particularly common when simulating reaction chemistries on pure transition metal catalysts [59]. In principle, all of the mass action kinetics concepts and parameterization techniques already discussed can be applied in order to formulate a kinetic model with multiple distinct types of sites. Progress has been reported in this area for systems involving transition metals [60] and pure metal oxides [61].

A key set of quantities that must be defined in a multi-site model is the surface site concentration of all j site types, Γ_j. Recalling that Γ represents the total concentration of sites, the values of the surface concentrations of sites are constrained according to:

$$\sum_j \Gamma_j = \Gamma_T \qquad \text{Equation 2.16}$$

Then, similar to the one-site model formulation, the surface concentrations of species for each particular site j (including vacancies) are constrained according to:

$$\sum_i C_j^i = \Gamma_j \qquad \text{Equation 2.17}$$

where i refers to a species on site j. Finally, for elementary steps involving multiple site types, it may be necessary (depending on the reaction rate units) to normalize the rate constant by a surface site concentration, as described in Section 2.1. In this work the total surface site concentration (Γ) was used for such normalizations.

2.7 Analysis Tools for Microkinetic Modeling

The previous sections described techniques employed for parameter estimation. These thermodynamic and kinetic parameters are input to a microkinetic

model that is solved numerically to describe material balances in a chemical reactor (e.g., a plug flow reactor). This section describes tools for the subsequent model analysis. During mechanism development, they can be used to assess which reactions and reactive intermediates are important in the model, which helps the modeler to focus on important features of the surface reaction mechanism. During this process, simulated macroscopic observables, e.g., global reaction orders and apparent activation energies, can be compared directly to experimental data. Then, once the model describes experimental data reasonably well, analytical tools can be used to develop further insights into the reaction mechanism, with applications that include catalyst design [62].

2.7.1 Rates in Microkinetic Modeling

Before describing the analytical tools, basic definitions about reaction rates in microkinetic modeling are reviewed. The species net production rate through surface reactions is:

$$r_i = \sum_j \nu_{ij} \dot{q}_j \qquad \text{Equation 2.18}$$

where ν_{ij} is the stoichiometric coefficient of species i in reaction j. The summation in Equation 2.18 runs over all reactions in the mechanism. The net rate of the j^{th} surface reaction is defined as:

$$\dot{q}_j = k_{f,j} \prod_i [C_i]^{|\nu_{ij}|} - k_{b,j} \prod_i [C_i]^{|\nu_{ij}|} \qquad \text{Equation 2.19}$$

where $[C_i]$ is the concentration of species i either on the surface (including vacancies) or in the gas phase. The products in Equation 2.19 run over all reactants of reaction j in the respective direction (either forward or backward). The units of the reaction rate

constants, $k_{f,j}$ and $k_{b,j}$, depend on the type of reaction (either adsorption or surface reaction) and on the reaction order.

2.7.2 Reaction Path Analysis and Partial Equilibrium Analysis

The main objective of reaction path analysis (RPA) is to determine which reactions exhibit the highest rates in converting reactants to products, and thus obtain an overall map of the reaction network. The analysis is performed by calculating which reactions are responsible for the production or consumption of species i through:

$$RP_{ij} = \frac{\dot{q}_j}{\sum_j \dot{q}_j} \qquad \text{Equation 2.20}$$

where RP_{ij} is the fraction of either the net production or net consumption rate of species i by reaction j. The summation in the denominator runs over either all production or all consumption reaction rates. After computing RP_{ij} for each species, one can reduce the mechanism by eliminating reactions for which the RP_{ij} for all species falls below a (small) threshold.

Partial equilibrium analysis investigates which reactions in the mechanism are partially equilibrated, i.e., the reactions for which the forward rate is nearly equal to the backward rate. The partial equilibrium ratio is defined as:

$$PE_j = \frac{\dot{q}_{j,f}}{\dot{q}_{j,f} + \dot{q}_{j,b}} \qquad \text{Equation 2.21}$$

where the subscripts f and b stand again for the forward and backward reaction rates, respectively. A value of PE_j of 0.5 means that the reaction is equilibrated. $PE_j = 1$ or 0 means that the forward or backward reaction dominates, respectively. A value of PE_j

between 0.45 and 0.55 implies that the specific reaction is practically partially equilibrated.

2.7.3 Rate-Determining Steps (RDS) and Most Abundant Surface Intermediates (MASI)

The concept of a rate-determining step (RDS) is common and useful in heterogeneous catalysis. It has been used as an *a priori* assumption in the development of reduced rate expressions from experimental data [63]. Knowledge of the RDS can provide insights into how to improve a catalyst. The identification of the RDS in chemical reaction networks has been discussed in the past three decades [64-66]. In this work, the RDS is determined using a methodology known as sensitivity analysis, utilizing the normalized sensitivity coefficient (NSC) as a metric:

$$\mathrm{NSC}_i = \frac{\partial \ln(\mathrm{R})}{\partial \ln(\mathrm{A}_{f,i})} \cong \frac{\mathrm{A}_{f,i}\,\Delta \mathrm{R}}{\mathrm{R}\,\Delta \mathrm{A}_{f,i}} \qquad \text{Equation 2.22}$$

where R is the response variable of interest (e.g., a reaction rate, conversion, etc.) and $A_{f,i}$ is the forward pre-exponential factor of reaction i. The larger the magnitude of the NSC, the greater the influence of reaction i on the response variable. Thus, when a global reaction rate is specified as the response, the NSC identifies the rate-determining step or steps of the mechanism.

Surface intermediates with high coverage have a higher probability to interact and change the thermochemistry of other intermediates and possibly be involved in surface reactions. By identifying the most abundant surface intermediate (MASI), model development is expedited because computational resources can be allocated to account for the significant effects, e.g., lateral adsorbate interactions, of the MASI on thermochemistry and reaction barriers. This hierarchical approach, identifying first the

dominant species and then including coverage effects on thermochemistry and reaction barriers, renders first-principles modeling tractable by reducing computational cost significantly, since only part of the interaction matrix is computed. In some cases, abundant intermediates can be identified by *in situ* spectroscopic methods, which help to validate models.

2.7.4 Model Reduction

Developing a microkinetic model consisting of a full set of elementary steps represents the best practice to ensure that critical elementary steps are included when exploring and analyzing a mechanism. Once the model's predictive performance has been established, its utility can be expanded by coupling with higher-level simulations, such as computational fluid dynamics (CFD) and process-level models. In such contexts, the reaction rates must be sufficiently accurate while keeping the computational cost of evaluating the kinetic expressions to a minimum. This motivates the development of a simplified kinetic expression that, in this case, benefits from the unique insights gained from the results of the full microkinetic model.

A methodology for *a posteriori* microkinetic model reduction has been set forth previously which involves two major steps, namely elimination of elementary steps that are non-essential to the mechanism and the consolidation of the remaining steps into a single rate expression [67]. The systematic identification of the essential elementary steps is achieved through principal component analysis of a sensitivity matrix. This step may be bypassed if the reaction network is already small. To derive the final rate expression, the quasi steady state assumption [68] is applied in order to develop balances on surface intermediates. Reduction principles (a.k.a. order 1 asymptotics) are then applied based on knowledge of the full mechanism. These

include neglecting contributions from surface species occupying less than 1% of the surface and elementary steps that contribute less than 1% to the production and/or consumption of a particular species. Knowledge of the PE ratios and the RDS is also essential. Application of these principles leads to a set of equations that can be solved for the overall reaction rate.

2.8 Acknowledgments

Some of the material in this chapter was reproduced from [69] Copyright 2014 John Wiley & Sons. I would like to thank the co-authors on that work, Prof. Rafael C. Catapan, Prof. Amir A.M. Oliveira, and Prof. Dionisios G. Vlachos, for their contributions and insights into these important topics.

Chapter 3

MICROKINETIC MODELING OF Pt-CATALYZED ETHYLENE GLYCOL STEAM REFORMING

3.1 Introduction

Interest in the production of biomass-derived fuels and chemicals continues to grow, spurred on by a number of different drivers [4, 70]. Recent work on the catalytic steam reforming of oxygenated hydrocarbons and sugars demonstrates that such compounds can be used to produce H_2 [71-72], which in turn can be used in fuel cells, feedstock upgrade, desulfurization, hydrogenation, and other processes. Obtaining a fundamental understanding of the mechanistic pathways of oxygenate reforming persists as a vital step towards fully utilizing these discoveries. Over the last 20 years, the development of microkinetic modeling has enabled successful replication of experimentally-observed reaction kinetics over heterogeneous catalysts [10, 49]. More recently, models have been integrated with first principles-based values of rate constants, providing a theoretical basis for model parameters and offering valuable insights into reaction mechanisms [10]. While a considerable number of microkinetic models have been developed, only a limited number have been reported for oxygenate chemistries, focused principally on thermal decomposition. Under steady-state reactor conditions over a Pt catalyst, Kandoi et al. demonstrated that initial C-H bond scission is rate-determining in methanol decomposition [73], similar to methane decomposition [74]. On the other hand, in ethane hydrogenolysis [75-76], C-C bond scission is kinetically controlling. In contrast, Salciccioli et al. reported that early C-H and O-H

bond scissions are rate-determining in ethylene glycol thermal decomposition on Pt [59]. Thus, it is not always clear when mechanistic analogies may be drawn between hydrocarbons and oxygenates containing equal numbers of carbon atoms.

Thermal decomposition often leads to catalyst deactivation. Co-reactants, such as H_2O, can limit deactivation. Therefore, understanding the influence of a co-reactant on the mechanism is also important. For example, Wei and Iglesia have elucidated experimentally that co-reactants (either H_2O or CO_2) have no detectable kinetic influence on C-H bond scission in methane reforming over Pt [74]. In the context of catalytic conversion of biomass-derived oxygenates to synthesis gas, water is a typical co-reactant because of its presence in biomass. A reduced, lumped model with parameters fitted to experimental kinetic data has been reported for steam reforming of ethylene glycol [77], but mechanistic details are still lacking. For example, ethylene glycol steam reforming may proceed as thermal decomposition of ethylene glycol to CO and H_2 (Equation 3.1), followed by a shift to CO_2 and H_2 (Equation 3.2):

$$C_2H_6O_2 \rightleftharpoons 2\ CO + 3\ H_2 \qquad \text{Equation 3.1}$$

$$CO + H_2O \rightleftharpoons CO_2 + H_2 \qquad \text{Equation 3.2}$$

Not only can the reaction in Equation 3.2 change the product distribution, but it can also free up catalyst sites from adsorbed CO and thus speed up the reaction in Equation 3.1. Furthermore, water-derived OH* (Equation 3.3), may also directly promote decomposition of oxygenates (such as ethylene glycol) by catalyzing C-H or O-H bond scission as shown in Equation 3.4:

$$H_2O^* + * \rightleftharpoons OH^* + H^* \qquad \text{Equation 3.3}$$

$$C_xH_yO_z^* + OH^* \rightleftharpoons C_xH_{y-1}O_z^* + H_2O^* \qquad \text{Equation 3.4}$$

To date, no detailed kinetic model has been reported for ethylene glycol steam reforming that includes reactions like Equation 3.4. Yet, previous work has shown that barriers for OH-assisted reactions with oxygenates are similar to or lower than the corresponding simple dehydrogenation steps [78-79], and are likely contributing steps in the overall mechanism [79]. As an example, Davis, Neurock, and co-workers demonstrated that ethanol and glycerol oxidation to the corresponding acids occurs on Au at high pH (whereas Au is inactive at neutral conditions), and attributed the activity to dehydrogenation reactions mediated by both solvent- and surface-OH [79].

Here we apply a hierarchical multiscale modeling approach [10, 80] to develop a predictive mean-field microkinetic model for steam reforming of ethylene glycol over Pt. Model predictions are compared to experimental data, and subsequent model analysis offers insights into the ethylene glycol reforming mechanism. Finally, a kinetic analogy is drawn between ethylene glycol and CH_4 steam reforming over Pt catalysts.

3.2 Model Development

The ethylene glycol steam reforming model consists of 147 reversible reactions (listed in Table A.1), which may be divided into several reaction subgroups. Ethylene glycol decomposition includes all possible C-H, O-H, and C-C bond cleaving reactions of $C_2H_6O_2$ for the formation of CO and H_2; C-O bond scission is neglected due to low selectivity over Pt [81]. Methanol decomposition is made up of an analogous set of elementary steps (except for C-C bond scission). Water-gas shift (WGS) includes water activation (Equation 3.3) as well as pathways for CO_2 formation from CO, either directly or via carboxyl or formate intermediates (depicted as an overall reaction in Equation 3.2). Finally, because of the presence of H_2O as a

co-reactant, oxidative dehydrogenation pathways are considered in which adsorbed OH intermediates mediate C-H and O-H scission in both C1 and C2 compounds (Equation 3.4).

H_2O can affect the rate of ethylene glycol decomposition in at least two kinetically interesting ways. First, H_2O can remove CO via the water-gas shift reaction to free up sites (blocking of sites via CO is observed under thermal decomposition conditions [59]). In this case, steam reforming can be thought of – in a simplistic manner – as the 'addition' of the reactions shown in Equation 3.1 and Equation 3.2. Second, H_2O* can dissociate to OH* (Equation 3.3), which can carry out oxidative dehydrogenation steps as shown generically in Equation 3.4; these steps are absent under thermal decomposition conditions. If these elementary reactions are important, then steam reforming of polyols is the result of strong chemical coupling that goes beyond availability of free sites. Inclusion of all these elementary steps permits a direct assessment of whether, and to what extent, H_2O catalyzes ethylene glycol dehydrogenation.

To parameterize the mean-field microkinetic model, in addition to values computed as part of this work, previously reported DFT-based thermochemical and kinetic parameters for reactions involving $C_2H_xO_2$, CH_xO, and WGS intermediates were utilized. A link to a CHEMKIN™ [17, 82] THERMDAT file containing NASA polynomial coefficients is provided in Appendix A.1, with entries that describe the thermochemistry of all gas and surface intermediates of this model. All entries for gas-phase intermediates were the same as in Salciccioli et al. [59], except the entries for CO_2 and H_2O which were obtained from the GRI mechanism (v. 3.0) [53]. Data from Salciccioli et al. [59] were also used for $C_2H_xO_2$* and CH_xO* intermediates, including

HCO* and CO*. The entry for H* was similar to Salciccioli et al. [59]. In [59] the entropy of H* was based on the assumption of a 2D surface fluid (i.e., loss of only 1 gas-phase translational degree of freedom), while in this work the entropy is calculated by assuming that all gas-phase translational degrees of freedom are converted to vibrational degrees of freedom. The thermochemistry for WGS surface intermediates is based on results from Stamatakis et al. [83], except for CO_2* which in that work was assumed to instantaneously desorb. In this work, CO_2* was treated using 2 translational degrees of freedom and 7 vibrational degrees of freedom (i.e., a 2D surface fluid assumption). $H_{f,298}$ of CO_2* is referenced from $HCOOH_{(g)}$ and H* adsorbed on separate slabs, in order to be consistent with the reference states for the other intermediates [59]. Finally, lateral repulsive adsorbate interactions that affect the thermochemistry of intermediates were used [59], except for the effect of CO* on the H* binding energy. Versions of the models were considered that both included and neglected cross lateral repulsive interactions of CO* and H*, using a value of 5 kcal $(\text{mole ML})^{-1}$ for both parameters. It was observed that results were qualitatively identical and quantitatively very similar; consequently, we chose to neglect those parameters to minimize model complexity.

To ensure thermodynamic consistency (i.e., closure of thermodynamic cycles) in a DFT-based surface microkinetic model, adjustment of DFT-computed thermochemical properties of at least some elementary steps involving surface species (either adsorption, reaction, or both) is required. This is because of differences between values of experimental and DFT-computed thermochemistry. Previously published methods for thermochemical parameterization offer in-depth discussion of this point [10, 45]. In this work an approach is adopted in which the DFT-computed

surface thermochemistry is largely preserved while adsorption thermochemistry is adjusted to ensure closure of thermodynamic cycles (note that the experimentally-based thermochemistry of gas phase compounds is taken to be 'correct' and is not adjusted). The premise of this approach is that the surface reaction thermochemistry is likely more accurate than adsorption thermochemistry because of cancelation of errors. The focus of the study is to understand the surface reaction pathways, so an approach was adopted that preserved that information from DFT. Specifically, consistent with the work of Salciccioli et al. [59], all oxygenates were referenced to the corresponding fully-hydrogenated gas-phase species (e.g. adsorbed $C_2H_xO_2$ compounds were referenced to $C_2H_6O_{2(g)}$) and H*. The consequence of this is that the enthalpies of reaction for C-C bond scission (and the reverse barriers) are altered from the DFT-predicted values. As will be shown below (and consistent with [59]) this does not affect the results because C-C bond scission reactions are irreversible in the forward direction.

For the kinetic parameterization, each forward reaction rate constant was defined according to one of the following expressions:

$$k_{i,f} = A_i e^{\left(\frac{-E_{a,i}}{k_B T}\right)} \qquad \text{Equation 3.5}$$

$$k_{i,f} = \frac{k_B T}{h} e^{\left(\frac{-\Delta G_i^{\ddagger}}{k_B T}\right)} \qquad \text{Equation 3.6}$$

$$k_{i,f} = \frac{s_j}{C_T^{\,n}} \sqrt{\frac{k_B T}{2\pi M_w}} \qquad \text{Equation 3.7}$$

Surface elementary steps involving CH_xO^* intermediates were parameterized according to Equation 3.5 to conform to a previous publication [73]; oxidative dehydrogenation pathways were also parameterized according to Equation 3.5.

Adsorption steps were parameterized according to collision theory following Equation 3.7, where s_j is the sticking coefficient of reactant j, C_T is the area density of surface sites, n is the number of sites onto which the reactant adsorbs, k_B is the Boltzmann constant, T is the temperature, and M_W is the molecular weight of the adsorbing reactant. To ensure thermodynamic consistency of rate constants, reverse rate constants were calculated from the forward rate constants and the equilibrium constant, according to Equation 3.8:

$$K_{eq,i} = e^{\left(\frac{-\Delta G_{rxn,i}}{k_B T}\right)} = \frac{k_{i,f}}{k_{i,r}} \qquad \text{Equation 3.8}$$

The THERMDAT file (see Appendix A.1) contains entries for the transition states of $C_2H_xO_2$ thermal dehydrogenation reactions and WGS reactions, which were used to compute free energy barriers, $\Delta G^{\ddagger}$; these barriers were obtained from calculations reported in previous publications on ethylene glycol decomposition [59, 84] and WGS [83] on Pt and used in Eq. (2). For reactions involving CH_xO* intermediates, the kinetic parameters were used as reported in Table 5 of Kandoi et al. [73]. Kinetic parameters for OH-mediated dehydrogenation reactions (see Equation 3.4) involving $C_2H_xO_2$* and CH_xO* intermediates were obtained either from DFT-derived Brønsted-Evans-Polanyi relationships (BEPs) (see Table 3.1) or from DFT calculations reported in Table 3.2 performed in this work; a value of 10^{13} was used as an order-of-magnitude estimate for the pre-exponential factors.

Table 3.1: Parameters for Brønsted-Evans-Polanyi relationships (BEPs) utilized in the model for calculation of reaction barriers.

Correlation Type	Parameter[a]	
	α	β (kcal mol^{-1})
C-H bond scission via OH	0.19	15.2
O-H bond scission via OH[b]	8.66×10^{-2}	0.364

[a] Correlations follow the functional form $E_a = \alpha\ \Delta H_{rxn} + \beta$. [b] This correlation was derived using reactants in the initial state co-adsorbed on the same slab, due to a large energetic stabilization of reactants resulting from hydrogen bonding.

BEPs and other semi-empirical techniques drastically reduce the computational cost of model parameters while being reasonably accurate [10, 46, 85]. They are particularly useful when applied in conjunction with the hierarchical modeling approach to obtain a "first-pass" kinetic model, followed by screening for and refinement of important reaction parameters [10]. We describe later how local sensitivity analysis [64-65] and DFT are used to obtain more accurate values of kinetically relevant reaction barriers.

DFT calculations performed in this work employed the Siesta code [30] with Troullier-Martins norm-conserving scalar relativistic pseudopotentials [86] and a double-ζ plus polarization basis set. The Perdew-Burke-Ernzerhof (PBE) form of the generalized gradient approximation (GGA) functional was used with a mesh cutoff of 200 Ry. The Pt(111) surface was simulated using a standard supercell with a four-layer, 3×3 unit cell and a minimum of 15 Å of vacuum between periodic slabs. The bottom two layers of Pt atoms were fixed in the bulk atomic positions (based on a calculated lattice constant of 4.02 Å) while the top two Pt layers and all adsorbate atoms were allowed to fully relax. The surface Brillouin zone was sampled using a

5×5×1 Monkhorst Pack k-point mesh. Transition states (TSs) were located according to a constrained optimization approach, as described in a previous publication [54].

To simulate the experimental reactor rates, the rate constants from the microkinetic model were integrated into a plug flow reactor model. The simulated reactor had a ¼-inch (0.64 cm) diameter and a length of 1 cm. The simulated catalyst bed contained 22 micromoles of Pt sites (based on an assumed site density of 1×10^{15} Pt sites cm^{-2}, and a reported CO uptake value for a 3.43% wt Pt/Al_2O_3 catalyst [87]).

3.3 Model Assessment and Analysis

Results were compared to published kinetically-limited experimental data for ethylene glycol steam reforming [77] in Figures 3.1-3.4. The absolute values of the model rates for H_2 and CO differ from experiments by approximately one order of magnitude or less, and reaction orders and apparent activation energies from the model are in good quantitative agreement with experimental trends. This is quite remarkable considering that no parameter fitting was performed to improve the quantitative agreement between the model and the experiments. Possible reasons for differences in model and measured rates include errors in the estimates of the entropic terms (alternatively considered as pre-exponential factors), an error in the estimate of catalyst sites (e.g., due to error in chemisorption measurements), catalyst modification during reaction, an experimentally more active catalytic site than that considered in the model, etc. In general, experimental CO_2 rates are underpredicted, but CO_2 is a minor product compared to CO under most conditions. The deviation in CO_2 rates is probably due to support effects [88-89]. The negative reaction orders in CO are consistent with the model prediction of partial blocking of Pt sites by up to 50% adsorbed CO*. Coverages range from ~40-50% for CO* and ~10-20% for H*

(depending on conditions) with the balance being vacant sites. Overall, the model is successful in capturing the experimental trends.

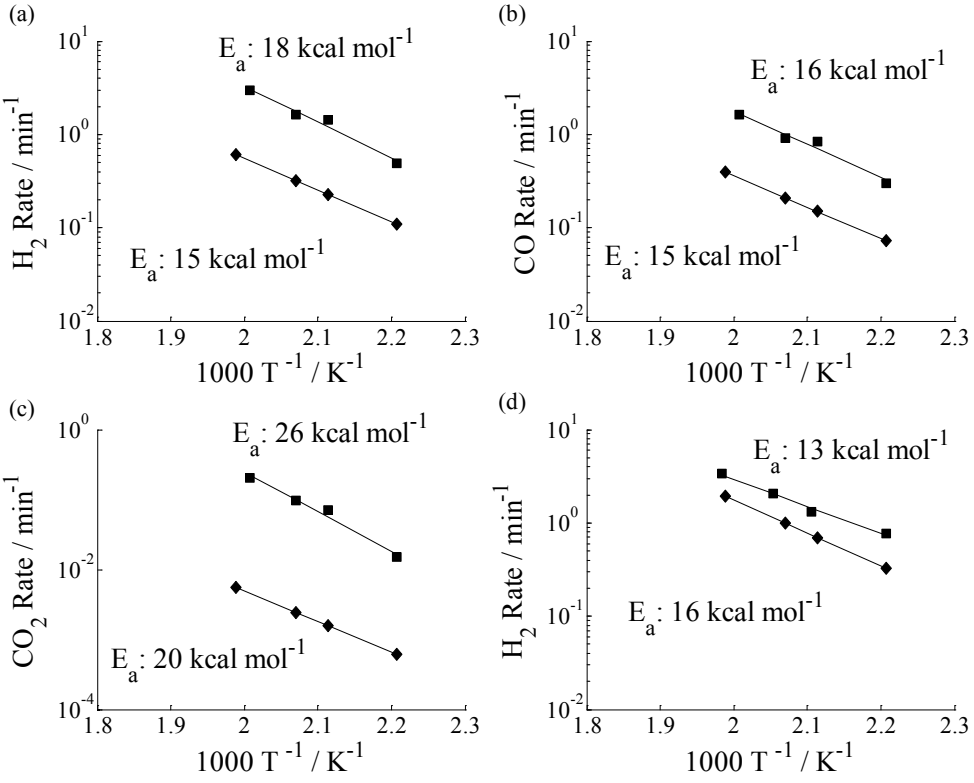

Figure 3.1: Temperature dependence of experimental (■) and model (♦) rates at 1 bar. Feed compositions are (a-c) 5% wt ethylene glycol in H_2O and (d) 63% wt ethylene glycol in H_2O. Rates shown are production of (a,d) H_2, (b) CO, and (c) CO_2. Apparent activation energies, E_a, are shown. Experimental CO rates were not reported, so they were calculated as shown in Appendix A.4.

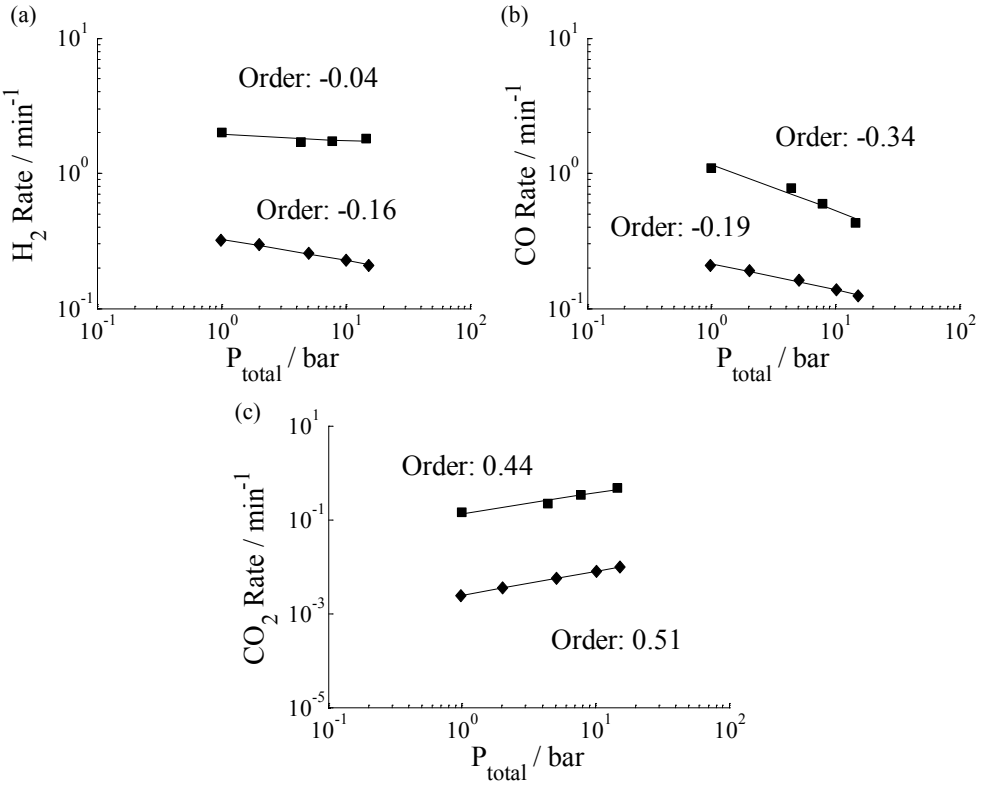

Figure 3.2: Pressure dependence of experimental (■) and model (♦) rates for (a) H_2, (b) CO, and (c) CO_2 with a feed composition of 5% wt ethylene glycol in H_2O at 483 K. Reaction orders are shown. Experimental CO rates were computed as described in the caption of Figure 3.1.

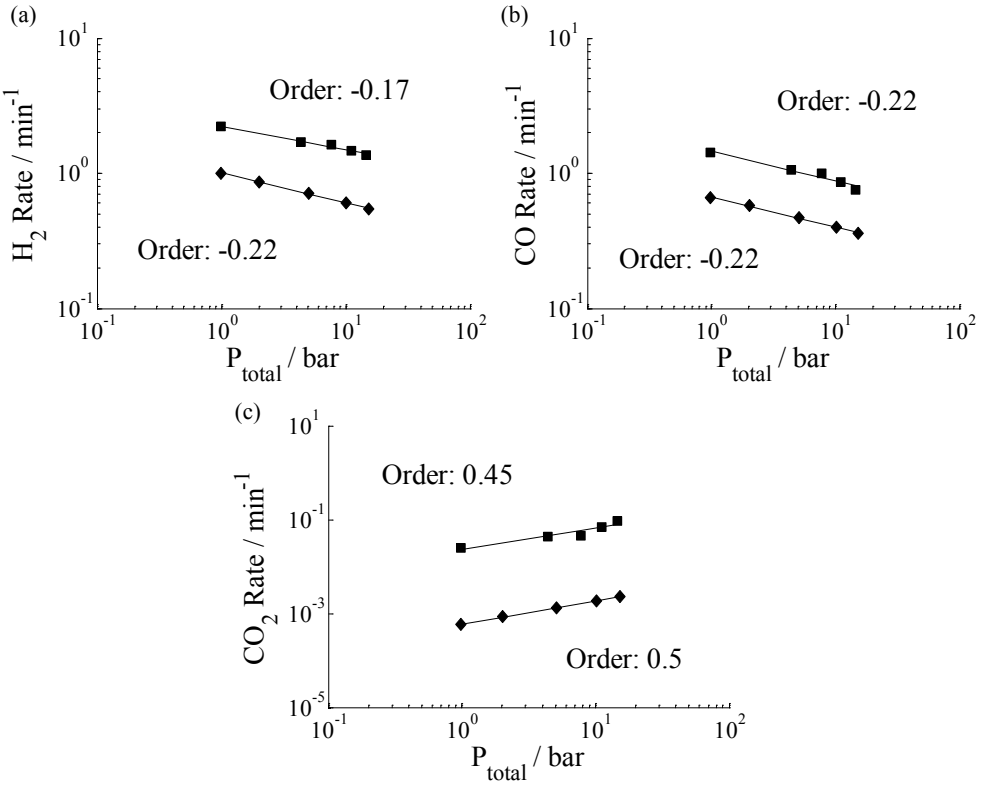

Figure 3.3: Pressure dependence of experimental (■) and model (♦) rates for (a) H_2, (b) CO, and (c) CO_2 with a feed composition of 63% wt ethylene glycol in H_2O at 483 K. Reaction orders are shown. Experimental CO rates were computed as described in the caption of Figure 3.1.

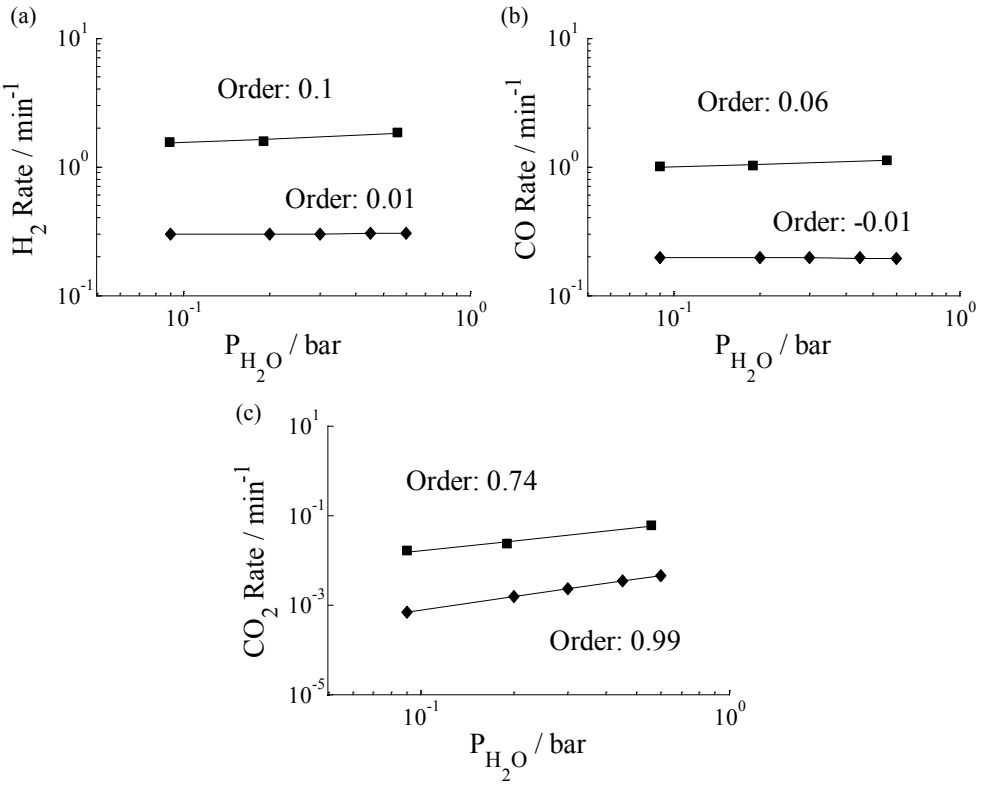

Figure 3.4: Effect of H_2O partial pressure on experimental (■) and model (♦) rates for (a) H_2, (b) CO, and (c) CO_2 at 483 K and 1 bar. Model rates were computed using an assumed fixed fraction of 0.5% mol ethylene glycol. Reaction orders are shown. Experimental CO rates were computed as described in the caption of Figure 3.1.

Next, an analysis of reaction fluxes through surface intermediates is carried out to obtain insights into dominant mechanistic pathways. Figure 3.5 provides an overview of the principal reaction pathways for conversion of ethylene glycol to C1 products at a representative set of conditions. As reported for pure ethylene glycol decomposition [59], initial O-H scission is the most dominant pathway. Initial C-H scission is a rather minor pathway; rates for initial OH-assisted O-H scission are even less important (~1% of total $C_2H_6O_2$** dehydrogenation). OH-assisted decomposition

pathways have negligible (much less than 1%) contributions to the production and consumption rates of other intermediates, even when excess water is co-reacted with ethylene glycol. After the initial bond scission, successive hydrogenation and dehydrogenation reactions take place until C-C bond scission occurs in highly dehydrogenated intermediates. This is once again consistent with previous findings for ethylene glycol thermal decomposition [59].

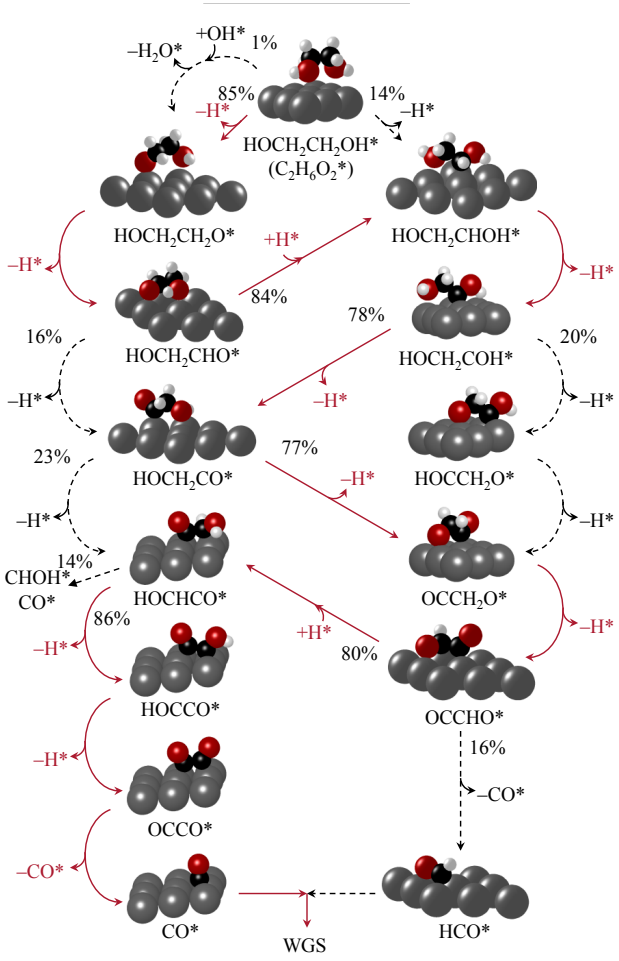

Figure 3.5: Principal reaction pathways in ethylene glycol steam reforming based on a feed of 5% wt ethylene glycol in H_2O at 483 K and 1 bar. Solid lines indicate major pathways, and dotted lines indicate minor pathways.

In order to understand which elementary steps have the greatest influence on the overall rate, the microkinetic model is easily probed using local sensitivity analysis [64-65]. The analysis consists of computing a normalized sensitivity coefficient (NSC) for each elementary reaction:

$$NSC_i = \frac{\partial \ln\left(R_{H_2}\right)}{\partial \ln\left(A_{f,i}\right)} \cong \frac{A_{f,i}\Delta R_{H_2}}{R_{H_2}\Delta A_{f,i}} \qquad \text{Equation 3.9}$$

where $A_{f,i}$ and R_{H2} are the forward pre-exponential factor for reaction i and the rate of H_2 production, respectively. The NSCs of largest magnitude correspond to the elementary steps that affect the rate of H_2 production the most.

Figure 3.6 plots the NSCs for key surface elementary steps at four different sets of conditions (all elementary steps other than those displayed were found to have very low NSCs). There are two key observations. First, under most conditions the most kinetically significant step is C-H scission of the alkoxide intermediate ($HOCH_2CH_2O$) to form glycolaldehyde. This is consistent with ethylene glycol thermal decomposition results [59]. Second, the overall rate is almost completely unaffected by the OH-assisted dehydrogenation pathways. This finding is consistent with the foregoing reaction path analysis.

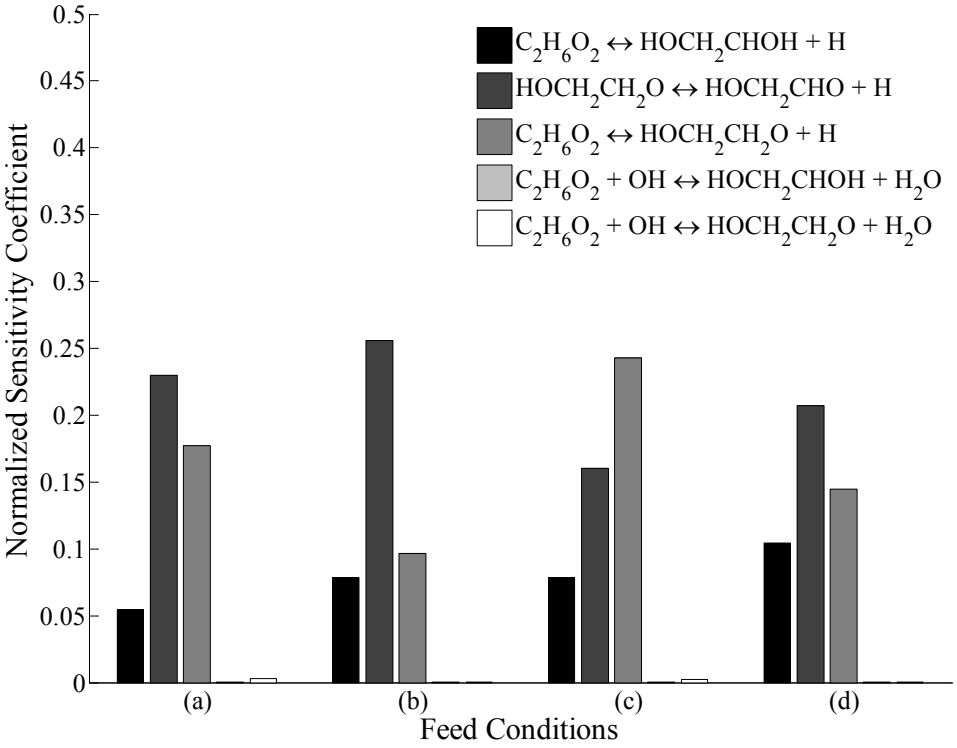

Figure 3.6: Normalized sensitivity coefficients for select surface elementary steps in the ethylene glycol steam reforming mechanism; feed conditions: (a) 483 K, 5% wt ethylene glycol in H_2O, (b) 483 K, 63% wt ethylene glycol in H_2O, (c) 543 K, 5% wt ethylene glycol in H_2O, (d) 543 K, 63% wt ethylene glycol in H_2O.

An important component of hierarchical model development [10] is to confirm the accuracy of reaction barriers computed in the model using the BEP correlations. Only the barriers of the rate-controlling reactions may affect the results, so sensitivity analysis is used to identify those reactions which require refinement. This greatly decreases the number of DFT calculations needed to generate a microkinetic model, without diminishing the accuracy of the results. Based on the results of Figure 3.6, the overall rate is not very sensitive to the values of the BEP-computed barriers for OH-

assisted dehydrogenation reactions. As a result, DFT refinement of those barriers is not crucial. Nevertheless, we sought to confirm this by performing DFT calculations for three of the most sensitive reactions with BEP-derived parameters; the results are summarized in Table 3.2. The DFT-calculated parameters were subsequently applied to the model, with negligible changes to the model predictions.

Table 3.2: Comparison of DFT- and BEP-computed barriers for ethylene glycol OH-mediated dehydrogenation.

Reaction	BEP-computed Barrier, T = 483 K [kcal mol^{-1}]	DFT-computed Barrier [a] [kcal mol^{-1}]
$C_2H_6O_2$** + OH* ⇌ $HOCH_2CH_2O$** + H_2O*	0.0[b]	0[b,c]
$C_2H_6O_2$** + OH* ⇌ $HOCH_2CHOH$** + H_2O*	11.6	16.6
$HOCH_2CH_2O$** + OH* ⇌ $HOCH_2CHO$** + H_2O*	9.0	3.5

[a] All transition states calculations converged within a tolerance of 0.075 eV $Å^{-1}$ or 1.7 kcal/mol $Å^{-1}$. [b] Barriers are referenced to the adsorbates co-adsorbed on the same slab. [c] A transition state could not be located after repeated attempts to do so; the elementary step is likely non-activated or has a very low barrier.

It has been shown that reactant fluxes through OH-mediated elementary steps make little or no contribution to the overall H_2 rate. To rationalize this, a direct comparison is made of relative rates for rate-controlling thermal and OH-mediated dehydrogenation pathways in Table A.2. Although the barriers for OH-mediated reactions are comparable to or smaller than those for unmediated pathways, the low coverage of OH^* renders these pathways unimportant on Pt under the conditions investigated. Related to that, the presence of H_2O decreases the CO* coverage only

slightly, and as a result it has only a minimal effect on the rate of thermal decomposition.

Analysis of reaction pathways and rate-determining steps also reveals parallels between ethylene glycol steam reforming and CH_4 steam reforming over Pt catalysts. Previous kinetic studies have shown that co-feeding H_2O with CH_4 does not affect the reaction rate, and initial C-H bond scission is the rate-controlling step [74]. Similar to what is observed for CH_4 steam reforming, OH-mediated pathways in ethylene glycol steam reforming are unimportant, and early thermal C-H bond scission is most rate-determining under most conditions. However, the model shows that O-H scission typically occurs prior to C-H scission in ethylene glycol steam reforming.

3.4 Conclusions

We have developed the first predictive mean-field microkinetic model for ethylene glycol steam reforming over Pt, using a hierarchical multiscale modeling approach. This work demonstrates that ethylene glycol steam reforming is kinetically equivalent to ethylene glycol thermal decomposition (catalytic pyrolysis) in the absence of H_2O co-reactant followed by small contributions of the water-gas shift reaction. It is expected that other supports that promote the water-gas shift reaction more may have a more substantial effect on the overall rate of steam reforming of ethylene glycol. Early thermal dehydrogenation reactions control the overall rate, and OH-mediated reactions play a negligible role due to very low OH* coverage on Pt. This finding is in contrast to recent work on Au under basic conditions [79] and indicates a significant effect of pH on the kinetics under certain conditions. Finally, these findings highlight an analogy between ethylene glycol steam reforming and CH_4

steam reforming on Pt catalysts, and offer insights into the key mechanistic aspects of steam reforming of oxygenates.

3.5 Acknowledgments

This chapter was reproduced with permission from [90] (http://dx.doi.org/10.1016/j.apcata.2012.04.010) Copyright 2012 Elsevier. This material was financially supported by the National Science Foundation (NSF) under grant EFRI-937706. I acknowledge the computational resources of the TeraGrid (a.k.a. XSEDE). I am grateful to Dr. Jonathan Sutton for providing the BEP correlations, and to Dr. Ying Chen, Dr. Michael Salciccioli, and Dr. Sarah Tupy for useful discussions.

Chapter 4

DFT-COMPUTED MECHANISMS OF ETHYLENE AND DIETHYL ETHER FORMATION FROM ETHANOL ON γ-Al_2O_3(100)

4.1 Introduction

γ-Al_2O_3 is widely used in heterogeneous catalysis as a support material, due to its good thermal stability and high surface area [91], and as a washcoat in automobile catalytic converters [92]. γ-Al_2O_3 itself also demonstrates activity for several reactions including the Claus process for sulfur removal [93], alkene double bond isomerization [94], and dehydration of alcohols [95]. The interest in dehydration chemistry has expanded in recent years, as it represents one important route for removing oxygen from biomass-derived compounds [96]. Understanding the origin of dehydration by solid acids, such as γ-Al_2O_3, is the first step towards rational development of materials with superior catalytic properties.

While the activity of γ-Al_2O_3 for alcohol dehydration has been known for some time [95], there are still significant research efforts aimed at understanding essential aspects of the active site(s) and reaction mechanisms [97-103]. In γ-Al_2O_3, bulk Al atoms display either tetrahedral or octahedral coordination. Exposed surface Al sites can display three-, four-, or five-fold coordination (see for example Ref. [104] and references therein), and exhibit Lewis acidity. Depending on the preparation method and catalyst operating conditions, the γ-Al_2O_3 surface is often at least partially hydrated and/or hydroxylated, creating potential Brønsted sites. The role of different active sites in alcohol dehydration is debated. Pines and Haag applied a variety of

probe molecules and indicators to study the surface, and concluded that Lewis sites are the dominant source of acidity [105]. In contrast, Knözinger et al. proposed that alcohols adsorb via hydrogen bonding to Brønsted sites [106]. More recently, Kwak et al. reported that Brønsted-bound ethanol is dehydrated to ethylene for catalysts calcined below 473 K, while ethylene originates from ethanol adsorbed on Lewis sites for catalysts treated above 673 K [98]. On the other hand, Roy et al. did not detect any evidence of Brønsted sites using catalysts treated at 573 K or higher, and they concluded that exposed Al surface sites (Lewis centers) are the primary adsorption sites for ethanol that lead to ethylene formation [101].

Apart from the type and role of the acid sites in alcohol dehydration, there has also been substantial work on the reaction mechanism. Knözinger and Köhne were among the first to systematically examine the dehydration pathways leading to ethers and olefins [107-108]. They demonstrated that only ethers form at low temperatures (488 K), while olefins form at higher temperatures (616 K), either directly from the alcohol, or via ether decomposition, or both [107-108]. Multiple experimental studies report a kinetic isotope effect (KIE) involving C-H bonds in olefin formation, and propose elimination-type mechanisms (either E1 or E2) to explain the observations [103, 109-110]. Experiments on ether formation indicate that a bimolecular nucleophilic substitution (S_N2) mechanism is active [111-113]. In addition to these studies, computational methods have also been applied to explore alcohol dehydration on alumina. Using density functional theory (DFT) calculations, both E1 and E2 concerted mechanisms have been proposed for olefin formation [97, 99, 101]. Two of these studies focused on butanol dehydration on the (100) facet [97, 99]. The other work examined dehydration of various alcohols on a Al_8O_{12} cluster model with a

tricoordinate Al site, which resembles the local environment of tricoordinate Al on γ-Al_2O_3(110) [101]; the tricoordinated Al surface atoms have been reported to be strong Lewis acid-type catalytic sites [114]. Existing computational studies of ether formation from alcohols on γ-Al_2O_3 are limited. To our knowledge, only one DFT study of methanol dehydration on the (110) facet has been reported, according to which dimethyl ether forms via reaction of two CH_3O groups [100].

In order to improve our understanding of both the role and nature of the active site(s) and the associated mechanisms for alcohol chemistry on γ-Al_2O_3, we have performed DFT calculations for dehydration and etherification reactions of ethanol on the (100) facet of γ-Al_2O_3. We are not aware of any previous DFT study examining ethanol dehydration on this facet, which contains pentacoordinated sites. Such pentacoordinate sites are observed to be experimentally active for ethanol dehydration [98, 115], motivating us to explore the (100) facet. We explore multiple pathways for ethylene formation including novel ether decomposition mechanisms and — to the best of our knowledge — we report the first DFT-computed diethyl ether formation mechanisms on γ-Al_2O_3. Both Lewis- and Brønsted-catalyzed mechanisms are considered in this study.

4.2 Computational Methods

The Vienna Ab initio Simulation Package (VASP) [26-29] was used to perform the calculations. We employed the PW91 functional developed by Perdew and Wang utilizing the generalized gradient approximation (GGA) [21, 116], and pseudopotentials developed using the projector augmented wave (PAW) method [117-118]. The PAW pseudopotentials were used as distributed by VASP (standard version of the potential for each element in our system). We simulated the (100) p(2×1)

surface using a supercell containing 80 atoms (corresponding to 4 atomic layers) with 15 Å of vacuum between periodic slabs, based on the nonspinel model for the bulk structure of γ-Al_2O_3 that was originally developed by Raybaud, Sautet and co-workers [119-120]. Note that the (100) is the lowest-energy fully-dehydrated facet reported for this alumina model [120]. The bottom atomic layer was held fixed in the bulk positions while all other atoms were allowed to relax. Consistent with previous literature [120], surface relaxation has little effect on the atomic positions; the maximum vertical relaxation of unconstrained atoms is 0.15 Å, or 2% of the slab thickness. To assess the convergence of adsorption properties, results were compared to calculations of a p(2×1) surface with the thickness doubled (an additional 80 atoms). The tested adsorption properties on the smaller slab were within 1 kcal/mol of the properties on the larger slab, when either the bottom two atomic layers or the entire bottom set of 80 atoms in the larger slab were kept fixed. The surface Brillouin zone was sampled using a 3×3×1 gamma-centered k-point grid. The plane wave basis set had a cutoff of 400 eV, and the forces in all calculations were converged to within 0.05 eV/Å (1.2 kcal/(mol Å)). Transition states (TSs) were located with either the climbing image nudged elastic band (CI-NEB) or Dimer methods [34-35]. These methods are often used in combination as described in Ref. [121].

4.3 Adsorbate Stability and Structure

The selection of the approach for computing adsorption energies on oxides merits careful consideration. Previous work has shown that the adsorption energy of Lewis acid-base adsorbate pairs on oxide surfaces is much stronger than the sum of the adsorbate energies of the isolated compounds [122-124]. The origin of this effect has been attributed to charge transfer between the adsorbates through the support, and

it has been shown that this effect is suppressed by performing spin-constrained calculations [122]. Consistent with those findings, we observe on γ-Al_2O_3 a substantial decrease in the total energy when co-adsorption takes place between ethoxy and atomic hydrogen radicals, and also between hydroxyl and hydrogen radicals (see Table B.1). The pairs of these radicals (each one carrying one unpaired electron) prefer to form a closed shell in the co-adsorbed state (see Table B.1). We also performed a Bader charge analysis [125] to examine the charges on atomic hydrogen and hydroxyl adsorbates. We find that for the singlet (triplet) state, an additional electron density of 0.2 (0.1) $|e^-|$ is transferred to adsorbed OH from the surface in the presence of adsorbed H, compared to the case of adsorbed OH without any co-adsorbate (see Table B.2). The amount of transferred charge in both spin states is similar. This suggests that, for this system, the change in spin states when comparing isolated adsorption with co-adsorption (rather than the charge transfer) has a significant contribution to the total energy of the co-adsorbed case. As a result of these observations, all calculations in this work utilize sets of adsorbates that are capable of forming closed-shell molecules without any leftover fragments so that the most stable adsorption states are used.

Figure 4.1 displays the (100) p(2×1) surface used for the calculations of this work. The four Al atoms exposed on the (100) plane (per unit area) are classified as pentacoordinated sites, whereas the six O atoms are tricoordinated. Site identifiers for Al and O sites are found in Figures 4.1 and B.1. In the superscript, we use a site identifier to indicate on which type of site an adsorbate sits (e.g., $H_2O^{V_a}$ indicates water sits on the Al V_a site, H^O or $H^{O'}$ means atomic hydrogen is on an oxygen site). While all sites of a given element have the same coordination, they do not exhibit

equivalent properties in terms of adsorption strength, electronic structure, etc. (particularly the Al sites) [120]. Therefore, ethanol was selected as a probe molecule to examine adsorption on all ten sites. The results for adsorption on the Al sites are presented in Table 4.1. Ethanol adsorbs through its oxygen in the alcohol group on the Lewis acidic Al sites. The strongest adsorption occurs on the Al V_a site with ΔE_{ads} = -19 kcal/mol, while it is -14 kcal/mol on sites V_b and V_d and -10 kcal/mol on site V_c. When adsorbed over a surface O site, the hydrogen in the alcohol group is oriented towards the surface. The adsorption energies, listed in Table B.3, range from -2 to -5 kcal/mol, consistent with a hydrogen bonding type of interaction. The adsorption energies for the other four stable gas-phase intermediates (water, ethylene, acetaldehyde, and diethyl ether) are reported for the Al sites (see Table 4.1). Similar to ethanol, they weakly interact with surface O sites. Although acetaldehyde is a dehydrogenation product, we include it to compare activation barriers of dehydration and dehydrogenation on alumina. The qualitative trends of relative binding strength on each Al site are consistent for ethanol, water, and diethyl ether. This means that the differences in adsorption strength on the various Al sites are due to electronic effects. Acetaldehyde differs slightly from other adsorbates in that it binds more strongly to the V_c site than to V_b and V_d (by 3 kcal/mol). All four oxygen-containing intermediates bind strongest to the V_a site. Ethylene binds weakly to all Al sites. Structures of these intermediates in their most stable configurations are found in Figure 4.2. Also, as shown in Table 4.1, water and ethanol have similar adsorption energies on all Al sites. This indicates that water and ethanol will compete for adsorption sites on the (100) surface. This is consistent with experimental observations that water strongly inhibits ethanol dehydration and etherification [103].

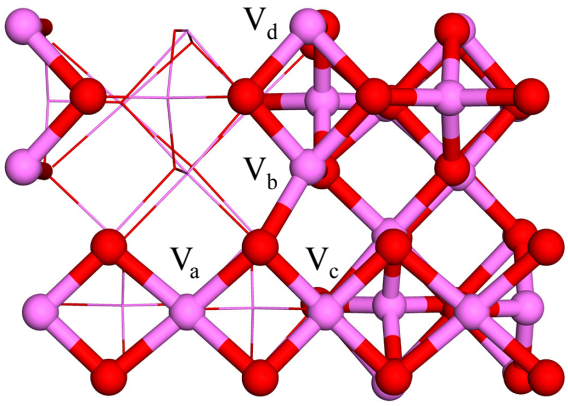

Figure 4.1: Top view of the γ-Al_2O_3(100) p(2×1) surface. Al atoms shown in pink, O atoms in red. The "V_x" labels refer to the different Al sites and "V" stands for the coordination number. The subsurface atoms on the left side of the figure are drawn differently so that the surface atoms are more easily identified.

Table 4.1: Energy of adsorption of stable gas-phase intermediates adsorbed at Al sites on the γ-Al_2O_3(100) surface. Refer to Figure 4.1 for site identification. Adsorption energies are defined with respect to the corresponding molecule in the gas phase.

Adsorbate	ΔE_{ads} [kcal/mol]			
	Site V_a	Site V_b	Site V_c	Site V_d
H_2O^{Al}	-20	-15	-13	-15
$C_2H_4{}^{Al}$	-4	-2	-2	-1
CH_3CHO^{Al}	-13	-5	-8	-4
$CH_3CH_2OH^{Al}$	-19	-14	-10	-14
$CH_3CH_2OCH_2CH_3{}^{Al}$	-12	-9	-8	-9

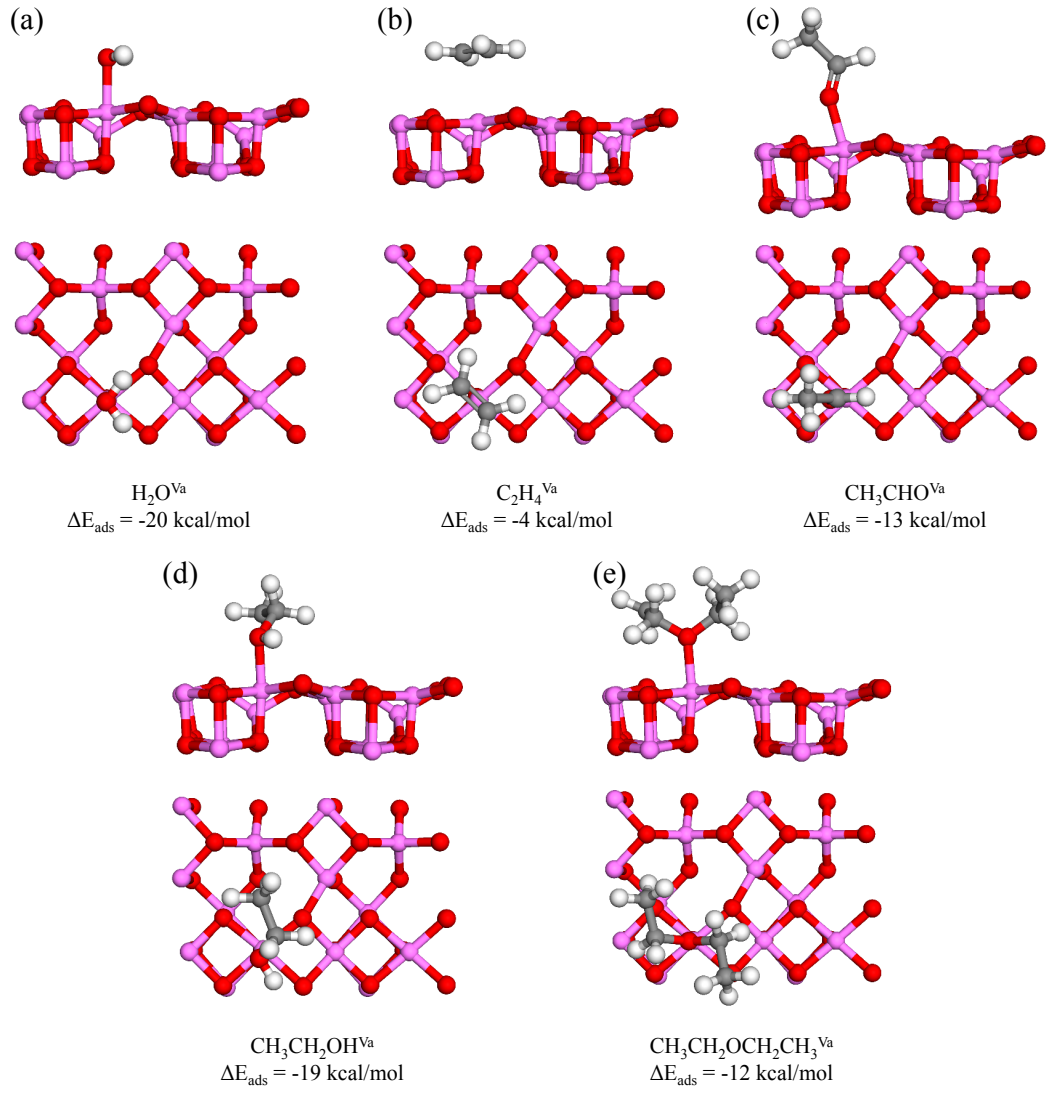

Figure 4.2: Structures and adsorption energies of the stable gas-phase intermediates of the ethanol reaction network in their most stable adsorbed configurations. (a) water, (b) ethylene, (c) acetaldehyde, (d) ethanol, (e) diethyl ether. Adsorption energies are defined with respect to the corresponding molecule in the gas-phase.

Figure 4.2 and Figure 4.3 contain the structures of all intermediates considered in the network in their most stable configurations. We examined different

conformations of adsorbates, and found that differences in adsorption energies arising primarily from hydrogen bonding were on the order of 4 kcal/mol or less. Alongside each subfigure, the energy of the featured adsorbate is listed with respect to a suitable reference (adsorbate in the gas-phase for Figure 4.2; for Figure 4.3, see caption). The reference state for many of the adsorbates in Figure 4.3 is either one or two gas-phase ethanol molecules, in order to examine the energetic preference to form these adsorbates from the reactant ethanol. The stability of both the $OH^{Va} + H^{O}$ and $CH_3CH_2O^{Va} + H^{O}$ adsorbed states is similar to (respectively) H_2O^{Va} and $CH_3CH_2OH^{Va}$ (see Figure 4.3(a)-(b)). $OH^{Va} + H^{O}$ is more stable than H_2O^{Va} by 8 kcal/mol, while $CH_3CH_2O^{Va} + H^{O}$ is more stable than $CH_3CH_2OH^{Va}$ by 3 kcal/mol. In the dissociated states, there is hydrogen bonding between the $R\text{-}O^{Al}$ group and H^{O}. The surface is also reconstructed upon dissociation, especially in the case of OH^{Va}, to accommodate hydrogen bond formation (see Figure 4.3(a)). The formation of ethyl and hydroxyl ($CH_3CH_2^{O} + OH^{Va}$) relative to gas-phase ethanol is also stable (-7 kcal/mol), but not as stable as $CH_3CH_2O^{Va} + H^{O}$ (22 kcal/mol) or $CH_3CH_2OH^{Va}$ (19 kcal/mol). The surface O atom on which $CH_3CH_2^{O}$ is adsorbed is deflected upwards from its starting position (see Figure 4.3(c)). All other adsorbates are less stable than their gas-phase reference (adsorption energies quantified in Figure 4.3). $CH_3CHOH^{Va\text{-}Vc}$ and $CH_2CH_2OH^{Va\text{-}Vc}$ bind on two Al sites with one C-Al bond each. The Al atom to which carbon binds (V_c site) is shifted upward to reduce the strain induced by cyclization with the surface (see Figure 4.3(d)-(e)). $CH_3CH_2OCH_2CH_2OH^{Va\text{-}Vc}$ and $CH_3CH_2OCH(CH_3)OH^{Va\text{-}Vc}$ were explored as possible intermediates for ether formation. Their binding configurations were chosen based on the most stable adsorption of the precursors $CH_2CH_2OH^{Va\text{-}Vc}$ and $CH_3CHOH^{Va\text{-}Vc}$, respectively. They are both much less stable than the gas-phase

reference (2 $CH_3CH_2OH_{(g)}$, see Figure 4.3(f)-(g)) and are not likely intermediates for diethyl ether. Finally, in order to test the effect that H^O (a Brønsted acid) may have on catalyzing dehydration when some Al (Lewis) sites are blocked by water (in the form of OH^{Va} + H^O), an adsorbed state of ethanol was considered that interacts with both OH^{Va} and H^O via hydrogen bonding (see Figure 4.3(h)). Accounting for the fact that OH^{Va} and H^O are pre-adsorbed on the surface (and therefore that the hydrogen bond between those two species must break), the adsorption energy of ethanol is -6 kcal/mol, which is fairly weak compared to ethanol adsorption on Lewis sites. This is consistent with weak binding of N_2 and CO probe molecules to Brønsted sites [120, 126].

The discussion in previous paragraphs has focused on isolated intermediates and dissociation products of those intermediates. Recent studies have shown how adsorbate dimers inhibit dehydration rates on the γ-Al_2O_3 surface [103], indicating that consideration of co-adsorption effects is important. Co-adsorption of two ethanol molecules has been tested on distinct pairs of Al sites, namely (1) V_a + V_b sites, and (2) V_a + V_c sites. We find that the adsorption energies of these "dimers" are virtually unchanged relative to the isolated adsorbates. For case (1), the adsorption energy of the co-adsorbed state (relative to 2 ethanols in the gas phase) is -30 kcal/mol, whereas the sum of the binding energies of the isolated adsorbates is (using values from Table 4.1) -33 kcal/mol. For case (2), the adsorption energy of the co-adsorbed state is -27 kcal/mol, whereas the sum of the binding energies of the isolated adsorbates is -29 kcal/mol. Therefore, we find no evidence of stabilizing effects from dimer formation on this facet. Similar to this, Digne et al. (see inset to Figure 7a in Ref. [120]) have found that increasing the water coverage on the (100) facet results in either an

invariant or a decreasing differential adsorption energy. This indicates that stabilizing interactions indicative of water dimer formation are not observed on this facet. Based on these observations for ethanol-ethanol and water-water interactions, we do not expect that co-adsorption of ethanol and water molecules will lead to significant stabilizing interactions. Further, dimers formed by ethanol and/or water adsorption involving the same Lewis center are not expected to be favorable on pentacoordinate sites because the Al becomes 6-coordinate after the first adsorbate binds. Dimer formation may be important on facets other than (100).

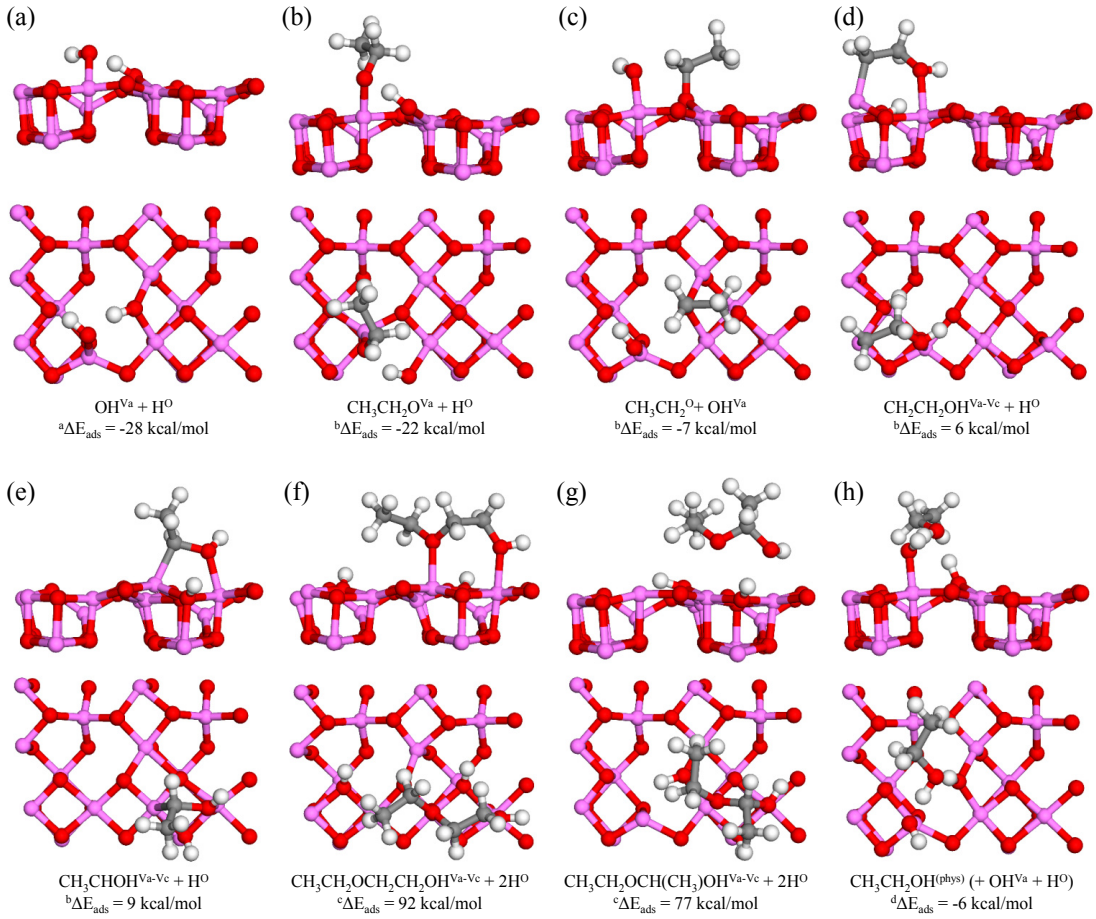

Figure 4.3: Structures of surface intermediates of the ethanol reaction network in their most stable adsorbed configurations. The adsorption energy of the featured adsorbate is listed adjacent to each subfigure with respect to a suitable reference. [a] Reference is $H_2O_{(g)}$. [b] Reference is $CH_3CH_2OH_{(g)}$. [c] Reference is 2 $CH_3CH_2OH_{(g)}$. [d] Reference is $CH_3CH_2OH_{(g)}$ and OH^{Va} + H^{O} pre-adsorbed on the Al_2O_3 slab.

4.4 Reaction Energetics and Kinetics

The global reactions for the ethanol reaction network are shown in Equation 4.1 and Equation 4.2:

$$CH_3CH_2OH \rightarrow C_2H_4 + H_2O \qquad \text{Equation 4.1}$$

$$2\ CH_3CH_2OH \rightarrow CH_3CH_2OCH_2CH_3 + H_2O \qquad \text{Equation 4.2}$$

The elementary steps of Equation 4.1 and Equation 4.2 considered in this work are summarized in Table B.4, while Figure 4.4 contains an overview of the reaction network. The elementary steps listed in Figure 4.4 are numbered, and these numbers are used in to reference the appropriate reaction in the discussion.

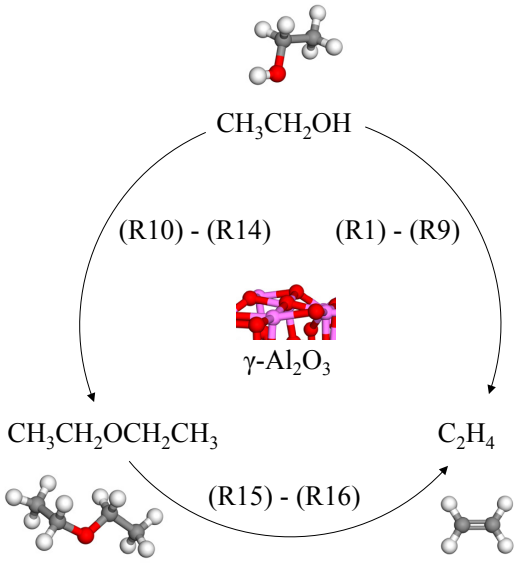

Ethanol to Ethylene

(R1) $CH_3CH_2OH^{Va} + O \rightarrow CH_3CH_2O^{Va} + H^O$

(R2) $CH_3CH_2OH^{Va} + O \rightarrow CH_3CH_2{}^O + OH^{Va}$

(R3) $CH_3CH_2{}^O + OH^{Va} + O' \rightarrow C_2H_4 + OH^{Va} + H^{O'} + O$

(R4) $CH_3CH_2OH^{Va} + Vc + O \rightarrow CH_2CH_2OH^{Va\text{-}Vc} + H^O$

(R5) $CH_2CH_2OH^{Va\text{-}Vc} + H^O \rightarrow C_2H_4 + OH^{Va} + H^O + Vc$

(R6) $CH_3CH_2OH^{Va} + O \rightarrow C_2H_4 + OH^{Va} + H^O$

(R7) $CH_3CH_2O^{Va} + H^O \rightarrow C_2H_4 + OH^{Va} + H^O$

(R8) $CH_3CH_2OH^{Va} \rightarrow C_2H_4 + H_2O^{Va}$

(R9) $CH_3CH_2OH^{(phys)} + OH^{Va} + H^O + O' \rightarrow C_2H_4 + H_2O^{O'} + OH^{Va} + H^O$

Ethanol to Diethyl Ether

(R10) $CH_3CH_2O^{Va} + H^O + CH_3CH_2OH^{Vb} \rightarrow CH_3CH_2OCH_2CH_3{}^{Va} + OH^{Vb} + H^O$

(R11) $CH_3CH_2O^{Va} + H^O + CH_3CH_2OH^{Vb} + O' \rightarrow CH_3CH_2O^{Va} + H^O + OH^{Vb} + CH_3CH_2{}^{O'}$

(R12) $CH_3CH_2O^{Va} + H^O + OH^{Vb} + CH_3CH_2{}^{O'} \rightarrow CH_3CH_2OCH_2CH_3{}^{Va} + OH^{Vb} + H^O + O'$

(R13) $CH_3CH_2OH^{Va} + CH_3CH_2OH^O \rightarrow OH^{Va} + H^O + CH_3CH_2OCH_2CH_3$

(R14) $CH_3CH_2OH^{(phys)} + OH^{Va} + H^O + CH_3CH_2O^{Vb} + H^{O'} \rightarrow CH_3CH_2OCH_2CH_3{}^{Vb} + H_2O^O + OH^{Va} + H^{O'}$

Diethyl Ether to Ethylene

(R15) $CH_3CH_2OCH_2CH_3{}^{Va} + O \rightarrow C_2H_4 + CH_3CH_2O^{Va} + H^O$

(R16) $CH_3CH_2OCH_2CH_3{}^{Va} \rightarrow C_2H_4 + CH_3CH_2OH^{Va}$

Figure 4.4: Reaction network for the production of diethyl ether and ethylene.

4.4.1 O-H Bond Scission and Formation

For both ethylene and ether formation, reactions involving O-H bonds are necessary to complete a catalytic cycle. O-H scission of both water and ethanol was explored and was found to be exothermic on V_a sites and slightly endothermic on other sites (see Table B.4). Multiple attempts to locate transition states for these steps were unsuccessful, even after optimizing the intermediates so that the forces on all

atoms were less than 0.01 eV/Å. The fact that the H in the R-OH group strongly interacts with (and is in close proximity to) the surface O site is consistent with a very low barrier or no barrier for O-H bond scission. This observation is similar to results of NEB calculations performed for (dissociated) water desorption on the γ-Al_2O_3(110) surface, in which no barriers were located [127]. Based on this result, and the fact that the stability of $CH_3CH_2OH^{Va}$, H_2O^{Va} and their O-H dissociation products are similar on sites V_b, V_c and V_d , we did not attempt to locate barriers on sites V_c and V_d for O-H scission reactions.

4.4.2 Ethylene Formation from Ethanol

To convert ethanol (or ethoxy) to ethylene, the C-O and C_β-H bonds of ethanol must break, leading naturally to a re-hybridization of the carbon atoms and formation of the C-C double bond. The elementary steps involve either sequential or simultaneous scission of these bonds. We focus first (and primarily) on Lewis-catalyzed mechanisms. The energetics for five different pathways are plotted in Figure 4.5. In the "$CH_3CH_2^O$ mechanism" (R2)-(R3), the C-O bond first breaks via a barrier of 52 kcal/mol, and C_β-H scission of $CH_3CH_2^O$ occurs subsequently with a 36 kcal/mol barrier (Figure B.2(a)-(b)). In the "$CH_2CH_2OH^{Va\text{-}Vc}$ mechanism" (R4)-(R5), first C_β-H and then C-O scission occurs with a barrier of, respectively, 46 and 8 kcal/mol (Figure B.2(c)-(d)). The other three pathways involve concerted bond-breaking mechanisms. In the "E1" pathway (R1) and (R7), the O-H bond breaks to form $CH_3CH_2O^{Va}$, and then the H_β is transferred to the O of $CH_3CH_2O^{Va}$ while the C-O bond is broken. The barrier is 57 kcal/mol (Figure 4.6(a)). The "E1′" pathway (R8) involves a similar mechanism except that there is no initial O-H scission, and ethylene and H_2O^{Va} form directly from ethanol with a barrier of 52 kcal/mol (Figure 4.6(b)). In

the "E2" pathway (R6), the H_β is abstracted by a surface O site as the C-O bond breaks, and the barrier is 37 kcal/mol (Figure 4.6(c)). Note that the terms "E1" and "E2" are indicative of the molecularity of the rate expression, including surface sites. For example, the E2 pathway (R6) is an elimination mechanism with two reactants involved in the forward rate expression ($CH_3CH_2OH^{Va}$ and a vacant O site). The E1 pathway (R7) has only one reactant ($CH_3CH_2O^{Va}$) participating in the forward rate expression; H^O is present but not involved in the reaction.

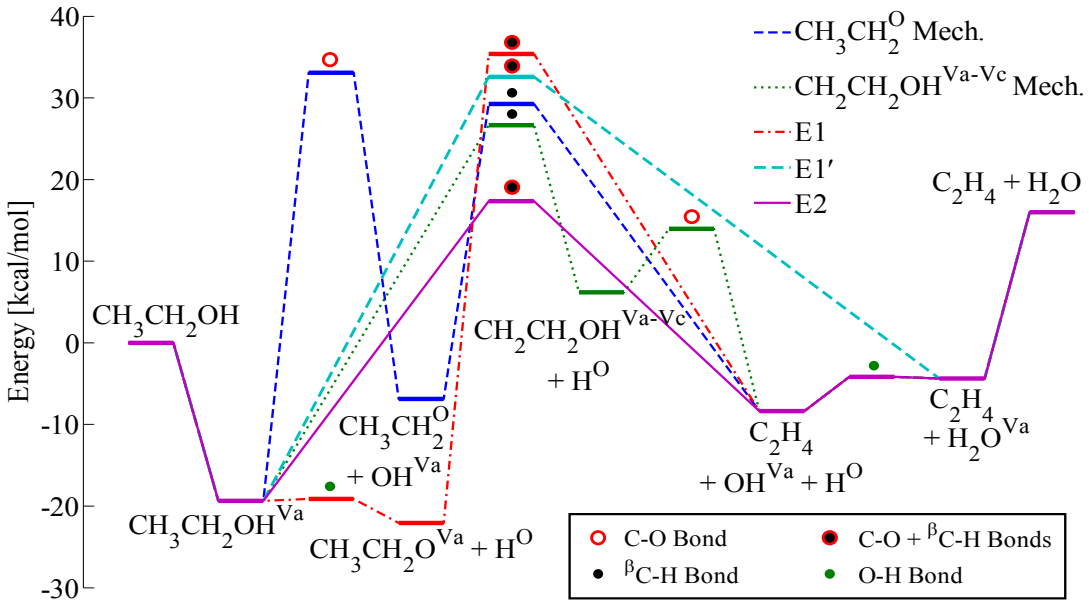

Figure 4.5: Energy diagram of principal reaction pathways for ethylene formation from ethanol. Each transition state is labeled to identify the bond(s) involved in the reaction.

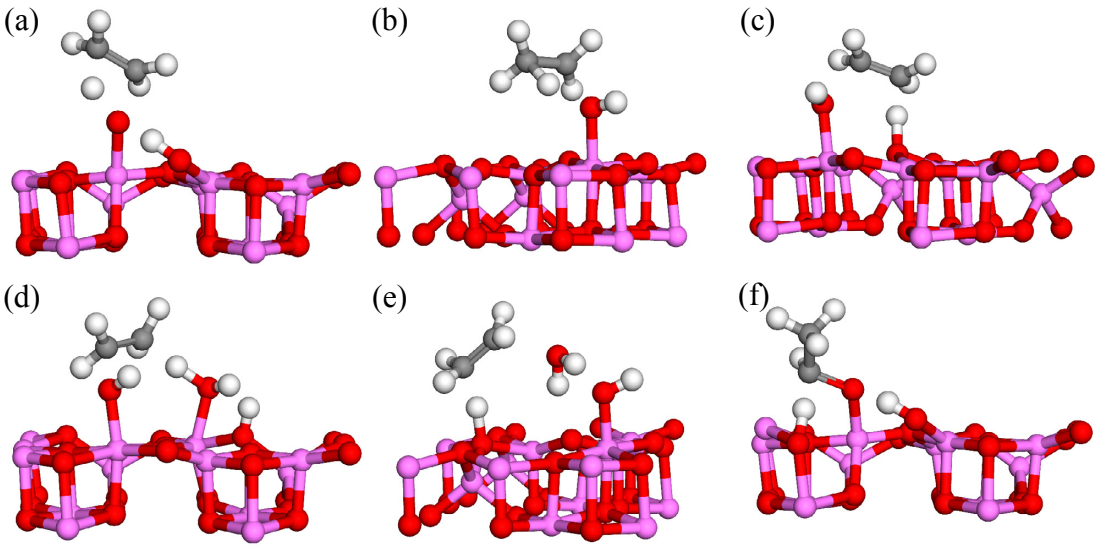

Figure 4.6: Transition state structures for ethylene and acetaldehyde formation from either ethanol or ethoxy. See Table B.4 and the text for energetic information. (a) $CH_3CH_2O^{Va} + H^{O} \rightarrow C_2H_4 + OH^{Va} + H^{O}$ (R7), (b) $CH_3CH_2OH^{Va} \rightarrow C_2H_4 + H_2O^{Va}$ (R8), (c) $CH_3CH_2OH^{Va} + {}^{O} \rightarrow C_2H_4 + OH^{Va} + H^{O}$ (R6), (d) $CH_3CH_2OH^{Va} + OH^{Vb} + H^{O} \rightarrow C_2H_4 + H_2O^{Vb} + OH^{Va} + H^{O}$, (e) $CH_3CH_2OH^{(phys)} + OH^{Va} + H^{O} + {}^{O'} \rightarrow C_2H_4 + H_2O^{O} + OH^{Va} + H^{O'}$ (R9), (f) $CH_3CH_2O^{Va} + H^{O} + {}^{Vc} + {}^{O} \rightarrow CH_3CHO^{Va\text{-}Vc} + 2H^{O}$.

The E1 pathway via $CH_3CH_2O^{Va}$ (R7) is similar to a pathway proposed for 2-butanol dehydration, for which the reported barrier was ~26 kcal/mol [99]. This barrier is much lower than the one computed herein for ethanol (57 kcal/mol). Dispersion effects were found to be important for 2-butanol dehydration barriers [99], but tests on our system revealed that barriers changed by less than 2 kcal/mol between calculations with and without dispersion. Our previously reported barrier for the E1 pathway on the alumina cluster exposing tricoordinated sites was 69 kcal/mol [101], which is higher than that found in the present work. The E2 pathway (R6) is identical to the dehydration mechanism we reported previously [101], and the barriers are very similar (within 5 kcal/mol). The E2 pathway is also similar to E2 mechanisms

proposed by Dabbagh et al. for 2-butanol dehydration, though the lowest barrier they reported was 47 kcal/mol [97].

From an energetic standpoint, the E2 mechanism (R6) is preferred for ethylene formation. For comparison, the pathway (R4) with the second-smallest barrier (forming $CH_2CH_2OH^{Va\text{-}Vc}$) is 46 kcal/mol. That results in a nearly 3 orders-of-magnitude difference in the rate constant (assuming an Arrhenius expression, equal values of the pre-exponential factor, and 500 K). The mechanism is also consistent with proposed mechanisms from literature and with observed KIEs for alcohols including ethanol [103, 109-110]. Based on the favorable energetics, other mechanisms were examined in connection with the E2 path. The initial E2 barrier was computed using ethanol adsorbed on the Al V_a site. The calculation was repeated on the second-most stable Al site V_b, and the resulting barrier was nearly identical (different by 1 kcal/mole), showing that the barrier is not particularly site-dependent. This is consistent with our reported correlation of the activation barrier of alcohol dehydration with the carbenium ion stability of the reacting molecule [101]. Since the reaction barrier is mainly determined by the property of the alcohol (carbenium ion stability) and there is no significant change in the Lewis acidity of the Al sites (all are pentacoordinated sites), we expect similar dehydration barriers. The adsorption energies differ on sites V_a and V_b. As a result, the stability of the transition state should also be different in order for the barriers to be invariant with the adsorption site. However, the carbenium ion stability is the same in these two cases, so the remaining component contributing to the total energy of the transition state is the hydroxyl adsorption on the surface. The hydroxyl stability on sites V_a and V_b follows

the stability of ethanol (the reactant) on these two sites, accounting for the invariance of the activation barrier with site.

We have treated so far dehydration reactions on the fully dehydrated (100) surface. However, alumina surfaces are often at least partially hydrated at reaction conditions [120]. Previous reports have discussed the effects of surface hydration on reactivity [98, 103, 126, 128]. We have therefore examined (in connection with the E2 mechanism) the effect of using OH^{Vb} (rather than a surface O site) to extract the H_β from $CH_3CH_2OH^{Va}$; the OH^{Vb} was formed by dissociating H_2O^{Vb}. The barrier was 37 kcal/mol, identical to the regular E2 case (R6), and consistent with the correlation to the carbenium ion stability (Figure 4.6(d)). We have also considered the effect of co-adsorbed (spectator) water on the E2 mechanism by adsorbing ethanol on the V_b site with dissociated water in its most stable position on the V_a site ($OH^{Va} + H^O$; note that during optimization H_2O^{Va} was reformed). The barrier of this elementary step is 33 kcal/mol (see Figure B.2(e) for transition state) and is slightly lower than the barrier of 36 kcal/mol in the absence of co-adsorbed water, which suggests that water may reduce slightly the dehydration barrier. On the other hand, the adsorption calculations in this work and previous experimental studies [101, 103] indicate that water also competes with ethanol for adsorption sites. In particular, steady-state experiments of DeWilde et al. demonstrate that increasing the amount of water co-fed with a constant ethanol feed results in a monotonic decrease in the reaction rate [103]. This suggests that water does not enhance the reaction rate of ethanol dehydration. In addition to the foregoing studies, possible catalytic effects of H^O when water blocks Al sites were explored using ethanol adsorbed on a dissociated water molecule ($OH^{Va} + H^O$) in its most stable configuration on the V_a site (R9). The H^O attacks the O atom of ethanol

(forming physisorbed water) as the C-O bond breaks and the H_β is abstracted by a surface O site (Figure 4.6(e)). The barrier for this pathway is ~13 kcal/mol higher than when ethanol is adsorbed directly on the V_a site, and this is at least partially related to the fact that water is only physisorbed rather than chemisorbed. The reactant configuration is not very stable either. As reported in Figure 4.2, the ethanol adsorption energy ΔE_{ads} = -6 kcal/mol on dissociated water, compared to -19 kcal/mol on the V_a site. In this type of mechanism, the H^O is acting as a Brønsted acid. Therefore this result suggests that, at least on the (100) facet, catalysis of ethanol dehydration to ethylene by a Brønsted-like site does not appear to be a favorable pathway.

To conclude this section, we briefly note that one potential side reaction of ethanol is dehydrogenation to acetaldehyde, typically observed only in low yields [129]. The computed dehydrogenation barrier for acetaldehyde formation from $CH_3CH_2O^{Va}$ is 45 kcal/mol (Figure 4.6(f)), which is 8 kcal/mol larger than the barrier for the E2 dehydration of ethanol. The alternative dehydrogenation sequence starting from ethanol (to form $CH_3CHOH^{Va\text{-}Vc}$) was found to be thermodynamically unfavorable (ΔE_{rxn} = 28 kcal/mol) and therefore the barrier was not computed. These observations rationalize the lack of selectivity to acetaldehyde over γ-Al_2O_3.

4.4.3 Diethyl Ether Formation

Elimination reactions (like those discussed for ethylene formation) are known to compete with substitution reactions [130]. Alcohols participate in nucleophilic substitution, and therefore multiple variants of S_N2 reactions have been examined, beginning with Lewis sites. The energetics of the principal pathways are summarized in Figure 4.7. The adsorption calculations indicate that $CH_3CH_2O^{Va}$ + H^O is more

stable than ethanol on V_a sites (by 3 kcal/mol), while ethanol is more stable than $CH_3CH_2O^{Va}$ + H^O on V_b sites (by 2 kcal/mol). This is adopted as the primary configuration, and a barrier of 35 kcal/mol for the formation of diethyl ether was found. As shown in Figure 4.8(a), $CH_3CH_2O^{Va}$ on the V_a site acts as the attacking nucleophile to which the ethyl group of ethanol is transferred, and the OH^{Va} fragment of ethanol is ejected as the leaving group. The nucleophile and leaving group interact with the attacked carbon atom from opposite sites (~145° O-C-O bond angle). At the transition state, the H-C_α-H bond angle of the transferring fragment is close to 120°, indicative of sp^2 hybridization. The C-C bond axis is oriented normal to the surface to minimize repulsion and maximize the stabilizing interactions between the C_α and the O atoms of both $CH_3CH_2O^{Va}$ and OH^{Va}. All of these observations are consistent with a classic S_N2 mechanism and specifically the backside route of attack. We refer to this pathway as (R10) in Figure 4.4 and as "S_N2" in Figure 4.7. Other configurations of the reactants were also examined, including swapping the positions of ethoxy and ethanol on the V_a and V_b sites, and also adsorbing ethoxy on V_a and ethanol on V_c. In the former case, the barrier was 31 kcal/mol which is lower than the barrier of (R10), but the adsorbates are not as stable in these sites. In the latter case, the barrier was ~15 kcal/mol higher (i.e., 46 kcal/mol), with the V_c site significantly tilted at the transition state, and the O-C-O bond angle measuring ~125° (Figure 4.8(b)). The V_a and V_c sites may be situated too close to one another to allow for the same transition state stabilization that occurs with the pairing of V_a and V_b sites. All of the foregoing S_N2 mechanisms involve a backside route of attack. It is also possible for a frontside nucleophilic attack to occur, but it is typically energetically unfavorable. In order to prove this, we have examined one frontside attack mechanism with ethanol on V_a and

ethoxy on V_b (Figure B.2(f)), and found the barrier to be 55 kcal/mol, 20 kcal/mol higher than in the backside route of attack. This is consistent with homogeneous chemistry and also with observations of stereochemical inversion for ether formation from 2-butanol, which takes place during an S_N2 backside attack [113]. In addition, in analogy to our study on the E2 barrier (R6), we have explored the hydration effect on the S_N2 reaction (R10). We calculated the barrier for the case in which ethanol, ethoxy, and H are adsorbed in the same configurations as in (R10), while water is adsorbed on the V_c site. The barrier is reduced to 27 kcal/mol (see Figure B.2(g) for transition state) compared to 35 kcal/mol without co-adsorbed water, suggesting that co-adsorbed water may make the reaction more favorable. However, the aforementioned opposing effect due to competitive adsorption between water and ethanol applies here as well. Further, similar to ethylene formation, experimental diethyl ether formation rates decrease monotonically with increasing water co-feed [103]. Thus, water appears to inhibit rather than accelerate ether formation rates.

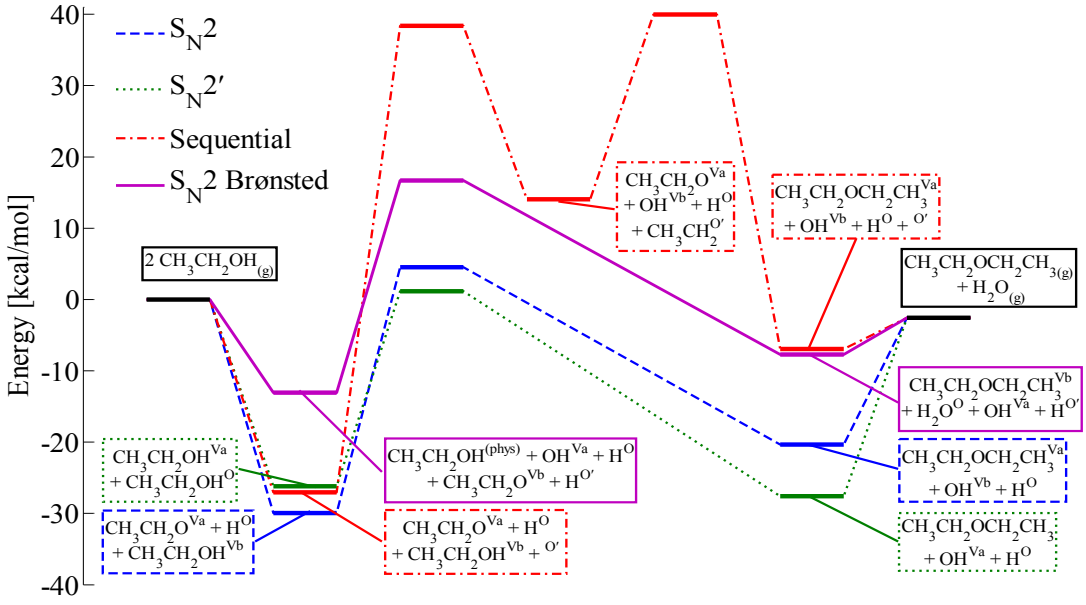

Figure 4.7: Energy diagram of principal reaction pathways for diethyl ether formation from ethanol. Note that for the "S_N2 Brønsted" mechanism, dissociated water as "$OH^{Va} + H^{O}$" is considered to be pre-adsorbed on the Al_2O_3 slab and remains there at the end of the catalytic cycle. In this way, all pathways in the diagram have the same gas-phase reference.

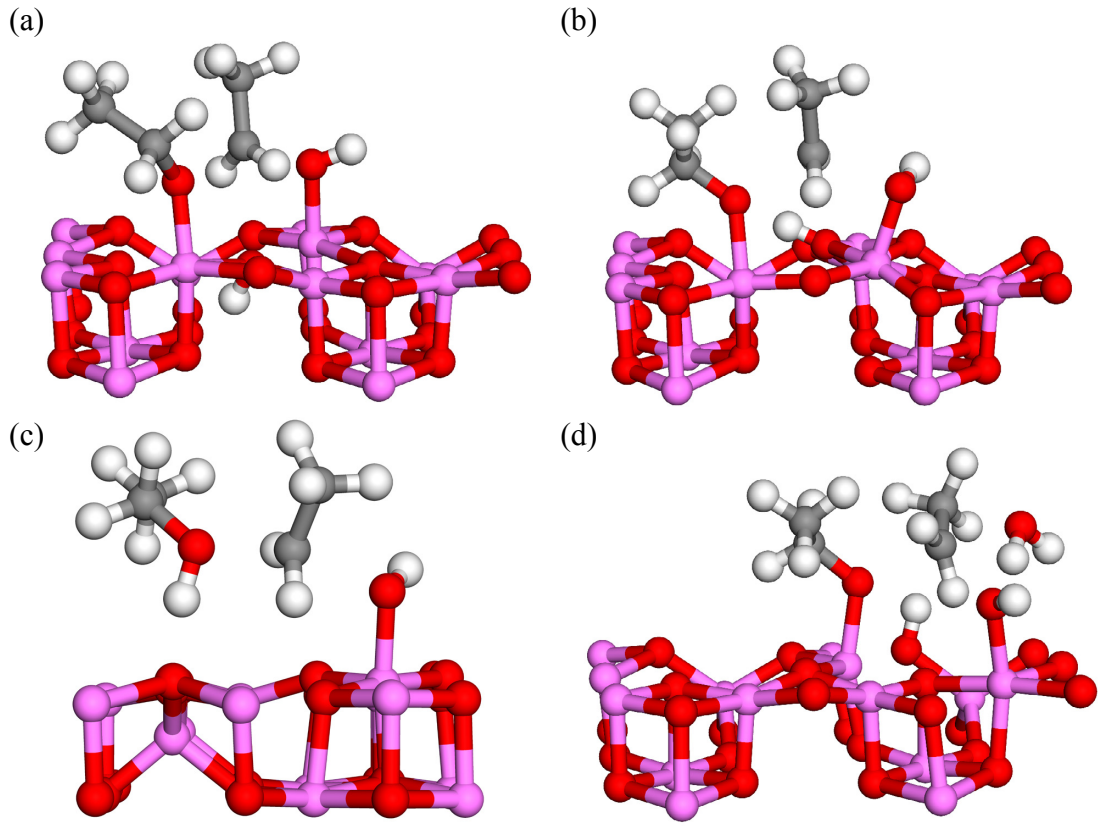

Figure 4.8: Transition state structures for diethyl ether production. See Table B.4 and the text for energetic information. (a) $CH_3CH_2O^{Va} + H^O + CH_3CH_2OH^{Vb} \rightarrow CH_3CH_2OCH_2CH_3{}^{Va} + OH^{Vb} + H^O$ (R10), (b) $CH_3CH_2O^{Va} + H^O + CH_3CH_2OH^{Vc} \rightarrow CH_3CH_2OCH_2CH_3{}^{Va} + OH^{Vc} + H^O$, (c) $CH_3CH_2OH^{Va} + CH_3CH_2OH^O \rightarrow OH^{Va} + H^O + CH_3CH_2OCH_2CH_3$ (R13), (d) $CH_3CH_2OH^{(phys)} + OH^{Va} + H^O + CH_3CH_2O^{Vb} + H^{O'} \rightarrow CH_3CH_2OCH_2CH_3{}^{Vb} + H_2O^O + OH^{Va} + H^{O'}$ (R14).

Additional postulated S_N2-type mechanisms involve alternative adsorption configurations for one of the ethanol molecules. In the first case, one of two ethanol molecules is adsorbed on a surface O site, rather than adsorbing both on Al centers (Figure 4.8(c)). Note that the O site may still be considered as a Lewis (base) site. This pathway is labeled (R13) in Figure 4.4 and "S_N2′" in Figure 4.7, and is similar to a

mechanism proposed by Jain and Pillai [111-112]. Consistent with the adsorption calculations, this type of reactant state is less stable than when two Al centers are involved (see Figure 4.7), but the barrier is also low (27 kcal/mol) and therefore the reaction is plausible. A second case features one ethanol physisorbed on a dissociated water molecule via hydrogen bonding, while ethoxy is stabilized on a nearby V_b site (R14). The H^O of dissociated water, acting as a Brønsted acid, attacks the O of the physisorbed ethanol as the C-O bond dissociates while a new C-O bond forms between adsorbed ethoxy and the C_2H_5 fragment (see "S_N2 Brønsted" mechanism in Figure 4.7 and Figure 4.8(d)). The barrier is 30 kcal/mol, which is competitive with the lowest barrier pathways. However this configuration is less stable than the analogous state with ethanol adsorbed directly on the V_a site. Referenced to the slab with $CH_3CH_2O^{Vb}$, OH^{Va}, and $2H^O$ pre-adsorbed, the ethanol adsorption energy is only -5 kcal/mol (compared to -19 kcal/mol for direct adsorption on the V_a site). The low adsorption energy suggests that this pathway may be less preferred than mechanisms with direct adsorption on Al sites. Considering the dependence of preferred adsorption states on condition-specific parameters (e.g., equilibrium constants and reactant partial pressures) and also the similarity of the Lewis- and Brønsted-catalyzed reaction barriers (30 vs. 35 kcal/mol), it is difficult in this case to determine the dominant pathway from the DFT information alone. We therefore couple our theoretical observations with recent experimental evidence. DeWilde et al. measured KIEs on ethanol dehydration over γ-Al_2O_3 using deuterated ethanol feeds, and did not observe any statistically significant effect on diethyl ether formation rates [103]. Isotopic scrambling of adsorbed H is expected given the low O-H dissociation barriers reported in this study. As a result, a KIE should be observed if the Brønsted-catalyzed pathway

is dominant because O-H dissociation is part of the mechanism. Since no isotope effect is observed, we conclude that while Brønsted-catalyzed ether formation is possible, it is not expected to be a dominant pathway. Finally, we note at this point the possibility of two alkoxy molecules reacting to form ether. This type of reaction was proposed as the dominant pathway for dimethyl ether formation from methanol on γ-Al_2O_3(110) [100]. Such a pathway involves the formation of an adsorbed O^{Al} species as one of the products, and we have found that this species is very unstable on the (100) surface (the nearby H^O prefers to recombine with the O^{Al} to form OH^{Al}). Therefore the pathway involving two ethoxys is not favorable on the (100) facet.

In the previous sets of pathways, a C-O bond breaks and a new C-O bond forms in the same elementary step. It is also plausible that these two bonds may break and form sequentially in two separate steps. Recall that the formation of $CH_3CH_2{}^O$ + OH^{Va} from ethanol was considered as an ethylene formation mechanism. The same step has been considered here again for ether formation but in the presence of ethoxy (R11), and we found it to exhibit an even higher barrier (66 kcal/mol, versus 52 kcal/mol without ethoxy). The barrier for the 2nd step (R12) is low, E_a = 26 kcal/mol (Figure B.2(h)-(i); "Sequential" pathway in Figure 4.7). The higher barrier in the presence of ethoxy is partly due to the fact that the mechanism takes place on a different site (V_b rather than V_a). When instead ethanol is adsorbed on the stronger V_a acid site and dissociates to $CH_3CH_2{}^O$ + OH^{Va} (with ethoxy on the V_b site), the barrier is 59 kcal/mol. Another contributing effect may be electron withdrawal from the surface by the ethoxy, leading to decreased basicity of the surface O on which $CH_3CH_2{}^O$ adsorbs and decreased stability at the transition state. We have also tested the barriers of some ethylene formation mechanisms (e.g., the E2 mechanism) and

found that the barriers were not significantly affected by the presence of another adsorbed ethanol. In summary, we find that single-step mechanisms for diethyl ether formation are preferred over a two-step mechanism via a $CH_3CH_2^O$ intermediate, and that the transition state structures of the most favorable pathways are consistent with an S_N2 mechanism.

4.4.4 Decomposition of Diethyl Ether to Ethylene

In a previous section, we discussed pathways leading from ethanol and related C2 intermediates to ethylene. There is also evidence that ethylene forms from the decomposition of diethyl ether. Knözinger and Köhne have performed a series of ethanol dehydration experiments at fixed temperatures with varying residence time [108]. At an intermediate temperature (571 K), a maximum in ether production as a function of residence time was observed. Since the ethanol pressure continues to drop, they concluded that at least some of the ethylene forms via decomposition of ether [108]. To corroborate this result, we investigated the decomposition of diethyl ether via both "$E1^E$" (R16) and "$E2^E$" (R15) mechanisms (Figure 4.9(a)-(b)); superscript "E" denotes that the elimination takes place from diethyl ether). These pathways are highly analogous to the E1′ and E2 mechanisms identified for direct ethylene formation from ethanol, since the H atom in the alcohol group of ethanol is simply substituted with an ethyl group for the case of diethyl ether. The barrier for the $E2^E$ and $E1^E$ mechanisms are 38 and 52 kcal/mol, respectively. These values are both within 1 kcal/mol of the corresponding ethanol dehydration mechanisms. This indicates that competition between ethylene formation from ethanol and from diethyl ether may exist depending on the relative partial pressures of ethanol and diethyl ether, which are dictated from the specific reaction conditions.

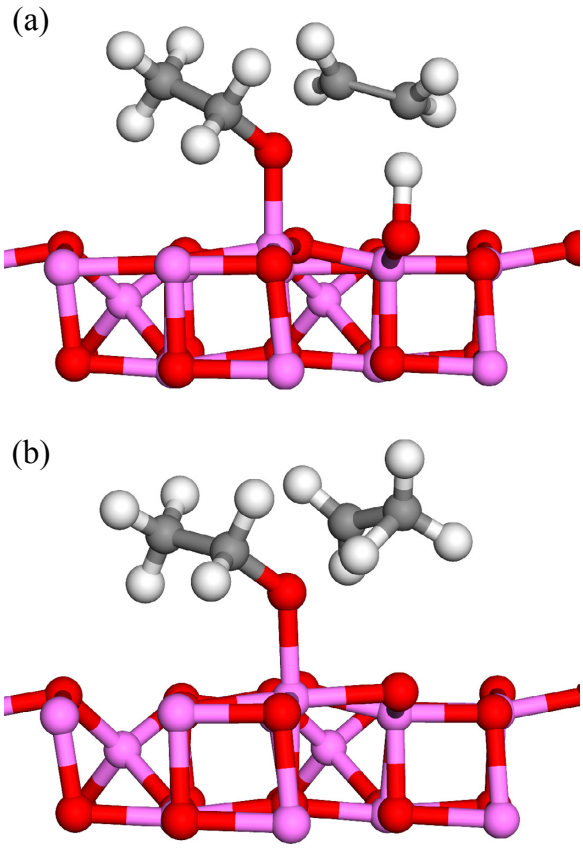

Figure 4.9: Transition state structures for ethylene formation from diethyl ether. See Table B.4 and the text for energetic information. (a) $CH_3CH_2OCH_2CH_3^{Va} + {}^{O} \rightarrow C_2H_4 + CH_3CH_2O^{Va} + H^{O}$ (R15), (b) $CH_3CH_2OCH_2CH_3^{Va} \rightarrow C_2H_4 + CH_3CH_2OH^{Va}$ (R16).

4.4.5 Insights into Selectivity for Alkenes and Ethers

As demonstrated in this work, on the most stable sites of the (100) surface, the lowest barrier for ethylene formation is 37 kcal/mol, while diethyl ether is formed with a barrier of 35 kcal/mol in the most favorable path (from the most stable set of reactants). These values are similar, indicating some possible preference to ether at low temperatures. This preference is enhanced when hydration effects on the rate constants are considered. We showed in previous sections how the E2 and S_N2

reaction barriers decrease in the presence of co-adsorbed (spectator) H_2O. With co-adsorbed H_2O, the E2 barrier was lowered by 3 kcal/mol and the S_N2 barrier by 8 kcal/mol, resulting in a larger barrier difference of the E2 and S_N2 reactions. Thus, although water is experimentally shown to inhibit the absolute reaction rates for both mechanisms, these results suggest a possible reason for the higher rate of etherification relative to dehydration at low temperatures (488 K) [107-108]. So far we have discussed rate constants, however coverages are also important. To illustrate this, we consider here rate expressions for the key reaction steps in the limit of low conversion so that the reverse rates are negligible. At low temperatures, higher coverages of ethanol and ethoxy cover the surface, favoring the etherification reaction:

$$r_{S_N2} = k_{S_N2}\left[CH_3CH_2OH^{Al}\right]\left[CH_3CH_2O^{Al}\right]$$

At higher temperatures, more surface vacant sites are exposed at the expense of ethanol and ethoxy, and high coverages of vacant sites promote dehydration rates:

$$r_{E2} = k_{E2}\left[CH_3CH_2OH^{Al}\right]\left[{}^{O}\right]$$

This leads to an increase in the relative rate of dehydration compared to etherification with increasing reaction temperature. This is consistent with experimental observations of primarily ether formation at low temperature (488 K) and primarily olefin formation at higher temperatures (616 K) [107-108]. It is also consistent with a "crossover" regime characterized by simultaneous ether and alkene production, from not only ethanol [103, 107-108, 129] but also larger primary alcohols [107-108]. Thus, our calculations and subsequent analysis provide fundamental insights into the mechanistic origins of competition between dehydration and etherification of alcohols on γ-Al_2O_3.

4.5 Conclusions

The ethanol reaction network on γ-Al_2O_3(100) has been systematically examined using DFT. Ethanol and water adsorb competitively on Lewis sites, consistent with previous reports that water strongly inhibits alcohol dehydration. Adsorption of ethanol on surface Brønsted sites (ΔE_{ads} = -6 kcal/mol) is much weaker than on Lewis sites (ΔE_{ads} = -10 to -19 kcal/mol, depending on site). As a result, Brønsted-catalyzed mechanisms for ethanol dehydration and etherification are less favorable than Lewis-catalyzed pathways. Stability of ethanol and/or water adsorbates is not affected by co-adsorption on this facet. Both concerted and sequential dehydration pathways to ethylene are examined, and a concerted E2 mechanism is the lowest energy pathway:

$$CH_3CH_2OH^{Al} + {}^{O} \xrightarrow{E_a=37\,kcal/mol} C_2H_4 + OH^{Al} + H^{O}$$

Ethylene may also form from decomposition of diethyl ether, via elimination mechanisms analogous to those proposed for ethanol. The $E2^E$ is the most favorable pathway:

$$CH_3CH_2OCH_2CH_3{}^{Al} + {}^{O} \xrightarrow{E_a=38\,kcal/mol} C_2H_4 + CH_3CH_2O^{Al} + H^{O}$$

Multiple routes to diethyl ether formation via S_N2 backside attack mechanisms are revealed. The lowest energy pathway is:

$$CH_3CH_2O^{Al} + H^{O} + CH_3CH_2OH^{Al} \xrightarrow{E_a=35\,kcal/mol} CH_3CH_2OCH_2CH_3{}^{Al} + OH^{Al} + H^{O}$$

Consistent with observed selectivity trends for primary alcohols, ether and ethylene formation are energetically competitive while ethanol dehydrogenation to acetaldehyde has higher barriers. Co-adsorbed (spectator) water lowers the S_N2 reaction barrier more than the E2 barrier, while low reaction temperatures are consistent with high coverages of ethanol and ethoxy. These observations are

consistent with enhanced rates of diethyl ether formation relative to ethylene formation at low temperatures.

4.6 Acknowledgments

This chapter was reproduced with permission from [131] (http://dx.doi.org/10.1021/cs4002833) Copyright 2013 American Chemical Society. The work was funded by the National Science Foundation (NSF) under grant EFRI-937706, and also partially financially supported by the Catalysis Center for Energy Innovation, an Energy Frontier Research Center funded by the U.S. Department of Energy, Office of Science, Office of Basic Energy Sciences under Award No. DE-SC0001004. I acknowledge computational resources of the Extreme Science and Engineering Discovery Environment (XSEDE), which is supported by National Science Foundation grant number OCI-1053575. In connection with XSEDE, the computations were performed on high performance computing clusters administered by the Texas Advanced Computing Center (TACC) and on the Kraken cluster administered by the National Institute for Computational Sciences (NICS). I would like to thank Prof. Giannis Mpourmpakis for technical guidance on this work and for providing feedback on the content of the chapter. I am also grateful to Dr. Jonathan Sutton and Vassili Vorotnikov for useful discussions.

Chapter 5

SITE-DEPENDENT LEWIS ACIDITY OF γ-Al_2O_3 AND ITS IMPACT ON ETHANOL DEHYDRATION AND ETHERIFICATION

5.1 Introduction

There is considerable effort today aimed at developing a more diverse and sustainable set of fuel and chemical feedstocks from biomass [132]. One approach to creating value from oxygen-rich biomass is to selectively remove oxygen using heterogeneous catalysts [4, 96]. γ-Al_2O_3 is a solid acid material that catalyzes oxygen removal and, by its nature, possesses multiple advantages over homogeneous acids, such as increased re-usability and decreased separation costs [133]. In particular, γ-Al_2O_3 is well-known for its significant activity in dehydration of alcohols [95], a topic that continues to be intensely studied even in recent years [97-98, 100-103, 131]. It is expected that identification of the relationship(s) between the structure of γ-Al_2O_3 and its alcohol dehydration activity could lead to improved catalytic systems for deoxygenation reactions.

The identity and strength of the catalytic sites on the γ-Al_2O_3 surface are important factors in the development of structure–activity relationships. Prior studies indicate that both Lewis and Brønsted-like types of acid sites may be present on γ-Al_2O_3 surfaces [104]. We have summarized the discussion in the literature about Lewis vs. Brønsted sites in our earlier work on ethanol dehydration and etherification on γ-Al_2O_3(100) [131]. We have also examined the Lewis- and Brønsted-catalyzed mechanisms of ethanol conversion to ethylene and diethyl ether, and have found that

the Lewis-catalyzed mechanisms are dominant [131]. We therefore focus hereafter on the Lewis-catalyzed mechanisms. The γ-Al_2O_3 surface model exposes a set of heterogeneous 3-, 4-, and 5-coordinate Al^{+3} sites on the various facets. As a consequence of this heterogeneity, the Al^{+3} sites exhibit considerable differences and complexity in terms of acid strength. Sautet and co-workers have characterized the acidity in terms of probe molecule binding strength, as well as an intrinsic acidity derived from a density of states analysis [120, 128]. In their latest work, this descriptor is the energy-weighted mean over the lowest-energy unoccupied states of the Al^{+3} sites [128]. These metrics help provide a way to rank and order the Al^{+3} sites according to their strength, but to date the intrinsic acidity metric has only been applied to adsorption and reaction properties of diatomic probe molecules and small hydrocarbons [128]. There has been no correlation of the effect of acid strength on reactions of larger oxygenated compounds, including alcohols.

Another critical consideration in the study of alcohol/γ-Al_2O_3 systems is the effect of water. Besides its role as a reaction product, water is frequently co-fed with the reactant alcohol and binds strongly to the γ-Al_2O_3 surface, prompting extensive spectroscopic surface studies [95, 104, 134]. More broadly, biomass processing will likely take place in the presence of at least some water, and so the effect of its presence on reaction chemistries merits examination. Among the earliest theoretical explorations of water adsorption and dissociation on this surface was the work of Sautet and co-workers [120, 135]. They utilized a "non-spinel" Al_2O_3 model to compute the surface energies as a function of temperature in the presence of different coverages of water on multiple facets, and reported that the (100) facet is dehydrated by 600 K, while the (110) facet remains hydrated until much higher temperatures (>

1000 K). Given that the typical alcohol dehydration reaction temperatures are in the range of 500-600 K [95, 103], their results indicate that the (110) facet will have significant coverages of water under reaction conditions. Additionally, some reports indicate that the (110) facet is the most abundant facet on γ-Al_2O_3 nanoparticles [136], which are commonly used in experimental studies. These observations motivate a deeper exploration of reactions of alcohols on the (110) facet in the presence of water.

In this work, we examine the effect of the heterogeneity of the Lewis acid strength in regards to its impact on the adsorption and reaction properties for oxygenated compounds on γ-Al_2O_3 surfaces. We explore, for the first time, the energetics and barriers for dehydration and etherification of ethanol on the (110) facet, both in the absence and presence of co-adsorbed water. In connection with these studies, we present and explore a new descriptor for Lewis acidity, the energy-weighted mean of the *s*-conduction band states for the Al^{+3} centers. The performance of the descriptor is evaluated and found to quantitatively predict adsorption energies as well as reaction barriers for ethanol dehydration, while providing a qualitative explanation for etherification reaction barriers.

5.2 Methods

5.2.1 γ-Al_2O_3 Structure Models

In modeling the (110) and (100) facets of γ-Al_2O_3, we employed the non-spinel bulk structure of Sautet and coworkers [119-120, 135]. We simulated the (100) and (110) surfaces using for each surface a supercell containing 80 atoms (a p(2×1) repetition) with 15 Å of vacuum between periodic slabs in the z-direction. The bottom atomic layer was held fixed in the bulk positions while all other atoms were allowed to

relax. In order to check the convergence of our binding energies with respect to Al_2O_3 slab thickness, we carried out a set of calculations with ethanol and water adsorbed onto a slab with double the number of Al_2O_3 units, and found that the binding energies are converged to within 0.05 eV. Based on this convergence test, we conclude that the thickness of the Al_2O_3 slab model employed in the current study is adequate. The (100) and (110) facets of γ-Al_2O_3 with the various 3-, 4-, and 5-coordinated sites are shown in Figures 5.1(a) and 5.1(b), respectively. Here the Roman numeral "V" refers to the 5-coordinate sites on the (100) facet, and emphasizes that these sites are located on a different facet than sites with Arabic numeral identifiers.

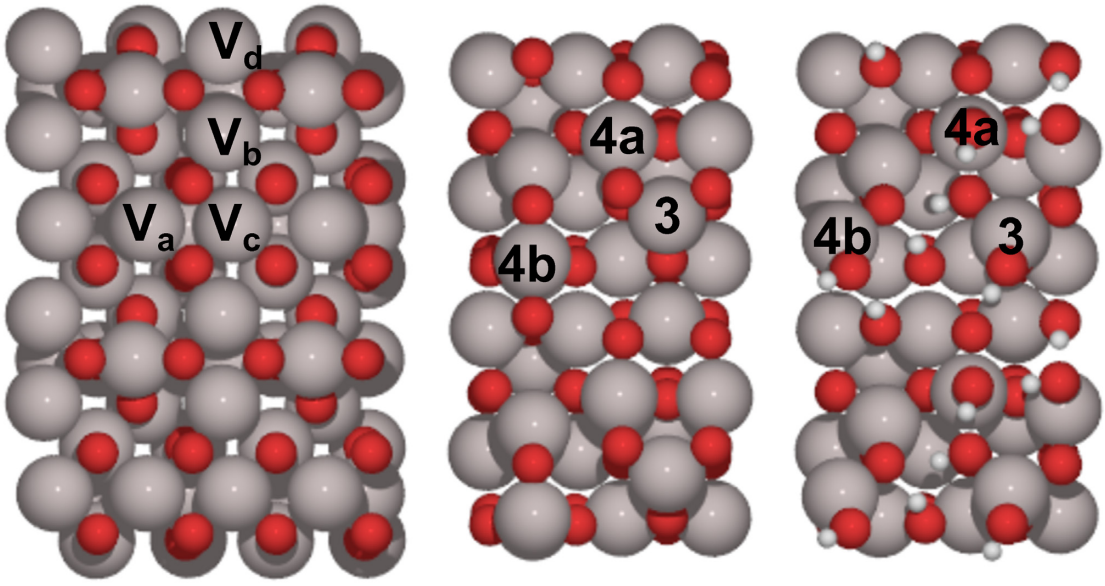

(a) γ-Al_2O_3(100) (b) γ-Al_2O_3(110) (c) γ-Al_2O_3(110) • 8 H_2O

Figure 5.1: Graphical representation of the γ-Al_2O_3 surfaces used in the current study, with the various Al^{+3} sites labeled.

To create the hydrated (110) facet, the number of adsorbed water molecules was selected based on information from Digne et al. [120]. In their study, they compute surface energies indicating that, at typical operating temperatures for ethanol dehydration and etherification (about 500 K) [103], there are four water molecules adsorbed per unit surface area. Based on our own tests and prior reports [120, 128], we identified the most stable configurations for a single water molecule to adsorb on each of the four different Al^{+3} sites per unit area. We then combined these separate adsorbed structures onto a single slab calculation and optimized approximately 10 different variations on this initial guess. We display in Figure 5.1(c) the structure with the lowest total energy; as shown, all the H_2O molecules are dissociatively adsorbed to form a hydroxylated surface. It should be noted that the 4b site is reconstructed into a 3-coordinate site, consistent with prior reports of the most stable (110) surface structures at high water coverage [128]. This structure was subsequently used as the starting point for adsorbing alcohols (both alone and in pairs) to examine the effect of hydration on the adsorption and reaction energetics. For each considered configuration, one or two water molecules are replaced with an alcohol (or alkoxy + H) and the structure subsequently optimized.

5.2.2 Computational Methodology

All DFT calculations were carried out using the Vienna Ab-initio Simulation Package (VASP, version 5.2) [26-29]. The core region of each atom was represented by the projector augmented wavefunction (PAW) method of Blöchl, Kresee, and Joubert [117-118], while the valence region employed the Perdew–Wang 1991 (PW91) density functional [21] and a planewave basis set with a kinetic energy cutoff of 400 eV. Reciprocal space was sampled using a 3×3×1 Monkhorst–Pack k-point grid

[137]. Discontinuities in the Fermi level were treated with a Gaussian smearing scheme, with a σ value of 0.10 eV. Atomic degrees of freedom were optimized using the conjugate-gradient algorithm as implemented in VASP with a force threshold of 0.05 eV $Å^{-1}$. Reaction barriers were located via a combined nudged elastic band (NEB) [138] /dimer method [35-37, 139], where an initial guess for the dimer calculation was generated by optimizing a NEB with 5 images to a force threshold of 0.20 eV $Å^{-1}$, and the dimer calculation was carried out to a force threshold of 0.05 eV $Å^{-1}$.

It should be emphasized that the current computational methodology neglects the issue of long-range electron correlation (i.e., dispersion interactions). Using the DFT+D3 methodology of Grimme et al. [140], we calculated out the dispersion correction and tabulated our results in Table C.2. While the dispersion corrections reported in Table C.2 are not negligible, given that the dispersion corrections are roughly constant for an adsorbate on a particular facet and that the focus of this work is on the electronic coupling between a set of oxygenates and a Lewis acid site, we do not include such corrections in the current study.

Finally, for the hydrated (110) facet, the water molecules are asymmetrically adsorbed; thus, it was necessary to utilize a dipole correction in the z-direction. In order to ensure that differences between the hydrated and clean surfaces are due to the effect of the hydration, and not due to the effect of a dipole correction, a subset of binding energy calculations was performed with the clean surface. It was found that the dipole correction resulted in small changes in the binding energy, < 0.05 eV, in line with previous results [141].

5.3 Results and Discussion

As a probe of the relative Lewis acidity of each facet, we employed the binding energies (E_{BE}) of a number of adsorbates on both the (110) and (100) facets of γ-Al_2O_3, calculated in the usual fashion, i.e.

$$E_{BE} = E_{ads+surface} - E_{ads} - E_{surface} \qquad \text{Equation 5.1}$$

where $E_{ads+surface}$ is the total energy of the adsorbate and γ-Al_2O_3 surface, E_{ads} is the gas-phase adsorbate energy, and $E_{surface}$ is the energy of the bare γ-Al_2O_3 surface. The binding energy as a probe of the Lewis acidity has previously been used in zeolite studies with varying Lewis acid sites, and has been found to be an unambiguous descriptor of the relative Lewis acidity [142]. Once the relative Lewis acidity of each Al^{+3} site has been identified via the binding energy, we examine the physical origin of these acidities by using the physical properties of the γ-Al_2O_3 surfaces. We then turn our attention to how we can use these properties in order to predict the trends in the binding energies for a collection of adsorbates and the trends in the reaction barriers for the dehydration and etherification of ethanol.

5.3.1 Binding Energies

The binding energies for the adsorbates shown in Figure 5.2 on the (110) and (100) facets of γ-Al_2O_3 are plotted in Figure 5.3 and tabulated in Table C.1. Representative images of the optimized geometries for these adsorbates are found in Figures C.1–C.5 for site 3 on the (110) facet. From Figure 5.3, the impact of the heterogeneity on the Al^{+3} binding sites becomes readily apparent, with the binding energies ranging from −1.37 eV to −0.34 eV, depending on the Al^{+3} site. Based on the binding energies, we can rank the relative acidities as 3 > 4b > 4a for the (110) facet, and as $V_a > V_b \approx V_d > V_c$ for the (100) facet (see Figure 5.1 for the site designations).

Additionally, the (110) facet is more acidic than the (100) facet, in line with previous studies [114, 120, 128]. Furthermore, the binding energies for the various alcohols (ethanol, *tert*-butanol, and isopropanol), are closely grouped together, which is expected on the basis of group additivity [46, 143]. Variation in the binding energies for these three species can be attributed to interactions of the differing side chains of these alcohols with the γ-Al_2O_3 surface.

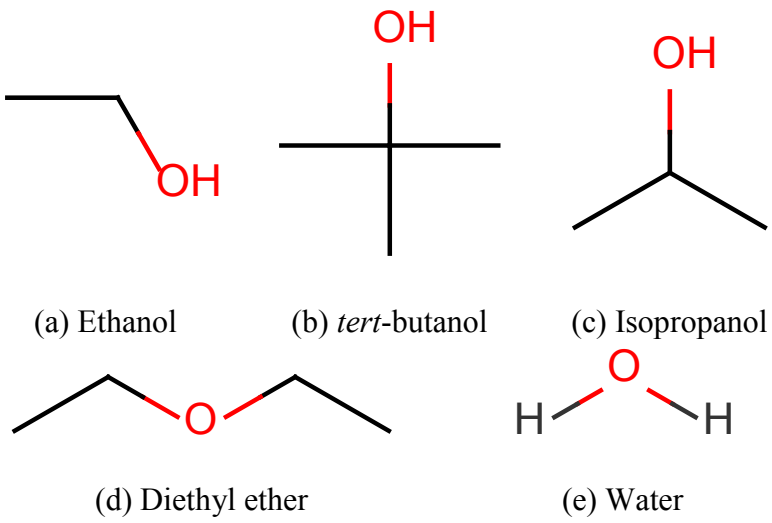

(a) Ethanol (b) *tert*-butanol (c) Isopropanol

(d) Diethyl ether (e) Water

Figure 5.2: Molecular adsorbates considered in the current study. The chemical structures were created using the Marvin chemical drawing package [144].

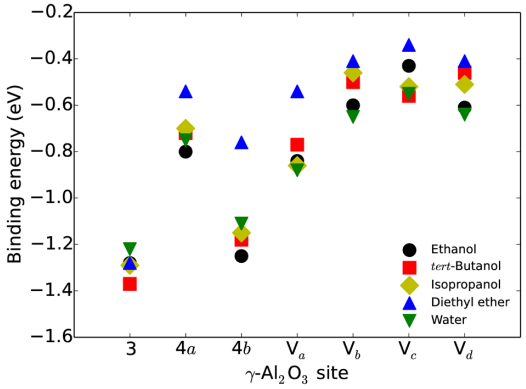

Figure 5.3: Binding energies for the adsorbates shown in Figure 5.2 on the Al^{+3} sites for the two facets of γ-Al_2O_3 shown in Figure 5.1.

In order to examine the physical origin of this trend, we turn to the key definition of what makes a molecule or a surface a Lewis acid, i.e. it functions as an electron acceptor. In molecular orbital terms, we are transferring electronic charge from the highest occupied molecular orbital (HOMO) of the adsorbate into the lowest unoccupied molecular orbital (LUMO) of the Lewis acid. If the LUMO of the Lewis acid is close in energy to the HOMO of the Lewis base, then the coupling between the two sets of molecular orbitals can occur, allowing a transfer of electrons from the Lewis base into a new molecular orbital created by the HOMO–LUMO coupling. Since our Lewis acid is a periodic solid surface, it is natural to examine the relationship between the HOMO energies of the adsorbates in Figure 5.2 and the conduction band of the γ-Al_2O_3 surface. The goal of the current study is to understand the Lewis acidity at an atomic level. Therefore, we transform the density of states of the conduction band into an atomically-resolved density of states. By taking the mean of the atomically-resolved density of states and comparing this value to the Fermi level (where, by definition, the HOMO of the adsorbates is located [145]), we can then

achieve an atomic level understanding of the Lewis acidity, and relate it to properties such as the binding energy [120].

Since the lowest energy bands are *s*-angular momentum in nature, we only consider the *s*-angular momentum terms, and thus define a new descriptor of the Lewis acidity E_s^* as

$$E_s^* = \frac{\int_{\varepsilon_F}^{\infty} \rho_s(\varepsilon)\varepsilon d\varepsilon}{\int_{\varepsilon_F}^{\infty} \rho_s(\varepsilon) d\varepsilon} \qquad \text{Equation 5.2}$$

where E_s^* is the mean of the *s*-conduction band, ε_F is the Fermi level (here set to zero), $\rho_s(\varepsilon)$ is the *s*-angular momentum resolved projected density of states (PDOS), and ε is the energy. The atom-resolved density of states for both the (110) and (100) facets are shown in Figure 5.4, with the values of E_s^* plotted in relation to the Fermi level. It should be noted that in carrying out the numerical integration in Equation 5.2, we are essentially summing over the number of unoccupied states, which is highly dependent on the type of wavefunction being used. Thus, in order to ensure consistent results between the two surfaces, we utilized 42 unoccupied bands for both the (110) and (100) facets. The E_s^* values for the (110) and (100) γ-Al_2O_3 surfaces are plotted in Figure 5.5 and tabulated in Table C.3.

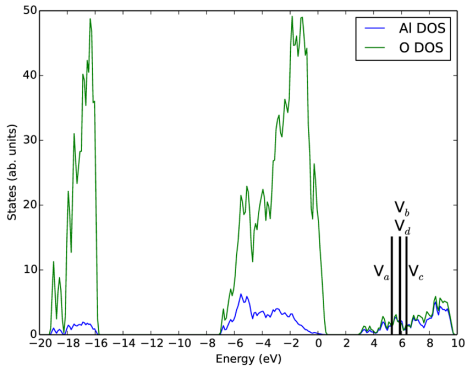

(a) γ-Al_2O_3(100)

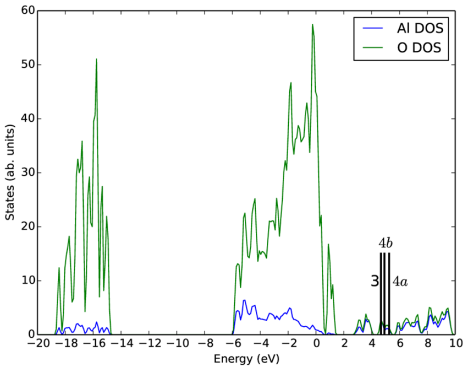

(b) γ-Al_2O_3(110)

Figure 5.4: Density of states for the (100) and (110) facets of γ-Al_2O_3, with the E_s^* values highlighted.

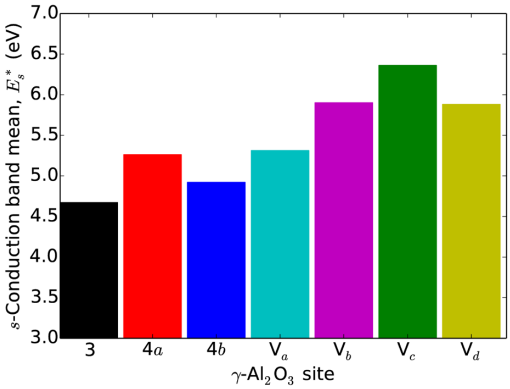

Figure 5.5: E_s^* calculated for the sites on the γ-Al_2O_3(110) and (100) surfaces shown in Figure 5.1.

By comparing the E_s^* values in Figure 5.5 and the binding energies in Figure 5.3 we can rationalize the origin of the relative acidity between the (110) and (100) facets of γ-Al_2O_3. For example, based on Figure 5.3, site 3 on the (110) facet is the

most acidic site due to the relatively high magnitude of the binding energy, and as Figure 5.5 indicates, we see that this site has the lowest (i.e. closest to the Fermi level) value of E_s^*. This indicates that site 3 can accept electronic charge from the adsorbate more readily than the other sites. Additionally, based off of the magnitude of the E_s^* for the (110) 4a site and the (100) V_a site, we can expect the binding energies for these two sites to be similar in strength. Figure 5.3 shows that this is indeed the case, with variations in the binding energy for these two sites being less than 0.1 eV. The results are compiled in Figure 5.6. These results highlight the origin of the Al^{+3} site heterogeneity shown in Figure 5.3; namely, as one moves from Al^{+3} to Al^{+3} site, the adsorbate interacts with a different E_s^*, which in turns affects the strength of the binding energy.

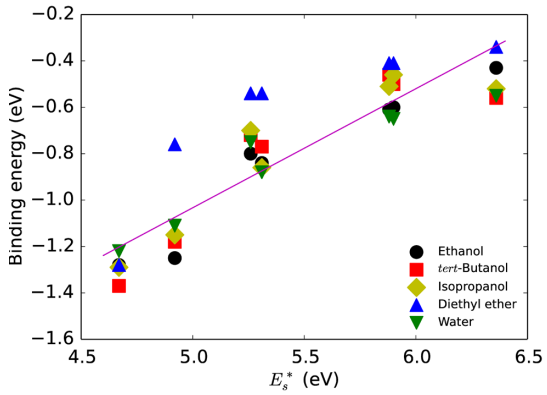

Figure 5.6: Binding energy versus E_s^* for the sites on the γ-Al_2O_3(100) and (110) surfaces shown in Figure 5.1. The magenta line plots the average of the α and β parameters from Table 5.1 for the alcohol species.

In order to assess how quantitatively we can predict the binding energy from the E_s^* descriptor, we fit the binding energy data to the following linear form,

$$E_{\mathrm{BE}} = \alpha E_s^* + \beta \qquad \text{Equation 5.3}$$

and we present the parameters in Table 5.1. The results in Table 5.1 and Figure 5.6 show a good linear relationship between E_s^* and the binding energy. In particular the R^2 values, confidence intervals (indicated by ± values), and mean absolute errors (MAEs) all attest to the quality of the fits and are consistent with values reported for other correlations describing surface phenomena [56-57, 146-147]. It should be noted for the *tert*-butanol and diethyl ether adsorbates that the correlation is not as good as it is for the other three adsorbates, most likely arising from surface interactions with the multiple methyl groups on these adsorbates. These interactions are a secondary effect, while the focus of this work is to demonstrate and explain the primary electronic effects of Lewis acid-base interactions. Having established the physical origins of the Lewis acidity of the Al^{+3} sites and its relationship to the binding energy of a series of adsorbates, we now turn our attention to using this information to categorize and understand reactions involving ethanol on the (110) and (100) facets of γ-Al_2O_3.

Table 5.1: Linear scaling parameters (Equation 5.3) for the γ-Al_2O_3 (110) and (100) surfaces. Centered β values refer to the parameter estimate and confidence intervals when the independent parameter has been mean centered.

Adsorbate	α	β (eV)	Centered β (eV)	R^2	MAE
Ethanol	0.52±0.17	−3.7±0.9	−0.83±0.10	0.93	0.17
tert-butanol	0.52±0.31	−3.6±1.7	−0.79±0.17	0.79	0.16
Isopropanol	0.50±0.25	−3.5±1.4	−0.78±0.14	0.84	0.15
Diethyl ether	0.46±0.32	−3.2±1.8	−0.61±0.18	0.73	0.16
Water	0.40±0.16	−3.0±0.9	−0.83±0.09	0.89	0.12

5.3.2 Reaction Barriers

In this section, we consider two primary reactions, the dehydration of ethanol to form ethylene, and the etherification of ethanol to form diethyl ether,

$$EtOH + Al_2O_3 \rightarrow Ethylene + Al_2O_3{\bullet}H_2O \qquad \text{Equation 5.4}$$

$$2\ EtOH + Al_2O_3 \rightarrow DEE + Al_2O_3{\bullet}H_2O \qquad \text{Equation 5.5}$$

Both reactions have been studied previously in detail for the (100) facet of γ-Al_2O_3 in our group [131]. Thus, we briefly summarize here the salient features of the ethanol dehydration and etherification mechanisms, and focus our attention primarily on the implications of the surface Lewis acidity for these mechanisms. The dehydration mechanism is an E2 reaction, since it is an elimination-type mechanism that has a second-order kinetic dependence (it requires both an adsorbed ethanol and a vacant O site). The reaction proceeds in a single step by an elongation of the ethanol C–O bond, together with a concerted transfer of a C_β-bound H to a vacant O site. This leads to an ethylene that is very weakly adsorbed and OH and H fragments bound to the γ-Al_2O_3 surface. The dehydration mechanism is shown schematically in Figure 5.7(a). The etherification mechanism begins with an ethanol molecule bound to one Al^{+3} site and an ethoxy bound to a second Al^{+3} site (the pair H fragment is bound to a nearby O site). The ethoxy executes a nucleophilic attack on the C_α of the nearby ethanol, leading to elongation of the C–O bond in that ethanol. At the same time a new C–O bond forms between the ethyl fragment and the adsorbed attacking ethoxy, leading to diethyl ether. The etherification is characterized as an S_N2-type reaction, and is shown schematically in Figure 5.7(b). The barriers for both reactions are presented in Figure 5.8 and tabulated in Tables C.4 and C.5. In addition, the transition state structures are shown in Figures C.6–C.8 for dehydration, and Figures C.9–C.15 for etherification.

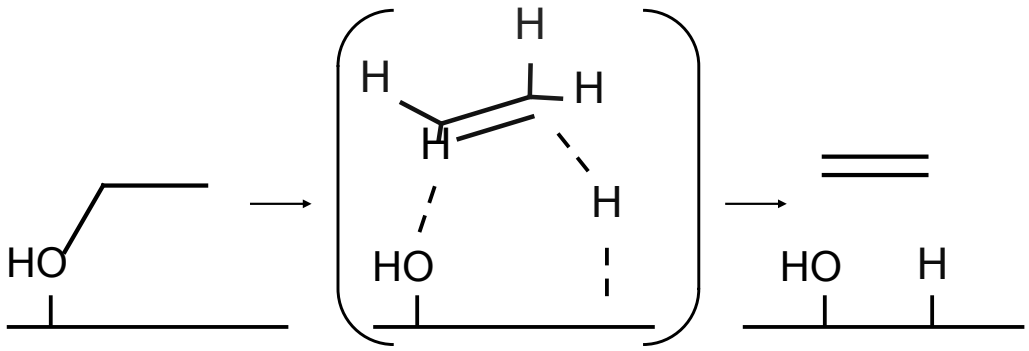

(a) Dehydration of ethanol

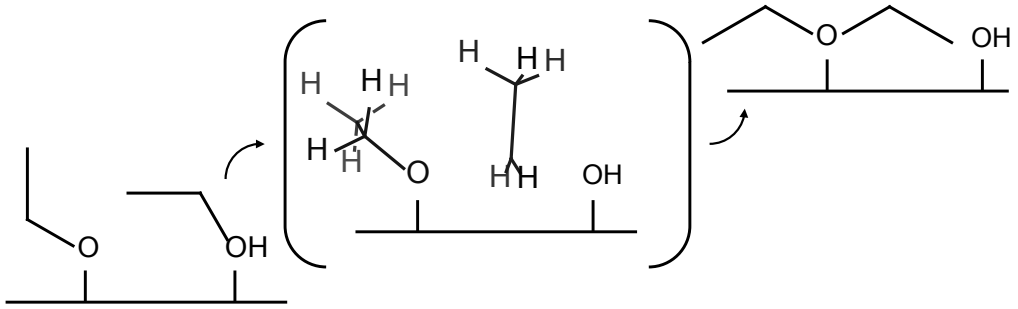

(b) Etherification of ethanol

Figure 5.7: Schematic of the dehydration and etherification reactions shown in Equation 5.4 and Equation 5.5. The chemical structures were created using the Marvin chemical drawing package [144].

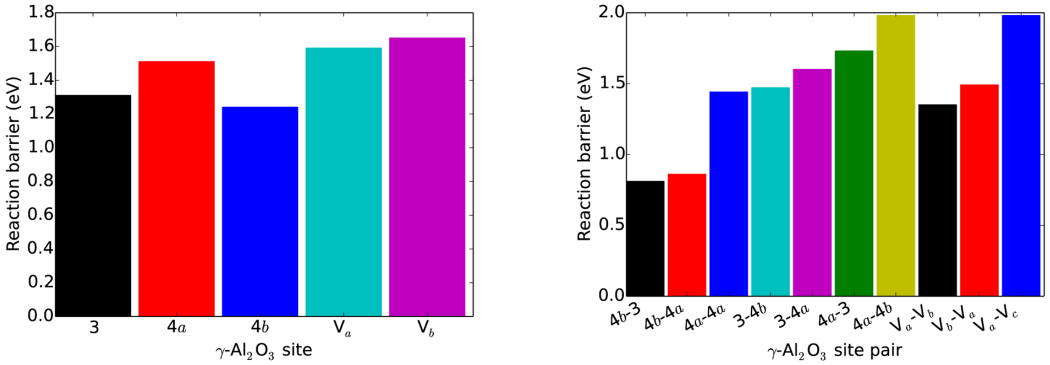

(a) Dehydration (b) Etherification

Figure 5.8: Reaction barriers for the reactions in Equation 5.4 and Equation 5.5 for the sites on the γ-Al_2O_3(110) and (100) surfaces shown in Figure 5.1.

In order to see how the Lewis acidity affects the dehydration barriers, we first plot the dehydration activation energies as a function of the binding energy in Figure 5.9. From this figure, we can easily see that the dehydration barriers have a near linear dependence on the binding energy, indicating that there is indeed an effect from the heterogeneity of the Lewis acidity on the reaction barriers. To rationalize the impact of the heterogeneity, we compare the dehydration barriers to the E_s^* parameter. From Figure 5.9(a), with the exception of the γ-Al_2O_3(110) 4b site, the barriers for the dehydration of ethanol follows the trend established for the E_s^* parameter. In order to quantify how well the E_s^* parameter describes the trends in the dehydration reaction barriers, the barriers were fit according to Equation 5.3 and the results are shown in Figure 5.10. We achieve a good quality linear fit (R^2=0.78), that improves upon exclusion of the (110) 4b site (R^2=0.89); see the caption of Figure 5.10 for additional measures of quality of fit. This trend is consistent with our understanding of the

dehydration mechanism for ethanol. The ethanol C–O bond must be broken in order to form ethylene, and the Lewis acid character of the Al^{+3} site facilitates weakening of this bond by withdrawing charge density from the C–O bonding region. The closer E_s^* of the Al^{+3} site is to the Fermi level, the stronger the Lewis acid and the greater the effect of weakening the C–O bond. The deviation from the trend of the point for the 4b site may be due to the H_β landing on the more basic two-coordinate oxygen site, in contrast to the three-coordinate oxygen involved in the reaction on site 3.

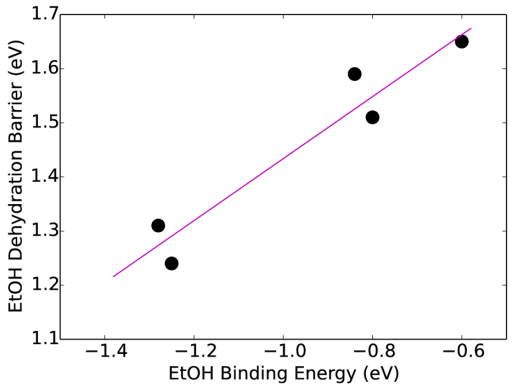

Figure 5.9: Dehydration reaction barrier vs. the ethanol binding energies for the sites on the γ-Al_2O_3(110) and (100) surfaces shown in Figure 5.1.

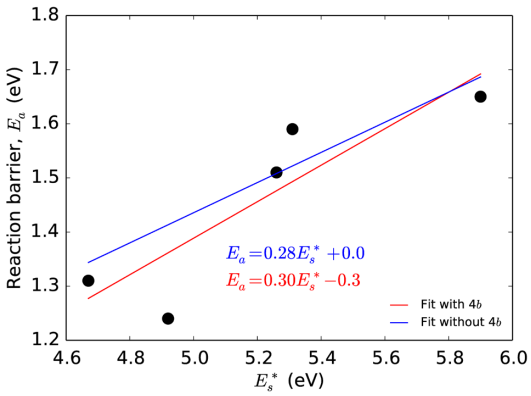

Figure 5.10: Reaction barrier (E_a) vs. E_s^* for the sites on the γ-Al_2O_3(110) and (100) surfaces shown in Figure 5.1. The errors in the slope and intercept are $\alpha \pm 0.32$ and $\beta \pm 1.7$ (R^2=0.79, MAE=0.11), and $\alpha \pm 0.29$ and $\beta \pm 1.6$ (R^2=0.89, MAE=0.04) for the fit with and without the 4b site, respectively.

The etherification reactions involve two sites — on the first site, we have an ethoxy species (created by a dissociative adsorption of an ethanol molecule), and on the second site we have an associatively adsorbed ethanol. The etherification barriers are shown in Figure 5.8(b). Focusing on the reactions for the (110) facet, Figure 5.8(b) shows several interesting trends. Based off of the E_s^* argument, we would expect the site pairs involving the 3 and 4b sites to have the lowest reaction barrier, and in fact, for the 4b-3 site combination (i.e. ethoxy on site 4b, and ethanol on site 3) this is indeed the case. However, swapping the order of the sites gives an almost two-fold rise in the reaction barrier, making the 3-4b site combination the fourth-highest reaction barrier. In addition, we should expect that the reactions involving the 4a site to have the highest barriers. However, the 4b-4a site combination has the second-lowest barrier, and swapping the site ordering results in a near threefold increase in the

reaction barriers. These results seem almost contradictory based on the trends previously established for the E_s^* parameter.

We can, however, rationalize these almost paradoxical trends by considering that upon surface adsorption of an ethanol molecule, the band centers of the Al^{+3} sites inevitably shift. This effect is further enhanced by the adsorption of a second ethanol molecule, thus creating an effective three-body effect on the mean of the *s*-conduction band for the Al^{+3} sites. The E_s^* parameters of the Al^{+3} sites for the (110) facet of γ-Al_2O_3 after the dual adsorption of ethanol are shown in Figure 5.11 and tabulated in Table C.6. Comparison of Figures 5.11 and 5.8(b) provides qualitative insight into these trends. First, the closer the E_s^* for the ethanol site lies to the Fermi level, the lower the etherification barrier, consistent with the discussion above regarding the weakening of the C–O bond. Second, the *further away* E_s^* of the ethoxy site is from the Fermi level, the lower the etherification barrier. The explanation of this second finding is that during the etherification process, the ethoxy species acts as a nucleophile, displacing the hydroxyl group on the ethanol. A lower E_s^* would result in a greater amount of charge being transferred to the Al^{+3} site, decreasing the relative nucleophilicity for the ethoxy species.

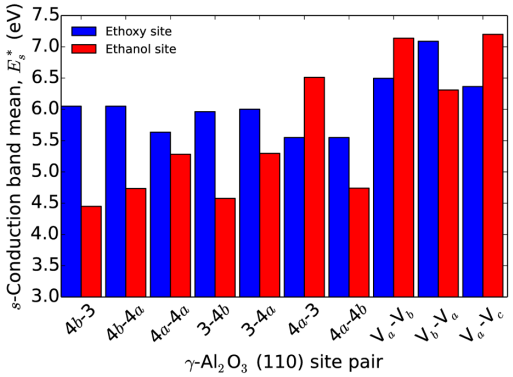

Figure 5.11: Al^{+3} E_s^* for the (110) facet of γ-Al_2O_3 upon adsorption of two ethanol molecules.

Reexamination of the 4b-4a site pair shows that upon adsorption of two ethanol molecules, the E_s^* of the 4a (ethanol) site shifts downwards to the Fermi level, thus making the 4a site more acidic, and thus more easily facilitates the nucleophilic substitution of the alcohol group for the ethoxy species. This also explains why the 4a-4a site pair has the third-lowest barrier, when we would expect it to have the highest barrier — dual adsorption of an ethanol results in a lowering of the Al^{+3} E_s^* for the ethanol site. In addition, the effect of the decreased nucleophilicity of the ethoxy species helps describe the difference between the 4b-4a and 4a-4b site pairs. Both site pairs have an equivalent E_s^* for the ethanol site, however, the E_s^* of the ethoxy site is closer to the Fermi level for the 4a-4b site pair than for the 4b-4a site pair. This results in the 4a ethoxy species being a poorer nucleophile than the 4b ethoxy species, resulting in a higher etherification barrier. These results illustrate the complexity in the etherification trends, arising from the heterogeneity in the Al^{+3} sites and the cooperative effects arising from the interactions between the ethanol and ethoxy species with the Al^{+3} sites of different Lewis acid strength.

5.3.3 Effects of Surface Hydration

Having established the origins of the relative Lewis acidities of the Al^{+3} sites for both the (110) and (100) facets of γ-Al_2O_3, we now turn our attention to the effects of surface hydration on the (110) facet of γ-Al_2O_3. We first examine the effect of hydration on the binding energies of ethanol, *tert*-butanol, isopropanol, and diethyl ether, and then turn our attention to the effect of hydration on the reaction barriers for the reactions presented in Equation 5.4 and Equation 5.5. In order to better highlight the effects of surface hydration on the binding energies and reaction barriers, we will consider *differences* in these values between the hydrated surface and dehydrated surface values. In this fashion, a negative binding energy difference will denote a stronger (i.e. more negative) binding energy, and a negative reaction barrier difference will denote a lowering of the reaction barrier. Representative images of the optimized geometries for the adsorbates interacting with the hydrated (110) facet are shown in Figures C.16–C.19. The transition state structures are shown in Figures C.20–C.22 for dehydration and Figures C.23–C.28 for etherification.

The binding energies of the aforementioned adsorbates on the hydrated γ-Al_2O_3(110) facet are reported in Table C.7. In order to highlight the change from the dehydrated (110) facet, we plot the difference in the binding energy between the hydrated and dehydrated surface for each site on the (110) facet in Figure 5.12. We can split the effect of hydration into two key effects: one caused by hydrogen bonding between the adsorbate and the surface waters, and one caused by a shift in the Al^{+3} E_s^* due to the effect of the surface waters. Here, we focus primarily on the electronic effects. The E_s^* parameter for the hydrated γ-Al_2O_3 surface is shown in Figure 5.13, along with the E_s^* for the dehydrated surface for comparison. It should be noted that since upon adsorption a single dissociated water molecule is replaced by an adsorbate,

the E_s^* in Figure 5.13 is for the hydrated surface with the dissociated water removed from the site indicated. We can see from Figure 5.13 that upon hydration of the surface, we get a noticeable down-shift in the E_s^*, indicating that the electronic component of surface hydration is to induce a stronger binding between the Lewis acid site and the adsorbate. Indeed Figure 5.12 shows that there is a tendency for stronger binding, with the exception of diethyl ether. For both the 3 and 4b sites, we observe a weaker binding energy for this adsorbate. This is most likely due to steric effects between the diethyl ether and the surface hydroxyls.

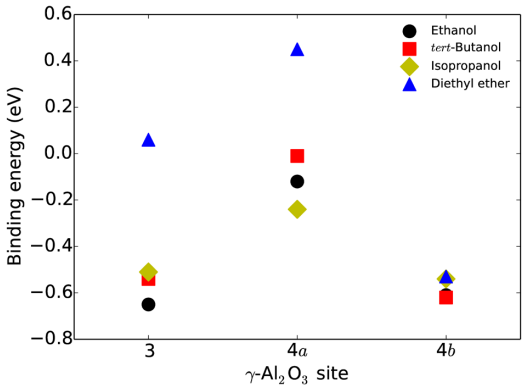

Figure 5.12: Binding energy differences for ethanol, *tert*-butanol, isopropanol, and diethyl ether due to surface hydration on the (110) facet of γ-Al_2O_3. A negative binding energy difference indicates a stronger adsorbate binding, while a positive binding energy difference indicates weaker adsorbate binding.

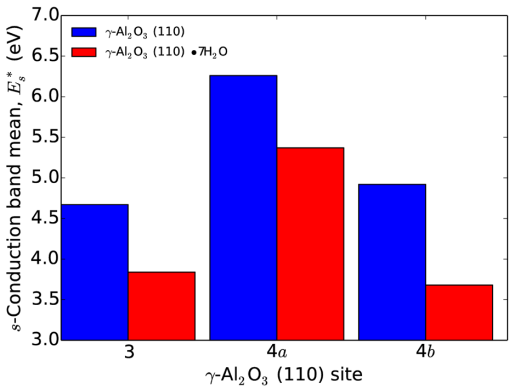

Figure 5.13: E_s^* for the γ-Al_2O_3 (110) surface, with and without surface hydration.

Figures 5.14(a) and 5.14(b) and Tables C.4 and C.5 show the differences in the reaction barriers due to the effect of surface hydration. As shown in Figure 5.14(a), for the 3 and 4a sites, the effect of surface hydration is small (less than 0.1 eV). However, for the 4b site, a relatively large shift of ~0.6 eV is found. Based off of the E_s^* arguments made above, we would expect a decrease in the reaction barrier, rather than an increase. This is further supported by a bond order conservation [148] argument — since the 4b site moves from a 4-coordinated to a 3-coordinated site upon hydration, this results in the 4b site being under-coordinated, which should make this site more catalytically active. It should be noted that in addition to the Al^{+3} site acting as a Lewis center, the reactions in Equation 5.4 and Equation 5.5 also require a neighboring surface oxygen atom to act as a basic center and accept a H_β from the ethanol. However, in the reconstructed 3-coordinated 4b site, the neighboring surface oxygen already has a hydrogen atom bound to it from the dissociatively adsorbed surface waters. This causes a reduction in the basicity for this site (and thus the ability of this site to accept the H_β from ethanol), leading to an increase in the reaction barrier.

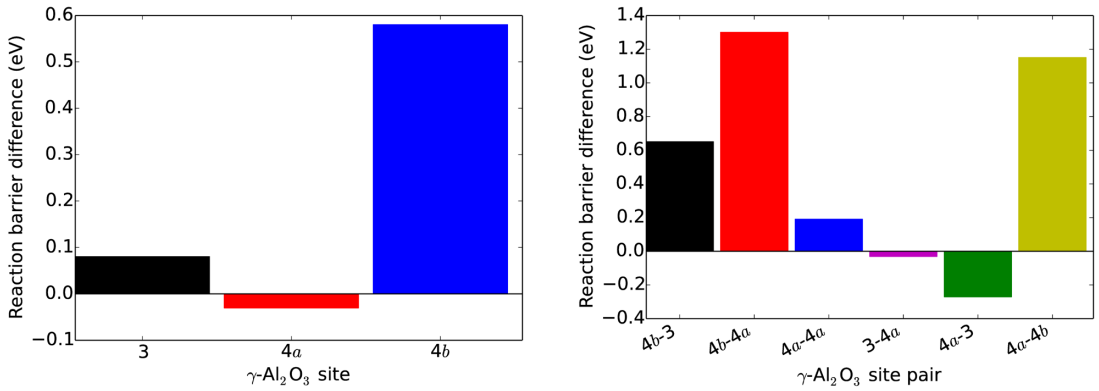

(a) Dehydration of ethanol (b) Etherification of ethanol

Figure 5.14: Reaction barrier differences due to surface hydration on the (110) facet of γ-Al_2O_3. A negative reaction barrier difference indicates a lower reaction barrier, while a positive reaction barrier difference indicates a higher reaction barrier.

Figure 5.14(b) shows that with the exception of the 3-4a and the 4a-3 site pair, the etherification barriers all increase due to surface hydration. While the 4a-4a site pair experiences a modest increase of ~0.2 eV, the remaining site pairs (4b-3, 4b-4a, and 4a-4b) experience changes between 0.6 eV and 1.2 eV. Similar to the etherification barriers for the clean surface, the increase in barriers for the 4b site arises from the changes in the relative nucleophilicity of the ethoxy group. As the 4b site is undercoordinated due to surface hydration, this causes a larger depletion of charge from the ethoxy, resulting in a lessening of the nucleophilicity, and thus an increase in the reaction barriers.

5.4 Conclusions

In the current study we examined the heterogeneity of the Al^{+3} binding sites for the (100) and (110) facets of γ-Al_2O_3. Each site was characterized in terms of its relative Lewis acidity using the binding energy of a set of oxygenates. We ranked the relative acidities as 3 > 4b > 4a for the (110) facet, and $V_a > V_b \approx V_d > V_c$ for the (100) facet of γ-Al_2O_3, in line with previous results [114, 120, 128]. We proposed a new descriptor for the Lewis acidity, the mean of the *s*-conduction band, E_s^*, that quantitatively predicts the trends in the binding energy.

The E_s^* descriptor was able to quantitatively predict the trends in the reaction barriers for the dehydration of ethanol arising from the heterogeneity of the Al^{+3} sites. For the etherification reaction, we have found that the adsorption of a second ethanol can modify the relative Lewis acidity of the neighboring Al^{+3} sites, and thus, the nucleophilicity of the ethoxy species. As a result of the bimolecular nature of the etherification reaction, only a qualitative description of the etherification barriers with the Lewis acid strength exists.

Lastly, we examined the effects of surface hydration on the binding energies and reaction barriers for the (110) facet of γ-Al_2O_3. We found that, with the exception of diethyl ether, the dissociatively adsorbed surface waters cause a down-shift in the E_s^*, resulting in a stronger binding energy. This result indicates that water increases the Lewis acid site strength. However, while this down-shift should have resulted in a lowering of the reaction barriers, we found relatively small changes, with the exception of the reactions involving the 4b site. Reactions involving this site exhibit an increase in the reaction barriers, which is attributed to the 4b site transitioning from a 4-coordinated site to a 3-coordinated site. For the case of ethanol dehydration, the surface waters retard the basicity of a neighboring surface oxygen site, which affects

the removal of the H_β from ethanol. For the etherification barriers, the under-coordination causes an increase in the charge depletion of the ethoxy species, and thus would result in a decreased nucleophilicity for this species and an increase in the etherification barriers.

5.5 Acknowledgments

I am grateful to Dr. Glen Jenness for fruitful collaborations on this work, particularly in the development of the E_s^* descriptor. I am also grateful to Prof. Giannis Mpourmpakis for encouragement of, and discussions about, the exploration of the (110) facet of γ-Al_2O_3. This chapter was reproduced with permission from [149] (http://dx.doi.org/10.1021/jp5028349) Copyright 2014 American Chemical Society. This work was funded through the Catalysis Center for Energy Innovation (CCEI), an Energy Frontier Research Center funded by the U.S. Department of Energy, Office of Science, Office of Basic Energy Sciences under Award No. DE-SC0001004. I acknowledge computational resources of the Extreme Science and Engineering Discovery Environment (XSEDE), which is supported by National Science Foundation Grant OCI-1053575. In connection with XSEDE, the computations were performed on high performance computing clusters administered by the Texas Advanced Computing Center (TACC) and on the Kraken cluster administered by the National Institute for Computational Sciences (NICS). I also acknowledge the resources of the National Energy Research Scientific Computing Center (NERSC), which is supported by the Office of Science of the U.S. Department of Energy under Contract No. DE-AC02-05CH11231.

Chapter 6

DFT-DRIVEN MULTI-SITE MICROKINETIC MODELING OF ETHANOL CONVERSION TO ETHYLENE AND DIETHYL ETHER ON γ-Al_2O_3(111)

6.1 Introduction

Biomass constitutes a vast and underutilized supply of renewable carbon for producing chemicals, fuels, and energy [3]. One of the most significant challenges in improving its utilization is the development of methods to efficiently process it into useful products. Substantial effort is being invested in developing catalytic materials, such as solid acids, to remove excess functionality from oxygen-rich biomass [150-151]. γ-Al_2O_3 is one such solid acid employed as a catalyst in, among other reactions, alcohol dehydration [95], which is the focus of this work. Rationalizing the activity of this material can form a foundation for understanding how to promote and control acid-catalyzed deoxygenation reactions.

Fundamental knowledge of the catalyst surface and of alcohol reaction mechanisms provides insights into the properties of γ-Al_2O_3 that promote dehydration and etherification [97-98, 100-103, 110, 131, 152]. For example, recent microscopy studies of γ-Al_2O_3 nanoparticles have highlighted the abundance and importance of (111) faceting on particle surfaces [102, 152]. In addition, steady-state reaction kinetics measurements with deuterium-labeled ethanol demonstrate a primary isotope effect for dehydration (likely involving H_β elimination), but not etherification [103]. The development of detailed, first-principles kinetic models to account for such fundamental insights offers a systematic approach to exploration and quantification of

reaction networks [10]. In this way, microkinetic models help to bridge the gap between site- or molecular-level observations and mesoscopic quantities such as reaction rates. First principles-based microkinetic modeling of heterogeneous catalysis is most frequently applied to transition metals [10]. There has recently been some progress in applying such techniques to the metal/metal-oxide interface [153] as well as pure metal oxides [61, 154]. It is known that for pure metal oxides frequently both metal and oxygen surface sites play an important catalytic role [128]. To our knowledge, there has been no microkinetic model reported with a fully first principles parameterization of multi-site surface kinetics for γ-Al_2O_3.

We present a theoretical investigation of the γ-Al_2O_3-catalyzed conversion of ethanol into ethylene and diethyl ether. Density functional theory (DFT) calculations have been performed on a γ-Al_2O_3(111) surface model to obtain quantitative information about the mechanisms for ethylene and diethyl ether production on that facet. The results of these calculations form the basis for a mean-field microkinetic model that features reactions on and among two distinct surface catalytic sites, Al and O. Based on *a posteriori* information from the full model, an analytical two-site reduced rate expression is derived to evaluate model performance by direct comparison to experimental data of steady-state ethanol reaction kinetics [103].

6.2 Computational Methods

The (111) facet of γ-Al_2O_3 was selected to model the catalyst surface, using in particular the defective spinel bulk unit cell model reported by Pinto et al. [155]. Observations from recent microscopy studies prompted the use of this facet [102, 152], and the (111) facet of the defective spinel model has a low surface energy which is indicative of a stable surface [155]. The (111) facet is displayed in Figure 6.1. Each

surface area unit contains four O sites (three of which are alike in their environment) and one Al site. A p(1×1) (5.64 Å × 5.64 Å) supercell containing 40 atoms was used with 15 Å of vacuum between periodic slabs. The atoms of the bottom half (19 atoms) of the approximately 12 Å thick slab were held fixed in the bulk positions while all other atoms were allowed to relax during optimizations. For calculations involving diethyl ether adsorption or formation, a p(2×1) (11.29 Å × 5.64 Å) supercell was used. Since both surface Al and O sites are present, hereafter a superscript "Al" ("O") appended to a species name indicates that it binds to an Al (O) site. All DFT calculations were carried out with the Vienna Ab initio Simulation Package (VASP) [26-29]. The PW91 functional developed by Perdew and Wang utilizing the generalized gradient approximation (GGA) was selected to represent the valence regions [21, 116], and the standard versions of pseudopotentials developed using the projector augmented wave (PAW) method represented the atomic cores [117-118]. A 5×5×1 gamma-centered k-point grid was used to sample the surface Brillouin zone (3×5×1 grid for p(2×1) calculations). The energy cutoff of the plane wave basis set was 400 eV, and the maximum force on atoms in all calculations was converged to less than 0.05 eV/Å (1.2 kcal/(mol Å)). Transition states (TSs) were located using a combination of the climbing image nudged elastic band (CI-NEB) and dimer methods [34-37], and were confirmed through frequency analysis by identification of a single imaginary mode. Computed frequencies for the transition state structures are available in Table D.1. When reporting adsorption energies, this work utilizes the convention that negative values denote stable adsorption.

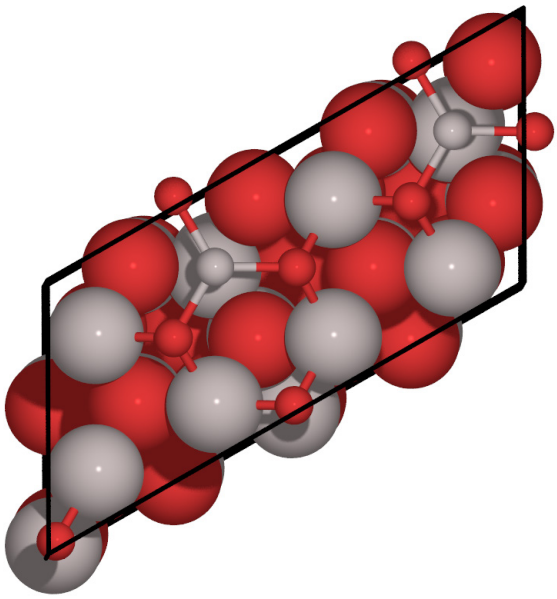

Figure 6.1: Top view of the γ-Al_2O_3 (111) p(2×1) surface model. Al atoms are shown in tan, O atoms in red. Atoms in the top-most layer are drawn with small spheres and bonds between nearest neighbors, while atoms in deeper layers are drawn as large spheres.

Previous work has demonstrated the critical role of both Al and O sites in ethanol dehydration and etherification chemistry on γ-Al_2O_3 [101, 131]. Consequently, the mean-field microkinetic model implementation utilized two independent sites. A similarly essential consideration is to ensure thermodynamic consistency during parameterization of the microkinetic model. Thermodynamic cycles involving gas-phase and adsorbed intermediates may not close when different sources or methods are used to obtain parameters. In this work, the Gibbs energies of formation of the gas-phase species were obtained from an established database of gas-phase thermochemistry [52] to ensure matching of known thermodynamic quantities and high thermodynamic accuracy of catalytic cycles involving reactants and products. Total energies and vibrational frequencies obtained from DFT calculations were used

in conjunction with standard statistical mechanics formulas [10, 47] to obtain Gibbs energies of formation of all adsorbed species (including transition states). In order to consistently integrate parameters from the distinct sources, an approach was adopted in which the DFT-computed relative surface reaction thermochemistry (ΔG_{rxn}) is preserved together with select relative adsorption thermochemistry (ΔG_{ads}). These relative quantities are used together with the (absolute) Gibbs energies of the gas-phase species to compute the final Gibbs energies of surface species, with the consequence that values of ΔG_{ads} for some species may differ from those computed directly from DFT in order to ensure closure of thermodynamic cycles [10, 45]. In this model, ΔG_{ads} values for ethanol, diethyl ether, and H are used as computed from DFT. Note that adsorption quantities of all other key surface intermediates change very little, e.g., the adjusted ΔG_{ads} of water is only about 1 kcal/mol different from the directly-computed DFT value. Ultimately Gibbs energies of reaction (ΔG_{rxn}) and Gibbs barriers ($\Delta G^{\ddagger}$) for the i^{th} reaction are computed and utilized in Equation 6.1 and Equation 6.2 to obtain the forward rate constant $k_{i,f}$ and the equilibrium constant $K_{eq,i}$ for the i^{th} reaction:

$$k_{i,f} = \frac{k_B T}{h} e^{\left(\frac{-\Delta G_i^{\ddagger}}{k_B T}\right)} \qquad \text{Equation 6.1}$$

$$K_{eq,i} = e^{\left(\frac{-\Delta G_{rxn,i}}{k_B T}\right)} = \frac{k_{i,f}}{k_{i,r}} \qquad \text{Equation 6.2}$$

The reverse rate constant $k_{i,r}$ is subsequently computed from equation Equation 6.2 using the corresponding equilibrium and forward rate constants. Desorption rate constants were computed using Equation 6.1 by assuming that the desorption barrier is equal to the Gibbs energy of desorption.

The full microkinetic model was solved in a plug flow reactor (PFR). The numerical solution is accomplished by representing the PFR as a set of equal-volume continuous stirred tank reactor (CSTR) models connected in series whose total volume equals the volume of the PFR, similar to Ref. [60]. Each CSTR is then integrated to long times to obtain the steady state solution, and this output forms the input to the next CSTR in the series. This approach has the advantage of being more robust than directly formulating and solving a set of differential-algebraic equations. The model is solved using an in-house Fortran code built around the Chemkin II chemical kinetics library of subroutines [17, 82]. The simulated reactor had a 1.0 cm inner diameter and a total volume of 1.6 cm^3. The simulated catalyst bed contained 46.5 micromoles of sites, based on an assumed site density of 3×10^{-9} moles cm^{-2} and corresponding to 20 mg of powdered γ-Al_2O_3 catalyst used in experimental steady-state kinetics measurements [103]. 20% of the surface sites were Al sites, consistent with the 1:4 Al:O surface site ratio of γ-Al_2O_3(111). All O sites were assumed to be identical in the model. The total volumetric flowrate of ethanol, water, and helium diluent was 200 cm^3 min^{-1}, and the reactor temperature was 488 K with an atmospheric operating pressure.

In order to enable reactor design calculations and analysis of experimental data, a reduced kinetic model was developed. Reaction rates of the reduced model were fitted to experimental data by incorporating the reduced expressions into a Matlab R2009a [156] program that utilized the built-in Matlab *lsqnonlin* nonlinear fitting routine. Minimization is accomplished via a trust-region-reflexive algorithm, and the quality of fit was determined by evaluating the sum of squares of the natural logarithm of the ratio of model-computed rates to experimental rates. Analytical

reduced rate expressions were developed and therefore rates were computed as part of a PFR design equation that requires a straightforward integration in reactor volume. The integration was accomplished using the Matlab routine *ode45*.

6.3 Reaction Energetics of Ethanol on γ-Al_2O_3(111)

The overall reactions for the conversion of ethanol over γ-Al_2O_3 are shown in Equation 6.3 and Equation 6.4:

$$CH_3CH_2OH \rightarrow C_2H_4 + H_2O \qquad \text{Equation 6.3}$$

$$2\ CH_3CH_2OH \rightarrow CH_3CH_2OCH_2CH_3 + H_2O \qquad \text{Equation 6.4}$$

A number of possible elementary steps of Equation 6.3 and Equation 6.4 were explored in our previous DFT work on γ-Al_2O_3(100) [131]. We have therefore applied that knowledge and focused in this work on the intermediates and associated mechanisms that were shown to be most energetically favorable. The optimized geometries of the various stable states and transition states are available in Figures D.1-D.13.

The energetics for the direct conversion of ethanol into ethylene on γ-Al_2O_3(111) are plotted in Figure 6.2. In the E2 mechanism, ethanol first adsorbs on the surface on an Al (Lewis acid) site with an adsorption energy ΔE_{ads} = -28 kcal/mol. The C–O and C_β–H bonds of ethanol are then broken in a single concerted elementary step to form weakly-adsorbed ethylene (ΔE_{ads} ~ -2 kcal/mol), with OH remaining on the Al site and the H_β landing on a neighboring surface O site (a Lewis base). The barrier for this process is 28 kcal/mol, and depends only weakly on the identity of the O site [101, 131]. Given its weak adsorption, the diagram displays ethylene as a gas-phase species following this step. To close the catalytic cycle, OH^{Al} and H^{O} fragments combine to

form H_2O^{Al} with a moderate barrier of 14 kcal/mol, and water overcomes ΔE_{ads} = -28 kcal/mol to enter the gas phase. Note that the barrier for O–H dissociation of water is 3 kcal/mol. The E1 pathway begins with ethanol adsorption just as in the E2 path, and then the O–H bond dissociates with a barrier of 2 kcal/mol to form $CH_3CH_2O^{Al}$ with H^O adsorbed nearby. The value of ΔE_{rxn} for this step is -12 kcal/mol, suggesting an energetic preference for ethanol to dissociate on the surface. Following ethanol dissociation, a H_β of ethoxy is transferred from the C_β to the O of ethoxy while at the same time the ethoxy C–O bond elongates and breaks. This leads to production of gas phase ethylene and OH^{Al}; the nearby H^O does not participate in this elementary step. Water then forms by recombination and desorbs in the same fashion as described in connection with the E2 pathway. The concerted transformation of $CH_3CH_2O^{Al}$ to ethylene and OH^{Al} has a barrier of 59 kcal/mol, twice as high as the E2 pathway.

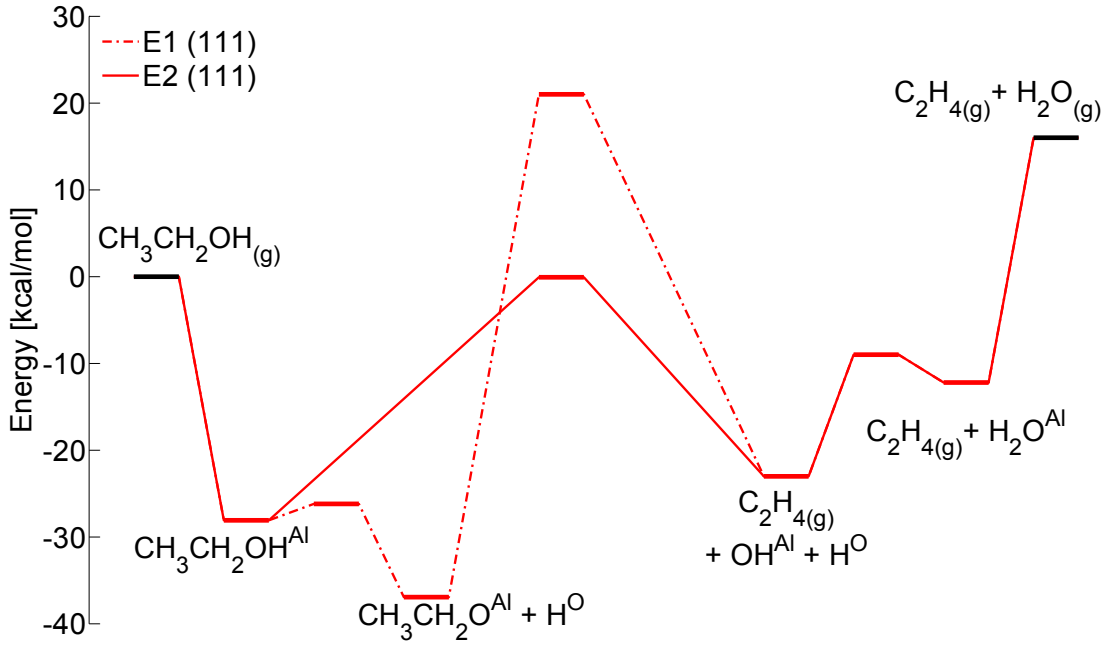

Figure 6.2: Energy diagram comparing alternative mechanistic pathways for ethylene formation from ethanol on γ-Al_2O_3(111).

In competition with the unimolecular dehydration pathways, ethanol may also undergo a bimolecular reaction to form diethyl ether. Two different pathways for this transformation are diagrammed in Figure 6.3. In the pathway labeled "S_N2", two ethanol molecules adsorb on two different but adjacent Al sites and one ethanol dissociates to form $CH_3CH_2O^{Al}$ and H^O. The C–O bond of ethanol then breaks while at the same time a new C–O bond forms between the C_α of the former ethanol and the O of the nearby ethoxy, leading to diethyl ether. OH^{Al} is left behind at the site where ethanol was located (the H^O fragment does not participate in this step). The ethoxy acts as the attacking nucleophile in this Lewis acid-catalyzed bimolecular nucleophilic substitution (S_N2) mechanism that proceeds with a 32 kcal/mol barrier. The diethyl ether that forms is bound with similar strength as the reactant ethanol (ΔE_{ads} = -34

kcal/mol). The second ether formation pathway labeled "S_N2''" is a variant of the first mechanism. The initial state consists of two ethanol molecules, one adsorbed on an Al site and the other adsorbed on an O site through a hydrogen bonding-type interaction of the H atom in the OH group of the alcohol. The O-bound ethanol (ΔE_{ads} = -10 kcal/mol) acts as the attacking nucleophile and the ethyl group of the Al-bound ethanol is transferred in the same manner as described for the S_N2 path. The H of the O-bound ethanol is simultaneously transferred to the surface O site as the new C–O bond forms, leading to diethyl ether adsorbed to the surface-bound H (ΔE_{ads} = -14 kcal/mol). The barrier for this step is 25 kcal/mol, i.e., 7 kcal/mol lower than that of the S_N2 mechanism. Thus, the S_N2' mechanism is kinetically favored over S_N2, but the S_N2 precursor state is much more stable than the corresponding state for S_N2'. Due to the weak adsorption of the O-bound ethanol, the S_N2' mechanism is reminiscent of an Eley-Rideal type mechanism.

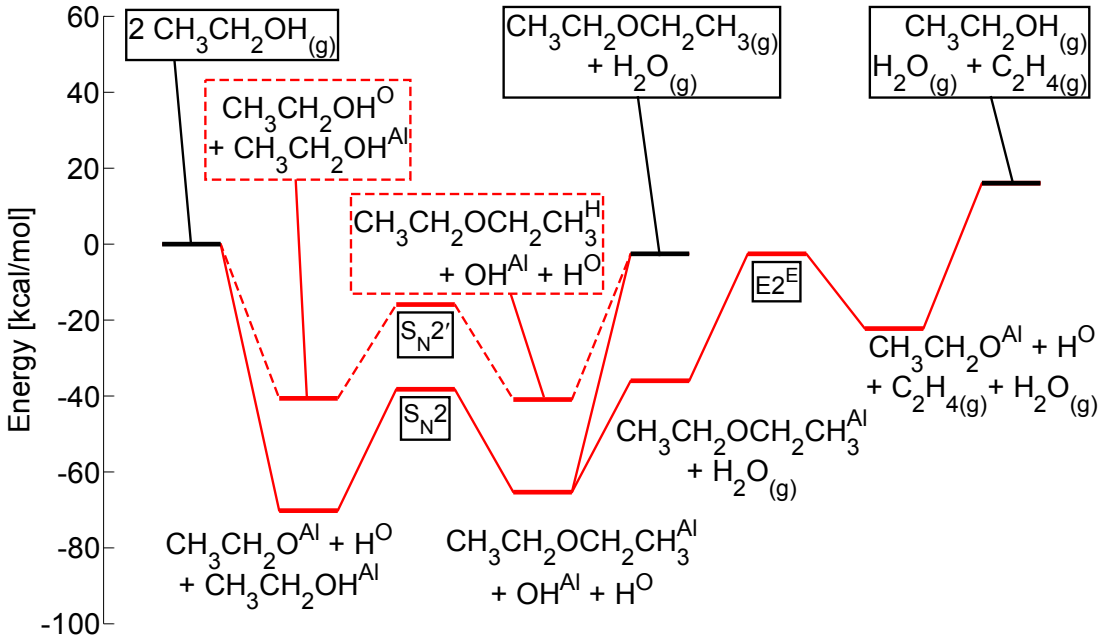

Figure 6.3: Energy diagram for mechanisms of diethyl ether formation from ethanol and ethylene formation from diethyl ether on γ-Al_2O_3(111). The "S_N2" and "S_N2'" labels indicate the transition states for ether formation, while the "$E2^E$" label identifies the transition state for ethylene formation from diethyl ether adsorbed on an Al site.

Finally, as an alternative to desorption, the Al-bound diethyl ether may undergo an elimination reaction to produce ethylene. This $E2^E$ step (superscript "E" denotes "ether"), which is mechanistically very similar to the E2 mechanism of ethanol, proceeds when a C–O and a C_β–H bond of the same ethyl "R" group are broken in a single elementary event. The reaction barrier is 34 kcal/mol, i.e., 6 kcal/mol higher than the E2 pathway (from ethanol). A comparison of reaction barriers suggests that the E2 mechanism is the preferred route for ethylene production, and this is confirmed below using the microkinetic model. The general trends for magnitude of reaction barriers are consistent with our previous calculations on γ-Al_2O_3(100), except that on the (100) facet S_N2 etherification is slightly more favorable than E2

dehydration [131]. This similarity on the reaction barriers is an important observation not only because they involve different facets (e.g. (111) vs. (100)) of γ-Al_2O_3, but also different theoretical models (γ-Al_2O_3 of Pinto et al. [155] vs. γ-Al_2O_3 of Raybaud, Sautet, and coworkers [119-120]).

While the discussion to this point has focused on energy trends computed at T = 0 K, consideration of Gibbs energies provides insight into thermodynamic and kinetic quantities at relevant (experimental) operating conditions. Table 6.1 provides a comparison of reaction energies and barriers for each elementary step considered. The Gibbs quantities are computed at 488 K, which is the operating temperature of the reactor that produced the kinetic data used for comparison in this work [103]. Looking first at the adsorption steps, the Gibbs energies of adsorption are substantially weaker than the corresponding values of ΔE_{ads}. In fact, at 488 K the O-bound ethanol is less stable than gas-phase ethanol. Recalling the thermodynamic relationship $\Delta G = \Delta H - T\Delta S$ and roughly equating ΔE and ΔH, the results are consistent with a large decrease in entropy when moving from the gas phase to the surface and a moderate value of T. The Gibbs properties for O–H bond dissociation reactions of water and ethanol are essentially unchanged from the low-temperature quantities. Regarding the five remaining elementary steps, the Gibbs barriers are 1-5 kcal/mol lower relative to the 0 K activation barriers, which is a fairly modest change. On the other hand, ΔG_{rxn} values for these steps are substantially decreased relative to the values of ΔE_{rxn} (by 16-23 kcal/mol), and in fact all change from positive to negative values. The origin of this effect for the three steps forming ethylene is that there is a substantial increase in entropy due to formation of gas-phase ethylene as a product. The changes in this value for the S_N2 and S_N2' reactions (formation of diethyl ether)

are largely due to the method of computing ΔG_{rxn}. The final state of these steps has a hydrogen atom situated on an O site near diethyl ether and spatially separated from OH, and the value of ΔE_{rxn} was computed based on this arrangement. The ΔG_{rxn} was computed based on energetics in which atomic hydrogen was located adjacent to OH, which is more stable. This assumption was made to facilitate incorporation of the Gibbs properties into the multi-site microkinetic model. However, as shown below, the values of ΔG_{rxn} for these specific steps do not affect the results of the model because the rates of these particular steps are kinetically controlled.

Table 6.1: Set of reactions and associated parameters computed using DFT on the γ-Al_2O_3(111) facet and subsequently included in the two-site microkinetic model. Differences in the last two columns are indicated in bold font.

Reaction	ΔE_{rxn} [kcal/mol]	$E_{a,f}$ [kcal/mol]	ΔG_{rxn} (488 K) [kcal/mol] [a]	$\Delta G^{\ddagger}$(488 K) [kcal/mol]	
				DFT [b]	Model [c]
$CH_3CH_2OH^{Al} \rightleftharpoons CH_3CH_2OH_{(g)} + {}^{Al}$	28	-	5	-	5
$CH_3CH_2OH^{O} \rightleftharpoons CH_3CH_2OH_{(g)} + {}^{O}$	10	-	-10	-	0
$CH_3CH_2OCH_2CH_3{}^{Al} \rightleftharpoons CH_3CH_2OCH_2CH_{3(g)} + {}^{Al}$	34	-	9	-	9
$H_2O^{Al} \rightleftharpoons H_2O_{(g)} + {}^{Al}$	28	-	6	-	6
$H_2O^{Al} + {}^{O} \rightleftharpoons OH^{Al} + H^{O}$	-11	3	-11	2	2
$CH_3CH_2OH^{Al} + {}^{O} \rightleftharpoons CH_3CH_2O^{Al} + H^{O}$	-10	4	-12	2	2
$CH_3CH_2O^{Al} + CH_3CH_2OH^{Al} \rightleftharpoons CH_3CH_2OCH_2CH_3{}^{Al} + OH^{Al}$ (S_N2)	5	32	-7	**28**	**24**
$CH_3CH_2OH^{O} + CH_3CH_2OH^{Al} \rightleftharpoons CH_3CH_2OCH_2CH_3{}^{H} + OH^{Al} + H^{O}$ (S_N2')	0	25	-16	**21**	**17**
$CH_3CH_2OH^{Al} + {}^{O} \rightleftharpoons C_2H_4 + OH^{Al} + H^{O}$ (E2)	3	28	-16	**25**	**29**
$CH_3CH_2O^{Al} \rightleftharpoons C_2H_4 + OH^{Al}$ (E1)	12	59	-4	58	58
$CH_3CH_2OCH_2CH_3{}^{Al} + {}^{O} \rightleftharpoons C_2H_4 + CH_3CH_2O^{Al} + H^{O}$ ($E2^{E}$)	14	34	-9	29	29

[a] Values computed using gas-phase Gibbs energies of formation from a thermochemical database, as described in the Computational Methods section.
[b] Denotes the value of the parameter as estimated from DFT.
[c] Denotes the actual value of the parameter used in the microkinetic model.

6.4 DFT-Parameterized Multi-Site Model

The computation and analysis of reaction quantities from DFT provide parameters for, and insights into, the reaction network. In order to quantify reaction rates and determine how well the proposed mechanisms describe experimental data, the DFT-computed parameters from γ-Al_2O_3(111) have been incorporated into a microkinetic model that contains site balances for two different types of surface sites

(Al and O sites). The model is made up of the set of elementary steps and the associated parameters summarized in Table 6.1. The Gibbs barriers for two steps in the model (E2 and S_N2) are adjusted within the approximate error of the calculation (~5 kcal/mol) in order to capture relative trends of experimentally-observed diethyl ether versus ethylene production rates. The barrier for the S_N2' step is also adjusted by an amount equal to the S_N2 barrier adjustment, so as to avoid disproportionately promoting the S_N2 step over S_N2'. No other adjustments were made to the DFT-computed parameters.

The reaction rates calculated from the microkinetic model are displayed alongside experimentally measured rates in Figures 6.4 and 6.5, with values of the reaction orders summarized in Table 6.2. The model captures well the experimental trends in reaction orders for production rates of both ethylene and diethyl ether as a function of either ethanol or water partial pressure. As the ethanol partial pressure varies (Figure 6.4 and Table 6.2), the model captures both the fractional reaction orders and the increasing magnitude of orders as the amount of co-fed water increases. The absolute values of the reaction orders are also similar. The model somewhat underpredicts the magnitude of the reaction orders as a function of water pressure (Figure 6.5 and Table 6.2), but does capture the negative orders which become strongly negative as co-fed ethanol is withdrawn. In an effort to improve the agreement in this latter set of reaction orders, we explored the effect of adding lateral adsorbate interaction terms to the model that influence the binding strength of adsorbates or the magnitude of reaction barriers as a function of adsorbate coverage. We found it is possible to improve agreement between the orders computed from varying water pressure, but only at the expense of poorer agreement between reaction

orders in ethanol. Consequently, lateral interaction terms were not included; note that the values of these interactions are small, on the order of 1 kcal/mol. The absolute rates predicted by the model are approximately two orders of magnitude lower than the experimentally-measured rates, which is reasonable given the limited adjustment of parameters as computed from DFT. It should be noted that the predictive ability of the model approaches the performance of state-of-the-art metal-based models that predict absolute rates within one order of magnitude [59]. The difference between model and experimental rates may be due to, for example, errors in the estimates of the entropic contributions, the treatment of exchange and correlation in DFT, the mean-field approximation, or differences between the postulated (model) and actual active site(s). Overall, the model is successful in describing the trends in the experimental data.

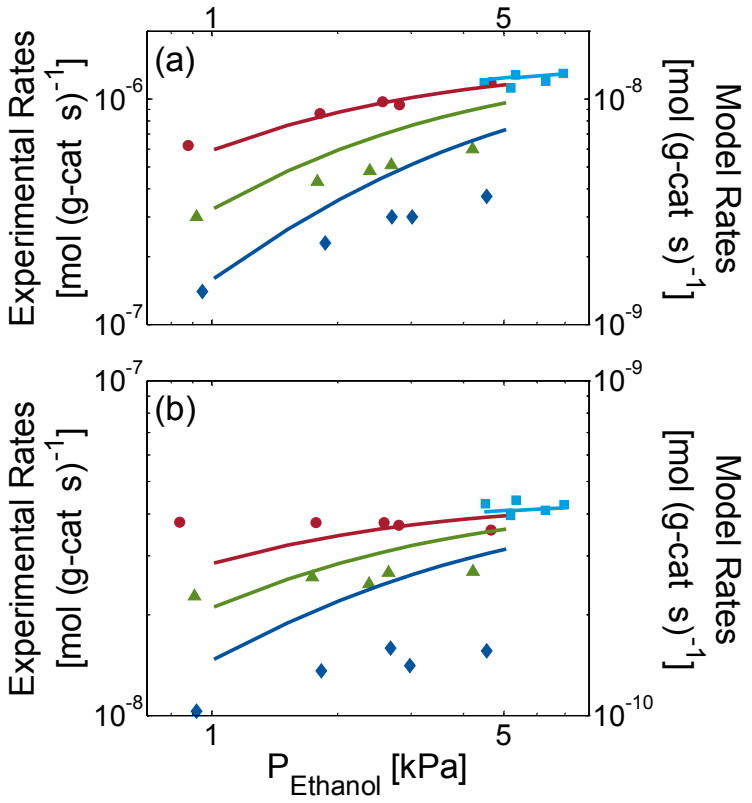

Figure 6.4: Comparison of rates computed using the two-site microkinetic model with experimentally measured rates for (a) diethyl ether production and (b) ethylene production. Solid lines represent model rates and symbols indicate rates from experiments. Colors indicate distinct water co-feed pressures of 0.4 kPa (cyan), 0.6 kPa (red), 1.2 kPa (green), and 2.2 kPa (blue). Reaction orders are tabulated in Table 6.2.

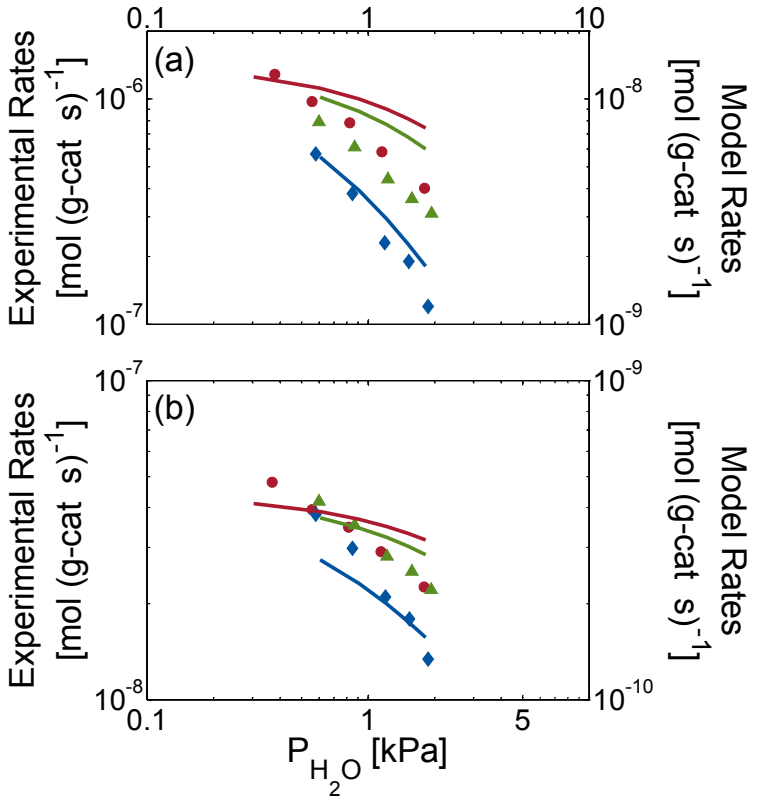

Figure 6.5: Comparison of rates computed using the two-site microkinetic model with experimentally measured rates for (a) diethyl ether production and (b) ethylene production. Solid lines represent model rates and symbols indicate rates from experiments. Colors indicate distinct ethanol co-feed pressures of 4.2 kPa (red), 3.0 kPa (green), and 0.9 kPa (blue). Reaction orders are tabulated in Table 6.2.

Table 6.2: Comparison of reaction orders obtained from the two-site microkinetic model (in parentheses) with experimentally-determined orders.

CH_3CH_2OH Partial Pressure [kPa]	H_2O Partial Pressure [kPa]	Reaction Order	
		$C_4H_{10}O$ Production	C_2H_4 Production
1 - 5	0.4	0.2 (0.1)	0 (0.1)
1 - 5	0.6	0.4 (0.4)	0 (0.2)
1 - 5	1.1	0.5 (0.7)	0.1 (0.3)
4 - 7	2.2	0.6 (0.9)	0.3 (0.5)
4.2	0.5 - 2	-0.7 (-0.3)	-0.5 (-0.1)
3.0	0.5 - 2	-0.8 (-0.5)	-0.5 (-0.2)
0.9	0.5 - 2	-1.3 (-1.0)	-0.9 (-0.5)

We turn now to a quantitative examination of the rates and surface coverages obtained as output from the microkinetic model to understand how these aspects of the mechanism connect to the observed mesoscopic trends. Application of sensitivity analysis allows for unambiguous assignment of the elementary step(s) that control overall reaction rates [64-65]. The metric used in the analysis is the normalized sensitivity coefficient (NSC):

$$\mathrm{NSC}_i = \frac{\partial \ln(R)}{\partial \ln(A_{f,i})} \cong \frac{A_{f,i}\,\Delta R}{R\,\Delta A_{f,i}} \qquad \text{Equation 6.5}$$

where $A_{f,i}$ and R are, respectively, the forward pre-exponential factor for reaction i and the response variable of interest. Figure 6.6 compares three sets of NSCs computed using three different response variables, namely ethanol conversion and the gas-phase mass fractions of diethyl ether and ethylene. The end-of-reactor mass fractions of

diethyl ether and ethylene are measures of the production rates of each species. The plot illustrates clearly that the pre-exponential factor (and therefore the rate constant) of the S_N2 elementary step has the most influence on both the overall conversion and the production rate of diethyl ether, while the rate of ethylene production is most strongly influenced by the rate constant for the E2 step. This indicates that the S_N2 and E2 steps exhibit almost exclusive control of the rates of (respectively) diethyl ether and ethylene production at the examined conditions. Also, since the model-computed absolute rates of ether production are approximately one order of magnitude higher than the ethylene rates, it is reasonable that both ethanol conversion and the rate of ether production are controlled by the S_N2 step. As multiple elementary steps in the network may produce ethylene, a detailed summary of relative rates for ethylene production is shown in Figure D.14. Despite having identical values of the rate constant in the model, the flux through the E2 pathway is more than two orders of magnitude higher than through the $E2^E$ pathway because there is much more ethanol than diethyl ether available to react. The small rate constant for the E1 step causes it to contribute the least to the production of ethylene. The S_N2' step is 1-2 orders of magnitude slower than the S_N2 step, despite having a lower barrier. The rationale for this observation comes by examining the surface coverages.

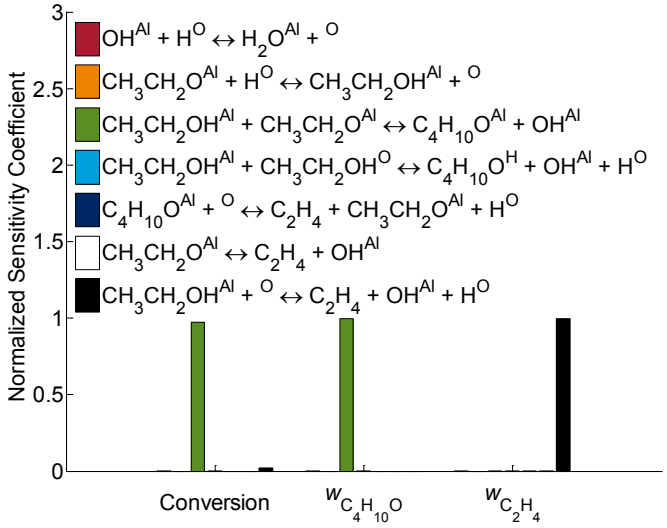

Figure 6.6: Normalized sensitivity coefficients for surface elementary steps in the two-site microkinetic model. The response variable for each group of bars is shown below the horizontal axis; w_j refers to the gas-phase mass fraction of species j. The coefficients corresponding to elementary steps for adsorption of ethanol, water, and diethyl ether are all negligibly small and are excluded for clarity. Coefficients are reported as calculated at the exit of the reactor operating at T = 488 K, with entrance partial pressures $P_{ethanol}$ = 1 kPA and P_{water} = 0.6 kPa.

As vital components of reaction rates, the surface coverages of adsorbates also merit discussion. The Al sites are essentially completely covered by a combination of ethoxy (θ = 0.20 – 0.95) and OH (θ = 0.05 – 0.80) over the range of considered conditions. Ethanol and water occupy very small fractions of the surface (θ = 1×10^{-7} – 1×10^{-6}) and diethyl ether is present in even smaller fractions (θ = 1×10^{-9}). The O sites are 25% covered by H, with the remaining 75% vacant. This ratio of occupied to vacant sites arises because the Al:O surface site ratio in the model is 1:4, and since all Al sites are covered by either ethoxy or OH, a proportional amount of H is present on the O sites. O-bound ethanol and diethyl ether bound to H^O sites occupy very small

fractions of sites ($\theta = 1\times10^{-7} - 1\times10^{-6}$ and $\theta = 1\times10^{-12} - 1\times10^{-11}$, respectively) and have a negligible impact on fractions of H^O and vacant O sites. Having described the trends in coverages on the surface, the fact that the Al sites are always covered sheds light on why fractional orders are observed as a function of ethanol pressure. At a specified reaction temperature, the values of the rate constants are fixed and so the only quantities changing in the surface mechanism as a function of pressure are the adsorbate coverages. When the surface is largely covered by ethoxy, an increase in partial pressure of ethanol has a much smaller effect on the rate than the effect that would be observed if the surface sites were mostly vacant. Thus, the reaction orders are fractional or near zero as a function of ethanol pressure for both ethylene and ether production. Following a similar line of reasoning, the presence of sufficient ethanol pressure leads to weakly negative orders in water pressure. Finally, the rate of the S_N2' reaction is low because the product of Al- and O-bound ethanol concentrations is more than 100,000 times smaller than the product of Al-bound ethanol and ethoxy concentrations required for the S_N2 path. While the S_N2' path does have a lower barrier, this leads to a rate constant that is only about 1,000 times larger than the S_N2 rate constant and is therefore insufficient to compensate for the substantial difference in available surface reactants.

Combining the knowledge and observations gleaned from the model analysis leads to an overall picture of the reaction network, summarized in Figure 6.7 at a select set of conditions. The production of ethylene and diethyl ether from ethanol takes place through a set of two interdependent cycles. In the first cycle, ethanol first adsorbs on the surface and then reacts via the E2 mechanism to form ethylene. OH and H subsequently recombine into water that desorbs from the surface. In the other cycle,

rather than forming ethylene, the O–H bond of ethanol dissociates to form CH_3CH_2O and H. CH_3CH_2O then reacts via the S_N2 mechanism with a second ethanol molecule to form diethyl ether which desorbs, and H and OH fragments recombine to form water and desorb as before. As depicted in Figure 6.7, all adsorption steps and O–H bond dissociation reactions are equilibrated. Only the E2 and S_N2 reactions are irreversible, consistent with the results of the sensitivity analysis that these two steps each control the overall rate of their respective cycles. The E2 and S_N2 mechanisms are also consistent with the observation of a kinetic isotope effect (or lack thereof) in experiments using deuterium-labeled ethanol [103]. Ethoxy and hydroxyl dominate the Al sites with their relative coverages determined by reaction conditions, while the fraction of O sites occupied by H remains constant across all tested conditions. Note that the ethoxy intermediate is an active participant in the major pathway for diethyl ether production, but is merely a spectator in the ethylene production pathway. This behavior clearly demonstrates that drawing conclusions about reaction mechanisms based solely on surface species information can be misleading.

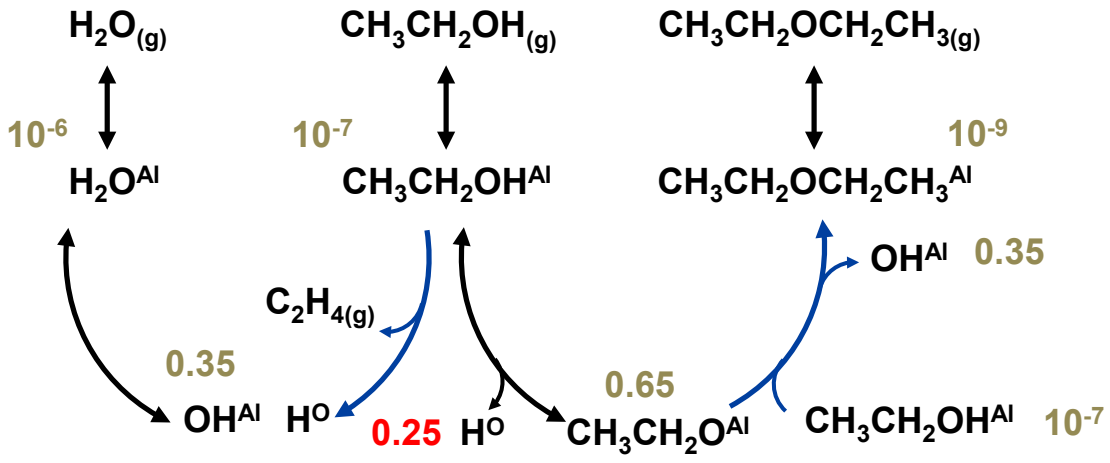

Figure 6.7: Reaction pathway diagram describing the interconnected catalytic cycles of ethanol dehydration and etherification, constructed using results of the two-site microkinetic model. Superscript "Al" ("O") refers to a species bound to a surface Al (O) site. Numbers denote surface coverages of adsorbates and are color-coded by site type (tan = Al sites, red = O sites). Coverages are reported as calculated at the exit of the reactor operating at T = 488 K, with entrance partial pressures $P_{ethanol}$ = 1 kPA and P_{water} = 0.6 kPa.

6.5 Microkinetic Model Reduction and Fitting

The objective of creating the full two-site microkinetic model was to determine how well the calculated mechanism and associated parameters are able to describe key trends in experimental data and understand the reaction network. The results of kinetic models achieve even greater utility when coupled with higher-level simulations, such as computational fluid dynamics (CFD) and process-level models. In such contexts, the reaction rates must be sufficiently accurate while keeping the computational cost of evaluating the kinetic expressions to a minimum. This motivates the development of a simplified kinetic expression that, in this case, benefits from the unique insights gained from the results of the full microkinetic model.

A methodology for *a posteriori* microkinetic model reduction has been set forth previously which involves two major steps, namely elimination of elementary steps that are non-essential to the mechanism and the encapsulation of the remaining steps into a single rate expression [67]. Since the number of steps in the mechanism of this work is relatively small, it is possible to prune the mechanism by inspection and based on knowledge of the full model, rather than resulting to a formal principal component analysis. As shown in Figure D.14, the rates of ethylene production from the E1 and $E2^E$ steps are minimal, so these steps can be safely excluded from the model. Likewise, the S_N2' step contributes negligible diethyl ether and, along with ethanol adsorption on O sites, may also be excluded. As also discussed, the S_N2 step is irreversible in the forward (ether-producing) direction and therefore, the surface coverage of diethyl ether does not enter into the final rate expression. As this is the only remaining place that surface diethyl ether appears in the network, it is also possible to exclude diethyl ether adsorption/desorption from the model. This leaves six remaining steps in the reduced mechanism:

$$CH_3CH_2OH + {}^{Al} \rightleftharpoons CH_3CH_2OH^{Al} \quad \text{(R1)}$$

$$H_2O + {}^{Al} \rightleftharpoons H_2O^{Al} \quad \text{(R2)}$$

$$CH_3CH_2OH^{Al} + {}^{O} \rightleftharpoons CH_3CH_2O^{Al} + H^{O} \quad \text{(R3)}$$

$$H_2O^{Al} + {}^{O} \rightleftharpoons OH^{Al} + H^{O} \quad \text{(R4)}$$

$$CH_3CH_2OH^{Al} + {}^{O} \rightarrow C_2H_4 + OH^{Al} + H^{O} \quad \text{(R5)}$$

$$CH_3CH_2OH^{Al} + CH_3CH_2O^{Al} \rightarrow CH_3CH_2OCH_2CH_3 + OH^{Al} + {}^{Al} \quad \text{(R6)}$$

Note that (R5) and (R6) are written as irreversible steps, and (R6) is written assuming direct production of gas-phase diethyl ether. In order to develop the reduced rate

expression, site balances are derived for each of the seven surface species including vacancies (diethyl ether is excluded as discussed before). The details of the derivation including the application of knowledge about reaction (ir)reversibility and dominant surface species are available in Appendix D, and we simply state here the final reduced rate expressions for the production of ethylene and diethyl ether:

$$r_{5f} = k_{5f} K_1 P_{ethanol} \left[{}^{Al} \right] \left[{}^{O} \right] \qquad \text{Equation 6.6}$$

$$r_{6f} = \frac{k_{6f} K_1^{\,2} K_3 P_{ethanol}^{2} \left[{}^{Al} \right]^{1.5} \left[{}^{O} \right]^{0.5}}{Q^{0.5}} \qquad \text{Equation 6.7}$$

$$\left[{}^{Al} \right] = \frac{-\left(2S_{Al} + \left(S_O - S_{Al}\right) Q\right) \pm \sqrt{\left(2S_{Al} + \left(S_O - S_{Al}\right) Q\right)^2 + 4\left(Q-1\right) S_{Al}^{\,2}}}{2\left(Q-1\right)} \qquad \text{Equation 6.8}$$

$$\left[{}^{O} \right] = \frac{-\left(2S_{O} + \left(S_{Al} - S_O\right) Q\right) \pm \sqrt{\left(2S_{O} + \left(S_{Al} - S_O\right) Q\right)^2 + 4\left(Q-1\right) S_{O}^{\,2}}}{2\left(Q-1\right)} \qquad \text{Equation 6.9}$$

$$Q = K_1 K_3 P_{ethanol} + K_2 K_4 P_{H_2O} \qquad \text{Equation 6.10}$$

where S_{Al} and S_O refer respectively to surface site densities of Al and O. As shown in Figures D.15-D.17, the reduced model does an excellent job of reproducing the rates computed from the full microkinetic model.

In order to determine what changes are needed in the model parameters to quantitatively describe experimental rates, the rate expressions were encoded in a script that utilizes built-in Matlab optimization routines. Details of the parameter fitting are described in the SI, and the results of the fitting procedure are summarized in Table 6.3. Note that while the equilibrium constants are the actual parameters utilized in the reduced model, their values are reported in Table 6.3 in a more accessible form that is equivalent to the Gibbs energy of reaction for each elementary

step. All estimates are situated within narrow confidence regions of ±2 kcal/mol or smaller. Comparison of the final estimates with the values computed from DFT indicates that the adsorption constants as well as the Gibbs barrier for the E2 reaction require little adjustment, whereas the Gibbs barrier for the S_N2 step is over-estimated by about 8 kcal/mol. The significant change in the latter quantity may be a result of challenges in accurately estimating the energetic effect of steric interactions in a bimolecular reaction. In addition, the electronic properties of surface sites on γ-Al_2O_3 can be modified by adsorption of species on neighboring sites [149] and such many-body effects may not be fully captured in the present model.

Table 6.3: Set of parameters used to fit the reduced model to experimental data. All values are computed at T = 488 K.

Parameter [kcal/mol]	DFT Value [kcal/mol]	Fitted Estimate [kcal/mol]	Confidence Intervals [kcal/mol]
$-RT \ln(K_1)$	-4.9	-5.0	[-3.0, -7.0]
$-RT \ln(K_2)$	-5.7	-6.0	[-4.0, -7.9]
$-RT \ln(K_3)$	-12.2	- [a]	- [a]
$-RT \ln(K_4)$	-11.3	- [a]	- [a]
$\Delta G_5^{\ddagger}$	24.8	24.3	[24.2, 24.4]
$\Delta G_6^{\ddagger}$	28.3	19.9	[19.8, 20.1]

[a] These values were held fixed at the original DFT estimate and not adjusted during the fitting procedure.

The reaction orders estimated from the reduced model are shown in Table D.2 and compared to the experimentally-determined orders. As with the full microkinetic

model there is good agreement, although the orders as a function of ethanol pressure are somewhat higher in the reduced model compared to the full model. Figure 6.8 provides a head-to-head comparison of reduced model and experimental rates for both ether and ethylene production. The parity in ether rates is good (R^2=0.87), indicating the experimental data is well-described by the postulated model. As described above, this agreement is partially due to significant adjustment of the Gibbs barrier of the S_N2 step. In addition to accounting for steric interactions and many-body effects mentioned above, using a different catalytic active site may improve the estimate of the S_N2 barrier. The ethylene production rates are not as well described by the model (R^2=0.69). As with ether production, a different site may be responsible for at least some of the ethylene production observed experimentally. It is important to emphasize, however, that the current site model does capture the general trends in reaction orders, indicating that it likely plays a role in ether and ethylene production.

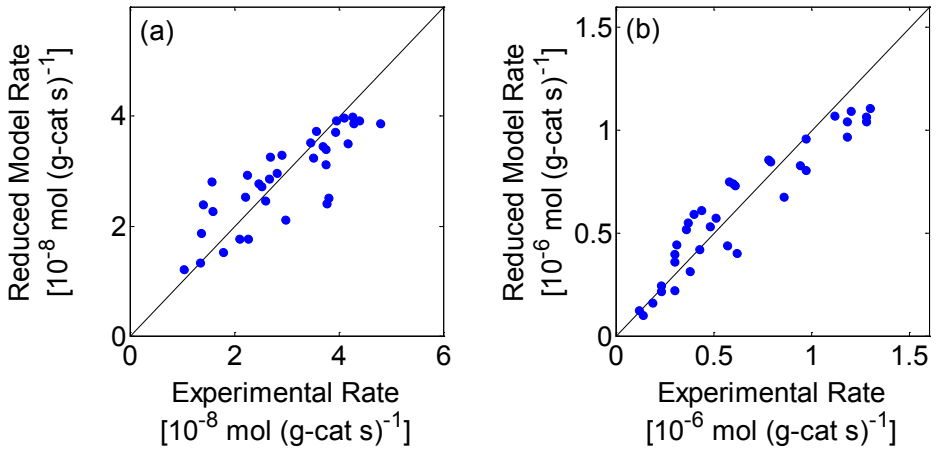

Figure 6.8: Parity plots of reaction rates predicted by the reduced model and experimentally measured reaction rates for (a) ethylene production and (b) diethyl ether production.

In addition to the kinetic data reported for ethylene conversion over γ-Al_2O_3, DeWilde et al. proposed a set of kinetic models to explain their data [103]. In their reaction scheme, adsorbates occupy a type of Lewis acid site that is composed of both a surface Al and surface O site. This means that an adsorbed ethoxy and the accompanying (dissociated) H fragment together occupy a single site. They also included terms that represent dimer formation between water, ethanol, or both. Using these assumptions, they proposed two distinct models for each of ethylene and diethyl ether production that successfully describe experimental rates. They supported the use of two different models with evidence from pyridine poisoning experiments that indicate there are distinct site requirements for ethylene and diethyl ether production. In the reduced model of the present work, Al and O vacancies are treated as distinct site types each with their own independent site balances. Consequently, due in part to the favorable thermodynamics for O–H bond dissociation, surface concentrations of ethoxy, OH and H all enter into site balance equations as dominant terms. The rate expressions for ether and ethylene formation naturally have distinct functional forms but are based on a common set of equations and parameters so that adjustment of a single value may affect rates of both species. Attractive lateral adsorbate interactions were tested for inclusion in the model in an effort to account for effects resembling dimer formation, but they did not improve the model performance. Overall, the reduced model is successful in predicting experimental trends for ether production (after adjustment of the S_N2 rate constant), with performance comparable to the model of DeWilde et al. Meanwhile, the expression of DeWilde et al. predicts ethylene production rates with greater accuracy. The proposed explanation of this difference in performance is that the reduced model assumes a common set of sites for ethylene and

ether production, while the model of DeWilde et al. asserts that the site requirements for ethylene production are distinct from diethyl ether. This is consistent with the hypothesis that at least some of the observed ethylene production comes from a site that is distinct from the site considered in the present work. On the other hand, the similarity in performance of the two models for predicting diethyl ether rates indicates that dimer formation may not be necessary to explain the kinetics of ether production. In the models of the present work, dissociated water and dissociated ethanol occupy virtually all of the available Al sites and thus exhibit considerable inhibitory influence on the reaction rates.

6.6 Conclusions

DFT calculations of the conversion of ethanol into ethylene and diethyl ether have been performed on the γ-Al_2O_3(111) facet for the first time. The reaction barrier for the S_N2 mechanism leading to diethyl ether is 32 kcal/mol. Among the pathways leading to ethylene, the E2 mechanism exhibits the most favorable barrier of 28 kcal/mol. O–H bond dissociation reactions of water and ethanol are slightly activated (2-4 kcal/mol). The 0 K energy profiles indicate that ethylene formation is endothermic, while consideration of Gibbs energies results in negative values of ΔG_{rxn} because of the entropic favorability of producing gas-phase ethylene.

The DFT-computed parameters were incorporated into a two-site mean-field microkinetic model to directly simulate reaction rates and surface coverages of intermediates. The model is able to successfully capture trends in experimentally-measured reaction orders with minor parameter adjustment, demonstrating the applicability of the DFT-computed mechanisms to powdered catalysts. Quantitative analysis reveals that the S_N2 and E2 elementary steps are irreversible and control the

reaction rates of ether and ethylene production, respectively. Alternative production pathways are at least 1-2 orders of magnitude slower than the dominant pathways. Al sites are covered by ethoxy and OH, while H covers a fraction (25%) of the O sites. The lack of vacant Al sites rationalizes the observed sub-unity reaction orders as a function of ethanol partial pressure. The model also demonstrates that ethoxy actively participates only in diethyl ether formation and, despite its surface abundance, is a spectator in ethylene production. This represents, to our knowledge, the first mean-field multi-site microkinetic model with full DFT-based parameterization on γ-Al_2O_3.

The full microkinetic model was reduced to a set of analytical rate expressions by application of *a posteriori* knowledge and fitted to experimental data to examine model performance for quantitative prediction of rates. Overall the reduced model captures reaction order trends with similar success as the full model. After adjustment of the S_N2 rate constant, the measured rates of diethyl ether production are described well by the model, further demonstrating the applicability of the S_N2 to mechanism to powdered catalysts. Ethylene production rates are predicted well at some conditions. The model indicates that another site (in addition to the present site model) may be responsible for some dehydration and etherification.

6.7 Acknowledgments

I would like to thank Prof. Giannis Mpourmpakis for technical guidance on this work and for providing feedback on the content of the chapter. This work was funded by the National Science Foundation (NSF) under Grant EFRI-937706. Additional financial support was provided as part of the Catalysis Center for Energy Innovation, an Energy Frontier Research Center funded by the U.S. Department of Energy, Office of Science, Office of Basic Energy Sciences under Award No. DE-

SC0001004. I acknowledge computational resources of the Extreme Science and Engineering Discovery Environment (XSEDE), which is supported by National Science Foundation Grant OCI-1053575. In connection with XSEDE, the computations were performed on the Kraken cluster administered by the National Institute for Computational Sciences (NICS). I also acknowledge the resources of the National Energy Research Scientific Computing Center (NERSC), which is supported by the Office of Science of the U.S. Department of Energy under Contract No. DE-AC02-05CH11231.

Chapter 7

SUMMARY AND OUTLOOK

7.1 Dissertation Conclusions

In this work the mechanisms pertaining to catalytic upgrade of oxygenate probe molecules have been explored using DFT methods and microkinetic modeling. Chapter 2 presented the principles, methods, and tools used to parameterize and analyze microkinetic models. Particular attention was given to explaining DFT calculations, as data from these calculations are at the heart of predictive models. The approaches for integrating the information from DFT into a consistent microkinetic model were also described, along with an alternative semi-empirical parameterization method (BEPs) and principles for generalizing to multi-site mean-field models.

Chapter 3 detailed the findings of a kinetic model for Pt-catalyzed steam reforming of ethylene glycol, as the production and management of hydrogen in catalytic upgrade is vital. The model was successful in capturing key trends in reaction orders and apparent activation energies shown from experiments. Subsequent analysis demonstrated that early thermal dehydrogenation steps of ethylene glycol control the overall reaction rate. OH-mediated dehydrogenation steps were included but had no influence on the overall rate due to extremely low surface coverages of OH. Thus, the role of steam in this system is limited to shifting CO to CO_2.

A three-chapter exploration of catalytic deoxygenation began in Chapter 4, focusing on dehydration and related mechanisms of ethanol on γ-Al_2O_3. In Chapter 4, the (100) facet of γ-Al_2O_3 was explored using DFT methods in order to identify and

quantify the reaction mechanisms responsible for dehydration and etherification of ethanol. Adsorption on Lewis rather than Brønsted acid sites is thermodynamically preferred. Several different mechanisms were explored and the reaction barriers are either more favorable on Lewis sites or are similar on Lewis and Brønsted sites, leading to an expected preference of Lewis-catalyzed mechanisms. The most energetically favorable mechanism for ethylene formation (from either ethanol or diethyl ether) involves a concerted breaking of C–O and C_β–H bonds in an E2 reaction mechanism. Diethyl ether formation takes place via an S_N2 mechanism. The barriers and site dependences for these reactions rationalize experimental selectivity trends for ethylene versus diethyl ether.

Chapter 5 related a study of both the (110) and (100) facets of γ-Al_2O_3 and the impact of site-to-site heterogeneity on adsorption of oxygenates as well as dehydration and etherification of ethanol. In addition, the (110) surface is expected to be hydrated at relevant reactor operating conditions, and so the effect of surface water was also examined. The adsorption strength of the tested oxygenates varied between -0.4 and -1.4 eV across all Al^{+3} sites. A new descriptor, the mean of the Al^{+3} *s*-conduction band, was developed to successfully rationalize these trends. The same descriptor also quantitatively explains the trends in ethanol dehydration barriers as a function of the Al^{+3} adsorption site. Qualitative explanations of ethanol etherification barriers and of the effects of surface hydration were achieved with the same descriptor. The limitations of the descriptor in this regard were attributed to multi-body adsorption effects that modulate the nucleophilicity of ethoxy species and the basicity of surface oxygen atoms.

Chapter 6 described the results of DFT calculations on γ-Al_2O_3(111) and the incorporation of the associated parameter estimates into a multi-site mean-field microkinetic model. Consistent with DFT findings on other facets, ethylene formation via E2 mechanisms and ether formation via an S_N2 mechanism were energetically preferred. The microkinetic model successfully captured experimental trends in reaction orders after minor adjustment of DFT estimates of rate constants. The surface was covered predominantly by ethoxy, hydroxyl and atomic hydrogen, rationalizing observed fractional reaction orders as a function of ethanol partial pressure. Ethoxy, as a dominant species on the surface, is an active participant in diethyl ether production but only a spectator of ethylene production. An analytical reduced mechanism was developed that reproduces the experimental trends with similar success as the full model. While an additional site may be required to explain some of the activity for ethanol conversion, the success of the models demonstrates the applicability of DFT-computed mechanisms to γ-Al_2O_3 powdered catalysts.

7.2 Future Directions in Modeling of Metal Oxides and Catalytic Upgrade

This work has examined detailed mechanisms for hydrogen generation and catalytic deoxygenation, two sets of elementary steps that are fundamental to HDO of biomass-derived compounds. A number of topics related to HDO mechanisms remain essentially unexplored and are important future directions to advance the field.

7.2.1 Combined Mean-Field Kinetic Modeling of Metal and Acid Sites

As described in Chapter 1, HDO catalysts are thought to contain both metallic and acidic active sites that each contribute to the overall activity. The conversion of several biomass-derived compounds such as hydroxymethylfurfural (HMF), furfural,

cresols, guaiacol, and others are currently studied using HDO catalysts [8, 14, 157-158]. Developing a multi-site microkinetic model for the conversion of one or more of these molecules is expected to provide insights into the synergy between metal and acid sites. This has the potential to guide the development of descriptors for HDO catalysts, and represents an important step in first principles mechanistic modeling of these processes. Nobel metals supported on γ-Al_2O_3 are excellent candidate catalysts for initial studies.

7.2.2 Deoxygenation Trends and Catalyst Screening

As mentioned in Section 7.2.1, the creation of descriptors and other semi-empirical tools for HDO catalyst screening will assist in accelerating future catalyst development. Substantial progress has already been reported in screening models for transition metal catalysts, most commonly employing atomic binding energies as the descriptors of choice [59, 159]. Besides the descriptor itself (and excluding the generation of the set of elementary steps), there are three different types of tools that make possible the rapid parameterization of catalyst screening models: group additivity, linear scaling relations, and linear free energy correlations. Group additivity is a method for thermochemical property estimation of molecular adsorbates with arbitrary composition, achieved by first tabulating properties of constituent "building-block" groups of atoms [46, 85]. Linear scaling relations connect adsorption properties of molecular fragments to atomic binding energies and permit the prediction of adsorption properties of a given fragment on a variety of surfaces [160]. Linear free energy correlations allow the estimation of kinetic properties from thermodynamic properties [56, 147]. Together, these tools allow for full parameterization of

microkinetic models at negligible computational cost, beginning simply from the values of the descriptors.

At present, the extension of these descriptors and tools to simulate (Lewis) acid-catalyzed reaction networks (e.g., on metal oxides) is incomplete. Chapter 5 described the development of a descriptor for Lewis acid-base interactions of oxygenates (alcohols, water, and diethyl ether) with γ-Al_2O_3. The extent to which this descriptor accounts for oxygenate binding on other metal oxides should be tested. Further work is also required to understand how to create unified descriptor-based models of multi-functional catalysts. While the atomic binding energy descriptors used for transition metals may apply to some metal oxides [161], they may not be easily extensible to all materials (see Section 4.3, paragraph 1). This also has implications for linear scaling relations [161] and group additivity. With respect to the latter, the effects of through-surface interactions and system spin states (see Section 4.3, paragraph 1) on adsorbate thermochemistry have not been previously explored. It is possible that such effects could be captured by adapting lateral adsorbate interactions and other existing techniques [46, 85], but further study is required. Regarding linear free energy correlations, each new class of reaction usually requires the development of a new correlation, while the extension of existing correlations to different catalyst materials should be tested. Some correlations for metal oxides are available, but they are limited to reactions of small molecules (diatomic compounds and methane) [57-58]. Recent work demonstrates that reactions of larger oxygenate molecules on metal oxides can also be described by such correlations (see Appendix E), but further work is needed for additional homologous series of reactions. In summary, several opportunities are available in the area of semi-empirical methods development.

7.2.3 Kinetic Monte Carlo Simulations of Multi-Body Interactions

The adsorbate composition on the surface of γ-Al_2O_3 under HDO conditions is poorly understood. During HDO reactions, it is typical to impose high H_2 pressures on the system, and water is a major byproduct. Even in excess H_2, whether the γ-Al_2O_3 surface is dominated by H_2- or H_2O-derived fragments is unclear because H_2O adsorbs much more strongly than H_2 [128]. The presence of surface H_2O is known to influence adsorption and reaction of other molecules on γ-Al_2O_3 (see Chapter 5 and [128]). This situation is further complicated by acid sites of varying strength and multi-body effects (see Chapter 5). Further, there is an effect of lateral separation on the stability of dissociated adsorbates. For example, the difference in energy between the two configurations shown in Figure E.3 is 0.64 eV (nearly 15 kcal/mol) and cannot be explained by hydrogen bonding interactions. It is unclear how multi-molecule adsorption (e.g. H_2O and H_2) will influence the energetics of configurations like those in Figure E.3. It is also noteworthy that, based on α-Al_2O_3 calculations, H diffusion barriers may be low on some facets [162].

Taken together, these observations paint a picture of a complex set of interactions on the surface. To accurately account for these interactions, the development of a DFT-parameterized cluster-expansion Hamiltonian [163] is recommended. The suggested focus is to describe dissociatively adsorbed H_2O and H_2, followed by incorporation of the Hamiltonian into kinetic Monte Carlo simulations to explore how the surface composition changes as a function of reaction conditions. Such a study could lead to the calculation of more accurate reaction barriers in DFT by providing knowledge of the coverage and positions of adsorbates at relevant HDO operating conditions.

BIBLIOGRAPHY

1. *Facing the Hard Truths about Energy*. 2007, Washington DC: The National Petroleum Council.
2. Huber, G. W., S. Iborra, and A. Corma, *Synthesis of transportation fuels from biomass: Chemistry, catalysts, and engineering*. Chemical Reviews, 2006. **106** (9): p. 4044-4098.
3. *U.S. Billion-Ton Update: Biomass Supply for a Bioenergy and Bioproducts Industry.* 2011, Oak Ridge, TN: Oak Ridge National Laboratory.
4. Vennestrøm, P. N. R., C. M. Osmundsen, C. H. Christensen, and E. Taarning, *Beyond Petrochemicals: The Renewable Chemicals Industry*. Angewandte Chemie International Edition, 2011. **50** (45): p. 10502-10509.
5. Zacher, A. H., M. V. Olarte, D. M. Santosa, D. C. Elliott, and S. B. Jones, *A review and perspective of recent bio-oil hydrotreating research*. Green Chemistry, 2014. **16** (2): p. 491-515.
6. Chia, M., Y. J. Pagán-Torres, D. Hibbitts, Q. Tan, H. N. Pham, A. K. Datye, M. Neurock, R. J. Davis, and J. A. Dumesic, *Selective Hydrogenolysis of Polyols and Cyclic Ethers over Bifunctional Surface Sites on Rhodium–Rhenium Catalysts*. Journal of the American Chemical Society, 2011. **133** (32): p. 12675-12689.
7. Ciftci, A., B. Peng, A. Jentys, J. A. Lercher, and E. J. M. Hensen, *Support effects in the aqueous phase reforming of glycerol over supported platinum catalysts*. Applied Catalysis A: General, 2012. **431–432**: p. 113-119.
8. Foster, A. J., P. T. M. Do, and R. F. Lobo, *The Synergy of the Support Acid Function and the Metal Function in the Catalytic Hydrodeoxygenation of m-Cresol*. Topics in Catalysis, 2012. **55** (3-4): p. 118-128.
9. Zu, Y., P. Yang, J. Wang, X. Liu, J. Ren, G. Lu, and Y. Wang, *Efficient production of the liquid fuel 2,5-dimethylfuran from 5-hydroxymethylfurfural over Ru/Co_3O_4 catalyst*. Applied Catalysis B: Environmental, 2014. **146**: p. 244-248.
10. Salciccioli, M., M. Stamatakis, S. Caratzoulas, and D. G. Vlachos, *A review of multiscale modeling of metal-catalyzed reactions: Mechanism development for complexity and emergent behavior*. Chemical Engineering Science, 2011. **66** (19): p. 4319-4355.
11. Jensen, F., *Introduction to Computational Chemistry*. 2nd ed. 2007, England: Wiley.

12. Sabbe, M. K., M. F. Reyniers, and K. Reuter, *First-principles kinetic modeling in heterogeneous catalysis: an industrial perspective on best-practice, gaps and needs*. Catalysis Science & Technology, 2012. **2** (10): p. 2010-2024.
13. Wang, D., A. Villa, D. Su, L. Prati, and R. Schlögl, *Carbon-Supported Gold Nanocatalysts: Shape Effect in the Selective Glycerol Oxidation*. ChemCatChem, 2013. **5** (9): p. 2717-2723.
14. Jae, J., W. Zheng, A. M. Karim, W. Guo, R. F. Lobo, and D. G. Vlachos, *The Role of Ru and RuO_2 in the Catalytic Transfer Hydrogenation of 5-Hydroxymethylfurfural for the Production of 2,5-Dimethylfuran*. ChemCatChem, 2014. **6** (3): p. 848-856.
15. Thananatthanachon, T., and T. B. Rauchfuss, *Efficient Production of the Liquid Fuel 2,5-Dimethylfuran from Fructose Using Formic Acid as a Reagent*. Angewandte Chemie, 2010. **122** (37): p. 6766-6768.
16. Raimondeau, S., and D. G. Vlachos, *Recent developments on multiscale, hierarchical modeling of chemical reactors*. Chemical Engineering Journal, 2002. **90** (1-2): p. 3-23.
17. Coltrin, M. E., R. J. Kee, and F. M. Rupley, *Surface Chemkin - A General Formalism and Software for Analyzing Heterogeneous Chemical-Kinetics at a Gas-Surface Interface*. International Journal of Chemical Kinetics, 1991. **23** (12): p. 1111-1128.
18. Kolasinski, K. W., *Surface Science: Fundations of Catalysis and Nanoscience*. 2nd ed. 2008, Wiley.
19. Hohenberg, P., and W. Kohn, *Inhomogeneous Electron Gas*. Physical Review B, 1964. **136** (3B): p. B864.
20. Kohn, W., and L. J. Sham, *Self-Consistent Equations Including Exchange and Correlation Effects*. Physical Review, 1965. **140** (4A): p. 1133.
21. Perdew, J. P., and Y. Wang, *Accurate and Simple Analytic Representation of the Electron-Gas Correlation-Energy*. Physical Review B, 1992. **45** (23): p. 13244-13249.
22. Perdew, J. P., K. Burke, and M. Ernzerhof, *Generalized gradient approximation made simple*. Physical Review Letters, 1996. **77** (18): p. 3865-3868.
23. Hammer, B., L. B. Hansen, and J. K. Norskov, *Improved adsorption energetics within density-functional theory using revised Perdew-Burke-Ernzerhof functionals*. Physical Review B, 1999. **59** (11): p. 7413-7421.
24. Neugebauer, J., and M. Scheffler, *Adsorbate-Substrate and Adsorbate-Adsorbate Interactions of Na And K Adlayers on Al(111)*. Physical Review B, 1992. **46** (24): p. 16067-16080.
25. Makov, G., and M. C. Payne, *Periodic Boundary-Conditions in Ab-Initio Calculations*. Physical Review B, 1995. **51** (7): p. 4014-4022.
26. Kresse, G., and J. Hafner, *Ab initio molecular dynamics for liquid metals*. Physical Review B, 1993. **47** (1): p. 558-561.

27. Kresse, G., and J. Hafner, *Ab initio molecular-dynamics simulation of the liquid-metal–amorphous-semiconductor transition in germanium*. Physical Review B, 1994. **49** (20): p. 14251-14269.
28. Kresse, G., and J. Furthmüller, *Efficiency of ab-initio total energy calculations for metals and semiconductors using a plane-wave basis set*. Computational Materials Science, 1996. **6** (1): p. 15-50.
29. Kresse, G., and J. Furthmüller, *Efficient iterative schemes for ab initio total-energy calculations using a plane-wave basis set*. Physical Review B, 1996. **54** (16): p. 11169-11186.
30. Soler, J. M., E. Artacho, J. D. Gale, A. Garcia, J. Junquera, P. Ordejon, and D. Sanchez-Portal, *The SIESTA method for ab initio order-N materials simulation*. Journal of Physics-Condensed Matter, 2002. **14** (11): p. 2745-2779.
31. Sholl, D. S., and J. A. Steckel, *Density Functional Theory: A Practical Introduction*. 1st ed. 2009, Hoboken, New Jersey: John Wiley & Sons, Inc.
32. Alavi, A., P. J. Hu, T. Deutsch, P. L. Silvestrelli, and J. Hutter, *CO oxidation on Pt(111): An ab initio density functional theory study*. Physical Review Letters, 1998. **80** (16): p. 3650-3653.
33. Zhang, C. J., P. Hu, and M. H. Lee, *A density functional theory study on the interaction between chemisorbed CO and S on Rh(111)*. Surface Science, 1999. **432** (3): p. 305-315.
34. Henkelman, G., B. P. Uberuaga, and H. Jonsson, *A climbing image nudged elastic band method for finding saddle points and minimum energy paths*. Journal of Chemical Physics, 2000. **113** (22): p. 9901-9904.
35. Henkelman, G., and H. Jónsson, *A dimer method for finding saddle points on high dimensional potential surfaces using only first derivatives*. Journal of Chemical Physics, 1999. **111** (15): p. 7010-7022.
36. Olsen, R. A., G. J. Kroes, G. Henkelman, A. Arnaldsson, and H. Jónsson, *Comparison of methods for finding saddle points without knowledge of the final states*. Journal of Chemical Physics, 2004. **121** (20): p. 9776-9792.
37. Heyden, A., A. T. Bell, and F. J. Keil, *Efficient methods for finding transition states in chemical reactions: Comparison of improved dimer method and partitioned rational function optimization method*. Journal of Chemical Physics, 2005. **123** (22): p. 224101.
38. *Density of States*. Available from: https://wiki.fysik.dtu.dk/gpaw/documentation/pdos/pdos.html, accessed June 5, 2014.
39. Stuckless, J. T., N. Alsarraf, C. Wartnaby, and D. A. King, *Calorimetric Heats of Adsorption For CO on Nickel Single-Crystal Surfaces*. Journal of Chemical Physics, 1993. **99** (3): p. 2202-2212.
40. Hodgson, A., and S. Haq, *Water adsorption and the wetting of metal surfaces*. Surface Science Reports, 2009. **64** (9): p. 381-451.

41. Meng, S., E. G. Wang, and S. W. Gao, *Water adsorption on metal surfaces: A general picture from density functional theory studies*. Physical Review B, 2004. **69** (19).
42. Hammer, B., *Coverage dependence of N_2 dissociation at an N, O, or H precovered Ru(0001) surface investigated with density functional theory*. Physical Review B, 2001. **63** (20).
43. Mhadeshwar, A. B., J. R. Kitchin, M. A. Barteau, and D. G. Vlachos, *The role of adsorbate-adsorbate interactions in the rate controlling step and the most abundant reaction intermediate of NH_3 decomposition on Ru*. Catalysis Letters, 2004. **96** (1-2): p. 13-22.
44. Inoglu, N., and J. R. Kitchin, *Simple model explaining and predicting coverage-dependent atomic adsorption energies on transition metal surfaces*. Physical Review B, 2010. **82** (4).
45. Blaylock, D. W., T. Ogura, W. H. Green, and G. J. O. Beran, *Computational Investigation of Thermochemistry and Kinetics of Steam Methane Reforming on Ni(111) under Realistic Conditions*. Journal of Physical Chemistry C, 2009. **113** (12): p. 4898-4908.
46. Salciccioli, M., Y. Chen, and D. G. Vlachos, *Density Functional Theory-Derived Group Additivity and Linear Scaling Methods for Prediction of Oxygenate Stability on Metal Catalysts: Adsorption of Open-Ring Alcohol and Polyol Dehydrogenation Intermediates on Pt-Based Metals*. Journal of Physical Chemistry C, 2010. **114** (47): p. 20155-20166.
47. McQuarrie, D. A., *Statistical Mechanics*. 1976, New York: Harper and Row.
48. Mhadeshwar, A. B., H. Wang, and D. G. Vlachos, *Thermodynamic consistency in microkinetic development of surface reaction mechanisms*. Journal of Physical Chemistry B, 2003. **107** (46): p. 12721-12733.
49. Dumesic, J. A., D. F. Rudd, L. M. Aparicio, J. E. Rekoske, and A. A. Treviño, *The Microkinetics of Heterogeneous Catalysis*. 1993, Washington, DC: American Chemical Society.
50. Grabow, L. C., A. A. Gokhale, S. T. Evans, J. A. Dumesic, and M. Mavrikakis, *Mechanism of the water gas shift reaction on Pt: First principles, experiments, and microkinetic modeling*. Journal of Physical Chemistry C, 2008. **112** (12): p. 4608-4617.
51. Catapan, R. C., *Multiscale Modeling of Ethanol Steam Reforming and Water Gas Shift on Nickel*. 2012, Florianópolis: Universidade Federal de Santa Catarina, Ph.D. Dissertation.
52. Goos, E., A. Burcat, and B. Ruscic. Extended Third Millenium Ideal Gas and Condensed Phase Thermochemical Database for Combustion with Updates from Active Thermochemical Tables. 2012.
53. Frenklach, M., H. Wang, M. Goldenberg, G. P. Smith, D. M. Golden, C. T. Bowman, R. K. Hanson, W. C. Gardiner, and V. V. Lissianski, *GRI-Mech---An Optimized Detailed Chemical Reaction Mechanism for Methane Combustion*.

Available from: http://www.me.berkeley.edu/gri_mech/, accessed October 21, 2010.
54. Chen, Y., and D. G. Vlachos, *Hydrogenation of Ethylene and Dehydrogenation and Hydrogenolysis of Ethane on Pt(111) and Pt(211): A Density Functional Theory Study*. The Journal of Physical Chemistry C, 2010. **114** (11): p. 4973-4982.
55. Jiang, T., D. J. Mowbray, S. Dobrin, H. Falsig, B. Hvolbaek, T. Bligaard, and J. K. Norskov, *Trends in CO Oxidation Rates for Metal Nanoparticles and Close-Packed, Stepped, and Kinked Surfaces*. Journal of Physical Chemistry C, 2009. **113** (24): p. 10548-10553.
56. Sutton, J. E., and D. G. Vlachos, *A Theoretical and Computational Analysis of Linear Free Energy Relations for the Estimation of Activation Energies*. ACS Catalysis, 2012. **2** (8): p. 1624-1634.
57. Vojvodic, A., F. Calle-Vallejo, W. Guo, S. Wang, A. Toftelund, F. Studt, J. I. Martínez, J. Shen, I. C. Man, J. Rossmeisl, T. Bligaard, J. K. Nørskov, and F. Abild-Pedersen, *On the behavior of Brønsted-Evans-Polanyi relations for transition metal oxides*. Journal of Chemical Physics, 2011. **134** (24).
58. Krcha, M. D., A. D. Mayernick, and M. J. Janik, *Periodic trends of oxygen vacancy formation and C–H bond activation over transition metal-doped CeO_2(111) surfaces*. Journal of Catalysis, 2012. **293**: p. 103-115.
59. Salciccioli, M., and D. G. Vlachos, *Kinetic Modeling of Pt Catalyzed and Computation-Driven Catalyst Discovery for Ethylene Glycol Decomposition*. ACS Catalysis, 2011. p. 1246-1256.
60. Blaylock, D. W., Y.-A. Zhu, and W. Green, *Computational Investigation of the Thermochemistry and Kinetics of Steam Methane Reforming Over a Multi-Faceted Nickel Catalyst*. Topics in Catalysis, 2011. **54** (13-15): p. 828-844.
61. Rankovic, N., C. Chizallet, A. Nicolle, and P. Da Costa, *Multiscale Modeling of Barium Sulfate Formation from BaO*. Industrial & Engineering Chemistry Research, 2013. **52** (26): p. 9086-9098.
62. Hansgen, D. A., D. G. Vlachos, and J. G. G. Chen, *Using first principles to predict bimetallic catalysts for the ammonia decomposition reaction*. Nature Chemistry, 2010. **2** (6): p. 484-489.
63. Xu, J. G., and G. F. Froment, *Methane Steam Reforming, Methanation And Water-Gas Shift. 1. Intrinsic Kinetics*. Aiche Journal, 1989. **35** (1): p. 88-96.
64. Rabitz, H., M. Kramer, and D. Dacol, *Sensitivity Analysis in Chemical Kinetics*. Annual Review of Physical Chemistry, 1983. **34** (1): p. 419-461.
65. Campbell, C. T., *Future Directions and Industrial Perspectives Micro- and macro-kinetics: Their relationship in heterogeneous catalysis*. Topics in Catalysis, 1994. **1** (3): p. 353-366.
66. Dumesic, J. A., *Analyses of reaction schemes using De Donder relations*. Journal of Catalysis, 1999. **185** (2): p. 496-505.
67. Mhadeshwar, A. B., and D. G. Vlachos, *Is the water-gas shift reaction on Pt simple? Computer-aided microkinetic model reduction, lumped rate*

expression, and rate-determining step. Catalysis Today, 2005. **105** (1): p. 162-172.
68. Rawlings, J. B., and J. G. Ekerdt, *Chemical Reactor Analysis and Design Fundamentals*. 2nd ed. 2010, Madison, WI: Nob Hill Publishing, LLC.
69. Catapan, R. C., M. A. Christiansen, A. A. M. Oliveira, and D. G. Vlachos. "Catalytic Kinetics and Dynamics". In *Heterogeneous Catalysis at Nanoscale and Energy Applications*, Tao, F.; Schneider, W. A.; Kamat, P. V., Eds. 2014, Chichester, UK: Wiley, in press.
70. Alonso, D. M., J. Q. Bond, and J. A. Dumesic, *Catalytic conversion of biomass to biofuels*. Green Chemistry, 2010. **12** (9): p. 1493-1513.
71. Huber, G. W., J. W. Shabaker, and J. A. Dumesic, *Raney Ni-Sn Catalyst for H_2 Production from Biomass-Derived Hydrocarbons*. Science, 2003. **300** (5628): p. 2075-2077.
72. Soares, R. R., D. A. Simonetti, and J. A. Dumesic, *Glycerol as a source for fuels and chemicals by low-temperature catalytic processing*. Angewandte Chemie-International Edition, 2006. **45** (24): p. 3982-3985.
73. Kandoi, S., J. Greeley, M. Sanchez-Castillo, S. Evans, A. Gokhale, J. Dumesic, and M. Mavrikakis, *Prediction of Experimental Methanol Decomposition Rates on Platinum from First Principles*. Topics in Catalysis, 2006. **37** (1): p. 17-28.
74. Wei, J. M., and E. Iglesia, *Mechanism and site requirements for activation and chemical conversion of methane on supported Pt clusters and turnover rate comparisons among noble metals*. Journal of Physical Chemistry B, 2004. **108** (13): p. 4094-4103.
75. Cortright, R. D., R. M. Watwe, B. E. Spiewak, and J. A. Dumesic, *Kinetics of ethane hydrogenolysis over supported platinum catalysts*. Catalysis Today, 1999. **53** (3): p. 395-406.
76. Salciccioli, M., Y. Chen, and D. G. Vlachos, *Microkinetic Modeling and Reduced Rate Expressions of Ethylene Hydrogenation and Ethane Hydrogenolysis on Platinum*. Industrial & Engineering Chemistry Research, 2010. **50** (1): p. 28-40.
77. Kandoi, S., J. Greeley, D. Simonetti, J. Shabaker, J. A. Dumesic, and M. Mavrikakis, *Reaction Kinetics of Ethylene Glycol Reforming over Platinum in the Vapor versus Aqueous Phases*. Journal of Physical Chemistry C, 2011. **115** (4): p. 961-971.
78. Lin, S., R. S. Johnson, G. K. Smith, D. Xie, and H. Guo, *Pathways for methanol steam reforming involving adsorbed formaldehyde and hydroxyl intermediates on Cu(111): density functional theory studies*. Physical Chemistry Chemical Physics, 2011. **13** (20): p. 9622-9631.
79. Zope, B. N., D. D. Hibbitts, M. Neurock, and R. J. Davis, *Reactivity of the Gold/Water Interface During Selective Oxidation Catalysis*. Science, 2010. **330** (6000): p. 74-78.

80. Vlachos, D. G., A. B. Mhadeshwar, and N. S. Kaisare, *Hierarchical multiscale model-based design of experiments, catalysts, and reactors for fuel processing*. Computers & Chemical Engineering, 2006. **30** (10-12): p. 1712-1724.
81. Zum Mallen, M. P., and L. D. Schmidt, *Oxidation of Methanol over Polycrystalline Rh and Pt: Rates, OH Desorption, and Model*. Journal of Catalysis, 1996. **161** (1): p. 230-246.
82. Coltrin, M. E., R. J. Kee, and F. M. Rupley *SURFACE CHEMKIN (Version 4.0) - A Fortran Package for Analyzing Heterogeneous Chemical Kinetics at a Solid-Surface -- Gas-Phase Interface*. 1991, Sandia National Laboratories Report SAND90-8003B.
83. Stamatakis, M., Y. Chen, and D. G. Vlachos, *First-Principles-Based Kinetic Monte Carlo Simulation of the Structure Sensitivity of the Water–Gas Shift Reaction on Platinum Surfaces*. The Journal of Physical Chemistry C, 2011. **115** (50): p. 24750-24762.
84. Salciccioli, M., W. Yu, M. A. Barteau, J. G. Chen, and D. G. Vlachos, *Differentiation of O–H and C–H Bond Scission Mechanisms of Ethylene Glycol on Pt and Ni/Pt Using Theory and Isotopic Labeling Experiments*. Journal of the American Chemical Society, 2011. **133** (20): p. 7996-8004.
85. Salciccioli, M., S. M. Edie, and D. G. Vlachos, *Adsorption of Acid, Ester, and Ether Functional Groups on Pt: Fast Prediction of Thermochemical Properties of Adsorbed Oxygenates via DFT-Based Group Additivity Methods*. Journal of Physical Chemistry C, 2012. **116** (2): p. 1873-1886.
86. Troullier, N., and J. L. Martins, *Efficient pseudopotentials for plane-wave calculations. II. Operators for fast iterative diagonalization*. Physical Review B, 1991. **43** (11): p. 8861-8869.
87. Shabaker, J. W., R. R. Davda, G. W. Huber, R. D. Cortright, and J. A. Dumesic, *Aqueous-phase reforming of methanol and ethylene glycol over alumina-supported platinum catalysts*. Journal of Catalysis, 2003. **215** (2): p. 344-352.
88. Bunluesin, T., R. J. Gorte, and G. W. Graham, *Studies of the water-gas-shift reaction on ceria-supported Pt, Pd, and Rh: Implications for oxygen-storage properties*. Applied Catalysis B: Environmental, 1998. **15** (1-2): p. 107-114.
89. Kalamaras, C. M., G. G. Olympiou, and A. M. Efstathiou, *The water-gas shift reaction on Pt/gamma-Al_2O_3 Catalyst: Operando SSITKA-DRIFTS-mass spectroscopy studies*. Catalysis Today, 2008. **138** (3-4): p. 228-234.
90. Christiansen, M. A., and D. G. Vlachos, *Microkinetic modeling of Pt-catalyzed ethylene glycol steam reforming*. Applied Catalysis A: General, 2012. **431–432**: p. 18-24.
91. Ross, J., *Heterogeneous Catalysis*. 2012, Amsterdam, The Netherlands: Elsevier, p 71-75.
92. *Wiley Critical Content - Petroleum Technology*. 2007, Hoboken, NJ: John Wiley & Sons, p 502-504.

93. *Wiley Critical Content - Petroleum Technology*. 2007, Hoboken, NJ: John Wiley & Sons, p 876-886.
94. Hightower, J. W., and W. K. Hall, *Tracer studies of acid-catalyzed reactions. Part 10.-Deuterium exchange and isomerization of cyclic olefins over alumina*. Transactions of the Faraday Society, 1970. **66**: p. 477-489.
95. Knözinger, H., *Dehydration of Alcohols on Aluminum Oxide*. Angewandte Chemie International Edition in English, 1968. **7** (10): p. 791-805.
96. Guo, N., S. Caratzoulas, D. J. Doren, S. I. Sandler, and D. G. Vlachos, *A perspective on the modeling of biomass processing*. Energy & Environmental Science, 2012. **5** (5): p. 6703-6716.
97. Dabbagh, H. A., M. Zamani, and B. H. Davis, *Nanoscale surface study and reactions mechanism of 2-butanol over the γ-alumina (100) surface and nanochannel: A DFT study*. Journal of Molecular Catalysis A: Chemical, 2010. **333** (1–2): p. 54-68.
98. Kwak, J. H., D. H. Mei, C. H. F. Peden, R. Rousseau, and J. Szanyi, *(100) facets of gamma-Al_2O_3: The Active Surfaces for Alcohol Dehydration Reactions*. Catalysis Letters, 2011. **141** (5): p. 649-655.
99. Kwak, J. H., R. Rousseau, D. Mei, C. H. F. Peden, and J. Szanyi, *The Origin of Regioselectivity in 2-Butanol Dehydration on Solid Acid Catalysts*. ChemCatChem, 2011. **3** (10): p. 1557-1561.
100. Zuo, Z., W. Huang, P. Han, Z. Gao, and Z. Li, *Theoretical studies on the reaction mechanisms of AlOOH- and γ-Al_2O_3-catalysed methanol dehydration in the gas and liquid phases*. Applied Catalysis A: General, 2011. **408** (1–2): p. 130-136.
101. Roy, S., G. Mpourmpakis, D.-Y. Hong, D. G. Vlachos, A. Bhan, and R. J. Gorte, *Mechanistic Study of Alcohol Dehydration on γ-Al_2O_3*. ACS Catalysis, 2012. **2** (9): p. 1846-1853.
102. Kovarik, L., A. Genc, C. Wang, A. Qiu, C. H. F. Peden, J. Szanyi, and J. H. Kwak, *Tomography and High-Resolution Electron Microscopy Study of Surfaces and Porosity in a Plate-like γ-Al_2O_3*. The Journal of Physical Chemistry C, 2013. **117** (1): p. 179-186.
103. DeWilde, J. F., H. Chiang, D. A. Hickman, C. R. Ho, and A. Bhan, *Kinetics and Mechanism of Ethanol Dehydration on γ-Al_2O_3: The Critical Role of Dimer Inhibition*. ACS Catalysis, 2013. **3** (4): p. 798-807.
104. Liu, X., and R. E. Truitt, *DRFT-IR Studies of the Surface of γ-Alumina*. Journal of the American Chemical Society, 1997. **119** (41): p. 9856-9860.
105. Pines, H., and W. O. Haag, *Alumina: Catalyst and Support. I. Alumina, its Intrinsic Acidity and Catalytic Activity*. Journal of the American Chemical Society, 1960. **82** (10): p. 2471-2483.
106. Knözinger, H., H. Bühl, and K. Kochloefl, *The dehydration of alcohols on alumina: XIV. Reactivity and mechanism*. Journal of Catalysis, 1972. **24** (1): p. 57-68.

107. Knözinger, H., and R. Köhne, *Catalytical Dehydration of Aliphatic Alcohols on Gamma-Al_2O_3*. Journal of Catalysis, 1964. **3** (6): p. 559-560.
108. Knözinger, H., and R. Köhne, *Dehydration of Alcohols Over Alumina. 1. Reaction Scheme*. Journal of Catalysis, 1966. **5** (2): p. 264-270.
109. Knözinger, H., and A. Scheglila, *Dehydration of Alcohols on Alumina. 12. Kinetic Isotope Effects in Olefin Formation from Butanols*. Journal of Catalysis, 1970. **17** (2): p. 252-263.
110. Shi, B. C., H. A. Dabbagh, and B. H. Davis, *Catalytic dehydration of alcohols. Kinetic isotope effect for the dehydration of t-butanol*. Topics in Catalysis, 2002. **18** (3-4): p. 259-264.
111. Jain, J. R., and C. N. Pillai, *An adsorbed phase substitution-elimination mechanism for catalytic dehydration of alcohols to ethers and to olefins over alumina*. Tetrahedron Letters, 1965. **6** (11): p. 675-678.
112. Jain, J. R., and C. N. Pillai, *Catalytic Dehydration of Alcohols over Alumina: Mechanism of Ether Formation*. Journal of Catalysis, 1967. **9** (4): p. 322-330.
113. Shi, B. C., and B. H. Davis, *Alcohol dehydration: Mechanism of ether formation using an alumina catalyst*. Journal of Catalysis, 1995. **157** (2): p. 359-367.
114. Wischert, R., C. Coperet, F. Delbecq, and P. Sautet, *Dinitrogen: a selective probe for tri-coordinate Al "defect" sites on alumina*. Chemical Communications, 2011. **47** (17): p. 4890-4892.
115. Kwak, J. H., J. Z. Hu, D. H. Kim, J. Szanyi, and C. H. F. Peden, *Penta-coordinated Al^{3+} ions as preferential nucleation sites for BaO on γ-Al_2O_3: An ultra-high-magnetic field ^{27}Al MAS NMR study*. Journal of Catalysis, 2007. **251** (1): p. 189-194.
116. Perdew, J. P., J. A. Chevary, S. H. Vosko, K. A. Jackson, M. R. Pederson, D. J. Singh, and C. Fiolhais, *Atoms, molecules, solids, and surfaces: Applications of the generalized gradient approximation for exchange and correlation*. Physical Review B, 1992. **46** (11): p. 6671-6687.
117. Blöchl, P. E., *Projector augmented-wave method*. Physical Review B, 1994. **50** (24): p. 17953-17979.
118. Kresse, G., and D. Joubert, *From ultrasoft pseudopotentials to the projector augmented-wave method*. Physical Review B, 1999. **59** (3): p. 1758-1775.
119. Krokidis, X., P. Raybaud, A.-E. Gobichon, B. Rebours, P. Euzen, and H. Toulhoat, *Theoretical Study of the Dehydration Process of Boehmite to γ-Alumina*. The Journal of Physical Chemistry B, 2001. **105** (22): p. 5121-5130.
120. Digne, M., P. Sautet, P. Raybaud, P. Euzen, and H. Toulhoat, *Use of DFT to achieve a rational understanding of acid–basic properties of γ-alumina surfaces*. Journal of Catalysis, 2004. **226** (1): p. 54-68.
121. Ide, M. S., B. Hao, M. Neurock, and R. J. Davis, *Mechanistic Insights on the Hydrogenation of α,β-Unsaturated Ketones and Aldehydes to Unsaturated Alcohols over Metal Catalysts*. ACS Catalysis, 2012. **2** (4): p. 671-683.

122. Schneider, W. F., K. C. Hass, M. Miletic, and J. L. Gland, *Dramatic Cooperative Effects in Adsorption of NO_x on MgO(001)*. The Journal of Physical Chemistry B, 2002. **106** (30): p. 7405-7413.
123. Mei, D., Q. Ge, J. Szanyi, and C. H. F. Peden, *First-Principles Analysis of NO_x Adsorption on Anhydrous γ-Al_2O_3 Surfaces*. The Journal of Physical Chemistry C, 2009. **113** (18): p. 7779-7789.
124. Metiu, H., S. Chrétien, Z. Hu, B. Li, and X. Sun, *Chemistry of Lewis Acid–Base Pairs on Oxide Surfaces*. The Journal of Physical Chemistry C, 2012. **116** (19): p. 10439-10450.
125. Tang, W., E. Sanville, and G. Henkelman, *A grid-based Bader analysis algorithm without lattice bias*. Journal of Physics: Condensed Matter, 2009. **21** (8): p. 084204.
126. Wischert, R., C. Copéret, F. Delbecq, and P. Sautet, *Optimal Water Coverage on Alumina: A Key to Generate Lewis Acid–Base Pairs that are Reactive Towards the C-H Bond Activation of Methane*. Angewandte Chemie International Edition, 2011. **50** (14): p. 3202-3205.
127. Joubert, J., P. Fleurat-Lessard, F. Delbecq, and P. Sautet, *Simulating Temperature Programmed Desorption of Water on Hydrated γ-Alumina from First-Principles Calculations*. The Journal of Physical Chemistry B, 2006. **110** (14): p. 7392-7395.
128. Wischert, R., P. Laurent, C. Copéret, F. Delbecq, and P. Sautet, *γ-Alumina: The Essential and Unexpected Role of Water for the Structure, Stability, and Reactivity of "Defect" Sites*. Journal of the American Chemical Society, 2012. **134** (35): p. 14430-14449.
129. Basagiannis, A., P. Panagiotopoulou, and X. Verykios, *Low Temperature Steam Reforming of Ethanol Over Supported Noble Metal Catalysts*. Topics in Catalysis, 2008. **51** (1-4): p. 2-12.
130. Loudon, G. M., *Organic Chemistry*. Fourth ed. 2002, New York: Oxford University Press.
131. Christiansen, M. A., G. Mpourmpakis, and D. G. Vlachos, *Density Functional Theory-Computed Mechanisms of Ethylene and Diethyl Ether Formation from Ethanol on γ-Al_2O_3(100)*. ACS Catalysis, 2013. **3** (9): p. 1965-1975.
132. Bruijnincx, P. C. A., and B. M. Weckhuysen, *Shale Gas Revolution: An Opportunity for the Production of Biobased Chemicals?* Angewandte Chemie International Edition, 2013. **52** (46): p. 11980-11987.
133. Clark, J. H., *Solid acids for green chemistry*. Accounts of chemical research, 2002. **35** (9): p. 791-797.
134. Morterra, C., and G. Magnacca, *A case study: surface chemistry and surface structure of catalytic aluminas, as studied by vibrational spectroscopy of adsorbed species*. Catalysis Today, 1996. **27** (3-4): p. 497-532.
135. Digne, M., P. Sautet, P. Raybaud, P. Euzen, and H. Toulhoat, *Hydroxyl Groups on γ-Alumina Surfaces: A DFT Study*. Journal of Catalysis, 2002. **211** (1): p. 1-5.

136. Nortier, P., P. Fourre, A. B. M. Saad, O. Saur, and J. C. Lavalley, *Effects of crystallinity and morphology on the surface properties ofalumina*. Applied Catalysis, 1990. **61** (1): p. 141-160.
137. Monkhorst, H. J., and J. D. Pack, *Special Points for Brillouin-Zone Integrations*. Physical Review B, 1976. **13** (12): p. 5188-5192.
138. Henkelman, G., and H. Jónsson, *Improved tangent estimate in the nudged elastic band method for finding minimum energy paths and saddle points*. Journal of Chemical Physics, 2000. **113** (22): p. 9978-9978.
139. Kästner, J., and P. Sherwood, *Superlinearly converging dimer method for transition state search*. Journal of Chemical Physics, 2008. **128** (1): p. 14106-14106.
140. Grimme, S., J. Antony, S. Ehrlich, and H. Krieg, *A consistent and accurate ab initio parametrization of density functional dispersion correction (DFT-D) for the 94 elements H-Pu*. Journal of Chemical Physics, 2010. **132** (15).
141. Hinnemann, B., and E. A. Carter, *Adsorption of Al, O, Hf, Y, Pt, and S atoms on alpha-Al_2O_3(0001)*. Journal of Physical Chemistry C, 2007. **111** (19): p. 7105-7126.
142. Deka, R. C., R. Kinkar Roy, and K. Hirao, *Local reactivity descriptors to predict the strength of Lewis acid sites in alkali cation-exchanged zeolites*. Chemical Physics Letters, 2004. **389** (1-3): p. 186-190.
143. Benson, S. W., and J. H. Buss, *Additivity Rules for the Estimation of Molecular Properties. Thermodynamic Properties*. Journal of Chemical Physics, 1958. **29** (3): p. 546-546.
144. ChemAxon, *Marvin 5.12.1*. 2013, http://www.chemaxon.com.
145. Hoffmann, R., *Solids and Surfaces: A chemist's view of bonding in extended structures*. 1988, New York, N. Y.: VCH Publishers, Inc.
146. Wang, S., V. Petzold, V. Tripkovic, J. Kleis, J. G. Howalt, E. Skúlason, E. M. Fernández, B. Hvolbæk, G. Jones, a. Toftelund, H. Falsig, M. Björketun, F. Studt, F. Abild-Pedersen, J. Rossmeisl, J. K. Nørskov, and T. Bligaard, *Universal transition state scaling relations for (de)hydrogenation over transition metals*. Physical Chemistry Chemical Physics, 2011. **13** (46): p. 20760-20765.
147. Wang, S., V. Vorotnikov, J. E. Sutton, and D. G. Vlachos, *Brønsted–Evans–Polanyi and Transition State Scaling Relations of Furan Derivatives on Pd(111) and Their Relation to Those of Small Molecules*. ACS Catalysis, 2014. **4** (2): p. 604-612.
148. Shustorovich, E., and H. Sellers, *The UBI-QEP method: a practical theoretical approach to understanding chemistry on transition metal surfaces*. Surface Science Reports, 1998. **31** (1-3): p. 5-119.
149. Jenness, G. R., M. A. Christiansen, S. Caratzoulas, D. G. Vlachos, and R. J. Gorte, *Site-Dependent Lewis Acidity of γ-Al_2O_3 and its Impact on Ethanol Dehydration and Etherification*. The Journal of Physical Chemistry C, 2014. **118** (24): p. 12899-12907.

150. Shimizu, K., and A. Satsuma, *Toward a rational control of solid acid catalysis for green synthesis and biomass conversion*. Energy & Environmental Science, 2011. **4** (9): p. 3140-3153.
151. Taarning, E., C. M. Osmundsen, X. Yang, B. Voss, S. I. Andersen, and C. H. Christensen, *Zeolite-catalyzed biomass conversion to fuels and chemicals*. Energy & Environmental Science, 2011. **4** (3): p. 793-804.
152. Rozita, Y., R. Brydson, T. P. Comyn, A. J. Scott, C. Hammond, A. Brown, S. Chauruka, A. Hassanpour, N. P. Young, A. I. Kirkland, H. Sawada, and R. I. Smith, *A Study of Commercial Nanoparticulate γ-Al_2O_3 Catalyst Supports*. ChemCatChem, 2013. **5** (9): p. 2695-2706.
153. Aranifard, S., S. C. Ammal, and A. Heyden, *On the importance of metal-oxide interface sites for the water-gas shift reaction over Pt/CeO_2 catalysts*. Journal of Catalysis, 2014. **309**: p. 314-324.
154. Piskorz, W., F. Zasada, P. Stelmachowski, A. Kotarba, and Z. Sojka, *DFT Modeling of Reaction Mechanism and Ab Initio Microkinetics of Catalytic N_2O Decomposition over Alkaline Earth Oxides: From Molecular Orbital Picture Account to Simulation of Transient and Stationary Rate Profiles*. Journal of Physical Chemistry C, 2013. **117** (36): p. 18488-18501.
155. Pinto, H. P., R. M. Nieminen, and S. D. Elliott, *Ab initio study of γ-Al_2O_3 surfaces*. Physical Review B, 2004. **70** (12): p. 125402.
156. *MATLAB and Statistics Toolbox Release 2009a*, The MathWorks, Inc.: Natick, Massachusetts, United States.
157. Li, G., N. Li, Z. Wang, C. Li, A. Wang, X. Wang, Y. Cong, and T. Zhang, *Synthesis of High-Quality Diesel with Furfural and 2-Methylfuran from Hemicellulose*. Chemsuschem, 2012. **5** (10): p. 1958-1966.
158. Sun, J., A. M. Karim, H. Zhang, L. Kovarik, X. S. Li, A. J. Hensley, J.-S. McEwen, and Y. Wang, *Carbon-supported bimetallic Pd–Fe catalysts for vapor-phase hydrodeoxygenation of guaiacol*. Journal of Catalysis, 2013. **306**: p. 47-57.
159. Jones, G., J. G. Jakobsen, S. S. Shim, J. Kleis, M. P. Andersson, J. Rossmeisl, F. Abild-Pedersen, T. Bligaard, S. Helveg, B. Hinnemann, J. R. Rostrup-Nielsen, I. Chorkendorff, J. Sehested, and J. K. Nørskov, *First principles calculations and experimental insight into methane steam reforming over transition metal catalysts*. Journal of Catalysis, 2008. **259** (1): p. 147-160.
160. Abild-Pedersen, F., J. Greeley, F. Studt, J. Rossmeisl, T. R. Munter, P. G. Moses, E. Skúlason, T. Bligaard, and J. K. Nørskov, *Scaling Properties of Adsorption Energies for Hydrogen-Containing Molecules on Transition-Metal Surfaces*. Physical Review Letters, 2007. **99** (1).
161. Fernández, E. M., P. G. Moses, A. Toftelund, H. A. Hansen, J. I. Martínez, F. Abild-Pedersen, J. Kleis, B. Hinnemann, J. Rossmeisl, T. Bligaard, and J. K. Nørskov, *Scaling Relationships for Adsorption Energies on Transition Metal Oxide, Sulfide, and Nitride Surfaces*. Angewandte Chemie International Edition, 2008. **47** (25): p. 4683-4686.

162. Wirth, J., and P. Saalfrank, *The Chemistry of Water on α-Alumina: Kinetics and Nuclear Quantum Effects from First Principles*. The Journal of Physical Chemistry C, 2012. **116** (51): p. 26829-26840.
163. Stamatakis, M., and D. G. Vlachos, *Unraveling the Complexity of Catalytic Reactions via Kinetic Monte Carlo Simulation: Current Status and Frontiers*. ACS Catalysis, 2012. **2** (12): p. 2648-2663.

Appendix A

THERMOCHEMICAL AND KINETIC INFORMATION FOR THE CREATION, PERFORMANCE ASSESSMENT, AND ANALYSIS OF THE $C_2H_6O_2$ STEAM REFORMING MICROKINETIC MODEL

A.1 Formatted thermochemical data for the microkinetic model

The thermochemical properties of each stable species and transition state considered in the model are available as a formatted THERMDAT file at the following Internet address:

http://dx.doi.org/10.1016/j.apcata.2012.04.010

More information about the THERMDAT format is available in [82].

A.2 Elementary steps of the microkinetic model

Table A.1: Summary of elementary steps included in the microkinetic model of ethylene glycol steam reforming on Pt.

Elementary Steps
Adsorption/Desorption[a]
$CO + * \rightleftharpoons CO*$
$H_2 + 2* \rightleftharpoons 2H*$
$CH_3OH + * \rightleftharpoons CH_3OH*$
$CH_2O + 2* \rightleftharpoons CH_2O**$
$C_2H_6O_2 + 2* \rightleftharpoons C_2H_6O_2**$
$HOCH_2CHO + 3* \rightleftharpoons HOCH_2CHO***$
$HOCHCHOH + 2* \rightleftharpoons HOCHCHOH**$
$OCHCHO + 2* \rightleftharpoons OCHCHO**$

Table A.1 continued.

$H_2O + * \rightleftharpoons H_2O*$[b]
$CO_2 + * \rightleftharpoons CO_2*$[b]
CH_xO Thermal O-H and C-H Scission[c]
$CH_3O* + H* \rightleftharpoons CH_3OH* + *$
$CH_3O* + 2* \rightleftharpoons CH_2O** + H*$
$CH_2O** \rightleftharpoons HCO* + H*$
$HCO* + * \rightleftharpoons CO* + H*$
$CH_3OH* + * \rightleftharpoons CH_2OH* + H*$
$CH_2OH* + * \rightleftharpoons CHOH* + H*$
$CHOH* + * \rightleftharpoons COH* + H*$
$COH* + * \rightleftharpoons CO* + H*$
$CHOH* + 2* \rightleftharpoons CO* + 2H*$
$CH_2O** + H* \rightleftharpoons CH_2OH* + 2*$
$C_2H_xO_2$ Thermal C-H Scission[a]
$C_2H_6O_2** + * \rightleftharpoons HOCH_2CHOH** + H*$
$HOCH_2CHOH** + * \rightleftharpoons HOCH_2COH** + H*$
$HOCH_2CHOH** + * \rightleftharpoons HOCHCHOH** + H*$
$HOCH_2CH_2O** + 2* \rightleftharpoons HOCH_2CHO*** + H*$
$HOCH_2CH_2O** + * \rightleftharpoons HOCHCH_2O** + H*$
$HOCH_2COH** + * \rightleftharpoons HOCHCOH** + H*$
$HOCHCHOH** + * \rightleftharpoons HOCHCOH** + H*$
$HOCH_2CHO*** \rightleftharpoons HOCH_2CO** + H*$
$HOCH_2CHO*** + * \rightleftharpoons HOCHCHO*** + H*$
$HOCHCH_2O** + * \rightleftharpoons HOCCH_2O** + H*$
$HOCHCH_2O** + 2* \rightleftharpoons HOCHCHO*** + H*$
$OCH_2CH_2O** + 2* \rightleftharpoons OCHCH_2O*** + H*$
$HOCHCOH** + * \rightleftharpoons HOCCOH** + H*$
$HOCH_2CO** + * \rightleftharpoons HOCHCO** + H*$
$HOCCH_2O** + * \rightleftharpoons HOCCHO** + H*$
$HOCHCHO*** \rightleftharpoons HOCHCO** + H*$
$HOCHCHO*** \rightleftharpoons HOCCHO** + H*$
$OCHCH_2O*** \rightleftharpoons OCCH_2O** + H*$
$OCHCH_2O*** \rightleftharpoons OCHCHO** + H*$
$HOCHCO** + * \rightleftharpoons HOCCO** + H*$
$HOCCHO** + * \rightleftharpoons HOCCO** + H*$
$OCCH_2O** + 2* \rightleftharpoons OCCHO*** + H*$

Table A.1 continued.

$OCHCHO^{**} + 2^* \rightleftharpoons OCCHO^{***} + H^*$
$OCCHO^{***} \rightleftharpoons OCCO^{**} + H^*$
$C_2H_xO_2$ Thermal O-H Scission[a]
$C_2H_6O_2^{**} + ^* \rightleftharpoons HOCH_2CH_2O^{**} + H^*$
$HOCH_2CHOH^{**} + 2^* \rightleftharpoons HOCH_2CHO^{***} + H^*$
$HOCH_2CHOH^{**} + ^* \rightleftharpoons HOCHCH_2O^{**} + H^*$
$HOCH_2CH_2O^{**} + ^* \rightleftharpoons OCH_2CH_2O^{**} + H^*$
$HOCH_2COH^{**} + ^* \rightleftharpoons HOCH_2CO^{**} + H^*$
$HOCH_2COH^{**} + ^* \rightleftharpoons HOCCH_2O^{**} + H^*$
$HOCHCHOH^{**} + 2^* \rightleftharpoons HOCHCHO^{***} + H^*$
$HOCH_2CHO^{***} + ^* \rightleftharpoons OCHCH_2O^{***} + H^*$
$HOCHCH_2O^{**} + 2^* \rightleftharpoons OCHCH_2O^{***} + H^*$
$HOCHCOH^{**} + ^* \rightleftharpoons HOCHCO^{**} + H^*$
$HOCHCOH^{**} + ^* \rightleftharpoons HOCCHO^{**} + H^*$
$HOCH_2CO^{**} + ^* \rightleftharpoons OCCH_2O^{**} + H^*$
$HOCCH_2O^{**} + ^* \rightleftharpoons OCCH_2O^{**} + H^*$
$HOCHCHO^{***} \rightleftharpoons OCHCHO^{**} + H^*$
$HOCCOH^{**} + ^* \rightleftharpoons HOCCO^{**} + H^*$
$HOCHCO^{**} + 2^* \rightleftharpoons OCCHO^{***} + H^*$
$HOCCHO^{**} + 2^* \rightleftharpoons OCCHO^{***} + H^*$
$HOCCO^{**} + ^* \rightleftharpoons OCCO^{**} + H^*$
$C_2H_xO_2$ Thermal C-C Scission[a]
$C_2H_6O_2^{**} \rightleftharpoons 2CH_2OH^*$
$HOCH_2CHOH^{**} \rightleftharpoons CH_2OH^* + CHOH^*$
$HOCH_2CH_2O^{**} + ^* \rightleftharpoons CH_2OH^* + CH_2O^{**}$
$HOCH_2COH^{**} \rightleftharpoons CH_2OH^* + COH^*$
$HOCHCHOH^{**} \rightleftharpoons 2CHOH^*$
$HOCH_2CHO^{***} \rightleftharpoons CH_2OH^* + HCO^* + ^*$
$HOCHCH_2O^{**} + ^* \rightleftharpoons CHOH^* + CH_2O^{**}$
$OCH_2CH_2O^{**} + 2^* \rightleftharpoons 2CH_2O^{**}$
$HOCHCOH^{**} \rightleftharpoons CHOH^* + COH^*$
$HOCH_2CO^{**} \rightleftharpoons CH_2OH^* + CO^*$
$HOCCH_2O^{**} + ^* \rightleftharpoons COH^* + CH_2O^{**}$
$HOCHCHO^{***} \rightleftharpoons CHOH^* + HCO^* + ^*$
$OCHCH_2O^{***} \rightleftharpoons CH_2O^{**} + HCO^*$
$HOCCOH^{**} \rightleftharpoons 2COH^*$

Table A.1 continued.

$HOCHCO^{**} \rightleftharpoons CHOH^{*} + CO^{*}$
$HOCCHO^{**} \rightleftharpoons HCO^{*} + COH^{*}$
$OCCH_2O^{**} + * \rightleftharpoons CH_2O^{**} + CO^{*}$
$OCHCHO^{**} \rightleftharpoons 2HCO^{*}$
$HOCCO^{**} \rightleftharpoons CO^{*} + COH^{*}$
$OCCHO^{***} \rightleftharpoons HCO^{*} + CO^{*} + *$
$OCCO^{**} \rightleftharpoons 2CO^{*}$
$C_2H_xO_2$ OH-Mediated C-H Scission*[d]
$C_2H_6O_2^{**} + OH^{*} \rightleftharpoons HOCH_2CHOH^{**} + H_2O^{*}$
$HOCH_2CHOH^{**} + OH^{*} \rightleftharpoons HOCH_2COH^{**} + H_2O^{*}$
$HOCH_2CHOH^{**} + OH^{*} \rightleftharpoons HOCHCHOH^{**} + H_2O^{*}$
$HOCH_2CH_2O^{**} + OH^{*} + * \rightleftharpoons HOCH_2CHO^{***} + H_2O^{*}$
$HOCH_2CH_2O^{**} + OH^{*} \rightleftharpoons HOCHCH_2O^{**} + H_2O^{*}$
$HOCH_2COH^{**} + OH^{*} \rightleftharpoons HOCHCOH^{**} + H_2O^{*}$
$HOCHCHOH^{**} + OH^{*} \rightleftharpoons HOCHCOH^{**} + H_2O^{*}$
$HOCH_2CHO^{***} + OH^{*} \rightleftharpoons HOCH_2CO^{**} + H_2O^{*} + *$
$HOCH_2CHO^{***} + OH^{*} \rightleftharpoons HOCHCHO^{***} + H_2O^{*}$
$HOCHCH_2O^{**} + OH^{*} \rightleftharpoons HOCCH_2O^{**} + H_2O^{*}$
$HOCHCH_2O^{**} + OH^{*} + * \rightleftharpoons HOCHCHO^{***} + H_2O^{*}$
$OCH_2CH_2O^{**} + OH^{*} + * \rightleftharpoons OCHCH_2O^{***} + H_2O^{*}$
$HOCHCOH^{**} + OH^{*} \rightleftharpoons HOCCOH^{**} + H_2O^{*}$
$HOCH_2CO^{**} + OH^{*} \rightleftharpoons HOCHCO^{**} + H_2O^{*}$
$HOCCH_2O^{**} + OH^{*} \rightleftharpoons HOCCHO^{**} + H_2O^{*}$
$HOCHCHO^{***} + OH^{*} \rightleftharpoons HOCHCO^{**} + H_2O^{*} + *$
$HOCHCHO^{***} + OH^{*} \rightleftharpoons HOCCHO^{**} + H_2O^{*} + *$
$OCHCH_2O^{***} + OH^{*} \rightleftharpoons OCCH_2O^{**} + H_2O^{*} + *$
$OCHCH_2O^{***} + OH^{*} \rightleftharpoons OCHCHO^{**} + H_2O^{*} + *$
$HOCHCO^{**} + OH^{*} \rightleftharpoons HOCCO^{**} + H_2O^{*}$
$HOCCHO^{**} + OH^{*} \rightleftharpoons HOCCO^{**} + H_2O^{*}$
$OCCH_2O^{**} + OH^{*} + * \rightleftharpoons OCCHO^{***} + H_2O^{*}$
$OCHCHO^{**} + OH^{*} + * \rightleftharpoons OCCHO^{***} + H_2O^{*}$
$OCCHO^{***} + OH^{*} \rightleftharpoons OCCO^{**} + H_2O^{*} + *$
$C_2H_xO_2$ OH-Mediated O-H Scission*[d]
$C_2H_6O_2^{**} + OH^{*} \rightleftharpoons HOCH_2CH_2O^{**} + H_2O^{*}$
$HOCH_2CHOH^{**} + OH^{*} + * \rightleftharpoons HOCH_2CHO^{***} + H_2O^{*}$
$HOCH_2CHOH^{**} + OH^{*} \rightleftharpoons HOCHCH_2O^{**} + H_2O^{*}$

Table A.1 continued.

$HOCH_2CH_2O^{**} + OH^* \rightleftharpoons OCH_2CH_2O^{**} + H_2O^*$
$HOCH_2COH^{**} + OH^* \rightleftharpoons HOCH_2CO^{**} + H_2O^*$
$HOCH_2COH^{**} + OH^* \rightleftharpoons HOCCH_2O^{**} + H_2O^*$
$HOCHCHOH^{**} + OH^* + * \rightleftharpoons HOCHCHO^{***} + H_2O^*$
$HOCH_2CHO^{***} + OH^* \rightleftharpoons OCHCH_2O^{***} + H_2O^*$
$HOCHCH_2O^{**} + OH^* + * \rightleftharpoons OCHCH_2O^{***} + H_2O^*$
$HOCHCOH^{**} + OH^* \rightleftharpoons HOCHCO^{**} + H_2O^*$
$HOCHCOH^{**} + OH^* \rightleftharpoons HOCCHO^{**} + H_2O^*$
$HOCH_2CO^{**} + OH^* \rightleftharpoons OCCH_2O^{**} + H_2O^*$
$HOCCH_2O^{**} + OH^* \rightleftharpoons OCCH_2O^{**} + H_2O^*$
$HOCHCHO^{***} + OH^* \rightleftharpoons OCHCHO^{**} + H_2O^* + *$
$HOCCOH^{**} + OH^* \rightleftharpoons HOCCO^{**} + H_2O^*$
$HOCHCO^{**} + OH^* + * \rightleftharpoons OCCHO^{***} + H_2O^*$
$HOCCHO^{**} + OH^* + * \rightleftharpoons OCCHO^{***} + H_2O^*$
$HOCCO^{**} + OH^* \rightleftharpoons OCCO^{**} + H_2O^*$

Water Gas Shift[e]

$H_2O^* + * \rightleftharpoons OH^* + H^*$
$OH^* + * \rightleftharpoons O^* + H^*$
$2OH^* \rightleftharpoons H_2O^* + O^*$
$CO^* + O^* \rightleftharpoons CO_2^* + *$
$CO^* + OH^* \rightleftharpoons COOH^* + *$
$HCO^* + O^* \rightleftharpoons HCOO^{**}$
$COOH^* + * \rightleftharpoons CO_2^* + H^*$
$COOH^* + O^* \rightleftharpoons CO_2^* + OH^*$
$COOH^* + OH^* \rightleftharpoons CO_2^* + H_2O^*$[f]
$HCOO^{**} \rightleftharpoons CO_2^* + H^*$
$HCOO^{**} + O^* \rightleftharpoons CO_2^* + OH^* + *$
$HCOO^{**} + OH^* \rightleftharpoons CO_2^* + H_2O^* + *$

CH_xO OH-Mediated O-H & C-H Scission*[d]

$CH_3O^* + OH^* + * \rightleftharpoons CH_2O^{**} + H_2O^*$
$CH_2O^{**} + OH^* \rightleftharpoons HCO^* + H_2O^* + *$
$HCO^* + OH^* \rightleftharpoons CO^* + H_2O^*$
$CH_3OH^* + OH^* \rightleftharpoons CH_2OH^* + H_2O^*$
$CH_2OH^* + OH^* \rightleftharpoons CHOH^* + H_2O^*$
$CHOH^* + OH^* \rightleftharpoons COH^* + H_2O^*$
$CH_3OH^* + OH^* \rightleftharpoons CH_3O^* + H_2O^*$

Table A.1 continued.

$CH_2OH^* + OH^* + * \rightleftharpoons CH_2O^{**} + H_2O^*$
$CHOH^* + OH^* \rightleftharpoons HCO^* + H_2O^*$
$COH^* + OH^* \rightleftharpoons CO^* + H_2O^*$

[a] Kinetic parameter source: Salciccioli et al. [59], unless otherwise noted. [b] A rate constant was assumed based on collision theory, with a value of 0.5 for the sticking coefficient. [c] Kinetic parameter source: Kandoi et al. [73] [d] Kinetic parameter source: BEPs (see Table 3.1). [e] Kinetic parameter source: Stamatakis et al. [83] [f] Vibrational frequencies for the transition state could not be obtained, and so in this work the values of the transition state frequencies for this reaction are assumed to be the same as for the transition state of $COOH^* + O^* \rightleftharpoons CO_2^* + OH^*$; this is a reasonable assumption because the frequencies of the non-reacting H atom in OH* will be similar in the transition state and the initial state, effectively canceling one another.

A.3 Comparison of thermal and OH-mediated pathways in the microkinetic model

Table A.2: Comparison of rate constants and rates for thermal and OH-mediated pathways in ethylene glycol steam reforming.

Reaction	DFT E_a [kcal mol^{-1}]	k(483 K)[a] [s^{-1}]	Rate Expression[b]	Ratio of Rates (Thermal: OH-med.)
$C_2H_6O_2$** + * ⇌ $HOCH_2CH_2O$** + H*	13.1[c]	1.1×10^{7}	k Θ_* Θ_{EG}	1.1×10^{3}
$C_2H_6O_2$** + OH* ⇌ $HOCH_2CH_2O$** + H_2O*	0[d]	1.0×10^{13}	k Θ_{OH} Θ_{EG}	
$C_2H_6O_2$** + * ⇌ $HOCH_2CHOH$** + H*	18.2[c]	5.6×10^{4}	k Θ_* Θ_{EG}	1.9×10^{8}
$C_2H_6O_2$** + OH* ⇌ $HOCH_2CHOH$** + H_2O*	16.6	3.0×10^{5}	k Θ_{OH} Θ_{EG}	
$HOCH_2CH_2O$** + * ⇌ $HOCH_2CHO$** + H*	9.5[c]	5.0×10^{10}	k Θ_* Θ_{C2H5O2}	1.9×10^{8}
$HOCH_2CH_2O$** + OH* ⇌ $HOCH_2CHO$** + H_2O*	3.5	2.7×10^{11}	k Θ_{OH} Θ_{C2H5O2}	

[a] A value of 10^{13} for the pre-exponential factor was assumed. [b] Rate calculations assume model-predicted values of Θ_* (0.1) and Θ_{OH} (10^{-10}). [c] Obtained from [84]. [d] Value was assumed to be zero; see Table 3.2.

A.4 Explanation of formula for estimating experimental CO production rates

Model rates were directly compared to the experiments. However experimental CO rates were not reported alongside H_2 and CO_2 rates [77], and so they were estimated to permit comparison. The stoichiometry for ethylene glycol thermal decomposition and water gas shift are as follows:

$$C_2H_6O_2 \rightleftharpoons 2CO + 3H_2 \qquad \text{Equation A.1}$$

$$CO + H_2O \rightleftharpoons CO_2 + H_2 \qquad \text{Equation A.2}$$

Let r_{H2}, r_{CO}, and r_{CO2} denote the experimentally reported rates of H_2, CO, and CO_2 production, respectively. Also, let r_1 denote the net rate of Equation A.1 and r_2 denote the net rate of Equation A.2. Applying the stoichiometry of Equation A.1 and Equation A.2, we obtain:

$$r_{H_2} = 3r_1 + r_2 \qquad \text{Equation A.3}$$

$$r_{CO} = 2r_1 - r_2 \qquad \text{Equation A.4}$$

$$r_{CO_2} = r_2 \qquad \text{Equation A.5}$$

After performing some algebra to put Equation A.3 in terms of r_{CO} and r_{CO2}, and after solving Equation A.3 for r_{CO}, the experimental CO production rate was calculated according to the following equation:

$$r_{CO} = \frac{2}{3}\left(r_{H_2} - \frac{5}{2}r_{CO_2}\right) \qquad \text{Equation A.6}$$

Appendix B

ADDITIONAL ENERGETIC AND STRUCTURAL INFORMATION AND ANALYSIS FOR DFT CALCULATIONS PERFORMED ON THE γ-Al_2O_3(100) SURFACE FACET

B.1 Analysis of the origin of adsorbate stabilization upon co-adsorption

Table B.1: Illustration of the energetic stabilization arising from co-adsorption of Lewis acid-base pairs on γ-Al_2O_3(100). Co-adsorbed calculations are performed with adsorbates spatially separated to eliminate intermolecular effects, such as hydrogen bonding. OH^{Va} and $CH_3CH_2O^{Va}$ radicals are adsorbed on the Al V_a site, and H^O radicals on the O1 site (see Figures 4.1 and B.1 for explanations of site identifiers). All calculations utilize spin polarization. The reference states for the reported adsorption energies are the energies of the isolated species in the gas phase. For the cases involving two adsorbates, the reference state is the sum of the energies of the isolated gas-phase species.

Adsorbate	Adsorption Energy [kcal/mol]		
	Separate Slabs (1)	Co-adsorbed (2)	(2) – (1)
H^O	-13	-	-
OH^{Va}	-43	-	-
$CH_3CH_2O^{Va}$	-28	-	-
$OH^{Va} + H^O$	-56	-140 (-65)[a]	-84 (-9)[a]
$CH_3CH_2O^{Va} + H^O$	-41	-118 (-46)[a]	-77 (-5)[a]

[a] Values without parentheses are for the singlet case, values with parentheses are for the triplet case.

Table B.2: Bader charges for isolated and co-adsorbed species on γ-Al_2O_3(100). OH^{Va} is adsorbed on the Al V_a site, and H^O on the O1 site (see Figures 4.1 and B.1 for explanations of site identifiers). Bader charges are in electrons (negative value denotes increased electron density relative to valence number).

System	Adsorbate	Bader Charge
H^O	H^O	0.62
OH^{Va}	OH^{Va}	-0.63
$OH^{Va} + H^O$ (triplet)	H^O	0.64
	OH^{Va}	-0.75
$OH^{Va} + H^O$ (singlet)	H^O	0.64
	OH^{Va}	-0.82

B.2 Energetic and structural information for adsorption and reaction of ethanol and related intermediates on γ-Al_2O_3(100)

Table B.3: Energy of adsorption of ethanol on O sites of the γ-Al_2O_3(100) surface. Refer to Figure B.1 for site identification.

Adsorbate	ΔE_{ads} [kcal/mole]					
	O1	O2	O3	O4	O5	O6
CH_3CH_2OH	-5.1	-2.5	-4.4	-4.4	-3.9	-2.5

Table B.4: Elementary steps of the ethanol reaction network and the associated reaction energies and (forward) activation barriers. "(phys)" denotes a species physisorbed to another surface species via hydrogen bonding.

Figure Index[a]	Reaction	ΔE_{rxn} [kcal/mol]	$E_{a,f}$ [kcal/mol]
-	$H_2O^{Va} + {}^{O} \rightleftharpoons OH^{Va} + H^O$	-8	0[b]
-	$H_2O^{Vb} + {}^{O} \rightleftharpoons OH^{Vb} + H^O$	2	0[b]

Table B.4 continued.

-	$H_2O^{Vc} + {}^{O} \rightleftharpoons OH^{Vc} + H^{O}$	4	-
-	$H_2O^{Vd} + {}^{O} \rightleftharpoons OH^{Vd} + H^{O}$	2	-
-	$CH_3CH_2OH^{Va} + {}^{O} \rightleftharpoons CH_3CH_2O^{Va} + H^{O}$	-3	0[b]
-	$CH_3CH_2OH^{Vb} + {}^{O} \rightleftharpoons CH_3CH_2O^{Vb} + H^{O}$	2	0[b]
-	$CH_3CH_2OH^{Vc} + {}^{O} \rightleftharpoons CH_3CH_2O^{Vc} + H^{O}$	1	-
-	$CH_3CH_2OH^{Vd} + {}^{O} \rightleftharpoons CH_3CH_2O^{Vd} + H^{O}$	3	-
B.2(a)	$CH_3CH_2OH^{Va} + {}^{O} \rightleftharpoons CH_3CH_2{}^{O} + OH^{Va}$	13	52
B.2(b)	$CH_3CH_2{}^{O} + OH^{Va} + {}^{O'} \rightleftharpoons C_2H_4 + OH^{Va} + H^{O'} + {}^{O}$	-2[c]	36
-	$CH_3CH_2OH^{Va} + {}^{Vc} + {}^{O} \rightleftharpoons CH_3CHOH^{Va\text{-}Vc} + H^{O}$	28	-
4.6(f)	$CH_3CH_2O^{Va} + H^{O} + {}^{Vc} + {}^{O} \rightleftharpoons CH_3CHO^{Va\text{-}Vc} + 2H^{O}$	24	45
B.2(c)	$CH_3CH_2OH^{Va} + {}^{Vc} + {}^{O} \rightleftharpoons CH_2CH_2OH^{Va\text{-}Vc} + H^{O}$	26	46
B.2(d)	$CH_2CH_2OH^{Va\text{-}Vc} + H^{O} \rightleftharpoons C_2H_4 + OH^{Va} + H^{O} + {}^{Vc}$	-15	8
4.6(c)	$CH_3CH_2OH^{Va} + {}^{O} \rightleftharpoons C_2H_4 + OH^{Va} + H^{O}$	11	37
-	$CH_3CH_2OH^{Vb} + {}^{O} \rightleftharpoons C_2H_4 + OH^{Vb} + H^{O}$	16	36
B.2(e)	$CH_3CH_2OH^{Vb} + H_2O^{Va} + {}^{O} \rightleftharpoons C_2H_4 + OH^{Vb} + H^{O} + H_2O^{Va}$	11	33
4.6(a)	$CH_3CH_2O^{Va} + H^{O} \rightleftharpoons C_2H_4 + OH^{Va} + H^{O}$	12	57
4.6(b)	$CH_3CH_2OH^{Va} \rightleftharpoons C_2H_4 + H_2O^{Va}$	11	52
4.6(d)	$CH_3CH_2OH^{Va} + OH^{Vb} + H^{O} \rightleftharpoons C_2H_4 + H_2O^{Vb} + OH^{Va} + H^{O}$	22	37
4.6(e)	$CH_3CH_2OH^{(phys)} + OH^{Va} + H^{O} + {}^{O} \rightleftharpoons C_2H_4 + H_2O^{O} + OH^{Va} + H^{O}$	22	50
4.6(a)	$CH_3CH_2OCH_2CH_3{}^{Va} + {}^{O} \rightleftharpoons C_2H_4 + CH_3CH_2O^{Va} + H^{O}$	10	38
4.6(b)	$CH_3CH_2OCH_2CH_3{}^{Va} \rightleftharpoons C_2H_4 + CH_3CH_2OH^{Va}$	10	52
4.8(a)	$CH_3CH_2O^{Va} + H^{O} + CH_3CH_2OH^{Vb} \rightleftharpoons CH_3CH_2OCH_2CH_3{}^{Va} + OH^{Vb} + H^{O}$	6	35

Table B.4 continued.

-	$CH_3CH_2O^{Vb} + H^O + CH_3CH_2OH^{Va} \rightleftharpoons CH_3CH_2OCH_2CH_3{}^{Vb} + OH^{Va} + H^O$	3	31
B.2(f)	$CH_3CH_2O^{Vb} + H^O + CH_3CH_2OH^{Va} \rightleftharpoons CH_3CH_2OCH_2CH_3{}^{Vb} + OH^{Va} + H^O$ (frontside attack)	3	55
4.8(b)	$CH_3CH_2O^{Va} + H^O + CH_3CH_2OH^{Vc} \rightleftharpoons CH_3CH_2OCH_2CH_3{}^{Va} + OH^{Vc} + H^O$	15	46
B.2(h)	$CH_3CH_2O^{Va} + H^O + CH_3CH_2OH^{Vb} + {}^{O'} \rightleftharpoons CH_3CH_2O^{Va} + H^O + OH^{Vb} + CH_3CH_2{}^{O'}$	41	66
B.2(i)	$CH_3CH_2O^{Va} + H^O + OH^{Vb} + CH_3CH_2{}^{O'} \rightleftharpoons CH_3CH_2OCH_2CH_3{}^{Va} + OH^{Vb} + H^O + {}^{O'}$	-35[c]	26
4.8(c)	$CH_3CH_2OH^{Va} + CH_3CH_2OH^O \rightleftharpoons OH^{Va} + H^O + CH_3CH_2OCH_2CH_3$	-1	27
B.2(g)	$CH_3CH_2O^{Va} + H^O + CH_3CH_2OH^{Vb} + H_2O^{Vc} \rightleftharpoons CH_3CH_2OCH_2CH_3{}^{Va} + OH^{Vb} + H^O + H_2O^{Vc}$	1	27
4.8(d)	$CH_3CH_2OH^{(phys)} + OH^{Va} + H^O + CH_3CH_2O^{Vb} + H^{O'} \rightleftharpoons CH_3CH_2OCH_2CH_3{}^{Vb} + H_2O^{Va} + OH^{Va} + H^{O'}$	5	30
-	$CH_3CH_2O^{Vb} + CH_2CH_2OH^{Va\text{-}Vc} + 2H^O \rightleftharpoons CH_3CH_2OCH_2CH_2OH^{Va\text{-}Vc} + 2H^O + {}^{Vb}$	95	-
-	$CH_3CH_2OH^{Va} + CH_3CH_2O^{Vb} + H^O + {}^{Vc} \rightleftharpoons CH_3CHOH^{Va\text{-}Vc} + CH_3CH_2O^{Vb} + 2H^O$	29	-
-	$CH_3CHOH^{Va\text{-}Vc} + CH_3CH_2O^{Vb} + 2H^O \rightleftharpoons CH_3CH_2OCH(CH_3)OH^{Va\text{-}Vc} + 2H^O + {}^{Vb}$	73	-

[a] Location of the figure displaying the structure of the transition state.
[b] A transition state was not located after multiple attempts. This reaction has either no barrier or a very low barrier.
[c] In the image of the transition state for this reaction, the products OH^{Va} + H^O are spatially separated. However, the energy of reaction has been computed assuming that they are adjacent in order to maintain consistency with other pathways leading to the same products.

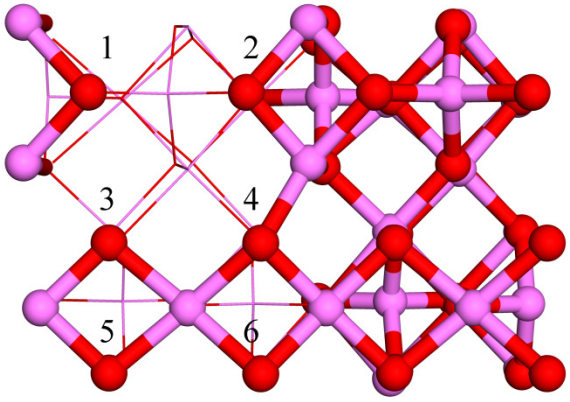

Figure B.1: Top view of the γ-Al_2O_3(100) p(2×1) surface; Al atoms shown in pink, O atoms in red. The numeric labels are identifiers for the nearest O site. The subsurface atoms on the left side of the figure are drawn differently so that the surface atoms are more easily identified.

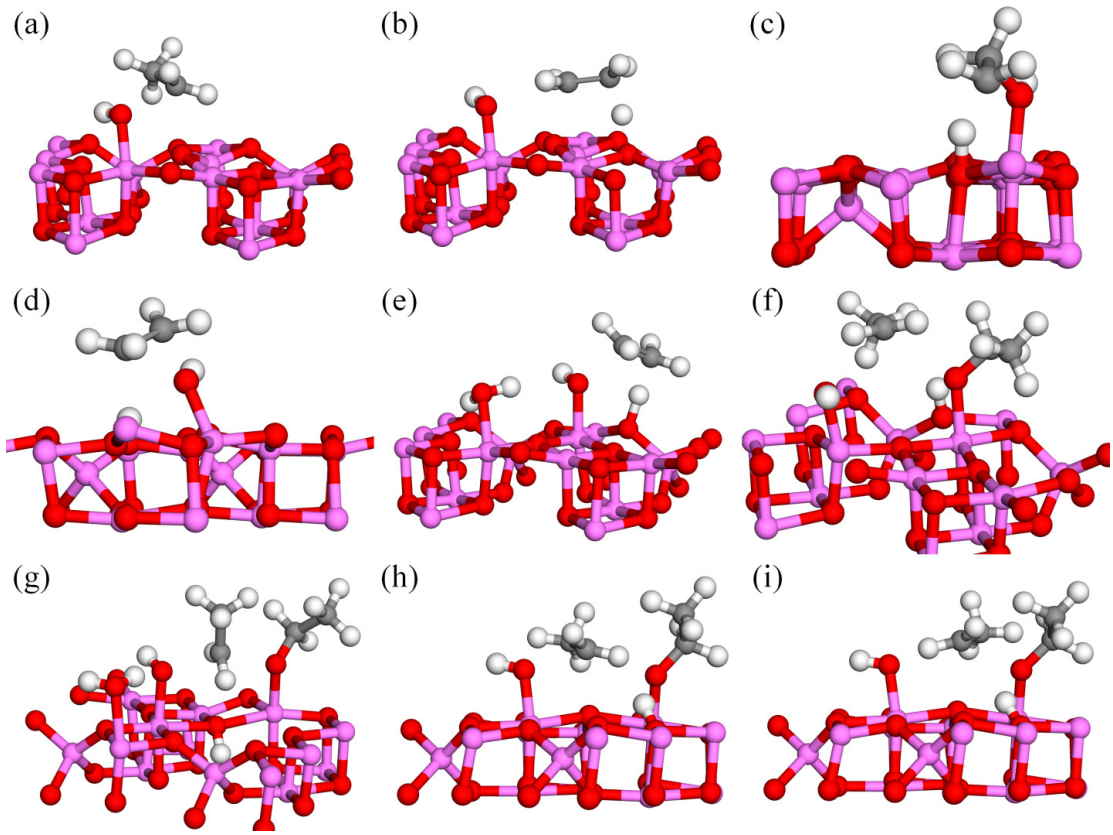

Figure B.2: Transition state structures for ethylene and diethyl ether formation. Refer to Table B.4 and Section 4.4 for information about each elementary step represented here.
(a) $CH_3CH_2OH^{Va} + {}^{O} \rightleftharpoons CH_3CH_2{}^{O} + OH^{Va}$ (R2),
(b) $CH_3CH_2{}^{O} + OH^{Va} + {}^{O'} \rightleftharpoons C_2H_4 + OH^{Va} + H^{O'} + {}^{O}$ (R3),
(c) $CH_3CH_2OH^{Va} + {}^{Vc} + {}^{O} \rightleftharpoons CH_2CH_2OH^{Va\text{-}Vc} + H^{O}$ (R4),
(d) $CH_2CH_2OH^{Va\text{-}Vc} + H^{O} \rightleftharpoons C_2H_4 + OH^{Va} + H^{O} + {}^{Vc}$ (R5),
(e) $CH_3CH_2OH^{Vb} + H_2O^{Va} + {}^{O} \rightleftharpoons C_2H_4 + OH^{Vb} + H^{O} + H_2O^{Va}$,
(f) $CH_3CH_2O^{Vb} + H^{O} + CH_3CH_2OH^{Va} \rightleftharpoons CH_3CH_2OCH_2CH_3{}^{Vb} + OH^{Va} + H^{O}$ "frontside attack",
(g) $CH_3CH_2O^{Va} + H^{O} + CH_3CH_2OH^{Vb} + H_2O^{Vc} \rightleftharpoons CH_3CH_2OCH_2CH_3{}^{Va} + OH^{Vb} + H^{O} + H_2O^{Vc}$,
(h) $CH_3CH_2O^{Va} + H^{O} + CH_3CH_2OH^{Vb} + {}^{O'} \rightleftharpoons CH_3CH_2O^{Va} + H^{O} + OH^{Vb} + CH_3CH_2{}^{O'}$ (R11),
(i) $CH_3CH_2O^{Va} + H^{O} + OH^{Vb} + CH_3CH_2{}^{O'} \rightleftharpoons CH_3CH_2OCH_2CH_3{}^{Va} + OH^{Vb} + H^{O} + {}^{O'}$ (R12).

Appendix C

SITE-DEPENDENT LEWIS ACIDITY OF γ-Al_2O_3: ADDITIONAL ENERGETIC AND STRUCTURAL INFORMATION FROM DFT CALCULATIONS

C.1 Adsorption Energies, Reaction Barriers, and Band Means

Table C.1: Binding energies (E_{BE}) for the various adsorbates on the (110) and (100) facets of γ-Al_2O_3 (in units of eV).

Adsorbate	(110) facet			(100) facet			
	3	4a	4b	V_a	V_b	V_c	V_d
Ethanol	−1.28	−0.80	−1.25	−0.84	−0.60	−0.43	−0.61
tert-butanol	−1.37	−0.72	−1.18	−0.77	−0.50	−0.56	−0.46
Isopropanol	−1.29	−0.70	−1.15	−0.86	−0.46	−0.52	−0.51
Diethyl ether	−1.28	−0.54	−0.76	−0.54	−0.41	−0.34	−0.41
Water	−1.22	−0.75	−1.11	−0.88	−0.65	−0.55	−0.64

Table C.2: DFT+D3 corrections to the binding energy for the various adsorbates on the (110) and (100) facets of γ-Al_2O_3 (in units of eV).

Adsorbate	(110) facet			(100) facet			
	3	4a	4b	V_a	V_b	V_c	V_d
Ethanol	−0.29	−0.21	−0.25	−0.36	−0.31	−0.34	−0.31
tert-butanol	−0.37	−0.33	−0.35	−0.47	−0.43	−0.38	−0.43
Isopropanol	−0.33	−0.28	−0.32	−0.36	−0.32	−0.34	−0.33
Diethyl ether	−0.46	−0.41	−0.45	−0.53	−0.53	−0.47	−0.52
Water	−0.10	−0.08	−0.09	−0.15	−0.15	−0.13	−0.14

Table C.3: Mean band energies for the (110) and (100) facets of γ-Al_2O_3 (in units of eV).

Site	E_s	E_p	E_s^*	E_p^*
		(110) facet		
3	−7.69	−6.27	4.67	5.47
4a	−8.33	−6.62	5.26	5.97
4b	−8.01	−6.44	4.92	5.80
		(100) facet		
V_a	−7.66	−6.16	5.31	5.91
V_b	−7.67	−6.08	5.90	6.51
V_c	−7.97	−6.21	6.36	6.61
V_d	−7.67	−6.08	5.88	6.50

Table C.4: Reaction barriers (E_a) for the dehydration of ethanol on the (110) and (100) facets of γ-Al_2O_3 (in units of eV).

Site	γ-Al_2O_3	γ-Al_2O_3•7 H_2O
	(110) facet	
3	1.31	1.39
4a	1.51	1.48
4b	1.25	1.83
	(100) facet	
V_a	1.59	
V_b	1.65	

Table C.5: Reaction barriers (E_a) for the etherification of ethanol on the (110) and (100) facets of γ-Al_2O_3 (in units of eV).

Site	γ-Al_2O_3	γ-Al_2O_3•6 H_2O
	(110) facet	
4b-3	0.81	1.46
4b-4a	0.86	2.17
4a-4a	1.44	1.63
3-4b	1.47	
3-4a	1.60	1.57
4a-3	1.73	1.46
4a-4b	1.98	3.12
	(100) facet	
V_a-V_b	1.35	
V_b-V_a	1.49	
V_b-V_c	1.98	

Table C.6: E_s^* upon dual adsorption of ethanol for the (110) and (100) facets of γ-Al_2O_3 (in units of eV).

Site	γ-Al_2O_3	γ-Al_2O_3•6 H_2O
	(110) facet	
4b-3	6.05	4.45
4b-4a	6.05	4.73
4a-4a	5.63	5.28
3-4b	5.96	4.58
3-4a	6.00	5.29
4a-3	5.55	6.51
4a-4b	5.55	4.74
	(100) facet	
V_a-V_b	6.49	7.14
V_b-V_a	7.09	6.31
V_b-V_c	6.36	7.20

Table C.7: Binding energies (E_{BE}) for the various adsorbates on the (110) facet of γ-Al_2O_3•7 H_2O (in units of eV).

Adsorbate	3	4a	4b
Ethanol	−1.82	−0.92	−1.87
tert-butanol	−1.75	−0.76	−1.73
Isopropanol	−1.88	−0.96	−1.71
Diethyl ether	−1.22	−0.09	−1.73

C.2 DFT-computed Adsorbate and Transition State Structures

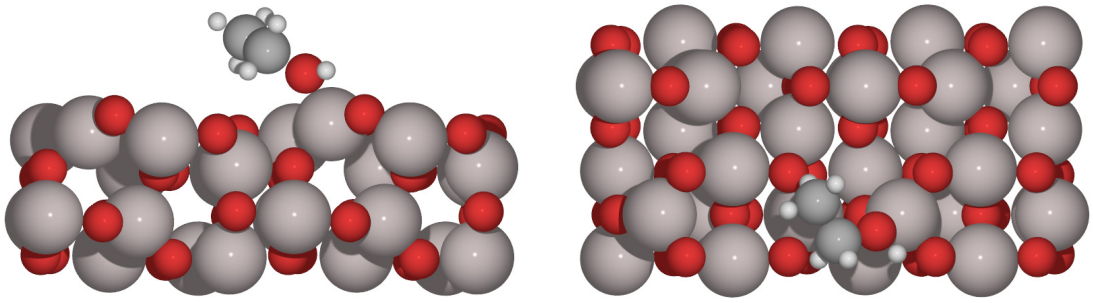

(a) Side View (b) Top View

Figure C.1: Ethanol adsorption on site 3 of γ-Al_2O_3(110).

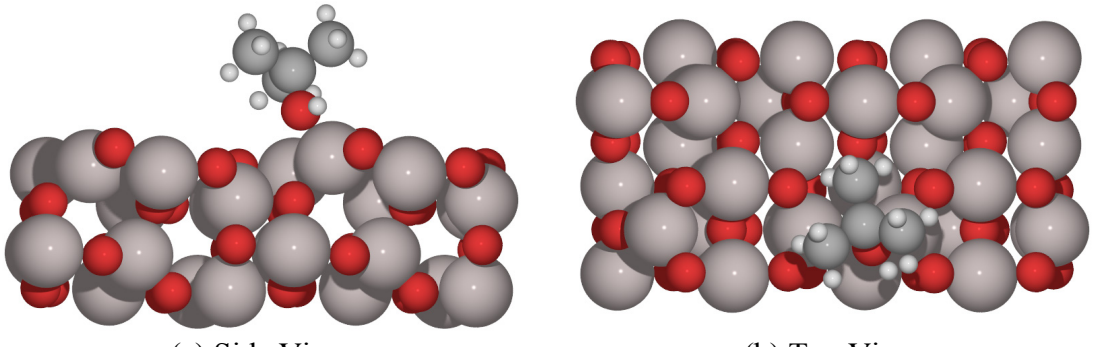

(a) Side View (b) Top View

Figure C.2: *tert*-butanol adsorption on site 3 of γ-Al_2O_3(110).

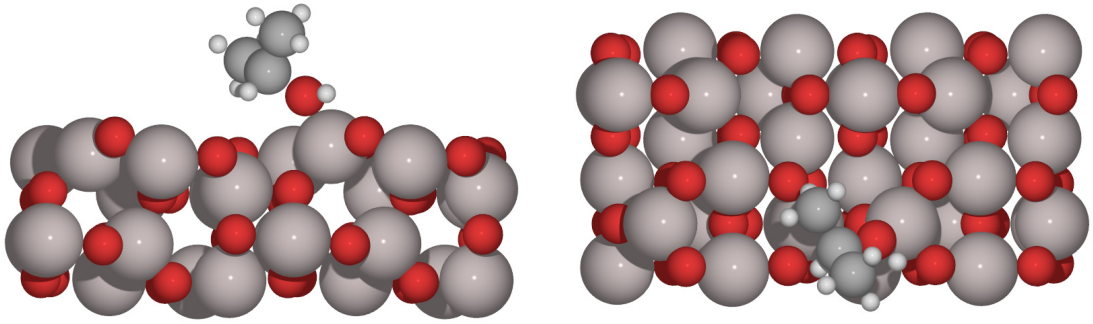

(a) Side View (b) Top View

Figure C.3: Isopropanol adsorption on site 3 of γ-Al_2O_3(110).

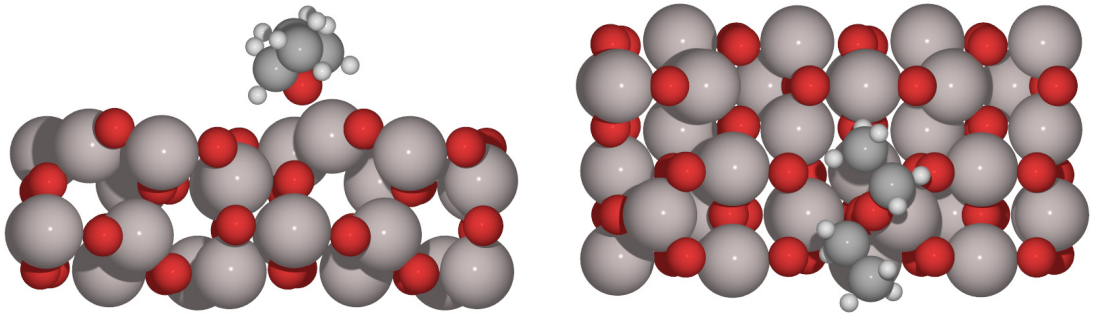

(a) Side View (b) Top View

Figure C.4: Diethyl ether adsorption on site 3 of γ-Al_2O_3(110).

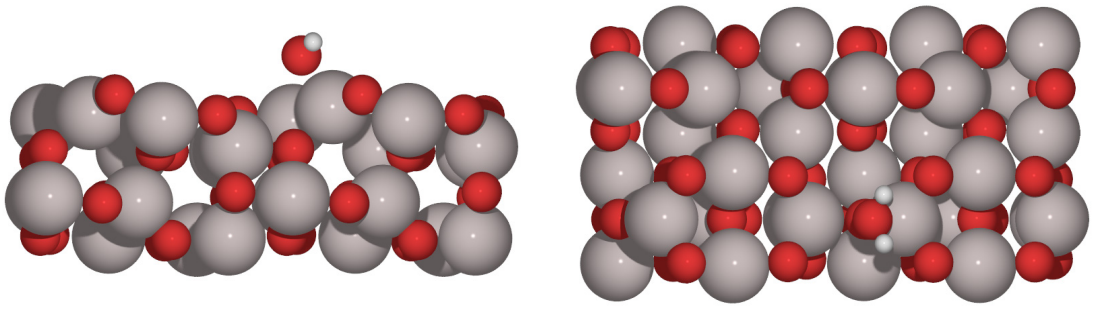

(a) Side View (b) Top View

Figure C.5: Water adsorption on site 3 of γ-Al_2O_3(110).

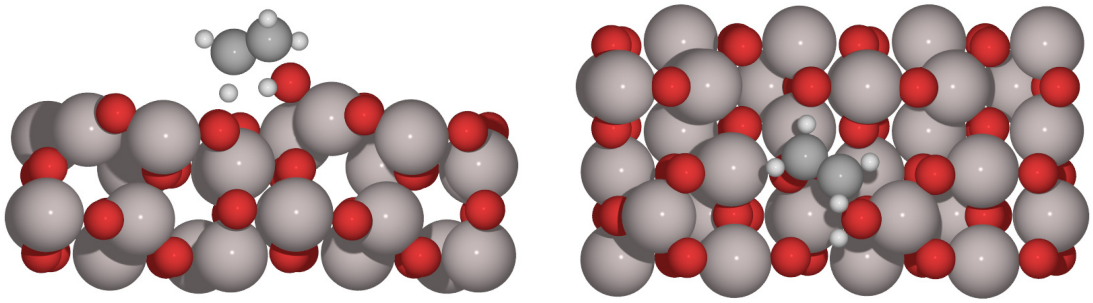

(a) Side View (b) Top View

Figure C.6: Transition state structure for the E2 mechanism of ethanol dehydration on site 3 of γ-Al_2O_3(110).

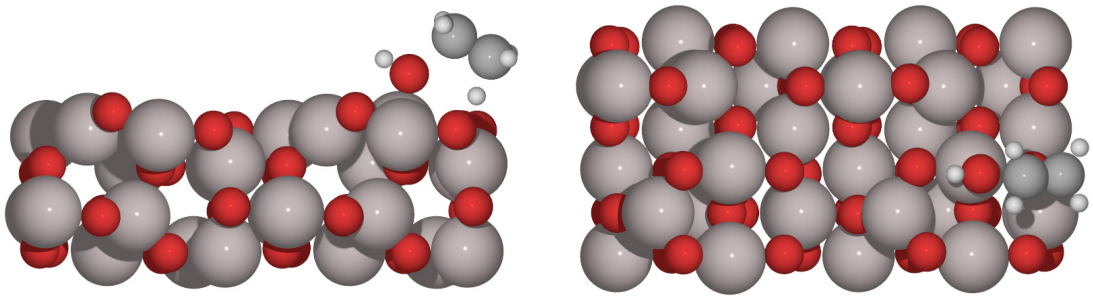

(a) Side View (b) Top View

Figure C.7: Transition state structure for the E2 mechanism of ethanol dehydration on site 4a of γ-Al_2O_3(110).

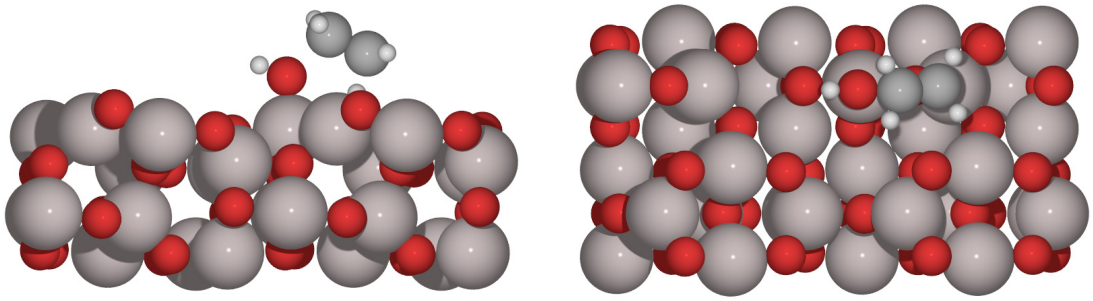

(a) Side View (b) Top View

Figure C.8: Transition state structure for the E2 mechanism of ethanol dehydration on site 4b of γ-Al_2O_3(110).

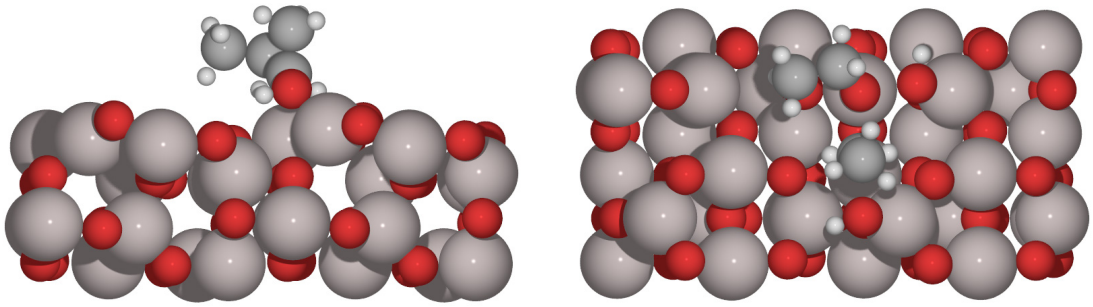

(a) Side View (b) Top View

Figure C.9: Transition state structure for the S_N2 mechanism of ethanol etherification on the 4b-3 site pair of γ-Al_2O_3(110).

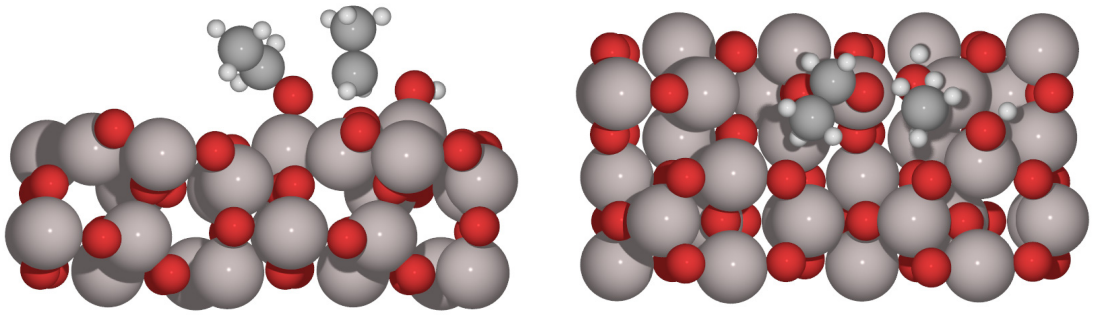

(a) Side View (b) Top View

Figure C.10: Transition state structure for the S_N2 mechanism of ethanol etherification on the 4b-4a site pair of γ-Al_2O_3(110).

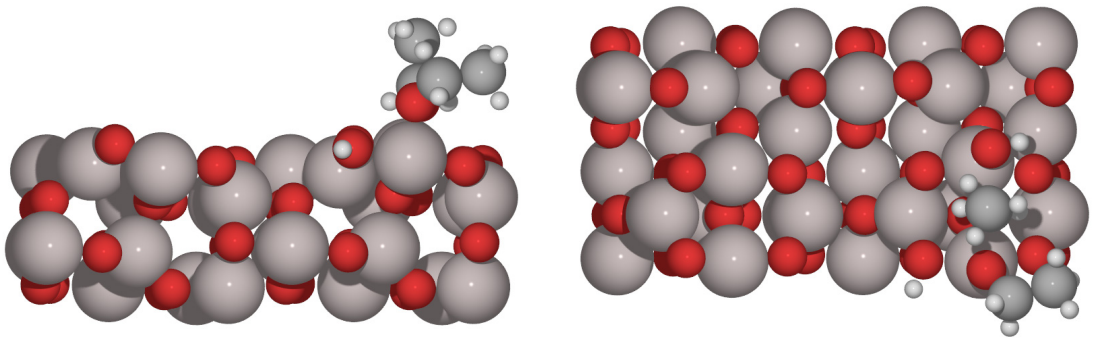

(a) Side View (b) Top View

Figure C.11: Transition state structure for the S_N2 mechanism of ethanol etherification on the 4a-4a site pair of γ-Al_2O_3(110).

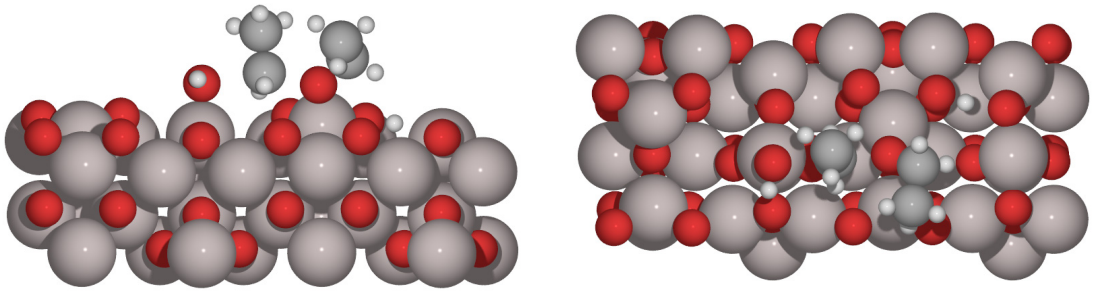

(a) Side View (b) Top View

Figure C.12: Transition state structure for the S_N2 mechanism of ethanol etherification on the 3-4b site pair of γ-Al_2O_3(110).

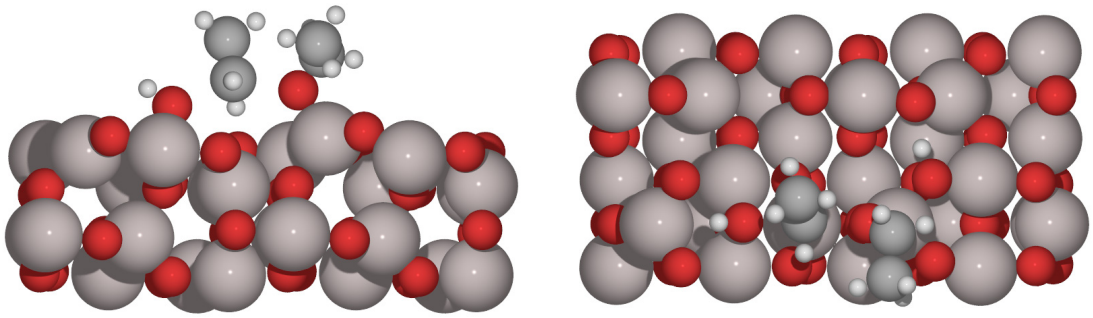

(a) Side View (b) Top View

Figure C.13: Transition state structure for the S_N2 mechanism of ethanol etherification on the 3-4a site pair of γ-Al_2O_3(110).

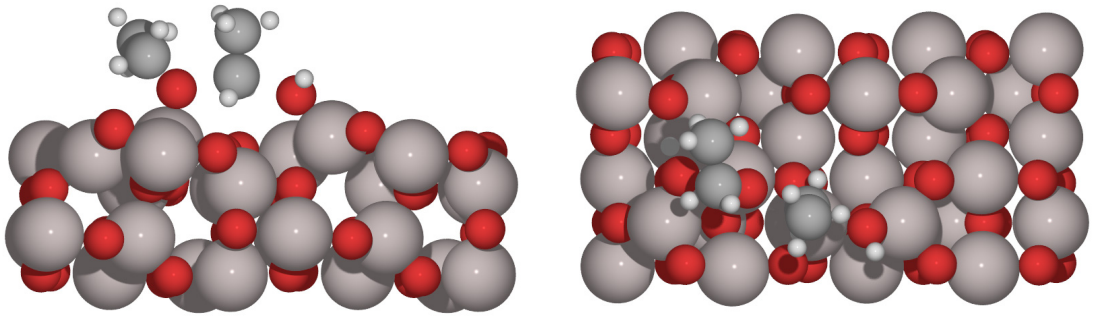

(a) Side View (b) Top View

Figure C.14: Transition state structure for the S_N2 mechanism of ethanol etherification on the 4a-3 site pair of γ-Al_2O_3(110).

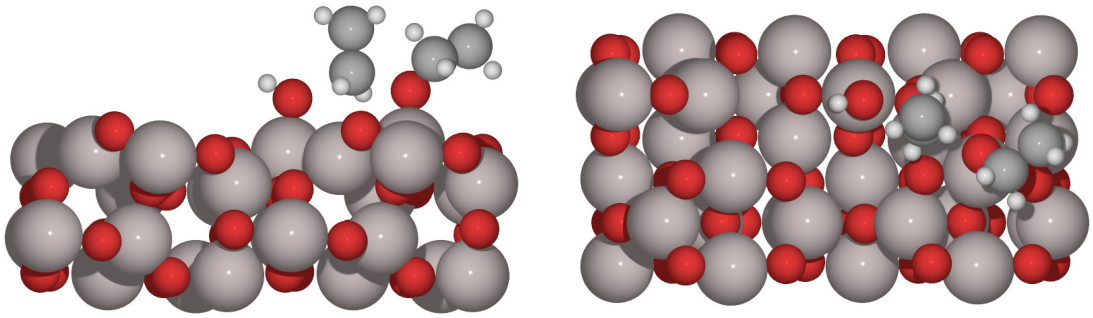

(a) Side View (b) Top View

Figure C.15: Transition state structure for the S_N2 mechanism of ethanol etherification on the 4a-4b site pair of γ-Al_2O_3(110).

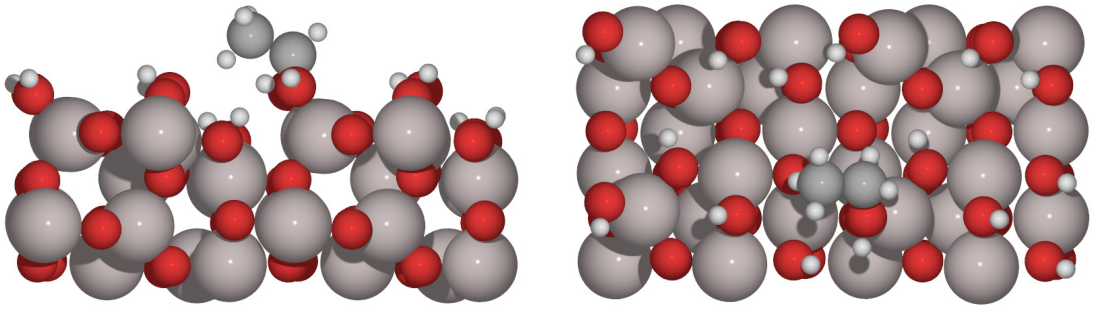

(a) Side View (b) Top View

Figure C.16: Ethanol adsorption on site 3 of γ-Al_2O_3(110)•7 H_2O.

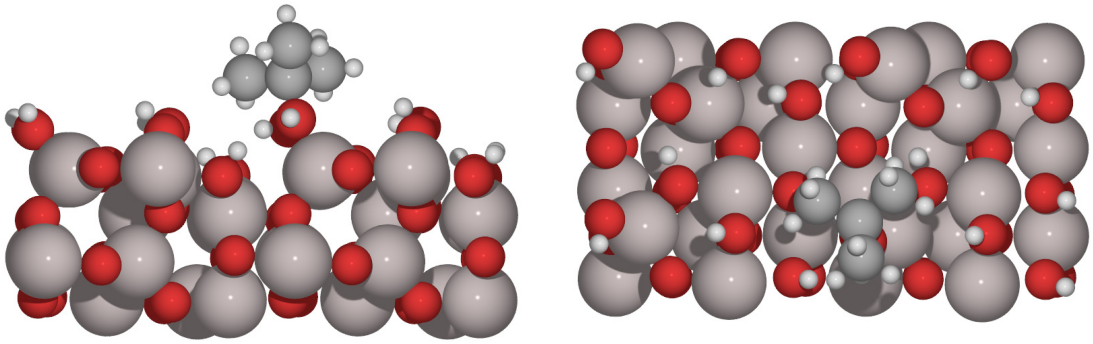

(a) Side View (b) Top View

Figure C.17: *tert*-butanol adsorption on site 3 of γ-Al_2O_3(110)•7 H_2O.

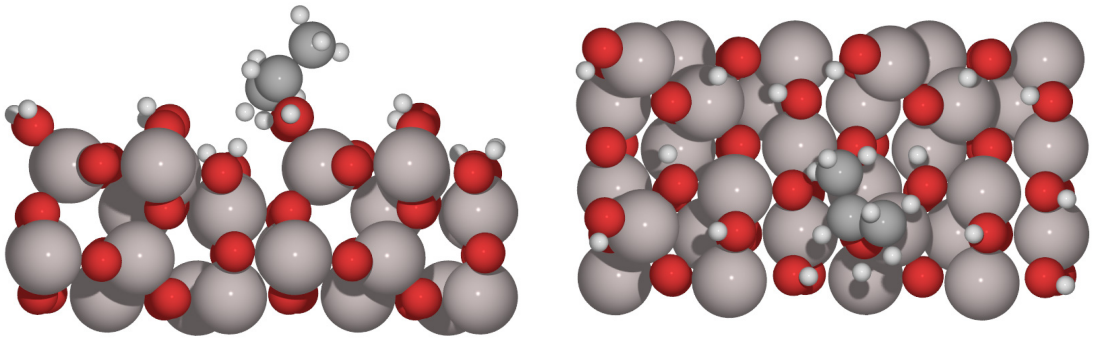

(a) Side View (b) Top View

Figure C.18: Isopropanol adsorption on site 3 of γ-Al_2O_3(110)•7 H_2O.

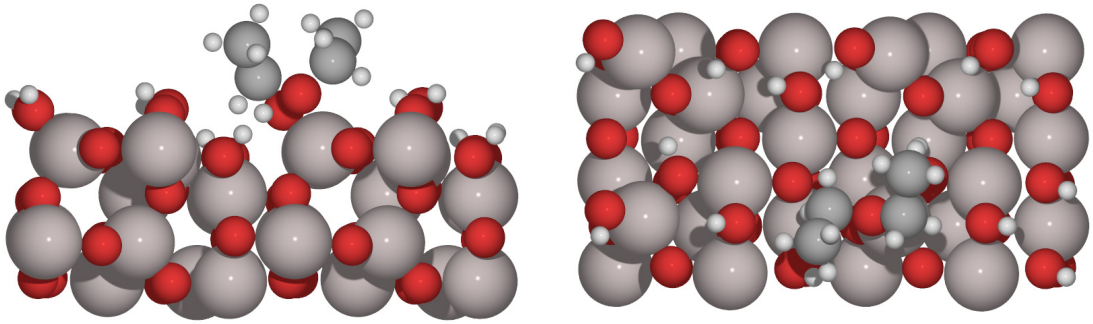

(a) Side View (b) Top View

Figure C.19: Diethyl ether adsorption on site 3 of γ-Al_2O_3(110)•7 H_2O.

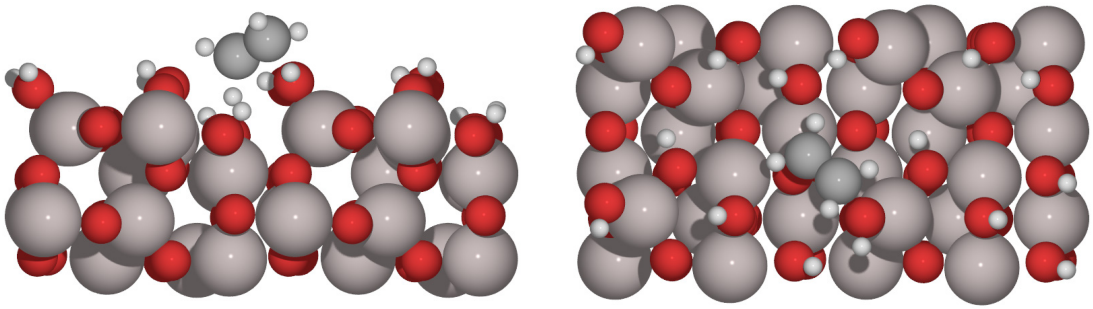

(a) Side View (b) Top View

Figure C.20: Transition state structure for the E2 mechanism of ethanol dehydration on site 3 of γ-Al_2O_3(110)•7 H_2O.

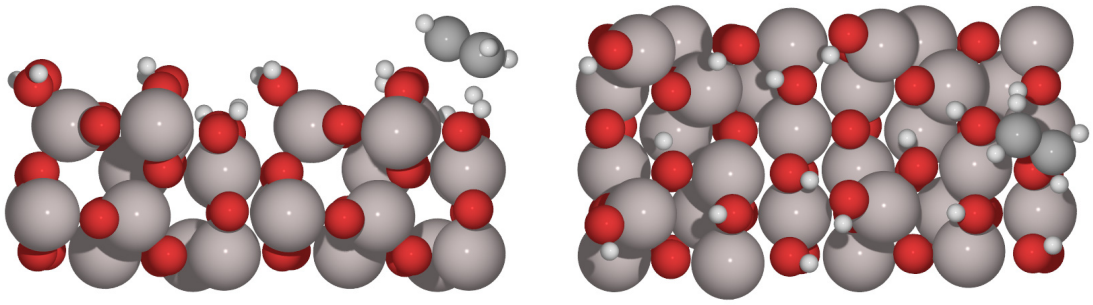

(a) Side View (b) Top View

Figure C.21: Transition state structure for the E2 mechanism of ethanol dehydration on site 4a of γ-Al_2O_3(110)•7 H_2O.

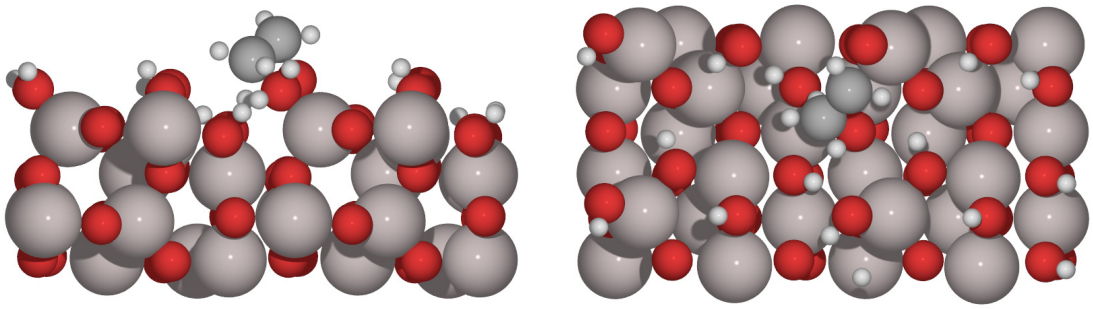

(a) Side View (b) Top View

Figure C.22: Transition state structure for the E2 mechanism of ethanol dehydration on site 4b of γ-Al_2O_3(110)•7 H_2O.

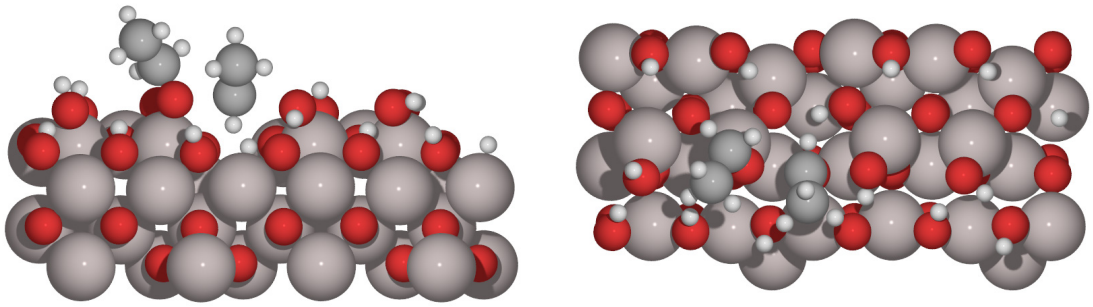

(a) Side View (b) Top View

Figure C.23: Transition state structure for the S_N2 mechanism of ethanol etherification on the 4b-3 site pair of γ-Al_2O_3(110)•6 H_2O.

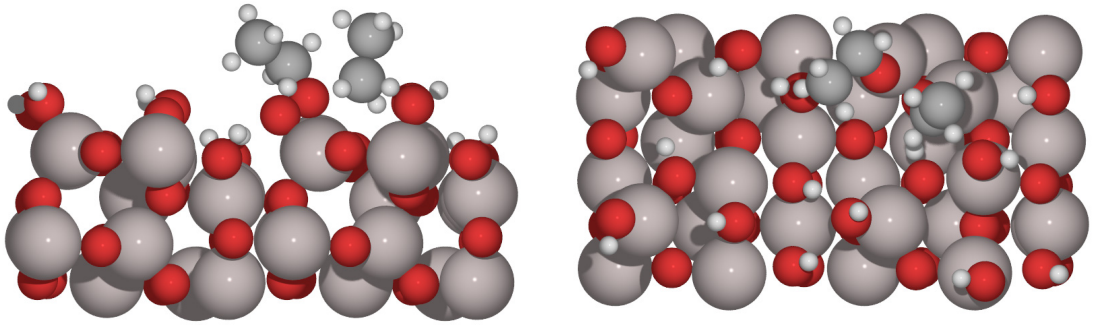

(a) Side View (b) Top View

Figure C.24: Transition state structure for the S_N2 mechanism of ethanol etherification on the 4b-4a site pair of γ-Al_2O_3(110)•6 H_2O.

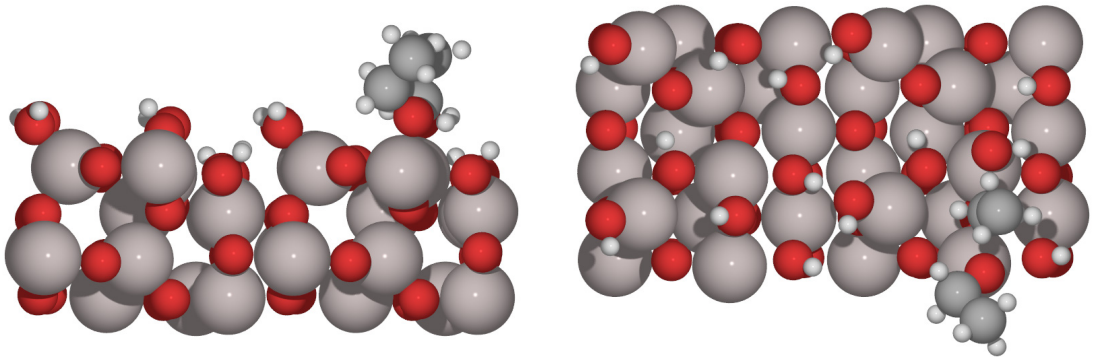

(a) Side View (b) Top View

Figure C.25: Transition state structure for the S_N2 mechanism of ethanol etherification on the 4a-4a site pair of γ-Al_2O_3(110)•6 H_2O.

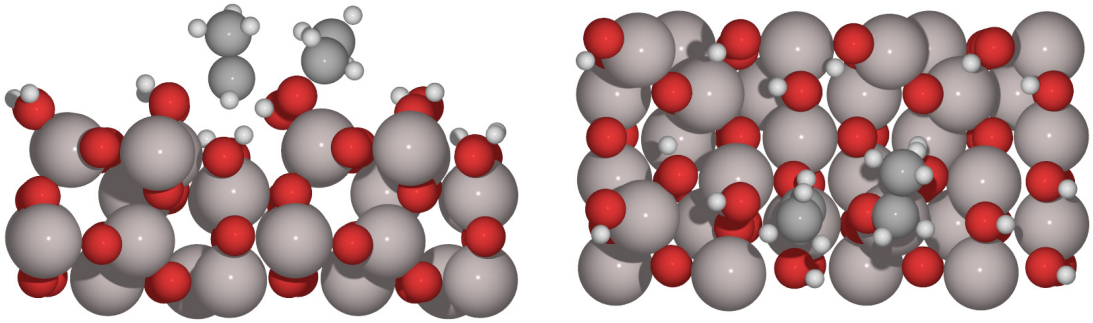

(a) Side View (b) Top View

Figure C.26: Transition state structure for the S_N2 mechanism of ethanol etherification on the 3-4a site pair of γ-Al_2O_3(110)•6 H_2O.

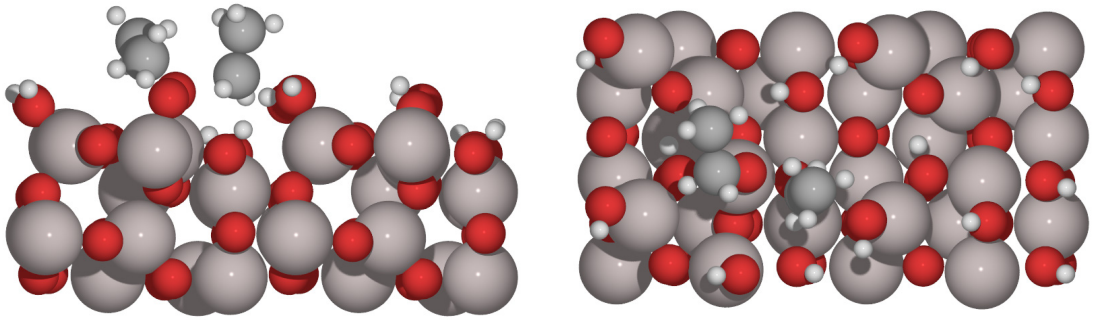

(a) Side View (b) Top View

Figure C.27: Transition state structure for the S_N2 mechanism of ethanol etherification on the 4a-3 site pair of γ-Al_2O_3(110)•6 H_2O.

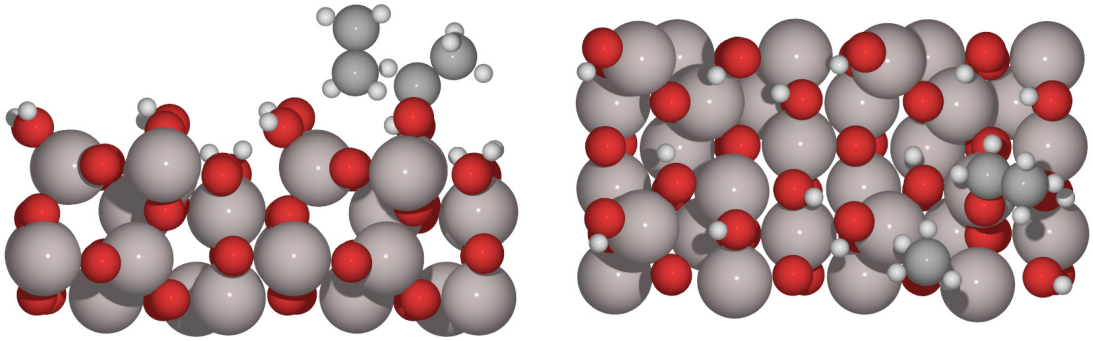

(a) Side View (b) Top View

Figure C.28: Transition state structure for the S_N2 mechanism of ethanol etherification on the 4a-4b site pair of γ-Al_2O_3(110)•6 H_2O.

Appendix D

DFT STRUCTUAL INFORMATION, PERFORMANCE ASSESSMENTS, AND RATE EXPRESSION DERIVATIONS ASSOCIATED WITH THE DFT-DRIVEN MULTI-SITE MICROKINETIC MODEL ON γ-Al_2O_3(111)

D.1 Structural and Vibrational Information from DFT Calculations on γ-Al_2O_3(111)

Table D.1: Calculated vibrational frequencies for each transition state structure computed on γ-Al_2O_3(111).

Reaction	Vibrational Frequencies [cm^{-1}]
$H_2O^{Va} + {}^{O} \rightleftharpoons OH^{Va} + H^{O}$	3757, 1833, 1368, 708, 676, 555, 295, 129, 549**i**
$CH_3CH_2OH^{Va} + {}^{O} \rightleftharpoons CH_3CH_2O^{Va} + H^{O}$	3045, 3041, 2999, 2972, 2967, 1855, 1479, 1455, 1442, 1379, 1356, 1279, 1251, 1149, 1082, 1057, 904, 797, 592, 422, 258, 227, 168, 81, 57, 41, 591**i**
$CH_3CH_2OH^{Va} + {}^{O} \rightleftharpoons C_2H_4 + OH^{Va} + H^{O}$ (E2)	3689, 3167, 3142, 3067, 3049, 1513, 1425, 1363, 1308, 1251, 1193, 1113, 980, 954, 919, 789, 734, 610, 524, 434, 355, 309, 147, 125, 66, 39, 608**i**
$CH_3CH_2O^{Va} + H^{O} \rightleftharpoons C_2H_4 + OH^{Va} + H^{O}$ (E1)	3497, 3171, 3142, 3076, 3065, 1557, 1471, 1414, 1219, 1217, 1190, 1082, 894, 878, 829, 784, 765, 703, 493, 461, 328, 191, 128, 55, 25, 10, 1755**i**
$CH_3CH_2OCH_2CH_3{}^{Va} + {}^{O} \rightleftharpoons C_2H_4 + CH_3CH_2O^{Va} + H^{O}$ ($E2^{E}$)	3168, 3139, 3074, 3050, 3043, 3030, 2990, 2961, 2927, 1519, 1466, 1453, 1440, 1420, 1373, 1352, 1334, 1292, 1287, 1250, 1184, 1145, 1094, 1079, 1038, 937, 924, 886, 801, 791, 632, 557, 450, 428, 314, 299, 272, 204, 168, 101, 74, 67, 56, 35, 671**i**

Table D.1 continued.

$CH_3CH_2O^{Va} + H^O$ $+ CH_3CH_2OH^{Vb}$ $\rightleftharpoons$ $CH_3CH_2OCH_2CH_3{}^{Va}$ $+ OH^{Vb} + H^O$ (S_N2)	3744, 3473, 3190, 3082, 3055, 3037, 3025, 2990, 2976, 2967, 2938, 2917, 1471, 1464, 1442, 1439, 1431, 1425, 1367, 1341, 1321, 1272, 1192, 1144, 1127, 1093, 1072, 1038, 898, 886, 869, 852, 829, 789, 778, 705, 507, 471, 440, 431, 275, 257, 233, 210, 190, 173, 155, 142, 115, 86, 70, 47, 30, 317**i**
$CH_3CH_2OH^{Va} + CH_3CH_2OH^O$ $\rightleftharpoons$ CH3CH2OCH2CH3 $+ OH^{Va} + H^O$ + (S_N2')	3733, 3274, 3192, 3084, 3075, 3055, 3031, 2995, 2994, 2977, 2941, 2720, 1484, 1463, 1453, 1446, 1443, 1433, 1420, 1372, 1354, 1345, 1273, 1208, 1153, 1123, 1092, 1083, 1065, 1020, 1000, 969, 849, 812, 805, 782, 550, 482, 431, 369, 299, 289, 253, 225, 172, 154, 113, 81, 74, 55, 37, 20, 13, 383**i**

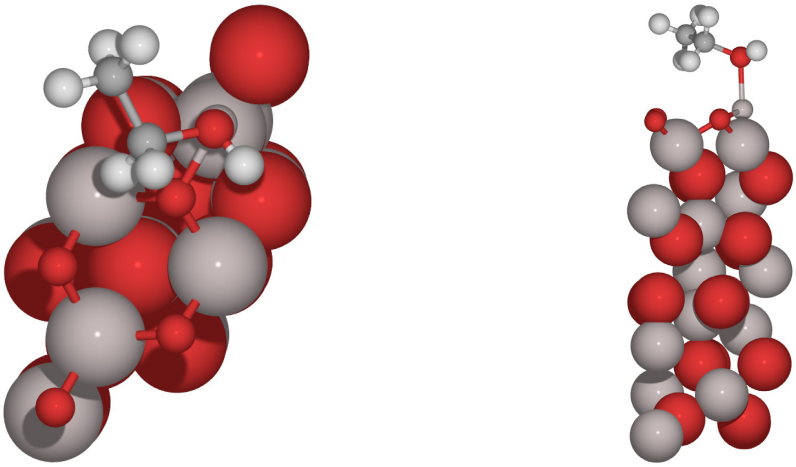

Figure D.1: Top and side views of optimized structure for $CH_3CH_2OH^{Al}$.

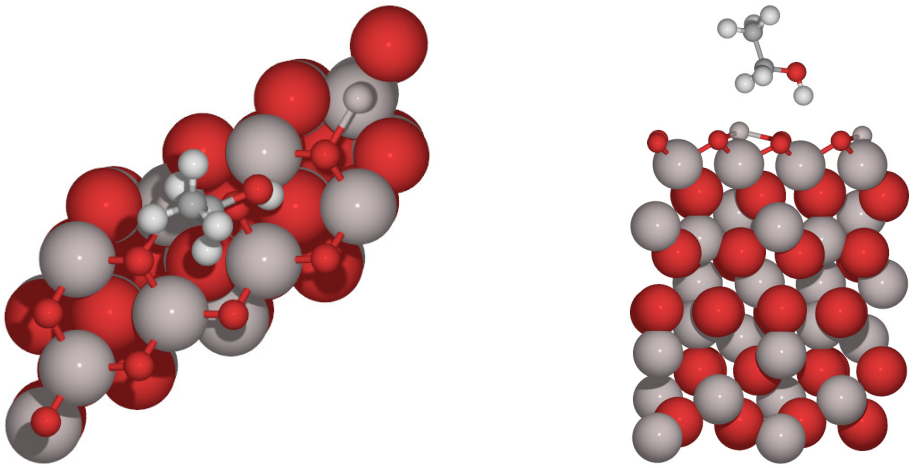

Figure D.2: Top and side views of optimized structure for $CH_3CH_2OH^O$.

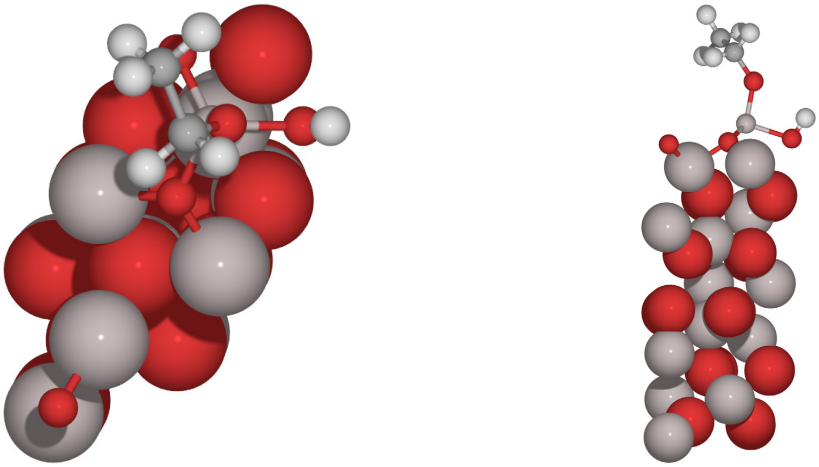

Figure D.3: Top and side views of optimized structure for $CH_3CH_2O^{Al} + H^O$.

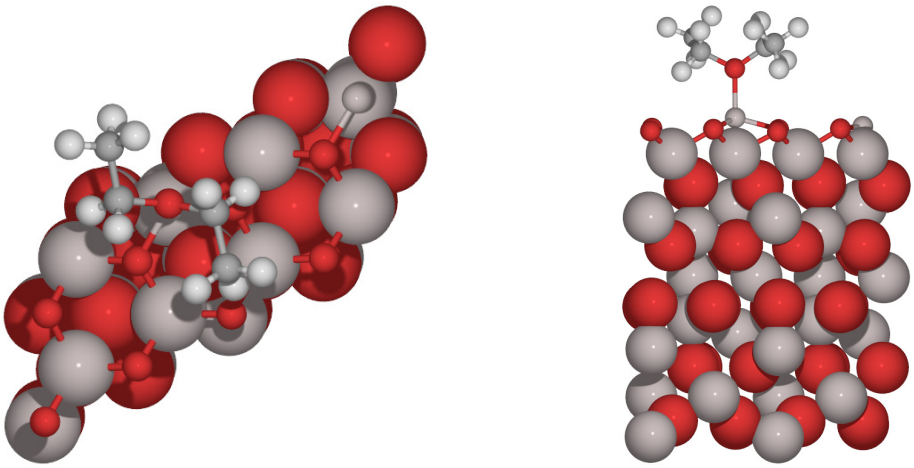

Figure D.4: Top and side views of optimized structure for $CH_3CH_2OCH_2CH_3^{Al}$.

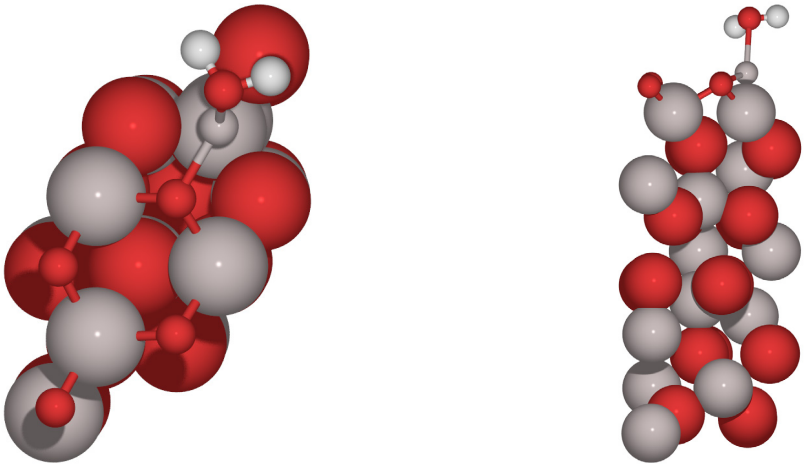

Figure D.5: Top and side views of optimized structure for H_2O^{Al}.

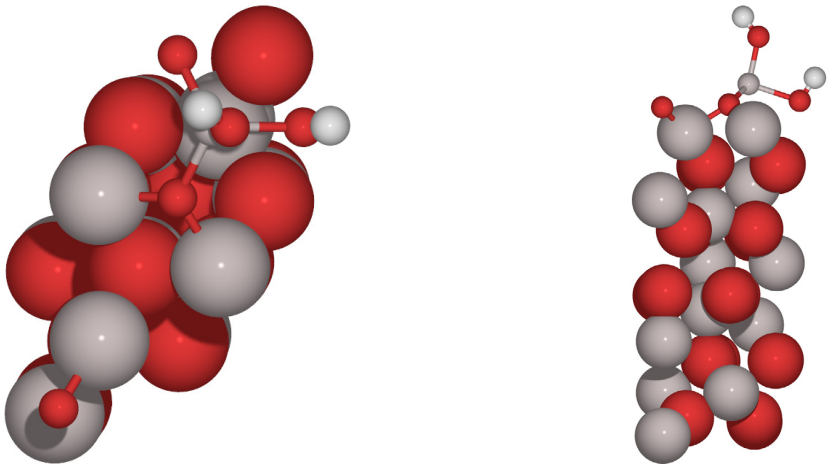

Figure D.6: Top and side views of optimized structure for $OH^{Al} + H^{O}$.

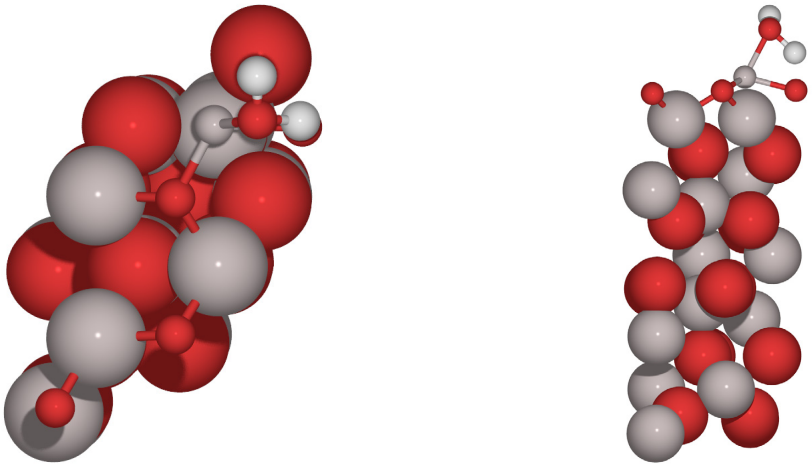

Figure D.7: Top and side views of optimized structure of the transition state for $H_2O^{Al} + {}^{O} \rightleftharpoons OH^{Al} + H^{O}$.

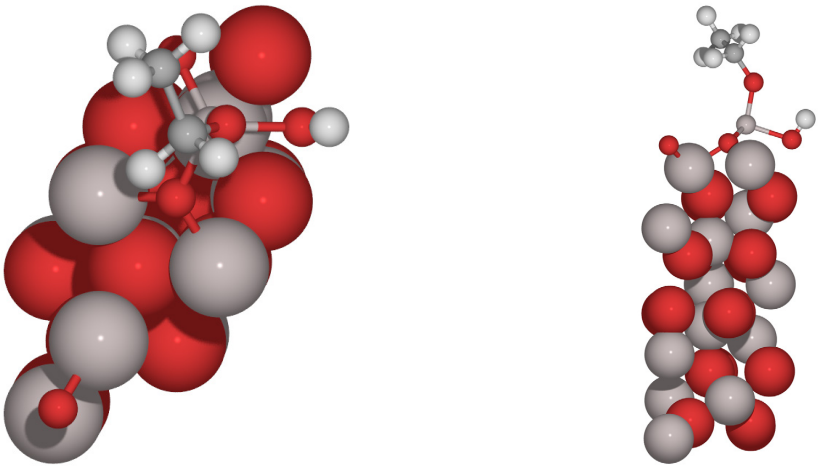

Figure D.8: Top and side views of optimized structure of the transition state for $CH_3CH_2OH^{Al} + {}^{O} \rightleftharpoons CH_3CH_2O^{Al} + H^{O}$.

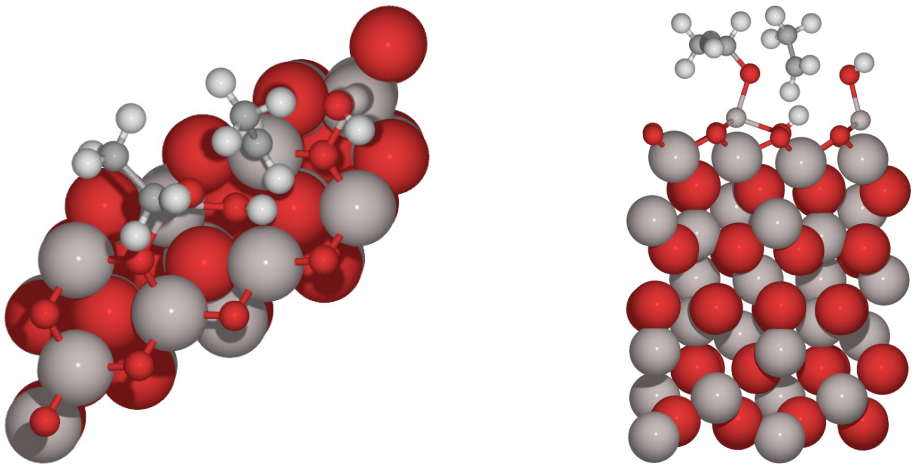

Figure D.9: Top and side views of optimized structure of the transition state for $CH_3CH_2O^{Al} + CH_3CH_2OH^{Al} \rightleftharpoons CH_3CH_2OCH_2CH_3{}^{Al} + OH^{Al}$ (S_N2).

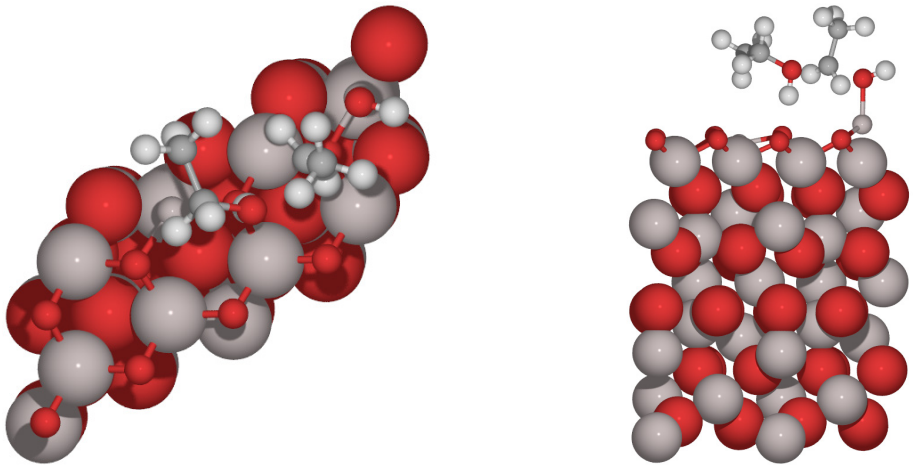

Figure D.10: Top and side views of optimized structure of the transition state for $CH_3CH_2OH^{O} + CH_3CH_2OH^{Al} \rightleftharpoons CH_3CH_2OCH_2CH_3{}^{H} + OH^{Al} + H^{O}$ (S_N2').

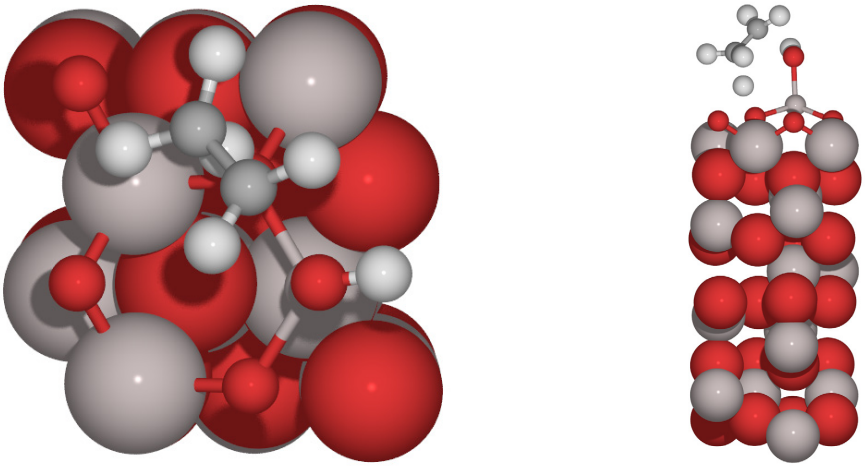

Figure D.11: Top and side views of optimized structure of the transition state for $CH_3CH_2OH^{Al} + {}^{O} \rightleftharpoons C_2H_4 + OH^{Al} + H^{O}$ (E2).

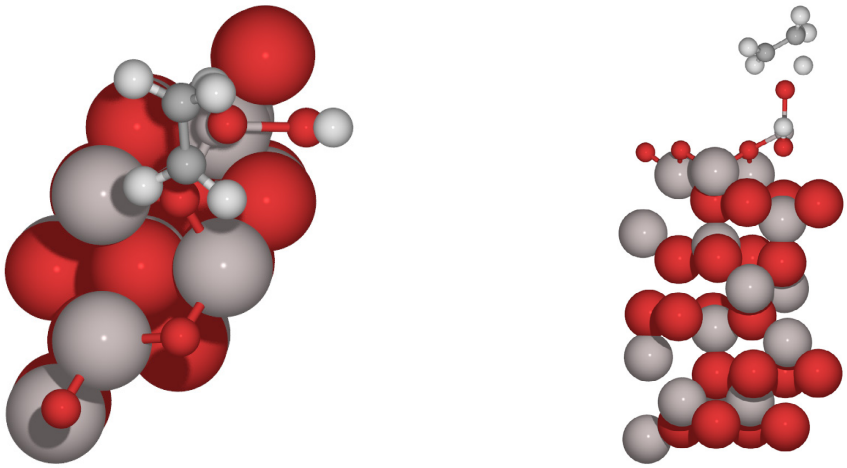

Figure D.12: Top and side views of optimized structure of the transition state for $CH_3CH_2O^{Al} \rightleftharpoons C_2H_4 + OH^{Al}$ (E1).

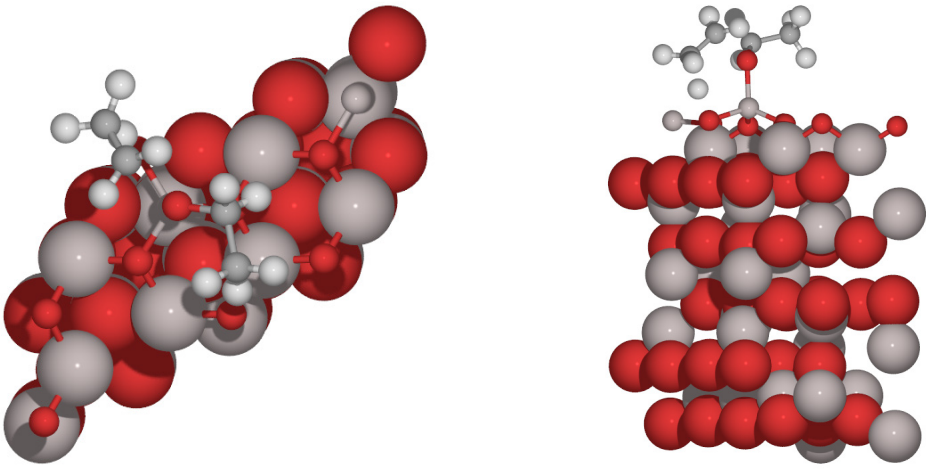

Figure D.13: Top and side views of optimized structure of the transition state for $CH_3CH_2OCH_2CH_3^{Al} + {}^{O} \rightleftharpoons C_2H_4 + CH_3CH_2O^{Al} + H^{O}$ ($E2^{E}$).

D.2 Kinetic Model Derivation and Analysis

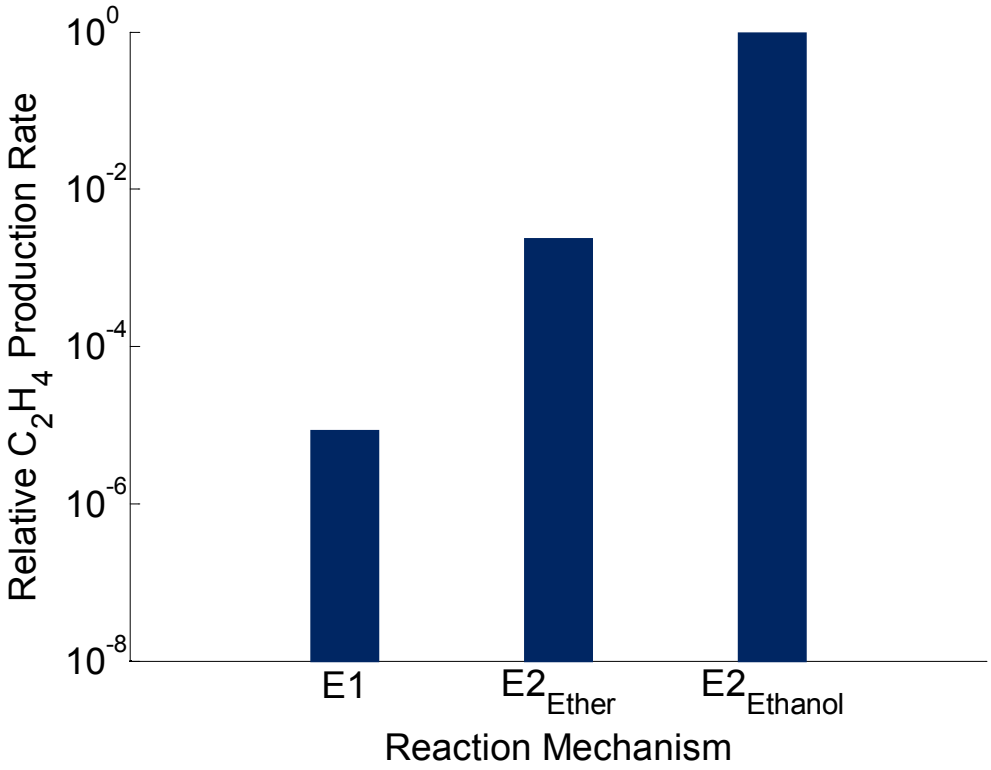

Figure D.14: Microkinetic model-computed rates of ethylene production for each ethylene-producing elementary step, normalized by the highest rate.

D.2.1 Derivation of Reduced Rate Expressions

The method used to select the elementary steps considered in the reduced model was described in the main text, and the equations are restated here for convenience:

$$CH_3CH_2OH + {}^{Al} \rightleftharpoons CH_3CH_2OH^{Al} \quad \text{(R1)}$$

$$H_2O + {}^{Al} \rightleftharpoons H_2O^{Al} \quad \text{(R2)}$$

$$CH_3CH_2OH^{Al} + {}^{O} \rightleftharpoons CH_3CH_2O^{Al} + H^{O} \quad \text{(R3)}$$

$$H_2O^{Al} + {}^{O} \rightleftharpoons OH^{Al} + H^{O} \quad \text{(R4)}$$

$$CH_3CH_2OH^{Al} + {}^{O} \rightarrow C_2H_4 + OH^{Al} + H^{O} \quad \text{(R5)}$$

$$CH_3CH_2OH^{Al} + CH_3CH_2O^{Al} \rightarrow CH_3CH_2OCH_2CH_3 + OH^{Al} + {}^{Al} \quad \text{(R6)}$$

The quasi-steady state assumption (QSSA) was subsequently applied to each surface species present in the mechanism (excluding vacancies) in order to write a set of differential equations describing the surface concentration with respect to time:

$$\frac{d\left[CH_3CH_2OH^{Al}\right]}{dt} = r_{1f} - r_{1r} + r_{3r} - r_{3f} - r_{5f} - r_{6f} = 0$$

$$\frac{d\left[H_2O^{Al}\right]}{dt} = r_{2f} - r_{2r} + r_{4r} - r_{4f} = 0$$

$$\frac{d\left[CH_3CH_2O^{Al}\right]}{dt} = r_{3f} - r_{3r} - r_{6f} = 0$$

$$\frac{d\left[OH^{Al}\right]}{dt} = r_{4f} - r_{4r} + r_{5f} + r_{6f} = 0$$

$$\frac{d\left[H^{O}\right]}{dt} = r_{3f} - r_{3r} + r_{4f} - r_{4r} + r_{5f} = 0$$

Note that the "f" and "r" subscripts of rates denote "forward" and "reverse" rates, respectively. The reverse rates of reactions (R5) and (R6) were not included as it was shown in the full model that these steps are irreversible in the forward direction. Two additional algebraic equations were written for species balances on Al and O sites:

$$S_{Al} = \left[CH_3CH_2OH^{Al}\right] + \left[CH_3CH_2O^{Al}\right] + \left[H_2O^{Al}\right] + \left[OH^{Al}\right] + \left[{}^{Al}\right]$$

$$S_{O} = \left[H^{O}\right] + \left[{}^{O}\right]$$

where S_{Al} and S_O are the total surface site densities of Al and O sites, respectively. Several reduction principles were then applied to simplify the equations. The full model provided values of surface concentrations (coverages) of all species, showing that the dominant surface species are $CH_3CH_2O^{Al}$, OH^{Al}, H^O, and ^{O}, while all others represent far less than 1% of the total surface coverage. Consequently, terms for ethanol and water were dropped from the site balance equations. ^{Al} was retained in the balances as it was necessary to retain both surface vacancy terms in order to solve the system of equations.

Regarding the differential equations, it is known from the reaction path analysis of the full model that the forward and reverse rates of reactions (R1) through (R4) are all much faster than those of (R5) and (R6). Consequently, these slower rates represent a negligibly small perturbation on the surface concentrations of species, and therefore terms related to (R5) and (R6) were dropped from the differential balances. From the balances on $C_2H_5OH^{Al}$, H_2O^{Al}, $CH_3CH_2O^{Al}$ and OH^{Al}, respectively, the following equilibrium expressions were obtained:

$$K_1 = \frac{\left[C_2H_5OH^{Al}\right]}{P_{ethanol}\left[^{Al}\right]}$$

$$K_2 = \frac{\left[H_2O^{Al}\right]}{P_{H_2O}\left[^{Al}\right]}$$

$$K_3 = \frac{\left[CH_3CH_2O^{Al}\right]\left[H^O\right]}{\left[CH_3CH_2OH^{Al}\right]\left[^O\right]}$$

$$K_4 = \frac{\left[OH^{Al}\right]\left[H^O\right]}{\left[H_2O^{Al}\right]\left[^O\right]}$$

where K_1 through K_4 are the equilibrium constants for (R1) through (R4), respectively. These equations are consistent with a partial equilibrium analysis of the full model that showed that these four elementary steps are equilibrated.

The above QSS balance on H^O, after dropping very slow rates (r_{5f}), contains rates that were shown to be in equilibrium by the above expressions ($r_{3f} = r_{3r}$, $r_{4f} = r_{4f}$). Consequently, no additional information could be obtained from this balance and the extent of reaction-concept was applied instead. H^O is present in reactions (R3), (R4), and (R5). r_{5r} is approximately 0 and r_{5f} is slow, so (R5) need not be included in the analysis but was included for completeness. In (R3), H^O is produced (consumed) in a one-for-one manner when $CH_3CH_2O^{Al}$ is produced (consumed). Similarly, in (R4) and (R5), H^O is produced (consumed) in a 1-for-1 manner when OH^{Al} is produced (consumed). As a result, the following balance was written:

$$\left[H^O\right] = \left[C_2H_5O^{Al}\right] + \left[OH^{Al}\right]$$

After applying the above simplifications, the final seven equations containing seven unknown surface species concentrations were obtained:

$$K_1 = \frac{\left[C_2H_5OH^{Al}\right]}{P_{ethanol}\left[{}^{Al}\right]}$$

$$K_2 = \frac{\left[H_2O^{Al}\right]}{P_{H_2O}\left[{}^{Al}\right]}$$

$$K_3 = \frac{\left[CH_3CH_2O^{Al}\right]\left[H^O\right]}{\left[CH_3CH_2OH^{Al}\right]\left[{}^{O}\right]}$$

$$K_4 = \frac{\left[OH^{Al}\right]\left[H^O\right]}{\left[H_2O^{Al}\right]\left[{}^{O}\right]}$$

$$\left[H^{O}\right]=\left[C_2H_5O^{Al}\right]+\left[OH^{Al}\right]$$

$$S_{Al}=\left[C_2H_5O^{Al}\right]+\left[OH^{Al}\right]+\left[{}^{Al}\right]$$

$$S_{O}=\left[H^{O}\right]+\left[{}^{O}\right]$$

To obtain the final rate expressions for ethylene and ether production, the expressions for K_1 through K_4 were combined with the equation relating $[H^O]$ to $[C_3H_7O^{Al}]$ and $[OH^{Al}]$, yielding a solution for $[H^O]$ as well as further simplified site balances for Al and O:

$$\left[H^{O}\right]=\sqrt{\left(K_1K_3P_{ethanol}+K_2K_4P_{H_2O}\right)\left[{}^{Al}\right]\left[{}^{O}\right]}=\sqrt{Q\left[{}^{Al}\right]\left[{}^{O}\right]}$$

$$S_{Al}=\sqrt{Q\left[{}^{Al}\right]\left[{}^{O}\right]}+\left[{}^{Al}\right]$$

$$S_{O}=\sqrt{Q\left[{}^{Al}\right]\left[{}^{O}\right]}+\left[{}^{O}\right]$$

Each site balance was solved for either $[^O]$ or $[^{Al}]$ and substituted into the other site balance expression to yield closed-form expressions for $[^O]$ and $[^{Al}]$:

$$\left[{}^{Al}\right]=\frac{-\left(2S_{Al}+\left(S_{O}-S_{Al}\right)Q\right)\pm\sqrt{\left(2S_{Al}+\left(S_{O}-S_{Al}\right)Q\right)^2+4\left(Q-1\right){S_{Al}}^2}}{2\left(Q-1\right)}$$

$$\left[{}^{O}\right]=\frac{-\left(2S_{O}+\left(S_{Al}-S_{O}\right)Q\right)\pm\sqrt{\left(2S_{O}+\left(S_{Al}-S_{O}\right)Q\right)^2+4\left(Q-1\right){S_{O}}^2}}{2\left(Q-1\right)}$$

The positive root in each of the balances was used to obtain physical (non-negative) values of species concentrations. The final rate expressions for ethylene and diethyl ether formation are:

$$r_{E2}=r_{5f}=k_{5f}\left[C_2H_5OH^{Al}\right]\left[{}^{O}\right]=k_{5f}K_1P_{ethanol}\left[{}^{Al}\right]\left[{}^{O}\right]$$

$$r_{S_N2} = r_{6f} = k_{6f}\left[C_2H_5OH^{Al}\right]\left[C_2H_5O^{Al}\right] = \frac{k_{6f}K_1^{\,2}K_3P_{ethanol}^{\,2}\left[^{Al}\right]^{1.5}\left[^{O}\right]^{0.5}}{Q^{0.5}}$$

where Q, $[^{Al}]$ and $[^{O}]$ were defined above, and k_{5f} and k_{6f} are the forward rate constants for (R5) and (R6), respectively.

In order to determine what changes are needed in the model parameters to quantitatively describe experimental rates, the rate expressions were encoded in a script that utilizes built-in Matlab optimization routines. The site densities of Al and O are fixed to match the values specified in the microkinetic model, and application of a sensitivity analysis indicates that the E2 and S_N2 reaction barriers have the largest influence on the rate, whereas the equilibrium constants have a considerably smaller but non-zero effect (results not shown). Using only the two reaction barriers to fit the model produces a good fit, while the lowest value of the objective function is obtained using four parameters to fit (use of five or more parameters produces a comparable fit but much larger confidence intervals for the parameter estimates). Since the equilibrium constants all have a similar effect on the values of the rates, the constants for ethanol and water adsorption (K_1 and K_2, respectively) were selected as adjustable parameters. The parameters not adjusted in the reduced model are held fixed at the estimates that were obtained from DFT calculations (and used in the full model).

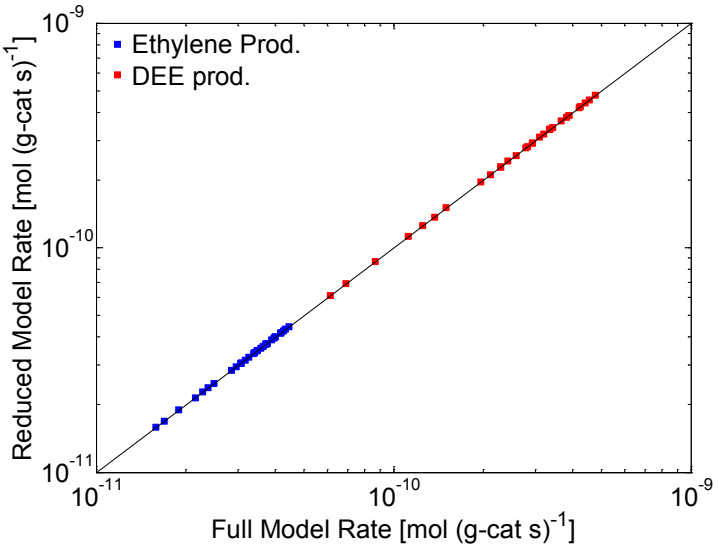

Figure D.15: Parity plot of reaction rates computed by the full microkinetic model and the reduced model.

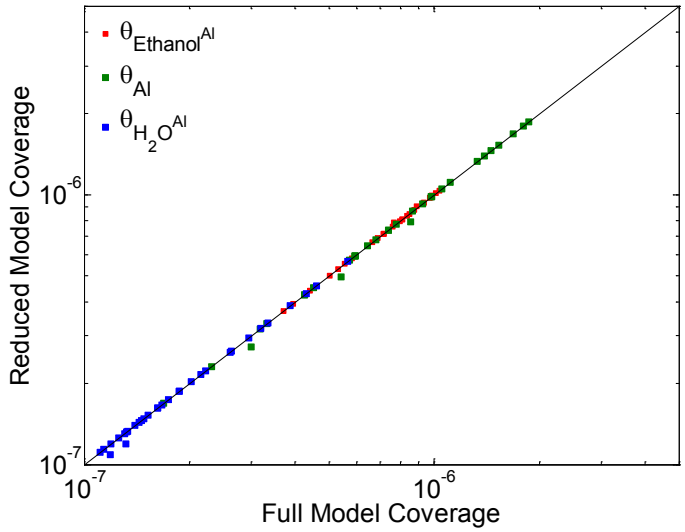

Figure D.16: Parity plot of ethanol, Al vacancy, and water species coverages computed by the full microkinetic model and the reduced model.

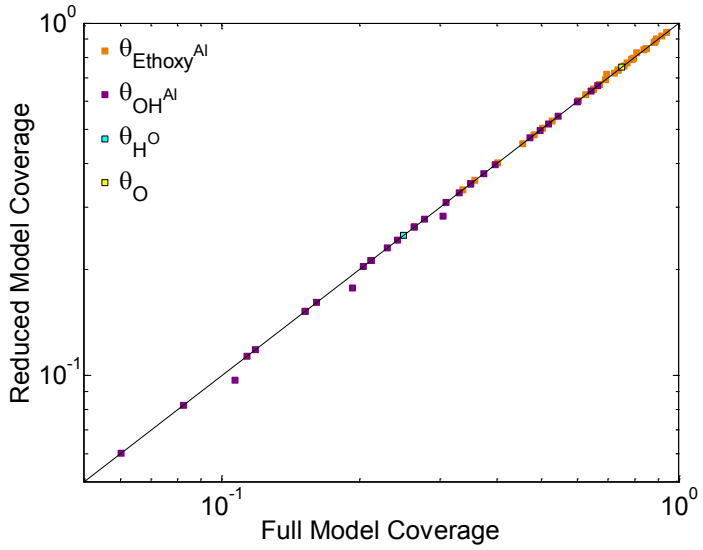

Figure D.17: Parity plot of ethoxy, hydroxyl, H, and O vacancy species coverages computed by the full microkinetic model and the reduced model.

Table D.2: Comparison of reaction orders obtained from the reduced model (in parentheses) with experimentally-determined orders.

CH_3CH_2OH Partial Pressure [kPa]	H_2O Partial Pressure [kPa]	Reaction Order	
		$C_4H_{10}O$ Production	C_2H_4 Production
1 – 5	0.4	0.2 (0.1)	0 (0.1)
1 – 5	0.6	0.4 (0.5)	0 (0.3)
1 – 5	1.1	0.5 (0.8)	0.1 (0.4)
4 – 7	2.2	0.6 (1.1)	0.3 (0.5)
4.2	0.5 - 2	-0.7 (-0.4)	-0.5 (-0.2)
3.0	0.5 - 2	-0.8 (-0.6)	-0.5 (-0.3)
0.9	0.5 - 2	-1.3 (-1.1)	-0.9 (-0.5)

Appendix E

FUTURE RESEARCH DIRECTIONS: EXAMPLE DATA

E.1 A Brønsted-Evans-Polanyi Relationship for Dehydration of Alcohols

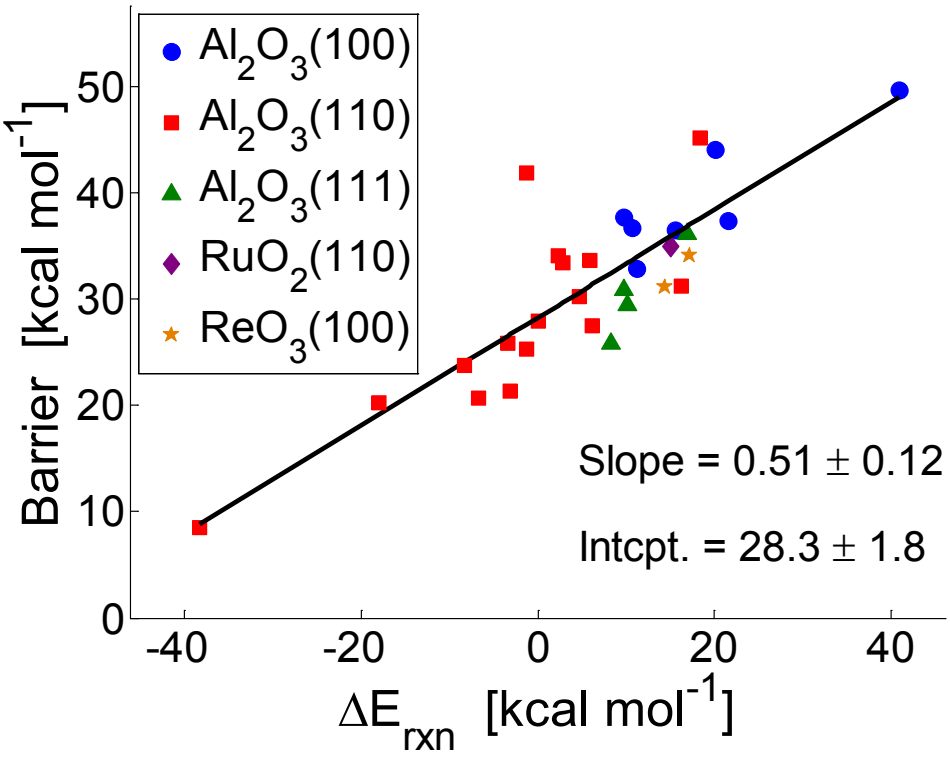

Figure E.1: A BEP for dehydration via the E2 mechanism, developed using several alcohols and ethers on different metal oxide surfaces. Data points are sorted by type of surface. 95% confidence intervals of the parameter estimates from the regression are indicated as ± values. Energetic data tabulated in Table E.1.

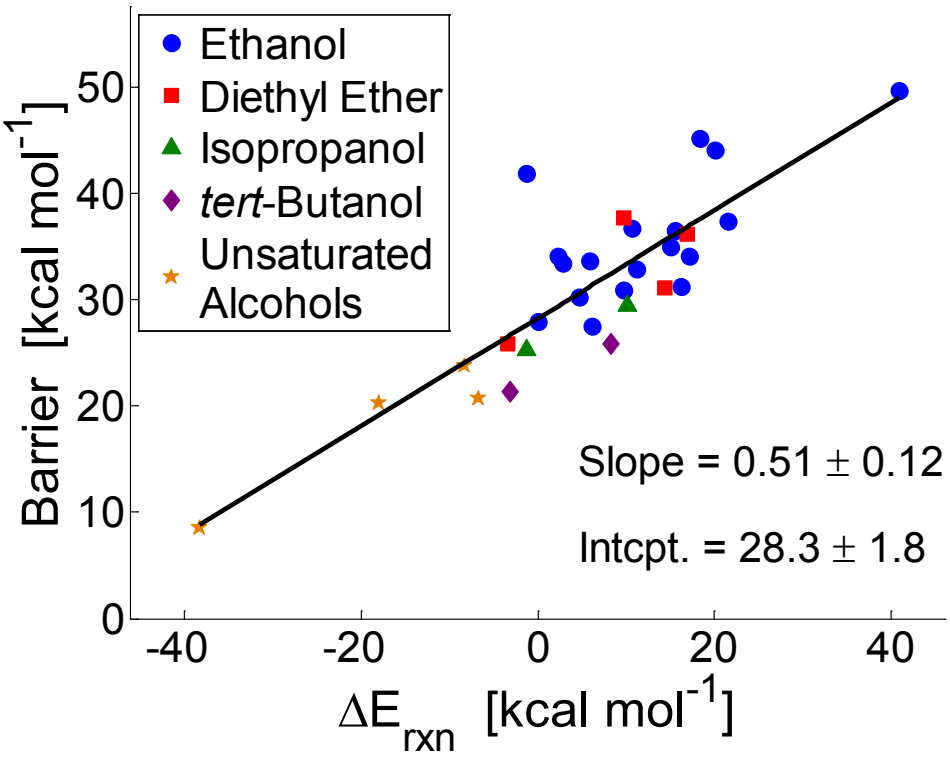

Figure E.2: A BEP for dehydration via the E2 mechanism, developed using several alcohols and ethers on different metal oxide surfaces. Data points are sorted by type of alcohol or ether. 95% confidence intervals of the parameter estimates from the regression are indicated as ± values. Energetic data tabulated in Table E.1

Table E.1: Data used to create the dehydration BEP displayed in Figures E.1 and E.2. Values reported in units of kcal mol^{-1}.

Reactant	ΔE_{rxn}	$E_{a,f}$	Reactant	ΔE_{rxn}	$E_{a,f}$
$Al_2O_3(100)$			$Al_2O_3(110)$		
Ethanol	10.7	36.7	Ethanol	0.0	28.0
Ethanol	15.5	36.5	Ethanol	16.2	31.2
Ethanol	21.5	37.4	Ethanol	6.2	27.5
Ethanol	40.9	49.7	Ethanol	4.7	30.3
Ethanol	20.1	44.1	Ethanol	5.9	33.7
Ethanol	11.2	32.8	Ethanol	2.9	33.5
Diethyl ether	9.7	37.7	Ethanol	-1.3	41.9
			Ethanol	18.3	45.1
$Al_2O_3(111)$			Ethanol	2.3	34.1
Ethanol	9.7	30.9	Diethyl ether	-3.4	25.9
Diethyl ether	16.9	36.1	Isopropanol	-1.2	25.3
Isopropanol	10.1	29.5	*tert*-Butanol	-3.1	21.4
tert-Butanol	8.2	25.8	m-cresol+2H	-38.2	8.5
			3-buten-1-ol	-8.3	23.7
$ReO_3(100)$			3-buten-2-ol	-6.8	20.7
Ethanol	17.2	34.0	1,5-hexadien-3-ol	-18.1	20.4
Diethyl ether	14.4	31.2			
			$RuO_2(110)$		
			Ethanol	15.1	35.0

E.2 An Example of the Effect of Configuration on Adsorption Energetics

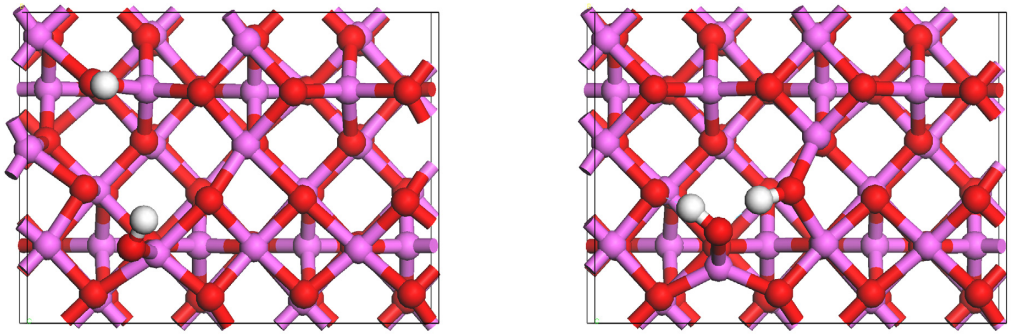

(a) $OH^{Va} + O^{H}$, ΔE_{ads} = -0.58 eV (b) $OH^{Va} + O^{H}$, ΔE_{ads} = -1.22 eV

Figure E.3: Adsorption energies for two different configurations of dissociated H_2O on γ-Al_2O_3(100). Adsorption energies are computed with respect to $H_2O_{(g)}$.

Appendix F

PERMISSIONS FOR REPRINT

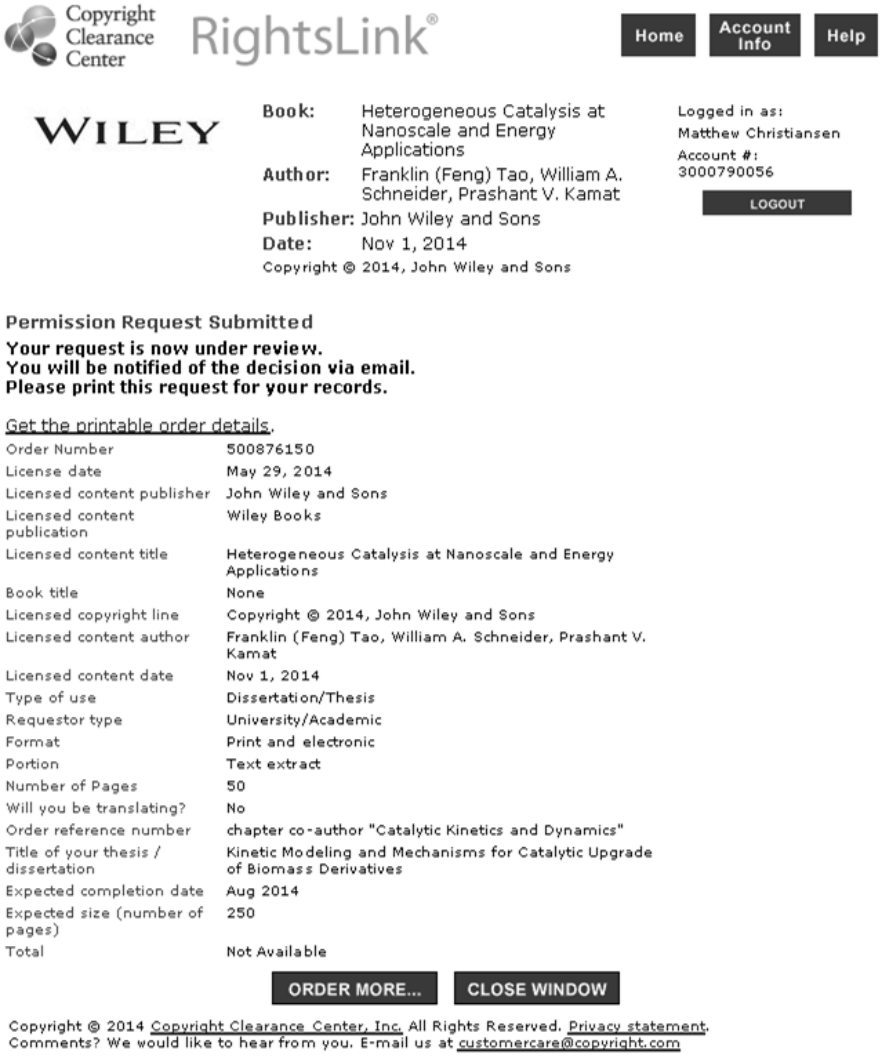

Copyright Clearance Center RightsLink®

Home | Account Info | Help

WILEY

Book: Heterogeneous Catalysis at Nanoscale and Energy Applications
Author: Franklin (Feng) Tao, William A. Schneider, Prashant V. Kamat
Publisher: John Wiley and Sons
Date: Nov 1, 2014
Copyright © 2014, John Wiley and Sons

Logged in as:
Matthew Christiansen
Account #:
3000790056
LOGOUT

Permission Request Submitted

Your request is now under review.
You will be notified of the decision via email.
Please print this request for your records.

Get the printable order details.

Order Number	500876150
License date	May 29, 2014
Licensed content publisher	John Wiley and Sons
Licensed content publication	Wiley Books
Licensed content title	Heterogeneous Catalysis at Nanoscale and Energy Applications
Book title	None
Licensed copyright line	Copyright © 2014, John Wiley and Sons
Licensed content author	Franklin (Feng) Tao, William A. Schneider, Prashant V. Kamat
Licensed content date	Nov 1, 2014
Type of use	Dissertation/Thesis
Requestor type	University/Academic
Format	Print and electronic
Portion	Text extract
Number of Pages	50
Will you be translating?	No
Order reference number	chapter co-author "Catalytic Kinetics and Dynamics"
Title of your thesis / dissertation	Kinetic Modeling and Mechanisms for Catalytic Upgrade of Biomass Derivatives
Expected completion date	Aug 2014
Expected size (number of pages)	250
Total	Not Available

ORDER MORE... CLOSE WINDOW

Copyright © 2014 Copyright Clearance Center, Inc. All Rights Reserved. Privacy statement.
Comments? We would like to hear from you. E-mail us at customercare@copyright.com

From: Willcox, Emma - Chichester
To: Matthew Christiansen
Subject: FW: RightsLink Job Ticket Number 500876150
Date: Thursday, June 05, 2014 11:36:13 AM

Dear Matt Christiansen,

Thank you for your request.

Permission is granted for you to use the material requested for your thesis/dissertation subject to the usual acknowledgements (author, title of material, title of book/journal, ourselves as publisher) and on the understanding that you will reapply for permission if you wish to distribute or publish your thesis/dissertation commercially.

You should also duplicate the copyright notice that appears in the Wiley publication in your use of the Material. Permission is granted solely for use in conjunction with the thesis, and the material may not be posted online separately.

Any third party material is expressly excluded from this permission. If any material appears within the article with credit to another source, authorisation from that source must be obtained.

We wish you every success with your thesis.

Kind Regards

Emma Willcox
Permissions Assistant

WILEY

Copyright Clearance Center RightsLink®

Home | Account Info | Help

Title: A review of multiscale modeling of metal-catalyzed reactions: Mechanism development for complexity and emergent behavior
Author: M. Salciccioli,M. Stamatakis,S. Caratzoulas,D.G. Vlachos
Publication: Chemical Engineering Science
Publisher: Elsevier
Date: 1 October 2011
Copyright © 2011, Elsevier

Logged in as:
Matthew Christiansen
Account #:
3000790056
LOGOUT

Order Completed

Thank you very much for your order.

This is a License Agreement between Matthew Christiansen ("You") and Elsevier ("Elsevier"). The license consists of your order details, the terms and conditions provided by Elsevier, and thepayment terms and conditions.

Get the printable license.

License Number	3403690217911
License date	Jun 07, 2014
Licensed content publisher	Elsevier
Licensed content publication	Chemical Engineering Science
Licensed content title	A review of multiscale modeling of metal-catalyzed reactions: Mechanism development for complexity and emergent behavior
Licensed content author	M. Salciccioli,M. Stamatakis,S. Caratzoulas,D.G. Vlachos
Licensed content date	1 October 2011
Licensed content volume number	66
Licensed content issue number	19
Number of pages	37
Type of Use	reuse in a thesis/dissertation
Portion	figures/tables/illustrations
Number of figures/tables/illustrations	1
Format	both print and electronic
Are you the author of this Elsevier article?	No
Will you be translating?	No
Title of your thesis/dissertation	Kinetic Modeling and Mechanisms for Catalytic Upgrade of Biomass Derivatives
Expected completion date	Aug 2014
Estimated size (number of pages)	250
Elsevier VAT number	GB 494 6272 12
Permissions price	0.00 USD
VAT/Local Sales Tax	0.00 USD / 0.00 GBP
Total	0.00 USD

ORDER MORE... CLOSE WINDOW

Copyright © 2014 Copyright Clearance Center, Inc. All Rights Reserved. Privacy statement.
Comments? We would like to hear from you. E-mail us at customercare@copyright.com

Copyright Clearance Center RightsLink®

Home | Account Info | Help

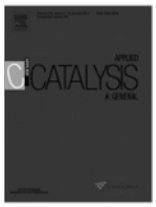

Title: Microkinetic modeling of Pt-catalyzed ethylene glycol steam reforming

Author: Matthew A. Christiansen,Dionisios G. Vlachos

Publication: Applied Catalysis A: General

Publisher: Elsevier

Date: 26 July 2012

Copyright © 2012, Elsevier

Logged in as:
Matthew Christiansen
Account #:
3000790056

LOGOUT

Order Completed

Thank you very much for your order.

This is a License Agreement between Matthew Christiansen ("You") and Elsevier ("Elsevier"). The license consists of your order details, the terms and conditions provided by Elsevier, and thepayment terms and conditions.

Get the printable license.

License Number	3403690419327
License date	Jun 07, 2014
Licensed content publisher	Elsevier
Licensed content publication	Applied Catalysis A: General
Licensed content title	Microkinetic modeling of Pt-catalyzed ethylene glycol steam reforming
Licensed content author	Matthew A. Christiansen,Dionisios G. Vlachos
Licensed content date	26 July 2012
Licensed content volume number	431–432
Number of pages	7
Type of Use	reuse in a thesis/dissertation
Portion	full article
Format	both print and electronic
Are you the author of this Elsevier article?	Yes
Will you be translating?	No
Title of your thesis/dissertation	Kinetic Modeling and Mechanisms for Catalytic Upgrade of Biomass Derivatives
Expected completion date	Aug 2014
Estimated size (number of pages)	250
Elsevier VAT number	GB 494 6272 12
Permissions price	0.00 USD
VAT/Local Sales Tax	0.00 USD / 0.00 GBP
Total	0.00 USD

ORDER MORE... CLOSE WINDOW

Copyright © 2014 Copyright Clearance Center, Inc. All Rights Reserved. Privacy statement.
Comments? We would like to hear from you. E-mail us at customercare@copyright.com

Copyright Clearance Center RightsLink®

Home | Account Info | Help

ACS Publications
MOST TRUSTED. MOST CITED. MOST READ.

Title: Density Functional Theory-Computed Mechanisms of Ethylene and Diethyl Ether Formation from Ethanol on γ-Al2O3(100)
Author: Matthew A. Christiansen, Giannis Mpourmpakis, and Dionisios G. Vlachos
Publication: ACS Catalysis
Publisher: American Chemical Society
Date: Sep 1, 2013
Copyright © 2013, American Chemical Society

Logged in as:
Matthew Christiansen
LOGOUT

PERMISSION/LICENSE IS GRANTED FOR YOUR ORDER AT NO CHARGE

This type of permission/license, instead of the standard Terms & Conditions, is sent to you because no fee is being charged for your order. Please note the following:

- Permission is granted for your request in both print and electronic formats, and translations.
- If figures and/or tables were requested, they may be adapted or used in part.
- Please print this page for your records and send a copy of it to your publisher/graduate school.
- Appropriate credit for the requested material should be given as follows: "Reprinted (adapted) with permission from (COMPLETE REFERENCE CITATION). Copyright (YEAR) American Chemical Society." Insert appropriate information in place of the capitalized words.
- One-time permission is granted only for the use specified in your request. No additional uses are granted (such as derivative works or other editions). For any other uses, please submit a new request.

BACK | CLOSE WINDOW

Copyright © 2014 Copyright Clearance Center, Inc. All Rights Reserved. Privacy statement.
Comments? We would like to hear from you. E-mail us at customercare@copyright.com

Copyright Clearance Center RightsLink®

Home | Account Info | Help

ACS Publications
MOST TRUSTED. MOST CITED. MOST READ.

Title: Site-Dependent Lewis Acidity of γ-Al2O3 and its Impact on Ethanol Dehydration and Etherification
Author: Glen Richard Jenness, Matthew A Christiansen, Stavros Caratzoulas, Dionisios G. Vlachos, and Raymond J. Gorte
Publication: The Journal of Physical Chemistry C
Publisher: American Chemical Society
Date: May 1, 2014
Copyright © 2014, American Chemical Society

Logged in as:
Matthew Christiansen
Account #:
3000790056
LOGOUT

PERMISSION/LICENSE IS GRANTED FOR YOUR ORDER AT NO CHARGE

This type of permission/license, instead of the standard Terms & Conditions, is sent to you because no fee is being charged for your order. Please note the following:

- Permission is granted for your request in both print and electronic formats, and translations.
- If figures and/or tables were requested, they may be adapted or used in part.
- Please print this page for your records and send a copy of it to your publisher/graduate school.
- Appropriate credit for the requested material should be given as follows: "Reprinted (adapted) with permission from (COMPLETE REFERENCE CITATION). Copyright (YEAR) American Chemical Society." Insert appropriate information in place of the capitalized words.
- One-time permission is granted only for the use specified in your request. No additional uses are granted (such as derivative works or other editions). For any other uses, please submit a new request.

BACK | CLOSE WINDOW

Copyright © 2014 Copyright Clearance Center, Inc. All Rights Reserved. Privacy statement.
Comments? We would like to hear from you. E-mail us at customercare@copyright.com

Copyright Clearance Center RightsLink®

Home | Account Info | Help

WILEY

Title: Carbon-Supported Gold Nanocatalysts: Shape Effect in the Selective Glycerol Oxidation
Author: Di Wang, Alberto Villa, Dangsheng Su, Laura Prati, Robert Schlögl
Publication: ChemCatChem
Publisher: John Wiley and Sons
Date: Nov 30, 2012
Copyright © 2013 WILEY-VCH Verlag GmbH %26 Co. KGaA, Weinheim

Logged in as:
Matthew Christiansen
Account #:
3000790056
LOGOUT

Order Completed

Thank you very much for your order.

This is a License Agreement between Matthew Christiansen ("You") and John Wiley and Sons ("John Wiley and Sons"). The license consists of your order details, the terms and conditions provided by John Wiley and Sons, and the payment terms and conditions.

Get the printable license.

License Number	3406100492861
License date	Jun 11, 2014
Licensed content publisher	John Wiley and Sons
Licensed content publication	ChemCatChem
Licensed content title	Carbon-Supported Gold Nanocatalysts: Shape Effect in the Selective Glycerol Oxidation
Licensed copyright line	Copyright © 2013 WILEY-VCH Verlag GmbH %26 Co. KGaA, Weinheim
Licensed content author	Di Wang,Alberto Villa,Dangsheng Su,Laura Prati,Robert Schlögl
Licensed content date	Nov 30, 2012
Start page	2717
End page	2723
Type of use	Dissertation/Thesis
Requestor type	University/Academic
Format	Print and electronic
Portion	Figure/table
Number of figures/tables	1
Original Wiley figure/table number(s)	Figure S1 (supporting information)
Will you be translating?	No
Title of your thesis / dissertation	Kinetic Modeling and Mechanisms for Catalytic Upgrade of Biomass Derivatives
Expected completion date	Aug 2014
Expected size (number of pages)	250
Total	0.00 USD

ORDER MORE... CLOSE WINDOW

Copyright © 2014 Copyright Clearance Center, Inc. All Rights Reserved. Privacy statement.
Comments? We would like to hear from you. E-mail us at customercare@copyright.com